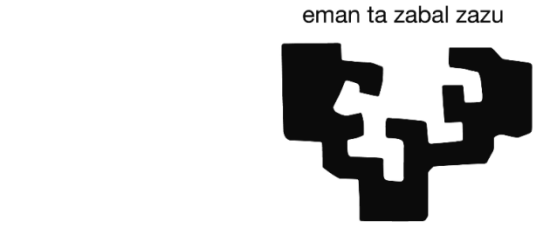

Universidad del País Vasco

Euskal Herriko Unibertsitatea

PLANETCAM-UPV/EHU: A DUAL CHANNEL LUCKY IMAGING CAMERA FOR SOLAR SYSTEM STUDIES. PERFORMANCE, CALIBRATION AND SCIENTIFIC APPLICATIONS

by

Iñigo Mendikoa Alonso

Advisors:

Agustín Sánchez-Lavega

Santiago Pérez-Hoyos

Thesis presented in partial fulfillment of the requirements for the degree of

Doctor of Philosophy

at the Department of Applied Physics I, Faculty of Engineering, UPV/EHU

2017

Acknowledgements

I would like to express my special gratitude to my thesis directors Agustin and Santi, who have supported me throughout all these years always with the right criteria and patience. Their invaluable expertise made me able to do things right at the first time where I would have otherwise lost so much time or even the right way. I also want to extend my gratitude to the rest of the *Grupo de Ciencias Planetarias* (GCP) team at the *UPV-EHU*, and in particular to Ricardo Hueso for his countless hours devoted to the development of the pipeline PLAYLIST as well as countless images processing, and José Felix Rojas for his support based on a deep expertise in all the technology relevant to *PlanetCam*. Making a PhD while having a different full time job is not an easy task, but within the GCP team, 'standing on the shoulders of giants', everything became much easier. In fact, I doubt I would have otherwise made the decision to go for a PhD in my circumstances.

I thank Drs. Asuncion Illarramendi and Dr. Iñaki Bikandi from *UPV/EHU* for their continuous support during laboratory measurements and Javier Lopez from the *Universidad Carlos III* for his stellar spectrum synthetic models. I also want to remember our friend and outstanding astrophysicist Javier Gorosabel, who supported *PlanetCam* team and was also there at *Calar Alto* during our GRB afterglow detection in 2013. His decease is the only thing I would like to forget from all my PhD experience.

Of course all this work would have been impossible without the observation 'missions' performed from 2012 to 2017 at *Pic-du-Midi*, *Instituto de Astrofísica de Canarias* and, in particular, *Calar Alto* observatories. Special thanks to the staff at *Calar Alto* for their support in so many long nights throughout these years, making easy to me even the remote connections and other information technology stuff. And, after all, the food up there was not so bad.

My family also had to suffer my absence not only during my trips to the observatories but also for many hours devoted to this work when I was expected to be with them, so somehow this work is also theirs.

And last, but not least, this work was supported, in a different way, by the Spanish *MICIIN* projects (*MINECO* AYA2012-36666/AYA2015-65041-P, *FEDER*, *UE*), *Grupos Gobierno Vasco* and '*Infraestructura'* grants from *Gobierno Vasco* (IT765-13) and *UPV/EHU* (INF13/74, INF15/37, UFI 11/55), as well as by *Aula Espazio Gela* funded by *Diputación Foral de Bizkaia* (OF-20/09/2012-2012-06274, 17-06-10-15-UPV 2-31-33-2015-47).

Contents

Chapter 6

Chapter 1

INTRODUCTION

Imaging astronomical objects at high spatial resolution requires overcoming the pernicious effects of atmospheric turbulence generically known as "seeing" in the astronomical context (Fried, 1965). The use of space telescopes and active and adaptive optical systems have been the classical solutions mainly applied in the near-infrared range (Hardy J.W., 2000). Adaptive optics evolves rapidly in particular for large fields of view and it is present and will be incorporated in most major telescopes (e. g. Extremely-European Large Telescope, E-ELT at ESO) as a key observing system. With lower costs, the "lucky imaging technique" based on the alignment and stacking of hundreds or thousands of short exposures (Lelièvre et al., 1988; Law et al., 2005), has been successfully employed for high resolution imaging at visible wavelengths in a number of astronomical contexts. In particular, the lucky-imaging technique has become popular in the amateur world (Mousis et al., 2014) allowing astronomical images acquired by amateurs operating small-size telescopes to be successfully used in planetary atmospheres research (Sánchez-Lavega et al., 2008, 2010, 2011, 2015; Barrado-Izagirre et al., 2013). There are a number of astronomical cameras based on the lucky imaging concept operating in different observatories, all of them at visible wavelengths. One of the earliest ones was *LuckyCam*[1] developed at the Cambridge University (Law, 2006) used at the Nordic Optical Telescope in Roque de los

[1] http://www.not.iac.es/instruments/luckycam/

Muchachos (La Palma, Canarias, Spain) and also at the 200-inches Hale telescope in Mount Palomar Observatory[2]. The lucky-imaging concept was also used by the camera *AstraLux*, developed by the Max Planck Institute for Astronomy (Hormuth, 2007). *AstraLux* is used at Calar Alto Observatory[3] (Almeria, Spain – AstraLux Norte) and on La Silla Observatory (Chile – AstraLux Sur). *FastCam* is another instrument designed by the Instituto de Astrofísica de Canarias and Universidad Politécnica de Cartagena (López-López, 2012). More sophisticated instruments are currently being developed like *OctoCam*, designed by the Instituto de Astrofísica de Andalucía[4], which will simultaneously observe in eight channels. Newer concepts include the ability to combine lucky imaging with adaptive optics, as the instrument AOLI (Mackay et al. 2012), Adaptive Optics Lucky Imager[5], being currently tested in the William Herschel Telescope and the 10.4m GTC telescope.

1.1 PlanetCam-UPV/EHU

PlanetCam-UPV/EHU, hereafter *PlanetCam* (Sánchez-Lavega et al., 2012; Mendikoa et al., 2016), is an astronomical camera designed for high-resolution imaging of Solar System targets, in particular supporting scientific research in atmospheric dynamics and vertical cloud structure of Solar System planetary atmospheres. It works simultaneously in two channels (by means of a dichroic beam splitter), each one with its own detector and filters of interest: Visible (0.38 – 1 μm) and short wave near infrared SWIR (1 – 1.7 μm) (Sánchez-Lavega et al., 2012). The instrument contains several filters selected for color, broad band continuum, methane and CO_2 absorption bands and their adjacent narrow continuum wavelengths selected for their interest for planetary studies. *PlanetCam* uses the 'lucky imaging' technique for broad band filters but longer exposures (a few seconds each and also stacked for building high signal-to-noise ratio images) can also be attained for narrow band imaging. The final stacked images can be processed to obtain high-resolution observations that largely remove the blur from atmospheric effect, while the selection of the best 1-10% of frames without adding any

[2] http://www.astro.caltech.edu/~nlaw/lucky_palomar/

[3] http://www.caha.es/

[4] http://www.iaa.es/

[5] http://www.ing.iac.es/PR/inst.php?inst=AOLI

additional image processing results in high-quality images that retain the photometry of the object observed.

PlanetCam has been designed for two possible operational independent configurations: *PlanetCam1* is aimed to perform observations only in the visible channel (380 nm – 1μm), and *PlanetCam2* provides simultaneous observations in Visible and the SWIR (1 – 1.7 μm) (Sánchez-Lavega et al., 2012). *PlanetCam1* is easily transportable and has been tested in a variety of telescopes, having been performed its first tests at the 0.5 m telescope at the Observatorio Aula Espazio Gela in the University of the Basque Country in 2012 (Sánchez-Lavega et al., 2014). *PlanetCam2* is a more complex instrument and currently operates only at the 1.23m and 2.2m telescopes at *Calar Alto Observatory*. The regular scientific use of *PlanetCam* has been performed since 2012 mainly at these telescopes, yet some tests have been run also at the 1.05m telescope at Pic du Midi Observatory (France) and the 1.5m Telescopio Carlos Sánchez (TCS) at *Teide Observatory* pertaining to the *Instituto de Astrofísica de Canarias* (IAC).

1.2 Objectives of PlanetCam

The main objective of *PlanetCam* is the study, on a regular basis and at various spatial and temporal scales of the atmospheres of Venus, Mars, Jupiter, Saturn, Uranus, Neptune and the satellite Titan. This comprises the evolution of the vertical distribution and properties of clouds and hazes, retrieval of atmospheric winds in Jupiter, Saturn and Venus, the study of their meteorological phenomena, and the study of occasional events such as transient major atmospheric disturbances (Sánchez-Lavega et al., 1982, 2008, 2011, 2015), impacts on Jupiter (Sánchez-Lavega et al., 2010; Hammel et al., 2010; Hueso et al., 2010, 2013) or major transient atmospheric features in Mars (Sánchez-Lavega et al. 2014).

Absolute reflectivity calibration of planetary images has been a major issue in this Thesis (Mendikoa et al., 2017). Knowledge of the absolute reflectivity is essential for modeling the light scattered by planetary atmospheres, and particular attention has been given to Jupiter and Saturn for which monitoring on a yearly basis is prescribed, given the spatial and temporal evolution of their atmospheres. The combination of observations at different wavelengths from the visible to the near infrared allows probing a wide range of altitudes in the atmospheres of these planets. The idea of using

images of the giant planets acquired in different methane absorption bands to gain insight into the horizontal and vertical structure of their atmospheres is not new (West et al., 1980, 1982, 1983) but acquiring enough images at multiple bands at high spatial resolutions is generally difficult. When using multispectral imaging, the loss of spectral resolution can be compensated by the gain in spatial resolution, particularly if filters are properly defined to match the absorption bands and adjacent continuums and other wavelengths of interest (such as the so-called chromophore absorptions at short wavelengths defining the Jupiter's red colors and Saturn's pale tones, West et al., 2005).

Although there are many works dealing with calibrated observations in the visible part of the spectrum for Jupiter and Saturn, including Hubble Space Telescope (HST) calibrated observations (e.g. Pérez-Hoyos et al., 2005; Karkoschka et al., 2005) or spacecraft imaging (Pérez-Hoyos et al., 2016), the near infrared side of the spectrum (SWIR, short wavelength infrared) has been analyzed less often (de Pater et al., 2010). In this thesis, we will profusely refer to a number of previous studies that served as an external reference for the absolute reflectivity values we get. It must be noted that, while no seasonal variability has been reported in Jupiter's atmosphere (except for planetary-scale) changes at particular belts and zones are observed not linked to seasonal changes; see Sánchez-Lavega and Gómez, 1996; Sánchez-Lavega et al., 2008; 2017; Fletcher et al., 2011; Pérez-Hoyos et al. 2012).

Saturn is known to display hemispherical seasonal changes as well as changing viewing/illumination geometry due to the tilt of its rotation axis (West et al., 2009). For this reason, Saturn photometric values usually only serve as a snapshot for a particular season. For visual wavelengths (380-1000 nm, covered by *PlanetCam* VIS channel), Karkoschka (1998) provided the giant planets geometric albedo through medium resolution spectroscopy, while Chanover et al. (1996) covered a wide visible wavelength range providing Jupiter absolute reflectivity values. A similar work for the near infrared part of the spectrum was presented by Vincent et al. (2005). More recently, and at the same time as *PlanetCam* observations, visible absolute reflectivity data were available from HST for both Saturn (July 2015) and Jupiter (OPAL[6], February 2016). Data in the SWIR channel are much scarcer, calibrated data were used from those presented in de Pater et al. (2010) for Jupiter and disk-integrated spectra at

[6] https://archive.stsci.edu/prepds/opal/

medium resolution from Clark and McCord (1979) as a reference for both Jupiter and Saturn. This makes clear that an updated reference for Jupiter's and Saturn's reflectivity in an ample wavelength range is of interest for future works dealing with calibrated images from these planets as well as other giant planets outside our Solar System.

Moreover, the availability of Jupiter and Saturn calibrated images in a consistent set of filters and through a number of observation campaigns can also provide support to space missions in the study of their atmospheres, as it was done by other ground based observations of Jupiter and Saturn at the time of Voyager 1 and 2 flybys (Bergstralh et al., 1981; West et al., 1982; Cochran, 1982). In the case of Jupiter, ground-based support is being given currently to NASA's Juno mission, in orbit around Jupiter since June 2016 (Sánchez-Lavega et al., 2017; Hueso et al., 2017b). In the case of Saturn's atmosphere, ground-based observations can provide complementary information at low phase angles when the near to end Cassini mission is observing the planet at other geometries with higher phase angles (Pérez-Hoyos et al., 2016). Here, the results of observations from 2012 to 2016 are presented, which has allowed the creation of a wide database of Jupiter and Saturn calibrated images in reflectivity. This database will hopefully be enlarged with further observations to be retrieved in the future. As the time of this writing we have some observing runs already awarded and waiting to be completed for semesters 2017A and 2017B at 2.2m telescope in Calar Alto Observatory.

Imaging of the planets at different wavelengths also allows study the aerosol and cloud properties, meteorological phenomena, measurement of global winds and assessments of the spatial and temporal scales of evolution. Absolute radiometric calibration using standard stars allows obtaining the spectral and spatial dependence of the reflectivity across the planetary disk (from center-to-limb or north-south scans) and/or for particular features (Sánchez-Lavega, 2011). Modeling of the absolute reflectivity allows retrieving the cloud and aerosol vertical distribution and their optical properties (Hansen and Travis, 1984; Pérez-Hoyos et al., 2005, 2009, 2012). *PlanetCam* images have been used so far for several works on Jupiter (Hueso et al., 2017b; Sánchez-Lavega et al., 2017), Saturn (Sánchez-Lavega et al., 2014, 2016), Venus (Sánchez-Lavega et al., 2016) and Neptune (Hueso et al., 2017a).

Finally, other Solar System objects are also potential targets for *PlanetCam*, particularly when high spatial or temporal resolution are required, such as activity in comets, asteroids, and occultation phenomena that require a high rate temporal sampling. *PlanetCam* has also been tested and occasionally used for a fast response to the detection of the visible afterglow from a Gamma Ray Burst (Gorosabel et al., 2013) and extrasolar planet transits. Finally, other potential astronomical targets for the camera are binary and multiple stellar systems, and globular clusters.

1.3 Goals and Structure of this Thesis

The main objective within the scope of this Thesis has been to characterize the radiometric and astronomic performance of the *PlanetCam* instrument, as well as its absolute reflectivity calibration, also providing values of Jupiter and Saturn absolute reflectivity over four years of observation campaigns. Also, a set of scientific applications to the Solar System planets have been performed in terms of atmospheric dynamics and Radiative Transfer modeling for atmospheric vertical structure analysis.

The structure of this Thesis is as follows:

- Chapter 1 provides a brief description of the rationale of the *PlanetCam* instrument and its main objectives.
- Chapter 2 describes *PlanetCam* instrument and its radiometric characterization in laboratory. The *PlanetCam* concept is described for the two configurations of the camera, including the characterization of the VIS and SWIR channels and their detectors. The camera control is also briefly described.
- Chapter 3 describes the astronomical performance of *PlanetCam*, including the image processing methods and the pipeline developed for this instrument, and a brief study of its astronomical performance for both the VIS and SWIR channels based on the analysis of some close binary systems and stellar clusters. The instrument's limiting magnitudes are also estimated for a number of cases.
- Chapter 4 describes the photometric calibration of *PlanetCam* performed over Jupiter and Saturn images. The calibration procedure is described and absolute reflectivity values of Jupiter and Saturn are presented and compared with available reference values, also discussing different sources of uncertainty.
- Chapter 5 reviews the specific research activities performed so far with *PlanetCam* images for the different planets, both in terms of atmospheric

dynamics and vertical structure based on radiative transfer modeling of photometry calibrated images.

- Chapter 6 summarizes the main conclusions from the work performed within this Thesis, and proposes further related research activities.

Chapter 2

INSTRUMENT DESIGN AND LABORATORY TESTS

This chapter describes the *PlanetCam* instrument and its radiometric characterization in laboratory. The organization of this chapter is as follows. In section 2.1 the *PlanetCam* concept is described for the two configurations of the camera. Section 2.2 is devoted to the characterization of the visible channel and its sCMOS detector while section 2.3 describes the SWIR channel and its InGaAs detector. Finally, section 2.4 deals with the camera control.

2.1 General Instrument Description

The *PlanetCam* concept includes two operationally independent configurations. *PlanetCam1* is a low weight, easily transportable and manageable camera for fast installation in a telescope when a quick observational response is needed in case of an unusual or unexpected event. It can be mounted in small telescopes (diameters ≥ 0.5m) and provides different magnifications. *PlanetCam2* is a more complex and heavier instrument with two channels that operate simultaneously and require independent operation and control. It is usually operated at 1.23m and 2.2m telescopes at Calar Alto Astronomical Observatory.

2.1.1 Configuration of PlanetCam1

Under the first configuration, *PlanetCam1* operates only in the visible channel and with high magnification at the focal plane. The main elements constituting the camera are a sCMOS detector (also employed in *PlanetCam2* visible channel), two

filter wheels and an interchangeable Barlow lens to provide the required magnification (Figure 2.1, Sánchez-Lavega et al., 2012). This camera was designed in collaboration with and constructed by the Advanced Design and Analysis division at IDOM[7].

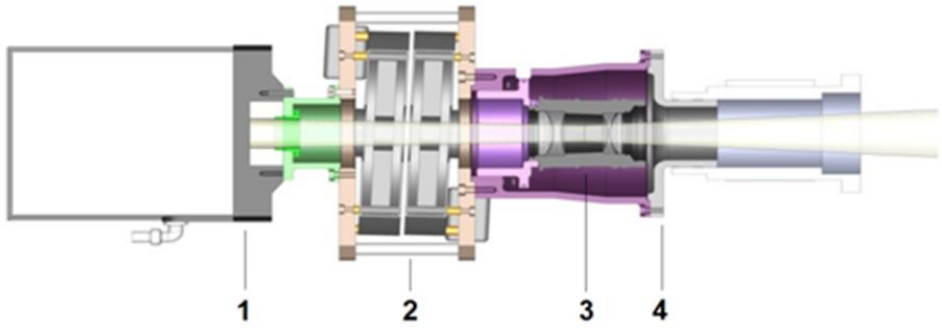

Figure 2.1. *PlanetCam1* engineering diagram showing from left to right: 1-sCMOS detector, 2-filter wheels, 3-Barlow lens and 4-telescope adaptor. Quick access to the Barlow lens is possible by removing one lid in the lateral structure supporting the instrument. The inclination of the filters wheels avoids internal reflections.

2.1.2 Configuration of PlanetCam2

This configuration has two channels (VIS and SWIR) operating simultaneously. A scheme of the instrument and its location at the telescope focus is shown in Figure 2.2, while Figure 2.3 shows its main dimensions, Figure 2.4 pictures of both Visible and SWIR detectors and Figure 2.5 the optical configuration of the camera. The beam from the telescope is first collimated and then split at 90° in two beams (visible and SWIR wavelengths) by the dichroic element. Before reaching the detector, the beam in each channel passes through a filter wheel and an optical magnification system (three possible magnifications are available).

Motorized modules are used on each channel for selection of one over three possible optical configurations. Each configuration requires focusing the camera by changing the position of the detector with respect to the focus of the telescope, which remains the same to obtain a collimated beam before the dichroic splitter. Focusing of each detector is achieved by a motorized automatic stage. This camera was designed in collaboration with and constructed by iTec Astronomica[8].

[7] http://ada.idom.com/en/

[8] http://astro-itec.es/

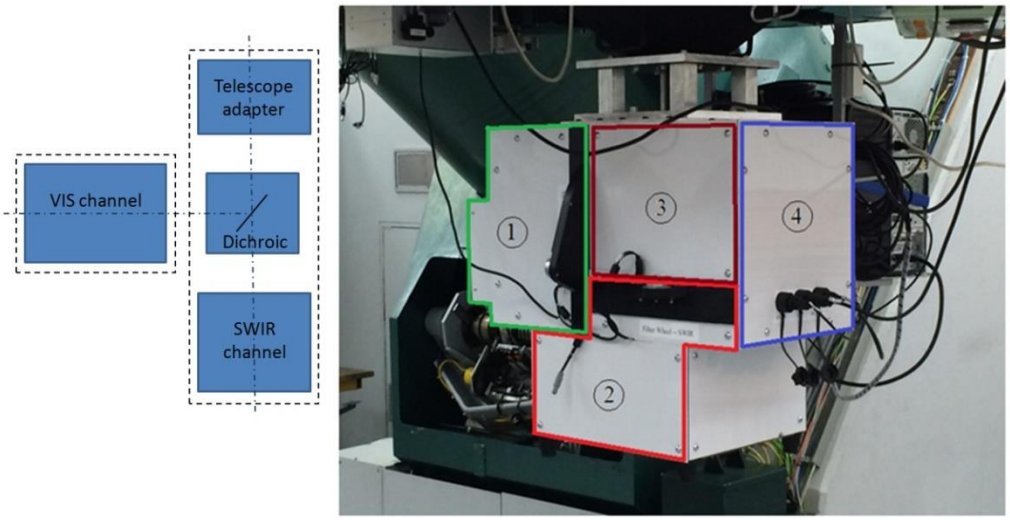

Figure 2.2. Left: *PlanetCam2* general scheme. Right: *PlanetCam2* attached to the Cassegrain focus of the 1.23m of Calar Alto Observatory. Each subsystem module has been colored in the picture: (1) Visible channel, (2) SWIR channel, (3) Collimator and dichroic, (4) Electronics.

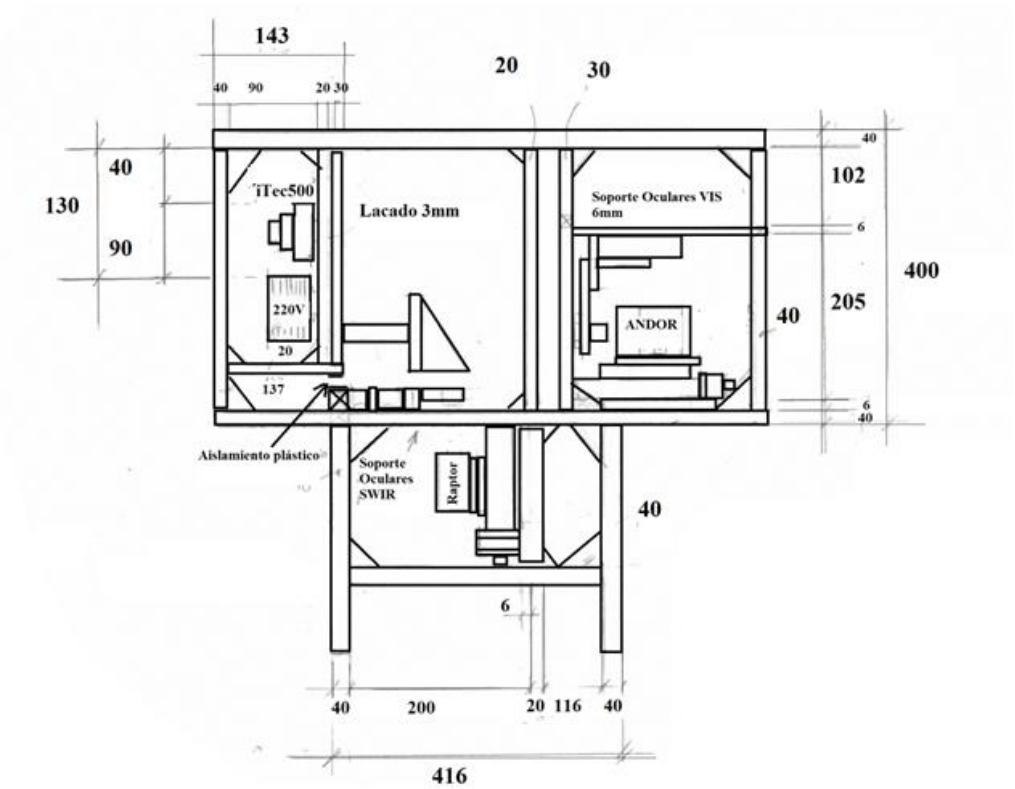

Figure 2.3. *PlanetCam2* main dimensions and components distribution (iTEC)

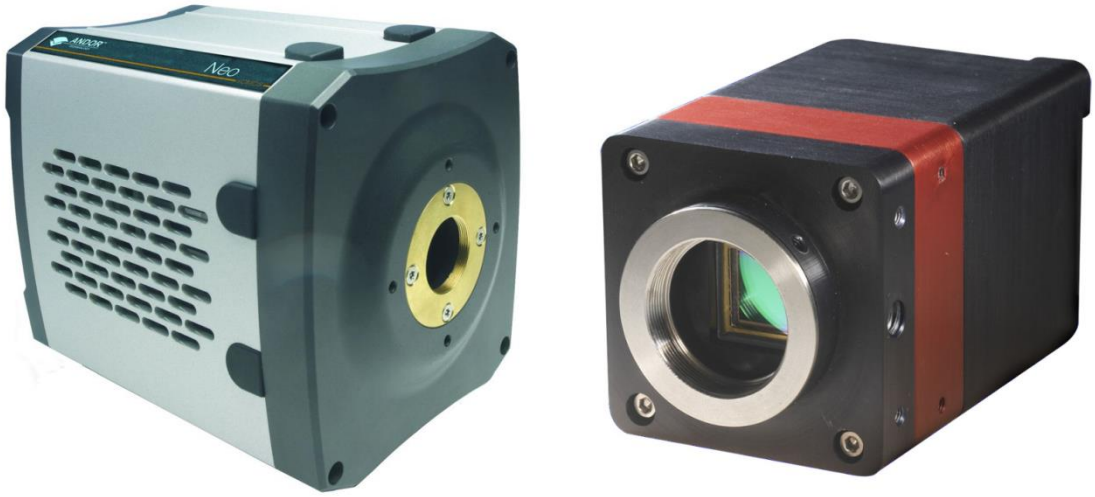

Figure 2.4. *PlanetCam* detectors for Visible channel (left) and SWIR channel (right)

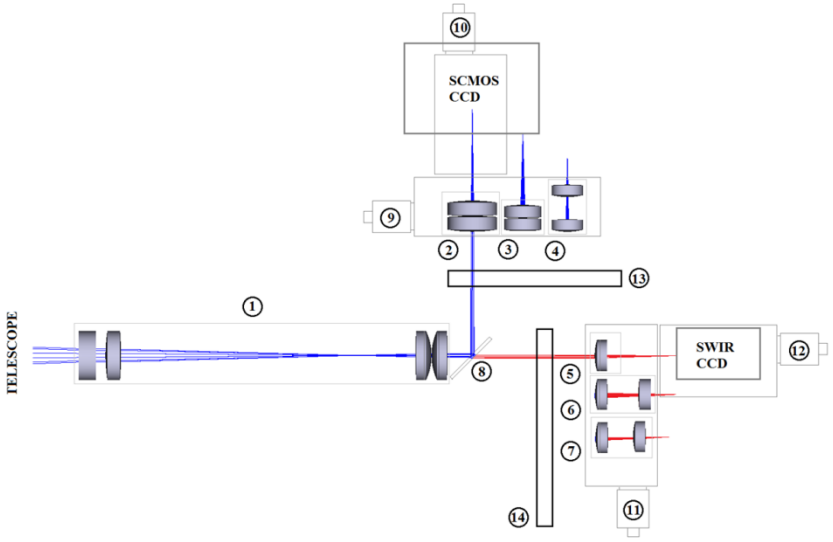

Figure 2.5. *PlanetCam2* diagram showing the following elements:(1) Collimator, (2-4) Optical magnification for the visible channel (high, medium, low), (5-7) Optical magnification for the SWIR channel (high, medium, low), (8) beam splitter, (9) motorized linear stage for visible scale selection, (10) motorized linear stage for focusing the visible arm, (11) motorized linear stage for SWIR scale selection, (12) motorized linear stage for focusing the SWIR arm, (13) visible filter wheel, (14) SWIR filter wheel.

Collimation of the telescope beam

In order to avoid optical distortions in the transmitted optical path, the light beam from the telescope is first collimated before arriving at the dichroic. A collimator based on commercial lenses has been designed as shown in Figure 2.6. It consists of a classic Keplerian refracting telescope and a negative doublet lens placed at its entrance. The purpose of this lens is to shorten the total length of the collimator. Furthermore, the

refracting telescope uses an achromatic doublet lens as objective and a set of two achromatic doublet lenses in a Ploss configuration as eyepiece. The focal length of each component has been set to produce an output beam diameter of about the dichroic width (i.e. 5mm). This facilitates the removal of any artifact induced by the dichroic later on. The spacing between each component has been optimized by the optical design software ZEMAX[9]. Such values and other properties of the lenses are shown in Table 2.1. The design is optimized for the camera operation in the whole spectral range (350 – 1700 nm). Figure 2.7 shows the transmission efficiency of the collimating system as provided by the manufacturer.

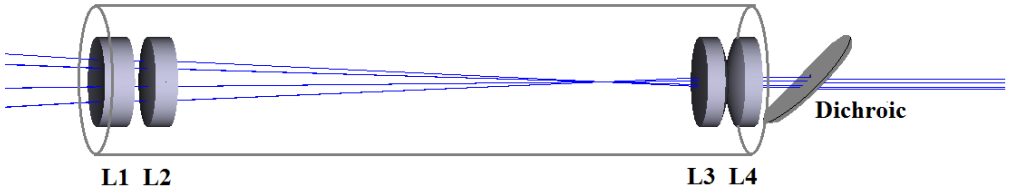

Figure 2.6. Ray diagram for the collimating optical system in *PlanetCam2*.

Table 2.1. Lenses employed in the Collimating System of *PlanetCam2*.

Reference (*)	Lens	Type	Diameter (mm)	Eff. focal length (mm)	Spacing (mm)	Substrate	Coating
63-767	L1	Negative-doublet	40	-150	0	N-BK7 / N-SF5	MgF_2
32-925	L2	Achromatic doublet	40	200	10	N-BK7 / N-SF5	MgF_2
63-701	L3	Achromatic doublet	40	100	239	N-BK7 / N-SF5	MgF_2
63-701	L4	Achromatic doublet	40	100	0	N-BK7 / N-SF5	MgF_2

* Commercial reference numbers from Edmund Optics[10] lenses.

[9] http://www.zemax.com/

[10] https://www.edmundoptics.es/optics/optical-lenses/

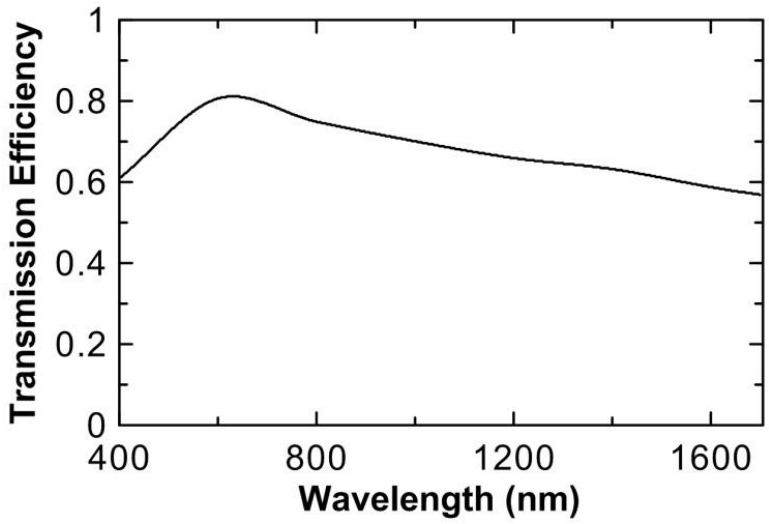

Figure 2.7. Transmission efficiency of the collimating system.

Dichroic element

A dichroic element manufactured by Omega Optics Inc[11] is used, with a nominal cut-on at 950 nm, a reflection ≥ 95% from 400 – 890 nm and maximum transmission between 1000 – 2000 nm for an angle of incidence (AOI) = 45°. The circular dichroic has a diameter of 50.0 mm and a clear aperture of 47.0 mm. Other relevant parameters are its thickness (6.0 mm) and flatness (1/8 wave at 633 nm before coating). Figure 2.8 shows the transmission curve for the dichroic.

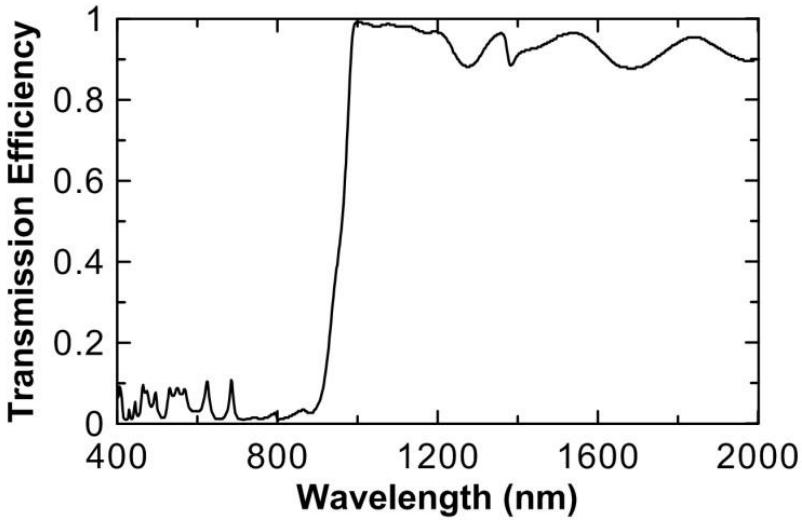

Figure 2.8. Dichroic spectral transmittance curve.

[11] http://www.omegafilters.com/

2.2 Visible Channel in PlanetCam 1 and 2

Considering that the observation of bright objects like planets is the main objective of *PlanetCam*, the detector selected for the visible channel is a scientific CMOS (sCMOS). Compared with CMOS, CCD or EMCCD detectors, the sCMOS is able to use bigger arrays with greater dynamical range providing an excellent combination of fast acquisitions over a large array.

2.2.1 VIS channel detector

Considering that observation of bright objects like planets is the main objective of *PlanetCam*, the detector selected for the visible arm was an ANDOR NEO sCMOS[12] (scientific CMOS) due to its high frame rate, reasonable quantum efficiency and low-noise (1.5 e/s). The detector is an array with 2560x2160 pixels (6.5 μm size each) and it is able to provide up to 100 fps in full frame mode. The low noise level of this detector allows accumulate thousands of frames although its quantum efficiency is relatively low compared to EMCCD technology based detectors. The detector also allows define Regions of Interest and binning up to 8x8 pixels for weak sources. For bright objects, this detector allows the accumulation of thousands of low noise high quality frames for lucky imaging.

Table 2.2. EMCCD vs sCMOS technology (Source: 'Scientific CMOS Technology. A High-Performance Imaging Breakthrough'. C.Coates, B.Fowler, G.Holst)

Parameter	sCMOS	Interline CCD	EMCCD
Sensor Format	5.5 megapixel	1.3 to 4 megapixel	0.25 to 1 megapixel
Pixel Size	6.5 μm	6.45 to 7.4 μm	8 to 16 μm
Read Noise	< 2 e^- at 30 frames/s	4 - 10 e^-	< 1 e^- (with EM gain)
Full Frame Rate (maximum)	100 frames/s at full resolution	3 to 16 frames/s	≈ 30 frames/s
Quantum Efficiency (QE)	60%	65%	90% 'back-illuminated' 65% 'virtual phase'
Dynamic Range	>16000:1 (at 30 frames/s)	≈3000:1 (at 11 frames/s)	8500:1 (at 30 fr/s low EM gain)
Multiplicative Noise	None	None	1.41x with EM gain (effectively halves the QE)

[12] http://www.andor.com/scientific-cameras/neo-and-zyla-scmos-cameras/neo-55-scmos

The above mentioned characteristics represent the main strengths of the sCMOS technology. Compared with other technologies, the sCMOS is able to use wider pixel arrays with greater dynamical range. Compared with CMOS, CCD or EMCCD detectors, the sCMOS provides the best combination for the relevant parameters in this context. However, it must be noted that not much effort has been done in assuring the use of sCMOS technology in the astronomical context (Qiu et al., 2012). In particular, the linearity in the response of the detector is strongly required in order to allow a photometric calibration of the observations. Considering the fast evolution of the detectors technology available, *PlanetCam* has been designed in a way that allows an easy substitution of the detector. In the following section, we will discuss the radiometric response of the current instrument and how it is feasible to use it for astronomical purposes.

2.2.2 sCMOS radiometric characterization

Laboratory tests have been performed at the Photonics Laboratory in the Faculty of Engineering at the University of the Basque Country in order to precisely characterize the response of the PlanetCam main components, in particular sCMOS detector.

Description of experimental set-up

The main components used in the laboratory tests were the following:

- Light source LDLS (Laser-Driven Light Source) EQ-99FC[13] (170nm to 2100nm), used for all the tests.
- Oriel Cornerstone™ 260 1/4 m Monochromator[14] used for the wavelength selection required in the sCMOS detector characterization.
- OCEAN[15] spectrometer needed for filters, barlow lenses and monochromator transmittance curves characterization.
- Lightwave multimeter HP8153A[16] for laser power measurement necessary for sCMOS sensitivity curve calibration.

[13] http://www.energetiq.com/html/eq99FC.html
[14] http://www.newport.com/Cornerstone153-260-1-4-m-Monochromator/375108/1033/info.aspx
[15] http://www.oceanoptics.com/Products/spectrometers.asp
[16] http://assetrelay.com/assetrelay_pdf_html/HP_8153A_815xx_Modules_specsheet.html

Different set-ups were used for each test as described in the following sections, where the results are shown and briefly discussed. Laboratory setup used for sCMOS spectral response is shown in Figure 2.9.

Figure 2.9. Laboratory layout including radiative source, monochromator and sCMOS detector

sCMOS quantum efficiency

Since there is a lack of information with respect to the sCMOS behavior under astronomical circumstances and sensitivity curves provided by the manufacturer do not include data below 400 nm, it was a major step to fully characterize *PlanetCam* visible channel. The spectral response of the sCMOS detector was obtained by capturing, at a fixed exposure time, the radiation provided by a monochromator while scanning the visible wavelength range. The monochromator response was previously characterized given the light source curve by the manufacturer. The sCMOS relative sensitivity curve was obtained in laboratory (Figure 2.10), while the maximum Quantum Efficiency value at 550 nm was assumed to be 0.57 according to the manufacturer. At the ultraviolet atmospheric cutoff at ~ 380 nm the detector has QE ~ 0.10. While very low, this may be enough when observing very bright targets, as Jupiter or Venus.

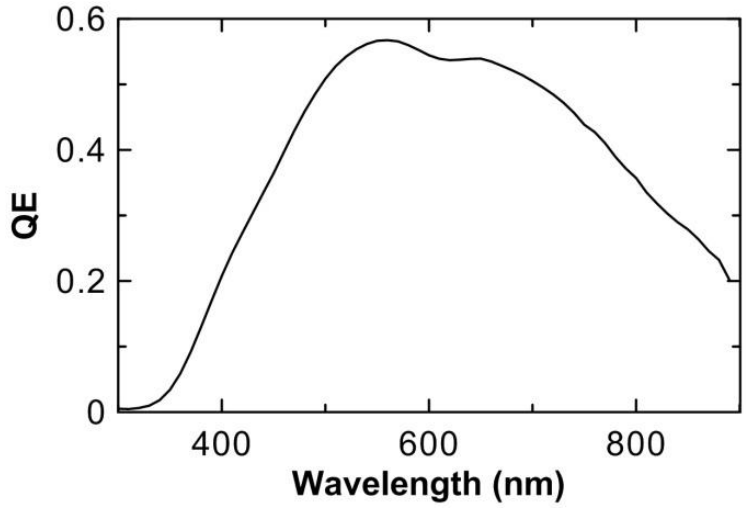

Figure 2.10. sCMOS Quantum Efficiency (QE) as measured in the laboratory.

The sCMOS detector has different electronic gain combinations. A linearity test has been performed for the sCMOS detector for the minimum electronic gain configuration. The maximum pixel count rate has been registered for different exposure times and incident wavelengths, constraining the range where the sCMOS has a linear response (Figure 2.11). Because of the variety in the brightness of planetary targets (that depends also on the filters used, see following chapters), the camera gain mode can be modified according to the observation circumstances. Therefore the linear response performances of the detector vary accordingly. In most cases the linear behavior is maintained up to a value of 85% of the maximum counts for different combinations of electronic gains. A practical consequence when image capturing for photometric studies is that counts at an individual pixel above 1800 approximately (at 11 bit configuration) may imply loss of linearity.

The sCMOS uniformity for different filters and number of frames has been examined over sky flat field images. Individual frames show that the stacked flat is uniform at small scales within a 0.3% and for narrow band filters (where less light is available) the signal is uniform within a 2.0%. By using a flat field correction in the science images the large-scale non-uniformities, such as a central bright ring caused by the optics, can be fully corrected. However, interpixel variability at these levels of 0.3-2.0% is more difficult to correct and result in small artifacts in the images when they are processed with high-pass filters.

The sCMOS temporal stability was tested by acquiring series of unfocused Moon and sky flat fields for filters I, R, and V using series of around 200 frames of 10 ms each. The variation of the number of counts of the brightest pixel in each frame shows a maximum variation of around 6% along the 200 frames series. However, the total number of counts in the frame presents a maximum variation of less than 2% along the whole 200 frame series.

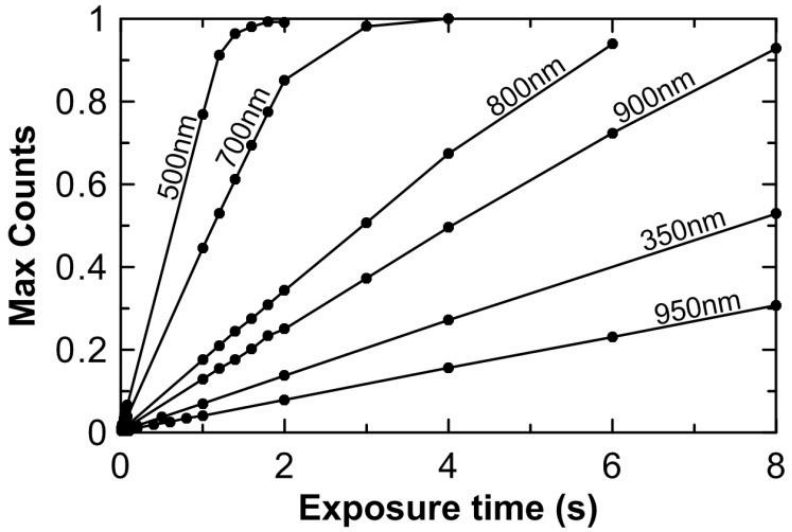

Figure 2.11. The sCMOS count rate measurements as a function of the exposure time at selected wavelengths using a monochromator at the laboratory. The curves have been traced to show the linear range of the detector.

2.2.3 Visible channel filters

PlanetCam1 works with two filter wheels with 8 positions each, whereas *PlanetCam2* visible channel uses a single larger filter wheel with 20 positions. The filters (1.25 inches in diameter) have been selected according to the interest of particular wavelengths to study planetary atmospheres. Broad-band filters allow high photon transmission making a "lucky imaging" filter series that can be used to fully exploit this methodology and attain high-resolution observations. Additionally, we use narrow band filters centered at wavelengths with some gaseous absorption bands and aerosol related phenomena, relevant for the observation of planetary atmospheres. Lucky imaging for such situation is restricted to a few filters, low magnifications, the brightest planets, and the use of a large telescope for high rate photon capture. VIS channel filters are listed in Table 2.3 with their main parameters, while Figure 2.12 shows their spectral

transmittance and Figure 2.13 shows these transmittance curves and that of VIS detector quantum efficiency over Jupiter spectrum, where the position of the main methane absorption bands can be seen.

Table 2.3. *PlanetCam2* Visible Channel Filters.

Filter	$\lambda_{central}$ (nm)	FWHM (nm)	Description
Lucky Imaging:			
U	380	40	Ultraviolet
Vio	400	20	Violet observations
B	445	94	Standard Photometry
V	551	88	Standard Photometry
R	658	138	Standard Photometry
I	-	-	Standard Photometry
Narrow Band:			
M1	619	5	Methane band
C1	635	5	Methane continuum
M2	727	5	Methane band
C2	750	5	Methane continuum
M3	890	5	Methane band
C3	935	5	Methane continuum
VC	980	10	Venus

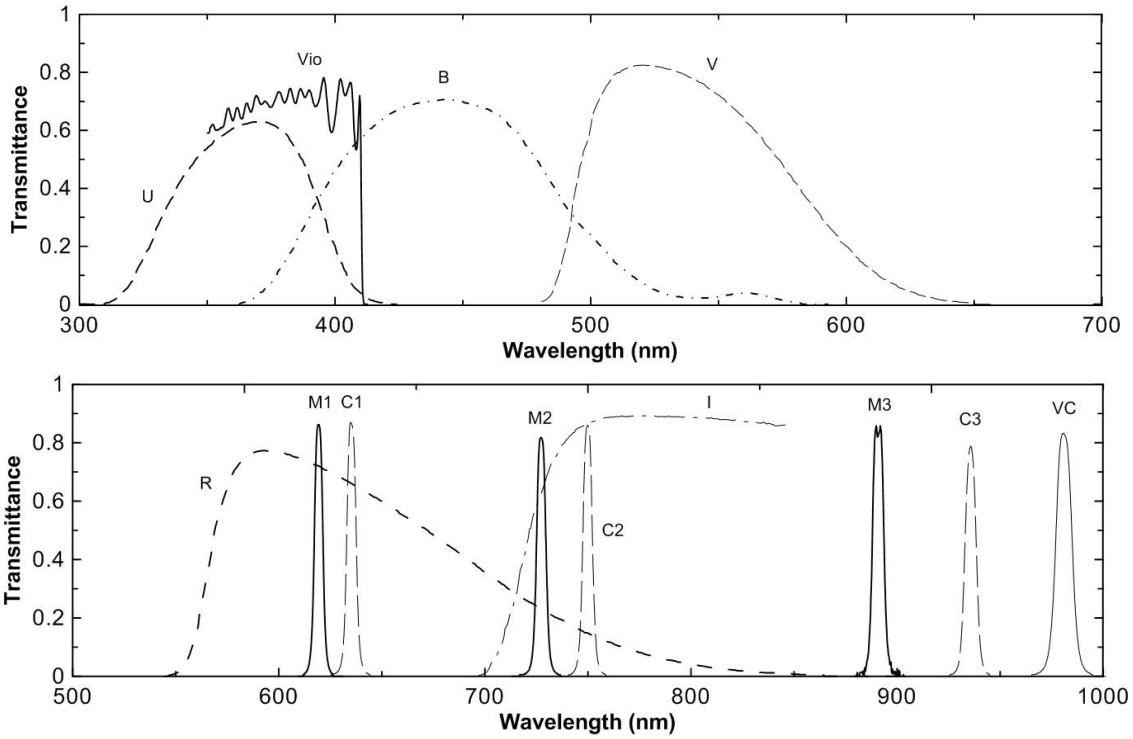

Figure 2.12. Spectral transmittance of the filters used in the visible channel (manufactured by Omega Optical Inc., USA).

The filters of the 'Lucky Imaging' series are common astronomical filters usable for other purposes. For example the B, V, R and I Bessel filters set is usually employed to make color composite images of the planets, as well as standard stellar photometry. When coupled to the detector response curve, they provide in general good contrast and high photon rate on planets that guarantees the use of the lucky imaging technique (Mousis et al., 2014).

There are three filters in the "lucky imaging" series in Table 2.3 that deserve particular comments (U, Vio and IH-long bandpass from 850nm). The Vio filter covers the spectral range below 410 nm down to the atmospheric and detector cut-off, complementing the classical U (ultraviolet) and B (blue) bands, placed at both wavelength sides. Those wavelengths are extremely interesting to capture images where chromophore agents strongly absorb solar radiation as in Jupiter and Saturn (Simon-Miller et al. 2001a, 2001b; Strycker et al., 2011; Ordoñez et al., 2015) and Venus (Travis, 1978; Titov et al, 2012). The Vio filter also provides high contrast for detection of cloud features on Mars (Parker et al., 1999; Sanchez-Lavega et al., 2015). The U-Vio-B absorption range allows to characterize a particular type of absorbing aerosols of unknown origin in the giant planets and Venus (Sánchez-Lavega et al., 2016) whose spatial distribution seems to be related to particular dynamical features (García-Melendo et al., 2009; Hueso et al. 2009; Pérez-Hoyos et al., 2009; Sánchez-Lavega et al., 2013). Ultraviolet markings on Jupiter and Saturn serve as tracers of high hazes motions at higher altitudes than those tracked with clouds seen at green-red wavelengths (Barrado-Izagirre et al., 2013; Garcia-Melendo et al, 2013; Peralta et al., 2007; Sánchez-Lavega et al., 2008, 2013). Finally, the IH filter is intended for the observation of the icy giants Uranus and Neptune (Hueso et al., 2017), since it integrates the continuum with the methane absorption bands located in the red side of the spectrum favoring the observation of atmospheric features that are otherwise difficult to see when using 1m to 2m class telescopes (Sromovsky et al., 2012; Mousis et al., 2014).

With respect to the 'Narrow band' series, most of the selected filters are designed to isolate methane absorption bands in the giant planets and Titan with increasing depths at the 619, 727 and 889 nm (M1, M2, M3), coupled to their adjacent continuums (C1, C2, C3), mostly free as much as possible of the methane absorption (Karkoschka, 2010). These filters are used for the observation of the giant planets Jupiter (West et al., 1980) and Saturn (West 1982, 1983; West et al., 1983).

Observations in these wavelengths peel-off the atmosphere sensing levels from the lower stratosphere to the upper troposphere (Pérez-Hoyos et al., 2005; Sanz-Requena et al. 2012) where many interesting meteorological phenomena are strikingly visible (e.g. Sánchez-Lavega et al. 2008, 2011; Pérez-Hoyos et al., 2012).

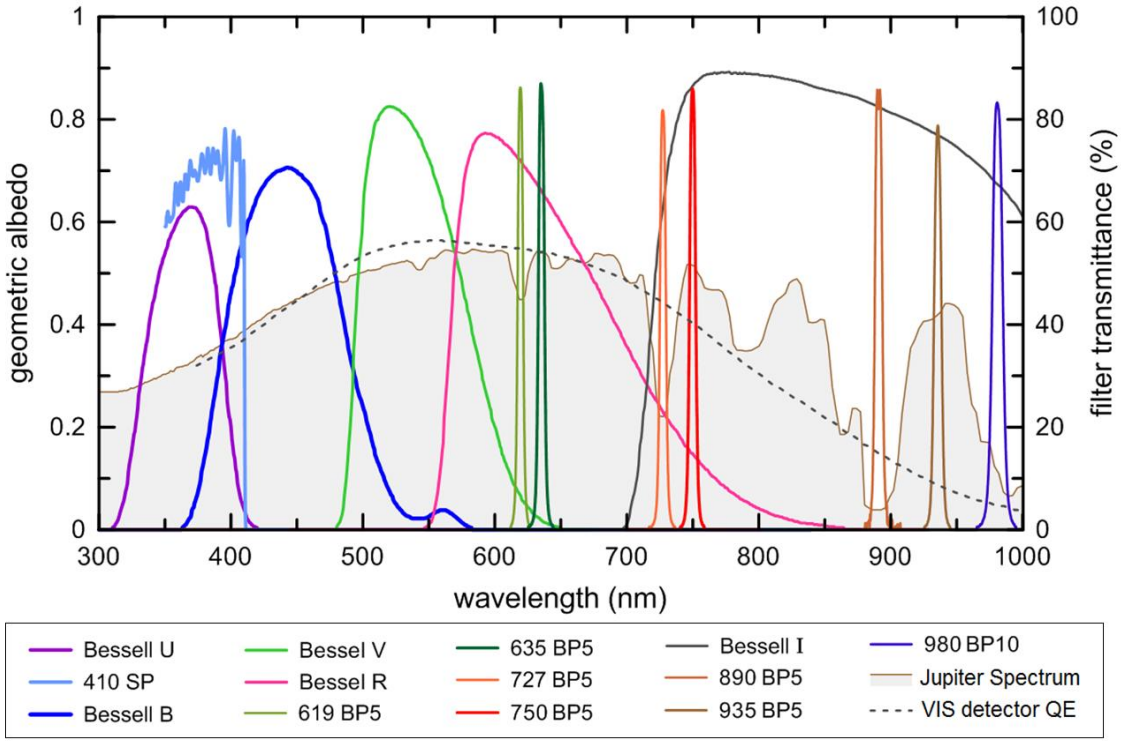

Figure 2.13. *PlanetCam2* VIS filters superimposed over Jupiter spectrum. VIS detector Quantum Efficiency is also represented (dashed line).

The combination of filters from both series allows high-resolution observations of atmospheric dynamics and vertical cloud structure at mid-resolution. For the giant planets, photometry in the U, B, M3 and R or I filters can be used to calculate color and altitudes indexes for atmospheric features in the giant planets (Sánchez-Lavega et al., 2013). For Venus, the Vio (also complemented by the U filter) and VC (980nm) filters provide high resolution images for cloud dynamics at two vertical levels giving vertical wind shear measurements (Belton et al., 1991; Sánchez-Lavega et al., 2008; Hueso et al., 2012, 2014). Additional filters with a 1.25-inch diameter can be mounted providing a good versatility to the instrument.

2.2.4 Magnification optical systems of VIS channel

In order to achieve the maximum angular resolution, the plate scale provided by the telescope focal ratio should match the detector pixel size in order to get an adequate image sampling. For planetary imaging, sampling is usually close to the Nyquist criterion, i.e. sampling frequency is greater than twice the maximum frequency of the input signal, which in this case means that the diffraction limit should be covered by at least two pixels.

Therefore, the recommended focal length (mm) of the telescope is given by $f(\lambda)=2000\ L_{px}D/\lambda$, being L_{px} the pixel size (μm), D the telescope objective diameter (mm) and λ the wavelength (nm). Our sCMOS detector has L_{px} = 6.5 μm, and this recipe gives a focal length of ~ 26 m for a 1 m-diameter telescope working at a wavelength of 500 nm. Since the telescopes where PlanetCam is expected to work range from f/8 (1,23m and 2.2 m telescopes at Calar Alto Obs.) to f/17 (1m at Pic du Midi Obs.), magnification optical systems are required to extend the effective focal length. It must be noted however, that this discussion assumes that lucky imaging is able to overcome the limitations of seeing during the observations. This is not very likely to be the case for large-aperture telescopes and an improvement factor of 4 to 5 with respect to seeing is a more realistic situation (Hormuth, 2007). All in all, a range of effective focal lengths from 10 m to 30 m is desirable in order to accommodate not only the telescope focus but also the local conditions at the observation time.

Magnification in PlanetCam1 visible channel

The solution designed for this case was to have a number of manually interchangeable Barlow lenses (divergent optical combinations) with magnifications from 2 to 4. The maximum amplification is provided by a commercial *Baader Planetarium Fluorite Flatfield Converter Barlow* (BPFFC)[17], which is formed by two doublet lenses providing a magnification of 4 and a diffraction-limited, apochromatic flat field over a 90 mm image circle. For lower amplifications we use commercial

[17] http://www.baader-planetarium.com/en/accessories/optical-accessories/barlow-lenses-coma-and-glaspathcorrectors/

Thorlab[18] *lenses* ACN254-050-B with a 50 mm focal length providing similar amplification to BPFFC, as well as ACN254-075-B (75 mm focal length) and ACN254-100-B (100mm focal length). All these lenses are negative achromatic doublets, and the anti-reflection (AR) coating is optimized for the near infrared side of the visible channel (650-1050 nm). Table 2.4 provides maximum resolution that can be achieved at different optical configurations with *PlanetCam1* at the different telescopes where it has been mounted.

Table 2.4. Maximum achievable resolution ("/pixel) with *PlanetCam1* at different telescopes (diffraction limits and seeing effects are excluded).

	No amplification	Barlow 2.65x	Barlow 4x
CAHA 1.23m	0.14	0.05	0.03
CAHA 2.2m	0.08	0.03	0.02
Pic 1m	0.08	0.03	0.02
IAC-TCS	0.06	0.02	0.02

Magnification in PlanetCam2 visible channel

The solution adopted for *PlanetCam2* optical magnification is different. It consists of three interchangeable optical elements (convergent ocular projection systems) whose position is motorized and electronically controlled by software. The lens system is selected by means of a lateral displacement motor (elements 2, 3, 4 and 9 in Figure 2.5). Essentially *PlanetCam2* visible channel provides three magnifications ranging from 1.18 to 2.65.

When used at the Calar Alto Observatory 1.23 m and 2.2 m diameter telescopes, they provide a plate scale ranging from 4.4 to 15.6 arcsec/mm and field of views (FOV) from 72 to 144 arcsec without vignetting. This guarantees that all the planets can be fully imaged. At maximum amplification, the scale at the plane detector is 0.03 arcsec/pixel, well below the diffraction limit of the 2.2m telescope.

[18] https://www.thorlabs.com/navigation.cfm?guide_id=2087

Table 2.5 summarizes the main optical features of the magnification system for the visible channel of *PlanetCam2* at CAHA 1.23 m and 2.2 m telescopes and different optical resolution modes.

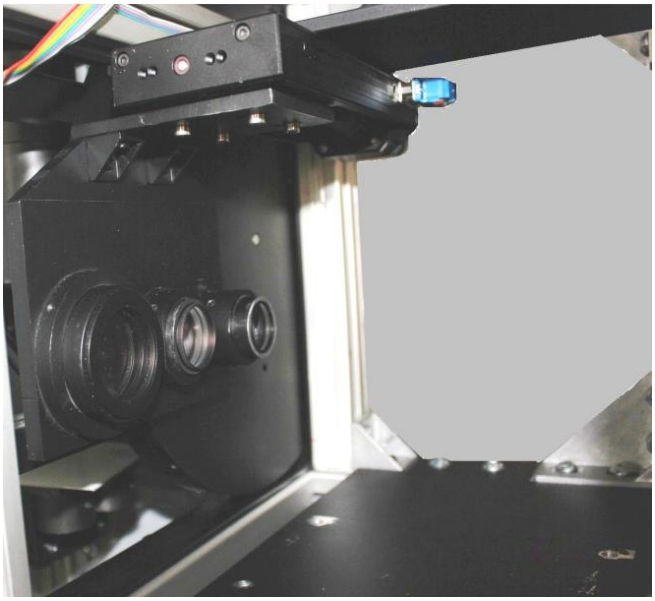

Figure 2.14. Configuration of the magnification optical system of *PlanetCam2* visible channel. The picture displays the motorized linear stage placed at the top holding the optical system from upward. From left to right, high resolution, mid resolution, low resolution. The filter wheel is shown behind the optical system.

Table 2.5. Optical Features of Magnification System in the Visible Channel

	1.23 m Telescope			2.2 m Telescope		
	Low res	Mid res	High res	Low res	Mid res	High res
Number of elements	2	2	2	2	2	2
Reference	49-794INK 49-794INK	49376INK 49376INK	49383INK 49383INK	49-794INK 49-794INK	49376INK 49376INK	49383INK 49383INK
Diameter (mm)	25.4	30	40	25.4	30	40
Effective focal length (mm)	76.2	150	200	76.2	150	200
Total magnification	1.18x	2.10x	2.65x	1.18x	2.10x	2.65x
Telescope effective focal length (mm)	11,631	20,700	26,121	20,781	36,983	46,669
Scale (“/mm)	15.60	9.95	7.86	8.78	5.56	4.40
Scale (“/pixel)	0.10	0.06	0.05	0.06	0.04	0.03
Coating	VIS-NIR	VIS-NIR	VIS-NIR	VIS-NIR	VIS-NIR	VIS-NIR
FoV (“) (*)	144	144	128	108	72	72
Spacing between lenses (mm)	18	0	0	18	0	0
Approx. distance from dichroic (mm)	95	95	95	95	95	95

* Area of the detector without vignetting.

2.3 The Short-Wave Infrared (SWIR) Channel in PlanetCam2

The beam direction for the Short Wave Infrared (SWIR) channel is at 90° with respect to the visible channel one so, after the beam split by the dichroic, it passes through the filter wheel and the magnification optical system before entering the SWIR detector (Figures 2 and 3). The individual elements of the SWIR channel are described in the following sections.

2.3.1 SWIR channel detector

For the SWIR channel detector we selected the commercial camera OWL SWIR 640 manufactured by Raptor Photonics[19]. The detector is an InGaAs PIN-photodiode with an area size of 640x512 pixel square elements (9.60 mm x 7.68 mm), of 15 x 15 μm each. The spectral range coverage extends from 0.4 μm to 1.7 μm with peak QE ~ 85% at 1.35 μm (Figure 2.15). The digital output format is 14 bit with a readout noise < 50 electrons (high gain mode). The faster frame rate is 120 Hz and exposure times range 8.5 ms – 22 s. Longer exposure times are not possible due to detector saturation by the dark current. For astronomical purposes the detector is cooled down at an operational temperature of -15°C using a cooling water circuit and a cool plate. The camera incorporates a gain control and on-board dynamic 3 point Non Uniform Correction (NUC) based on a baseline offset, gain and dark current calibrated for this temperature. Nevertheless, low light images or long exposures require additional dark currents calibration and flat fielding.

SWIR channel Raptor detector photometric linearity was tested by taking frames series at different frame exposure time of standard star HIP98571 at CAHA 2.2m. Frame exposure time varied from 0.0082s to 3s, and frames series taken were from 1000 frames to 50 respectively. For this test constant High Gain mode of 260 was used, as well as High Resolution mode with Filter V2. Raptor sensor temperature was kept at -14.5C.

[19] http://www.raptorphotonics.com/products/owl-640-cameralink-stabilized/

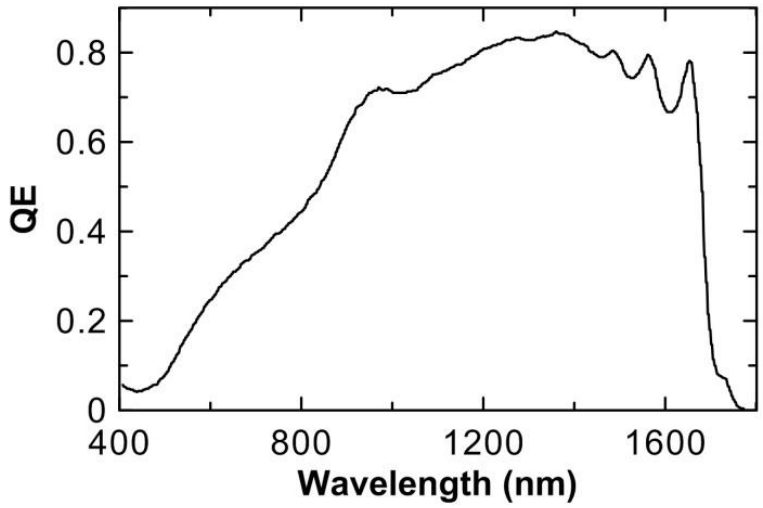

Figure 2.15. Spectral Quantum Efficiency (QE) of the SWIR detector as provided by the manufacturer.

Figure 2.16 shows values of maximum pixel count rate using images for different frame exposure time values. Sensor saturation was achieved when frames reaches the expected limit corresponding to the 14bit sensor. A practical consequence when image capturing for photometric studies is that counts above 14000 approximately may imply loss of linearity. Small deviations from linearity observed in these curves can be attributed to the method inaccuracy, yet the loss of linearity is clearly shown.

In order to test the sensor linearity for increasing gain modes at a given frame exposure time of 0.01s, an additional test was done taking 1000 frame series with increasing Low Gain mode (RG1000 filter) values from 400 to 4000. Similar test for High Gain modes from 260 to 4000 and filter V2 was done, also taking 0.01s exposure time 1000 frames series. Figure 2.16 shows the resulting linearity for different exposure time values and high gain values.

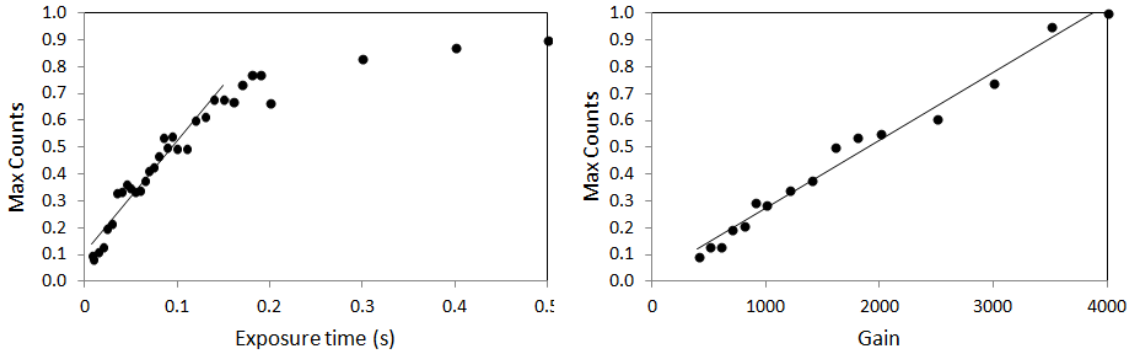

Figure 2.16. SWIR detector counts rate as a function of exposure time (left) and High Gain mode value (right).

The SWIR detector uniformity has been tested over sky flat field images for different filters. Stacked flats show deviations of up to 3%, which has been found to be up to 9% in narrower filters with higher exposure time values. In any case, these non-uniformities are corrected in planetary images by using these flat field images. Regarding the temporal stability, it was tested by acquiring series of sky flat fields for filters J, H, and RG1000 using series of 50 or 100 frames of 1s each. The variation of the total number of counts in the frame presents a maximum variation of around 1% along the whole frame series.

2.3.2 SWIR channel filters

SWIR filters were selected to isolate particular absorption bands in planetary atmospheres (essentially CO_2 for Venus and CH_4 for the giant and icy planets and Titan), and at the same time to work in two complementary modes, lucky imaging for high spatial and temporal resolution (broad-band filters), and short sequences of longer exposures required in deep absorption bands. Table 2.6 lists the SWIR filters and their main purpose and Figure 2.17 shows their spectral transmittance curves. Some of the observing bands are also affected by water absorption in Earth's atmosphere and are only available for images under exceptionally dry conditions. Figure 2.18 shows the SWIR channel filters and detector quantum efficiency over Jupiter spectrum.

Table 2.6. *PlanetCam2* SWIR Channel Filters

Filter	$\lambda_{central}$ (nm)	FWHM (nm)	Description
Lucky Imaging:			
RG1000			Long red bandpass >1μm
J			Standard photometry
H			Standard photometry
Narrow Band:			
YC	1090	30	Methane continuum (C4) (*)
YM	1160	40	Methane band (M4)
V1	1190	20	CO2 continuum
V2	1220	50	CO2 band
JC	1275	50	Methane continuum (C5)
JM	1375	50	Methane band (M5) (*)
V3	1435	20	CO2 band (*)
HC	1570	50	CO2 continuum
			Methane continuum (C6)
HM	1650		Methane band (M6)
			Long red bandpass >1.62μm detector cut.

* Affected by water absorption in Earth's atmosphere.

The SWIR wavelength range is very well suited for capturing high clouds in the outer planets and Titan, as well as for studying their properties using a combination of methane absorption band filters and their adjacent continuums. A similar procedure can be use in Venus with the CO_2 absorption bands. In addition, the night side of Venus can be imaged with filters in the range 1 – 1.2 μm to capture surface features (Helbert et al., 2008) and at 1.27 μm to map the atmospheric airglow emission (Gerard et al., 2008; Hueso et al., 2008).

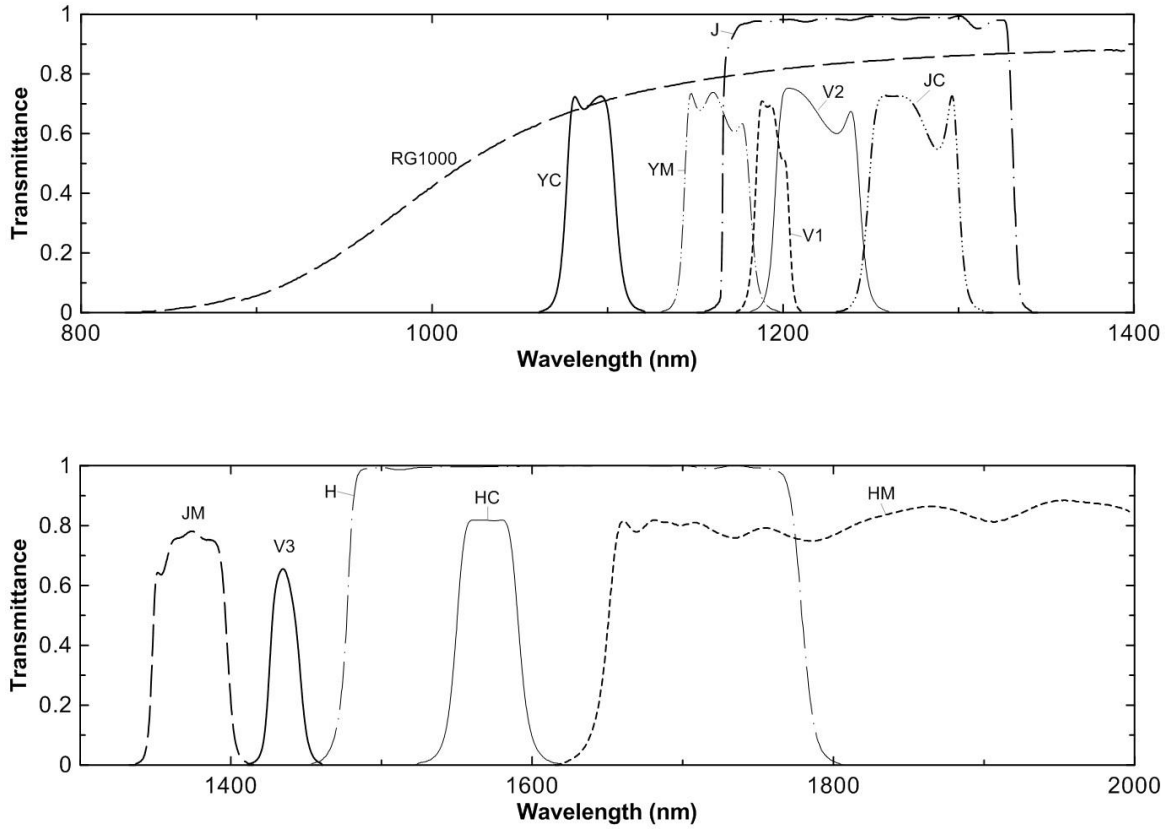

Figure 2.17. Spectral transmittance of the filters used in the SWIR channel.

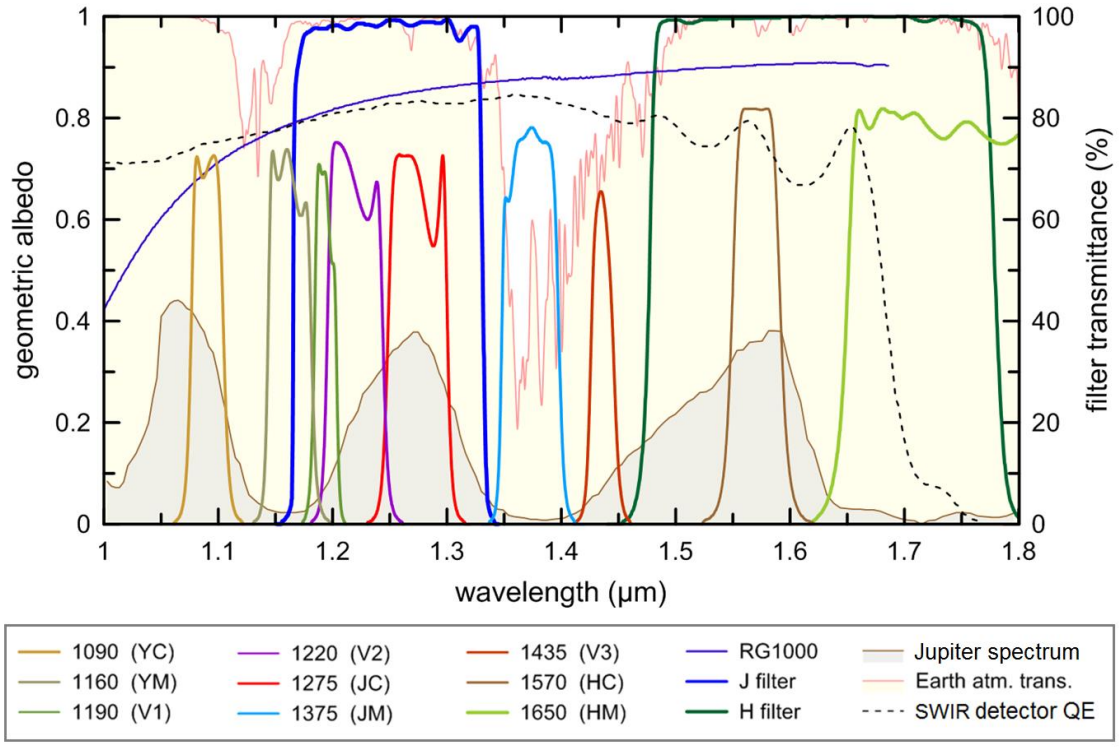

Figure 2.18. *PlanetCam2* SWIR filters superimposed over Jupiter spectrum (brown shadowed). Earth atmosphere transmittance curve (yellow shadowed) shows how JM filter is affected. SWIR detector Quantum Efficiency is also represented in dashed line.

2.3.3 Magnification optical system in PlanetCam2 SWIR channel

Similarly to the visible channel, the SWIR channel on *PlanetCam2* has three interchangeable magnifications made by convergent projection systems whose position is motorized and electronically controlled by software independently from the visible channel. The lens system is selected by means of a lateral displacement (elements 5, 6, 7 and 11 in Figure 2.5). Essentially, *PlanetCam2* SWIR channel provides three magnification possibilities ranging from 1.10x to 2.00x. When used at the Calar Alto Observatory 1.23m and 2.2m diameter telescopes they provide a plate scale ranging from 5.74 to 15.1 arcsec/mm and field of views (FOV) from 56 to 144 arcsec, as for the visible channel. This guarantees that all the planetary disks can be imaged in a single exposure. The comments made for the vignetting affecting the VIS field of view are also applicable here. At maximum amplification, taking into account that the OWL Raptor camera has a pixel size of 15 μm, the scale at the plane detector is 0.088 arcsec/pixel.

Table 2.7 summarizes the main optical features of the magnification system for the infrared channel of *PlanetCam2* at CAHA 1.23 m and 2.2 m telescopes and different optical resolution modes.

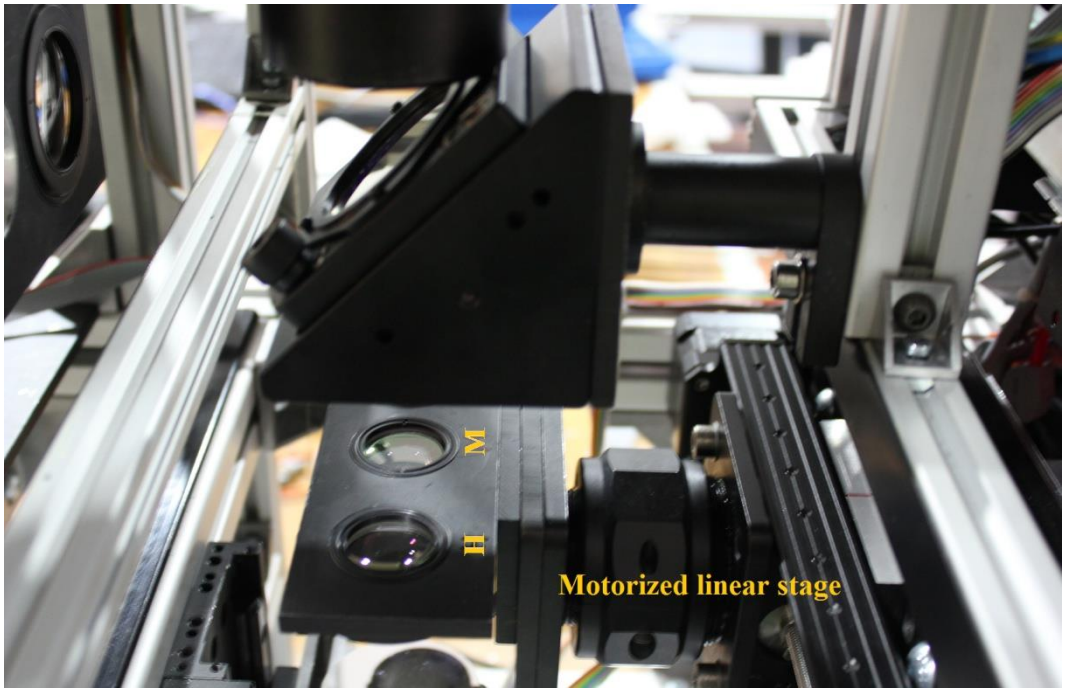

Figure 2.19. Picture of the magnification optical system of *PlanetCam2* SWIR channel. A motorized linear stage is used to select the adequate optical resolution. The image shows the high resolution (H) and the medium one (M).

Table 2.7. Optical features of Magnification System in the SWIR Channel

	1.23 m Telescope			2.2 m Telescope		
	Low res	Mid res	High res	Low res	Mid res	High res
Number of elements	2	2	1	2	2	1
Reference	45-805 45-805	85-986 47-380	85-986	45-805 45-805	85-986 47-380	85-986
Diameter (mm)	25.4	25.4	25.4	25.4	25.4	25.4
Effective focal length (mm)	75	75/150	75	75	75/150	75
Total magnification	1.10	1.65x	2.00x	1.10x	1.65x	2.00x
Telescope effective focal length (mm)	10,843	16,264	19,714	10,843	29,058	35,222
Scale (“/mm)	15.10	12.40	10.20	8.47	6.88	5.74
Scale (“/pixel)	0.23	0.19	0.15	0.13	0.10	0.09
Coating	NIRII	NIRII	NIRII	NIRII	NIRII	NIRII
FoV (“) (*)	144	116	102	86	70	56
Spacing between lenses (mm)	20	25	0	20	25	0
Approx. distance from dichroic (mm)	100	100	100	100	100	100

* Area of the detector without vignetting.

2.4 Camera Control

PlanetCam1 is controlled by means of a GUI based on LabView which provides full control for the detector and the filter wheel (Figure 2.20). This GUI allows the user to acquire sequences of images and to program series of acquisitions in different filters. The interface also allows defining binning and regions of interest over the image as well as zoom over the actual image that it is being acquired. It is also possible to control the temperature of the Andor detector, and to turn on/off the fans. The code is based on the software development kit provided by the manufacturer while the filter wheel control software was designed from scratch.

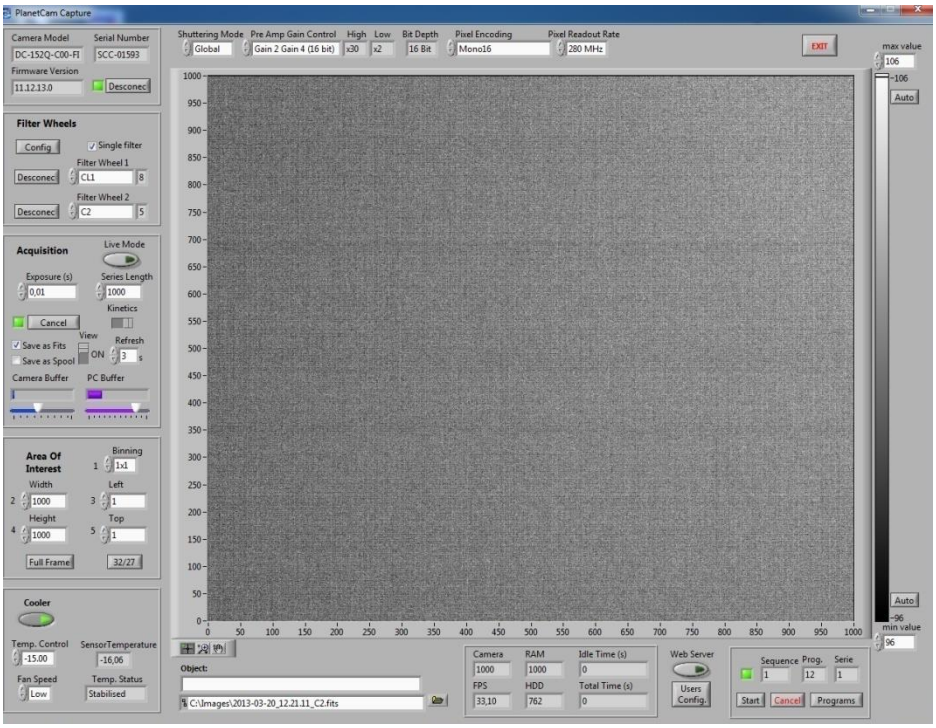

Figure 2.20. Control software for *PlanetCam1*

The mechanic devices that constitute *PlanetCam2* are controlled by a simple electronics module located at one side of the instrument (Figure 2.21). The visible and SWIR modules are identical to each other and are controlled by two PCs. The main component of each module is the motor controller of the focus and optical selector stages, and is based on an ARDUINO[20] microcontroller and a stepper shield. In order to minimize the external connectors, a USB hub is included to collect the signals from the

[20] https://www.arduino.cc/

filter wheel and the ARDUINO board. Cameras connection with the PCs is done using CameraLink communications protocol ensuring a fast data transfer. The PC controlling the visible detector has solid state disks to maximize the speed of data storage. Each detector is controlled through custom design software written in C++ which allows the instruments to acquire simultaneous sequences for both channels and control the mechanics and optics of the instrument. The graphical interfaces are identical for the Visible and SWIR channels (Figure 2.22), and the detectors control is based on the software development kits from their respective manufacturers. This software allows the following functionalities:

- Selection of optical resolution: The software moves the focus and the optical selector stages for each arm to the proper positions for each configuration.
- Display and control of the internal temperature values of the detectors.
- Selection of filter.
- Display of the acquired frames: Visualization is done at a maximum rate of 0.5 Hz for the visible channel and the acquisition rate for the SWIR channel.
- Acquisition of sequences of images with a given exposure time, gain, number of frames, as well as selection of region of interest and binning in the visible channel.
- Zoom over cursor position.
- Data saving in standard FITS cubes (Flexible Image Transport System).

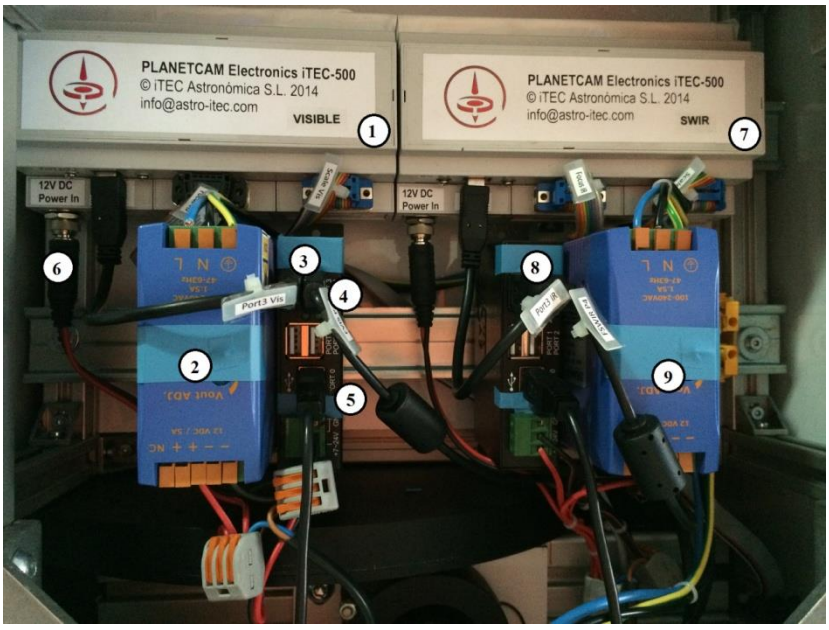

Figure 2.21. Picture of the electronics control module of *PlanetCam* 2. 1- Controller of the visible focus and optics stage, 2- Visible power supply, 3- Visible USB hub, 4- visible filter

wheel USB connector, 5- USB output, 6- visible 12V input, 7- Controller of the SWIR focus and optics stage, 8- SWIR USB hub, 9- SWIR power supply.

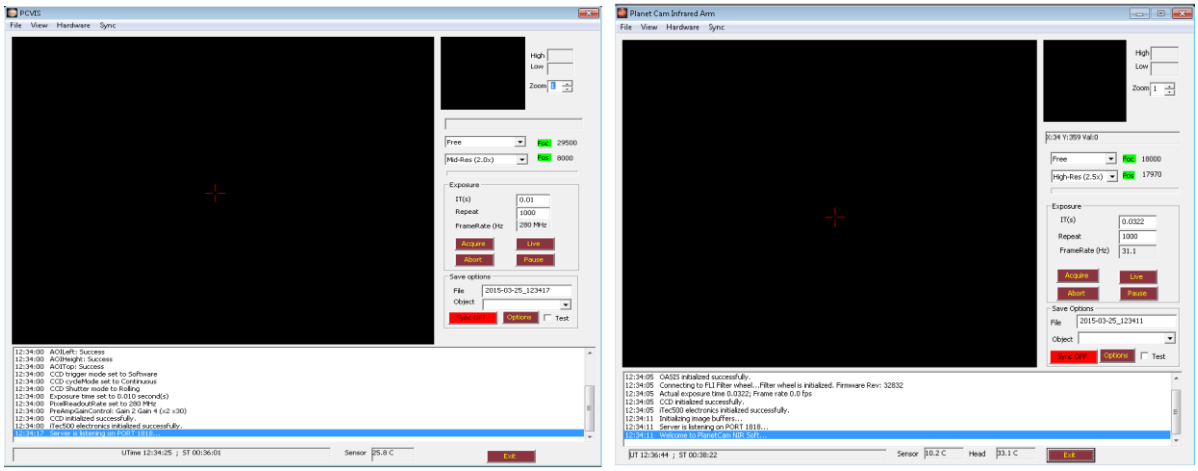

Figure 2.22. Control software for *PlanetCam2* channels, visible (left) and SWIR channel (right).

Chapter 3

PLANETCAM ASTRONOMICAL PERFORMANCE

This chapter describes the astronomical performance of *PlanetCam*. Section 3.1 briefly describes the image processing methods and the pipeline developed for *PlanetCam*, while a brief study of the astronomical performance of the instrument is presented in section 3.2 for both the VIS and SWIR channels, based on the analysis of some close binary systems and stellar clusters. We also present a discussion on the instrument limiting magnitudes.

3.1 Lucky Imaging Processing

Images are processed with a pipeline written in IDL (Interactive Data Language) specifically designed for *PlanetCam* by Ricardo Hueso but also suitable for analysis of data from other lucky imaging cameras such as AstraLux (Hormuth, 2007). The software is called PLAYLIST (PLAnetarY Lucky Images STacker) and is used to analyze without human interaction the large sequence of observations obtained in a given observing night. PLAYLIST builds a list of files from a selected folder, but it can also be used to analyze a single file (Figure 3.1). For each file, PLAYLIST finds the proper dark current and flat files to be used in the image reduction, and each frame is then reduced with the corresponding dark and flat. Hot and cold pixels that could remain after the frame reduction process are identified and removed with an adaptive median filter technique (González and Woods; 2008).

The quality of the resulting frame is analyzed by first finding the scientific object in the frame using a center of brightness algorithm that identifies the center of the planet (or star) and its size defining a Region of Interest (ROI) of constant size throughout the sequence. Then, the quality of each frame is provided by a numeric metric based on the Sobel differential filter (González and Woods; 2008). Sharp images have higher values of their spatial derivatives while unfocused or smooth images provide lower values. By summing up the absolute values of the Sobel filtered ROI containing the scientific target. a good estimation of the frame quality is obtained.

The software allows Lucy Richardson deconvolution (Richardson, 1972; Lucy, 1974) on a frame by frame basis but this option is generally not used since it requires bright images with low levels of noise. The planet or object of interest is automatically located with an algorithm based on the evaluation of the center of brightness of the image. Images are then co-registered using a multi-scale image correlation algorithm that matches images with a precision of 1 pixel. PLAYLIST also allows correlation of images based on several points by moving each frame into a reference image initially created from a subset of the images, this procedure corrects image distortions created by the atmospheric seeing in large objects like Jupiter which cover a significant fraction of the beam at the focal plane.

For each image sequence PLAYLIST generates several FITS files with different trade-offs between image quality in terms of spatial resolution and dynamic range. For instance: the best 1% of all individual frames typically contain little atmospheric blurring but low dynamic range, but the co-registered stack of all frames contains the maximum dynamic range but with the highest level of atmospheric blurring. PLAYLIST then generates several FITS files with different levels of image quality by selecting only the best 1%, 2%, 10%, 30% or all frames in the sequence, and photometric images are saved in FITS files containing double precision real numbers that represent the total digital counts per second for each pixel. SWIR images are typically best represented by the images based in the best 1%-5% frames while visible images in short wavelengths are generally better represented by the versions containing the best 10% and very dark acquisitions in the strongest methane absorption filters generally require the versions based in the stack of all frames.

A full night of observations with the SWIR channel can be analyzed with a standard computer in a few hours. Observations with the VIS channel at large spatial resolution are more demanding requiring a few days for a typical observing campaign. The software can also be used to produce a quick analysis of images at the telescope, while acquiring the observations. This is useful to judge exposition time values used and observation strategies depending on the object and atmospheric seeing. The quick analysis does not perform dark or flats corrections, deconvolution or image warping and simply stacks the images using the center of brightness algorithm for co-registration of the frames. PLAYLIST will be publicly released and described extensively elsewhere (Hueso et al. in preparation).

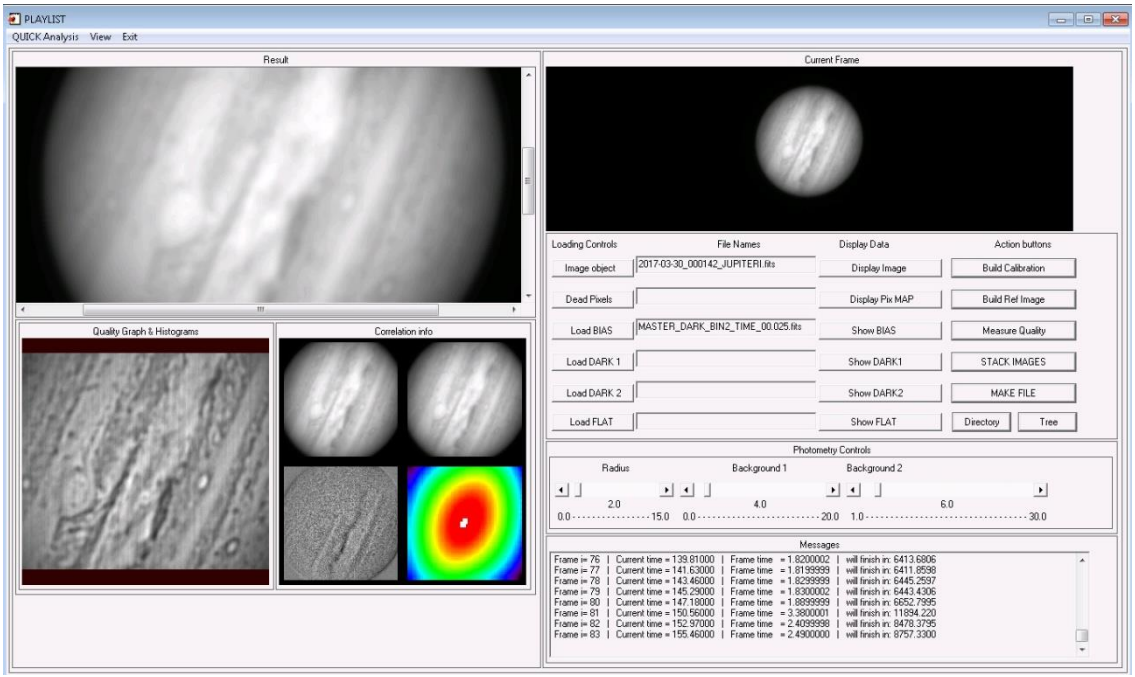

Figure 3.1. PLAYLIST graphical user interface

3.2 Astronomical Characterization of PlanetCam

In this section several astronomical tests performed are described, with the camera in its different available modes in order to characterize its performance with real targets. Astrometry tests estimate the image scale and its uniformity over the field of view, while tests with faint targets allow an estimation of the observable limiting magnitude.

3.2.1 PSF and resolution on stars

Point Spread Function model

The combination of the object being observed, the diffraction pattern of the telescope and the atmospheric seeing produces a light intensity distribution map in the detector plane. For point sources, the pattern is described by a Point Spread Function (PSF) which, under normal conditions, has radial symmetry and can be represented by a weighted sum of a Gaussian function and a Moffat profile (Hormuth 2007, 2008). For lucky imaging applications, Law et al. (2006) showed that the PSF of a star improves with a selection of frames based on their quality (lower Gaussian FWHM).

$$PSF(r) = W\left(\frac{1}{r^2/\sigma_m^2 + 1}\right)^{\beta} + (1-W)\left[\exp\left(\frac{-r^2}{2\sigma_g^2}\right)\right] \qquad (3.1)$$

where *PSF(r)* refers to the theoretical radial PSF profile, *W* weights the two PSF components, β is the Moffat power law index (Moffat, 1969), and σ_g and σ_m define the widths of the Gaussian and Moffat profile, respectively. As parameter β increases the Moffat profile tends to approximate to the Gaussian profile core. It is often set to a typical value of 3 to 5, otherwise the optimal PSF function can be found assuming the four above mentioned parameters free.

The theoretical PSF is fitted to several scans (typically at 0º, 45º, 90º and 135º) of the observed star image, for each one being the fitting error estimation χ_λ^2:

$$\chi_\lambda^2 = \frac{1}{N}\sum_{i=1}^{N}\frac{\left[PSF_{obs}^{(i)} - PSF^{(i)}\right]^2}{\sigma^2} \qquad (3.2)$$

where σ^2 is a reference value for the error estimation, which has been set at 10% of the maximum observed PSF value. This function simply throws values for χ_λ^2 below 1 (i.e., below assumed error) for acceptable models and above 1 for models far from observations. Theoretical PSF is finally taken as that of minimum total error.

Further research can be done in order to analyze the influence of different factors in the PSF fitting process and results, including factors like image wavelength, percentage of selected frames considered when processing the star image (as in the

following case), seeing, asymmetries due to atmospheric dispersion, etc. In addition, in larger fields the influence of the star position in the image on the PSF model parameters can be further investigated so that photometry for star clusters based on PSF models can be considered.

Camera resolution on stars

The resolution of the camera has been tested with the double star STF439 (HD281159, magnitude V = 8.80 and 10.30, separated 0.6", WDS2014) with *PlanetCam2* Visible channel (high resolution optics) at CAHA 2.2 m telescope and normal seeing conditions. In total 1000 frames were taken with 0.1s frame exposure time. Figure 3.2 shows the PSF fitting to both stars for different image quality thresholds measured by the percentages of selected images according to their quality. Seeing limited and diffraction limited profiles are also shown for comparison. Using the best frames the PSF fitting improves, reducing FWHM from 0.51 arcsec (using all the frames) to 0.39 arcsec (using the best 1%), and increasing Strehl ratios from 7.1% to 11.7% for star STF439A (100% frames stacked to the best 1%), and from 5.8% to 9.1% for STF439B as shown in Table 3.1, where both stars angular separation is also estimated for all cases. Although the resolution improvement by comparison of Strehl ratios is only modest (2.2 in this example with normal seeing conditions) the quality of the images is undoubtedly much better in the lucky imaging result.

This PSF fitting process has been tested for other exposure time values. A series of 10.000 frames of 1 ms exposure time using standard star HD164136 (V magnitude 4.4) provided FWHM from 0.59" (100% frame selection) to 0.53" (1% best frame selection), with respective Strehl ratios of 10.19% and 12.74%. Additionally, a 20.000 frame series of 5ms exposure time provided FWHM from 0.68" (100% frame selection) to 0.49" (1% best frame selection), with respective Strehl ratios of 7.94% and 13.17%. Comparing these series with the previous case we can see that shorter exposure times can improve the Strehl ratios, but in general very short exposure time values do not provide significant improvement in FWHM and Strehl ratios due to the inherent difficulties in detecting the best frames for images of stars or extended objects.

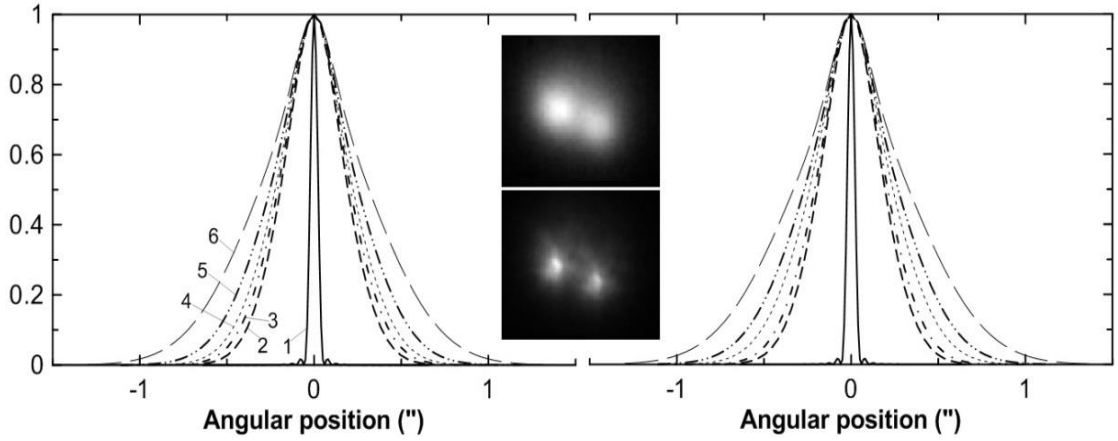

Figure 3.2. The normalized PSF profiles for the double star STF439 (left A, right B) at CAHA2.2 m (Dec. 2014) with *PlanetCam2*–VIS for different percentage frame selection levels and the seeing limited images. Seeing limited images formed by adding all images in the sequence without computing their relative shifts, and PSF profiles for the diffraction limit are also shown: 1- Diffraction limited, 2- Best 1%, 3- Best 10%, 4- Best 30%, 5- All stacked, 6- Seeing limited. The double star picture in the centre shows the result of the seeing limited image (up) and that from best 1% frame selection (down).

Table 3.1. Strehl ratios, FWHM and angular separation of STF-439 for different percentage frame selection (*PlanetCam2*-VIS at CAHA 2.2m telescope)

	STF439-A		**STF439-B**		
	Strehl Ratio (%)	FWHM (")	Strehl Ratio (%)	FWHM (")	Separation (")
Best 1%	11.75	0.39	9.13	0.39	0.60
Best 10%	10.01	0.42	7.96	0.42	0.61
Best 30%	8.84	0.45	7.06	0.48	0.61
100% Stacked	7.11	0.51	5.82	0.54	0.60
Seeing limited	5.28	0.63	4.30	0.66	0.47

A similar procedure has been followed for the *PlanetCam2* – SWIR channel. In this case the double star HIP107310 (μ Cygnus, magnitude J 3.49, separation 1.6") was observed at CAHA 2.2 m telescope on July 3, 2016. In total 5000 frames were taken with 0.01s frame exposure time (RG1000 filter, high resolution). Figure 3.3 shows the PSF fitting to both stars, again for different image quality thresholds. In this case, with ordinary seeing conditions, using the best frames the PSF fitting hardly improves, reducing FWHM from 1.16 arcsec (using all the frames) only to 1.14 arcsec (using the best 1%) and only for star HIP107310A, and increasing Strehl ratios from 15.3% to 18.6% for star HIP107310A and from 5.2% to 6.0% for HIP107310B as shown in Table 3.2, where both stars angular separation is also estimated similarly all cases.

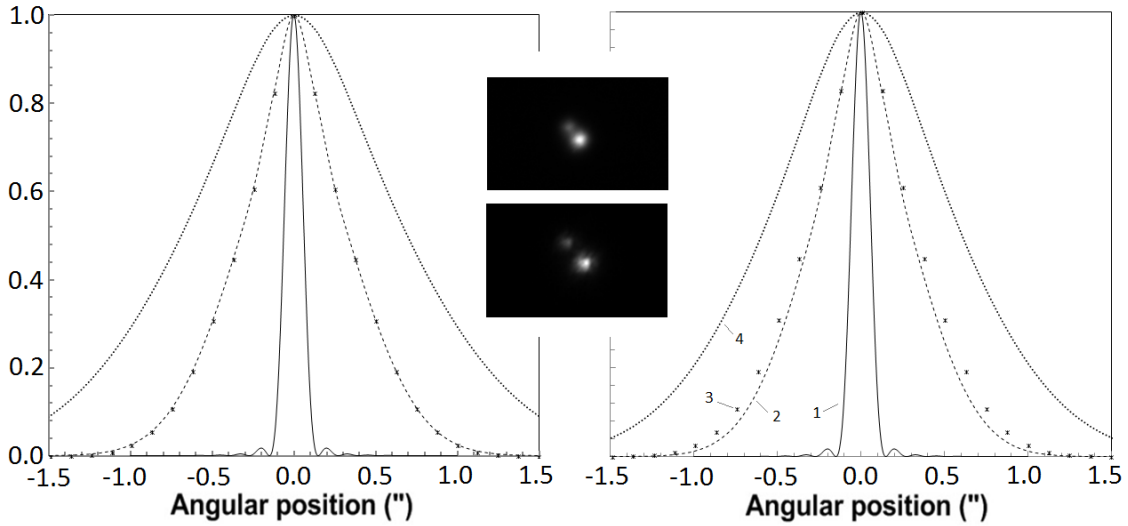

Figure 3.3. The normalized PSF profiles for the double star HIP107310 (left B, right A) at CAHA2.2 m (July 2016) with *PlanetCam2*–SWIR for different percentage frame selection levels and the seeing limited images. Seeing limited images and PSF profiles for the diffraction limit are also shown: 1- Diffraction limited, 2- Best 1%, 3- All stacked, 4- Seeing limited. The double star picture in the centre shows the result of the seeing limited image (up) and that from best 1% frame selection (down).

Table 3.2. Strehl ratios, FWHM and angular separation of HIP107310 for different percentage frame selection (*PlanetCam2*-SWIR at CAHA 2.2m telescope)

	HIP107310_A		**HIP107310_B**		
	Strehl Ratio (%)	FWHM (")	Strehl Ratio (%)	FWHM (")	Separation (")
Best 1%	18.65	1.14	6.03	1.16	1.62
Best 10%	16.10	1.16	5.46	1.16	1.62
Best 30%	16.05	1.16	5.49	1.16	1.62
100% Stacked	15.31	1.16	5.22	1.16	1.62
Seeing limited	6.56	1.61	2.29	1.76	1.57

3.2.2 Resolution on planetary images

Planets are extended objects so resolving details on planetary images depends not only on the resolving power of the instrument, as ideally dictated by diffraction (through Rayleigh criterion valid for two sources of equal brightness), but also on the intensity contrast between a given feature and its background. The spatial resolution and contrast performance of an optical system are described by the Modulation Transfer Function (MTF) represented as a function of the spatial frequency (Smith, 2000; see D. Peach description in reference to Solar system observations, 2015[21]). We have tested the

[21] http://www.damianpeach.com/simulation.htm

capability of *PlanetCam2* to resolve atmospheric features on our best images of Jupiter, which is so far the most observed target with our instrument. With the 2.2m telescope, under good seeing conditions we typically resolve in the visible range contrasted features with a size ~ 0.25 – 0.30" (about 800 km in Jupiter) (see details in chapter 5). At this resolution, *PlanetCam2* allows to study the cloud structure, dynamics and meteorological phenomena at the synoptic scale on most planetary atmospheres.

3.2.3 Astrometry

The uniformity or flatness of the field of view (FOV) given by the camera has been tested performing astrometry on a known calibrated star field. This analysis has been performed for both VIS (*PlanetCam1* and *PlanetCam2* configurations) and SWIR detectors on the open cluster M103.

Figure **3.4** shows the central field of the cluster M103 imaged by *PlanetCam1* at CAHA 1.23m telescope. The stars are identified by capital letters and the measured angular distance between selected pairs has been identified using the International Celestial Reference System (Souchay and Feissel-Vernier, 2006).

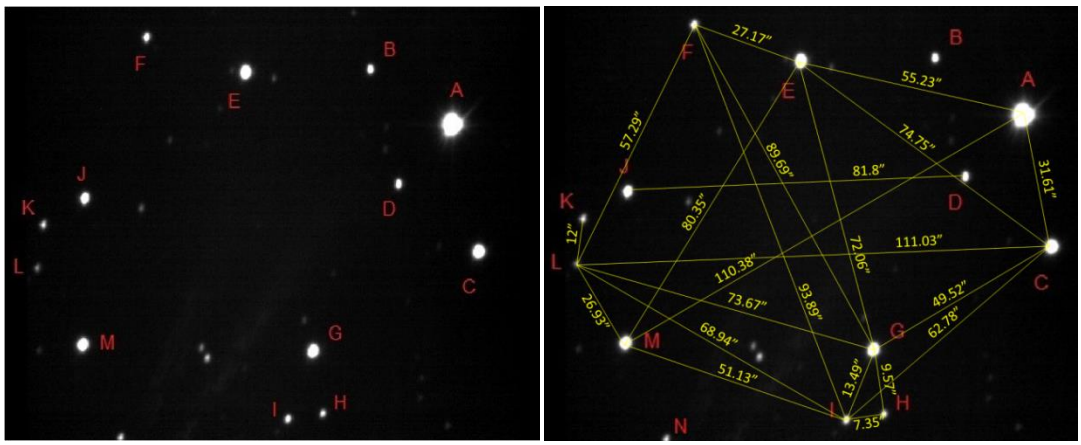

Figure 3.4. M103 cluster in an image taken at CAHA 1.23m with *PlanetCam1*, sCMOS detector and a magnification of 2.65x.

Table 3.3. *PlanetCam1* (magnification of 2.65x) image scale values estimations from different star pairs in M103 (CAHA 1.23m)

Stars	**Ang dist** (")	**Mean dist to center** (pixel)	**Scale** ("/pixel)
A-E	55.23	907	**0.0502**
E-M	80.35	960	**0.0506**
E-C	74.75	918	**0.0499**
E-G	72.06	715	**0.0505**
A-M	110.38	1095	**0.0504**
F-G	89.69	901	**0.0503**
D-J	81.80	837	**0.0500**
I-M	51.13	1051	**0.0454**
I-F	93.89	1048	**0.0464**
I-C	62.78	1010	**0.0494**
L-F	57.29	1190	**0.0448**
L-C	111.03	1151	**0.0488**
L-I	68.94	1095	**0.0465**
A-C	31.61	1054	**0.0494**
G-C	49.52	863	**0.0501**
G-L	73.67	948	**0.0501**

For each star the centre of brightness pixel is considered as star position and the angular separation between several pairs of stars is in this way calculated. Comparing this angular separation with the reference values in the literature, the image scale can be estimated. This estimation is therefore performed with stars at different positions and at different angles in the image field, as shown in Table 3.3. From this analysis a scale of 0.049 ± 0.002 "/pixel was estimated for *PlanetCam1* with 2.65 magnification used, in agreement with the theoretical estimation predicted by this specific optical configuration.

Similar analysis was performed for *PlanetCam2* Visible channel in the low resolution mode at the CAHA 1.23m telescope (Figure 3.5), and a scale of 0.116 ± 0.007 "/pixel was estimated (Table 3.4), also in agreement with the theoretical estimation. For example, for a FOV of 144" in *PlanetCam2* at CAHA 1.23 m telescope in low-resolution mode, the measured scale uncertainty of 0.007"/pixel causes a maximum star position uncertainty of around 1" for relative astrometry of stars at opposite sides of the frame. In the non-vignetting region, the scale or distance between pairs of stars shows no dependence with the position/orientation of the stars in the image or with the angular separation between the two stars when this value is large

enough to neglect the uncertainty in the stars position given by their FWHM. The FOV shows no optical distortion within our detection limits, which is in agreement with the planetary images and their measurements.

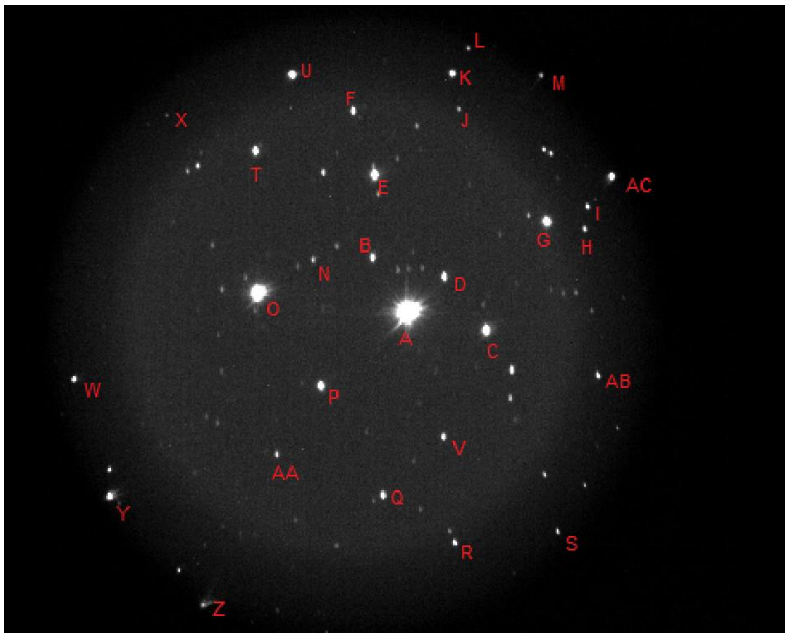

Figure 3.5. M103 cluster in an image taken at CAHA 1.23 m with *PlanetCam2* visible channel at low resolution.

Table 3.4. *PlanetCam2* – VIS (low resolution) image scale values estimations from different star pairs in M103 (CAHA 1.23).

Stars	**Ang sep** (")	**Mean dist to center** (pixel)	**Scale** ("/pixel)
E-C	74.75	399	**0.1150**
E-G	72.06	547	**0.1171**
L-C	111.03	625	**0.1167**
L-I	68.94	847	**0.1024**
B-X	100.28	627	**0.1170**
B-W	125.26	671	**0.1134**
B-M	108.22	583	**0.1281**
B-S	131.03	563	**0.1170**
B-AA	79.58	416	**0.1078**
W-S	206.76	1021	**0.1187**
W-U	150.67	1009	**0.1187**
W-AC	234.43	1005	**0.1188**
Y-M	245.63	1055	**0.1197**
S-M	183.36	932	**0.1195**
S-X	229.91	977	**0.1183**
S-AA	118.56	766	**0.1183**

Finally, the image scale of the *PlanetCam2* SWIR channel has also been analyzed in the same way with M103 star cluster. Figure 3.6 shows M103 imaged by *PlanetCam2–SWIR* in low resolution mode at CAHA 2.2m telescope. An image scale of 0.116 ± 0.007 "/pixel was estimated (Table 3.5), in agreement with the theoretical estimation.

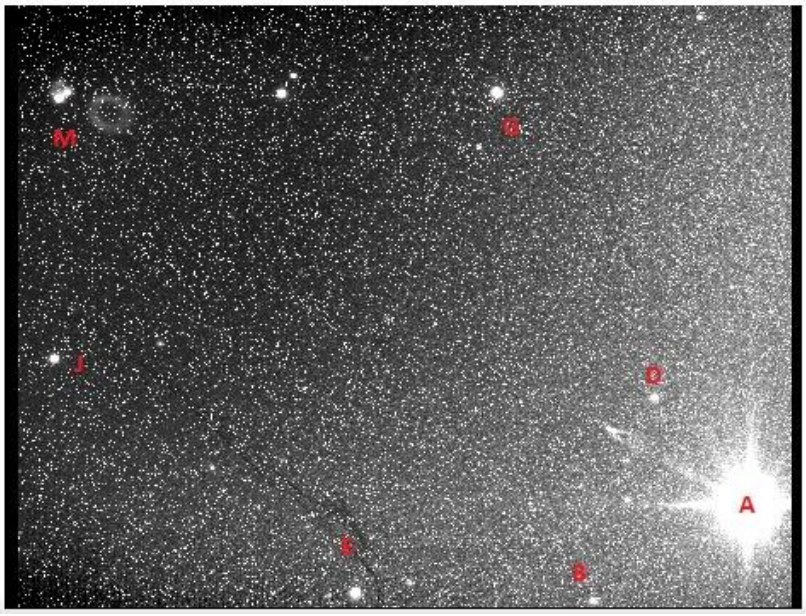

Figure 3.6. M103 cluster in an image taken at CAHA 2.2 m with *PlanetCam2* SWIR channel at low resolution.

Table 3.5. *PlanetCam2* – SWIR (low resolution), image scale values estimations from different star pairs in M103 (CAHA 2.2 m).

Stars	Ang dist (")	Mean dist to center (pixel)	Scale ("/pixel)
E-M	80.35	292	**0.1652**
E-D	48.79	328	**0.1647**
E-G	72.06	221	**0.1638**
D-J	81.80	256	**0.1649**
E-J	52.47	373	**0.1646**
D-G	47.35	410	**0.1636**
D-M	91.48	410	**0.1653**
J-M	36.67	410	**0.1659**
G-J	70.65	303	**0.1644**
G-M	59.88	303	**0.1654**

3.2.4 Limiting magnitudes

Several tests have been performed on the 1.23 m and 2.2 m telescopes in order to estimate the limiting magnitude for objects potentially to be observed with PlanetCam for different optical configurations, filters and exposure times. In Figure 3.7 we show four examples of the detection of faint objects with PlanetCam under different configurations mounted at these telescopes. Limiting magnitudes measured for the main PlanetCam2 filters in both lucky imaging and non-lucky imaging modes at CAHA 2.2m telescope are summarized in Table 3.6, where the corresponding values for CAHA 1.23m telescope are also estimated. In the lucky imaging case we try to sample a typical value for atmospheric oscillations of around 20Hz, which implies frames with exposure times of 50 ms. In these conditions magnitudes around 10 can be observed in V, R, I and J filters, while for filters B and H we need brighter objects around magnitude 8 for lucky imaging. In the non-lucky imaging case with longer exposure time values, limiting magnitudes around 15 can be easily achieved in filters V, R and I in exposure times of 60 s (around 14 estimated in B) and around 12 in J with 5 s exposure time (estimated similar in H filter). Moreover, with longer exposure time values like 3 min in filter R and V, magnitude of almost 19 was observed as shown in Figure 3.7.

Table 3.6. Limiting magnitudes with different *PlanetCam2* filters for 50 ms exposure time (lucky imaging) and 60 s (no lucky imaging)

		B	V	R	I	J	H
CAHA 2.2m	Lucky Imaging	8	10	10	10	10	8
	No Lucky Imaging	14	14.5	15	15.5	12.5	11
CAHA 1.23m	Lucky Imaging	6.7	8.7	8.7	8.7	8.7	6.7
	No Lucky Imaging	12.7	13.2	13.7	14.2	11.2	9.7

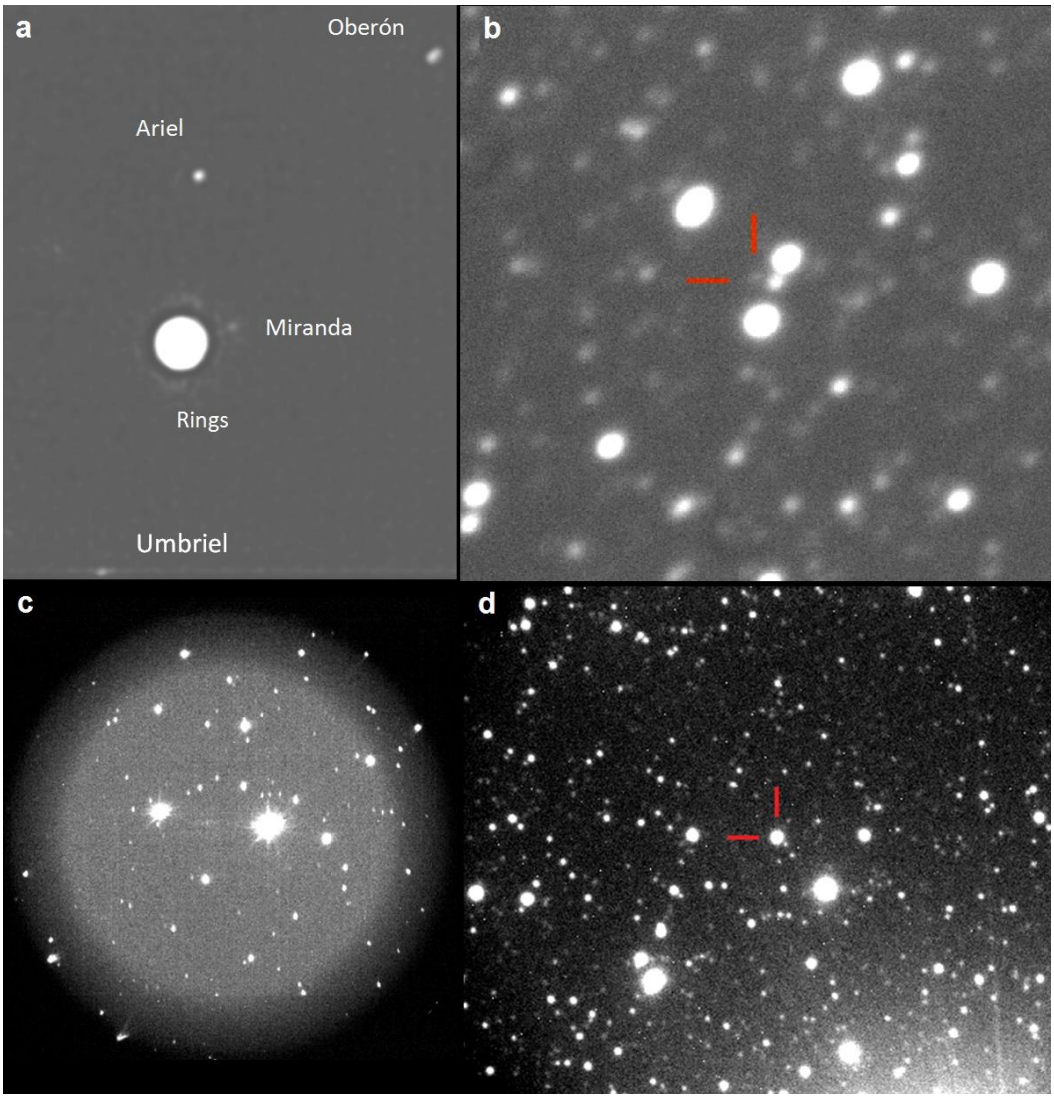

Figure 3.7. Limiting magnitude tests: (a) Uranus and its rings and main satellites including Miranda (magnitude 15.9) observed with *PlanetCam2* SWIR channel and RG1000 filter (2.2 m telescope; 300 exposures of 1 s); (b) Quaoar KBO (magnitude 18.8) with *PlanetCam1* without filter (single frame of 5 s and binning 8x8 during capture; this observing mode has utilities in star occultations observations); (c) Globular cluster M103 in an image taken at CAHA 1.23 m with *PlanetCam2* visible channel at low resolution (180 s from 6 frames of 30s exposure). Stars of magnitude up to 19 can be recognized; (d) Pluto with *PlanetCam1* with no magnification and I-filter at CAHA 2.2 m (single exposure of 512 s). Stars of magnitude over 15 are easily recognized and fainter sources can be identified.

Chapter 4

PLANETCAM PHOTOMETRIC CALIBRATION: JUPITER AND SATURN

This chapter describes the photometric calibration of *PlanetCam* performed over Jupiter and Saturn images, presenting the absolute reflectivity values obtained for both planets over the four years period of observation campaigns. The organization of the chapter is as follows: the set and timeline of observations performed so far is presented in section 4.1, while section 4.2 describes the calibration procedure and presents a set of *PlanetCam* photometric images of Jupiter and Saturn for all the filters available in both VIS and SWIR channels. Jupiter's and Saturn's absolute reflectivity values are presented in section 4.3, followed by a review of the different sources of uncertainty. Finally, in section 4.4 these results are discussed and compared with available reference values.

4.1 Observation Campaigns

Several Jupiter and/or Saturn observation campaigns have been performed since the commissioning of the instrument in 2012 at Calar Alto Observatory in Spain, using both the 1.23m and 2.2m telescopes. Table 4.1 provides details on these campaigns, including the telescope and *PlanetCam* configuration (Mendikoa et al., 2016). *PlanetCam1* configuration means that only the visible channel (VIS) was available at the time, while *PlanetCam2* means that both the visible and infrared (SWIR) channels were available. There are also some differences in the optics between both configurations but they are of no interest here since both planet and standard star are

always observed with the same configuration and hence any influence is cancelled out. Table 4.1 also shows the standard stars used for absolute reflectivity calibration including their spectral type.

Table 4.1. Observation campaigns at Calar Alto and standard stars used.

Campaign	Telescope	Instrument	Channel(s)	Objects	Standards	Spec. type
Jul 28/30, 2012	CAHA 1.23	PlanetCam1	VIS	Jupiter/Saturn	HD195034	G5D [4]
					HD192281	O5f [1]
Dec 2/3, 2012	CAHA 1.23/2.2	PlanetCam1	VIS	Jupiter	HD19445	sdF [1]
					HD28068	G1V C [4]
Apr 17/20, 2013	CAHA 1.23	PlanetCam1	VIS	Jupiter/Saturn	HD84937	sdF [1]
					HD217086	O7V [1]
					HD93521	O9Vp [1]
May 24/28, 2013	CAHA 1.23	PlanetCam1	VIS	Saturn	BD+26_2606	sdF [1]
					Hiltner102	B0III [1]
					HD217086	O7V [1]
Nov 21/24, 2013	CAHA 1.23	PlanetCam1	VIS	Jupiter	HD93521	O9Vp [1]
					HD217086	O7V [1]
					HD84937	sdF [1]
Dec 13/20, 2013	CAHA 1.23	PlanetCam1	VIS	Jupiter	HD19445	sdF [1]
					HD93521	O9Vp [1]
Apr 5/10, 2014	CAHA 1.23/2.2	PlanetCam1	VIS	Jupiter/Saturn	HIP40047	O5p [1]
					HD93521	O9Vp [1]
					HD84937	sdF [1]
May 12/15, 2014	CAHA 1.23	PlanetCam1	VIS	Jupiter/Saturn	BD+17_4708	sdF [1]
					HIP40047	O5p [1]
Jul 21/25, 2014	CAHA 2.2	PlanetCam1	VIS	Saturn	HD217086	O7V [1]
Dec 11/13, 2014	CAHA 2.2	PlanetCam2	VIS/SWIR	Jupiter	HD26965	K0.5V C [1]
					HD219477	G2 II-III [2]
Mar 2/4, 2015	CAHA 1.23	PlanetCam2	VIS/SWIR	Jupiter	HD95128	G1V [2]
					HD87822	F4V [2]
					HD108519	F0V [2]
May 21/25, 2015	CAHA 2.2	PlanetCam2	VIS/SWIR	Jupiter/Saturn	HD95128	G1V [2]
Jul 10/13, 2015	CAHA 2.2	PlanetCam2	VIS/SWIR	Saturn	HD1160	A0 [3]
					HD4656	K4 IIIb [3]
					HD4628	K2V [3]
					HD173638	F1 II [2]
					HD16139	G7.5 IIIa [2]
Dec 28/30, 2015	CAHA 2.2	PlanetCam2	VIS/SWIR	Jupiter	HD28068	G1V C [4]
					HD93521	O9Vp [1]
					HD10307	G1V [2]
					HD75732	G8V [2]
Mar 3/7, 2016	CAHA 2.2	PlanetCam2	VIS/SWIR	Jupiter/Saturn	HD19445	sdF [1]
					BD+33 2642	B2IVp D [1]
May 16/20, 2016	CAHA 2.2	PlanetCam2	VIS/SWIR	Jupiter/Saturn	HD192281	O5f [1]
					HD84937	sdF [1]
					HD93521	O9Vp [1]
					HD179821	G5Ia C [2]
					HD95128	G1V [2]
					HD75555	F5 C [2]
Jul 1/5, 2016	CAHA 2.2	PlanetCam2	SWIR	Jupiter/Saturn	HD102870	F8.5IV-V [2]
					HD100006	K0III D [2]
					HD124850	F7III C [2]
					HD165782	K0Ia B [2]

(1) Isaac Newton Group of telescopes spectrophotometric database, (2) IRTF spectral library, (3) SIMBAD database, (4) Solar Analog

A timeline representation of all these observation campaigns is shown in Figure 4.1, indicating Jupiter and Saturn opposition dates as well as HST relevant observations of Saturn (July 2015) and Jupiter (Feb 2016) used in this chapter as reference values for absolute reflectivity. The number of calibrated filter sequences is indicated below each campaign date.

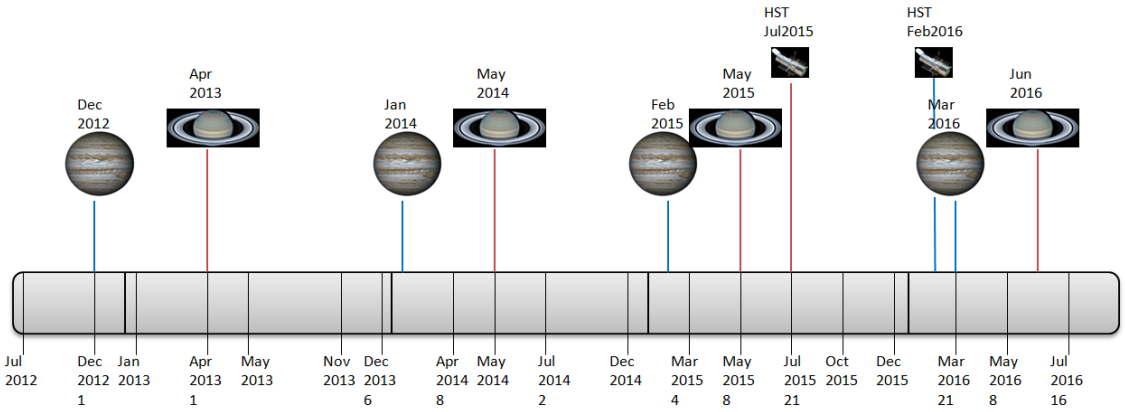

Figure 4.1. Timeline of Jupiter and Saturn observations at Calar Alto. Images of the planets are shown at the opposition date, while HST indicates the availability of observations for cross-calibration. The number of calibrated series available at each date is shown below the graph.

As standard stars, we used a selection of stars from the Isaac Newton Group of telescopes spectrophotometric database[22] for the VIS channel and from the InfraRed Telescope Facility (IRTF) spectral library[23] for the SWIR channel (Rayner et al., 2009). These databases provide medium to low resolution spectra of the stars that can be convolved with our filters plus system response, thus getting accurate calibration factors as it will be explained later. Whenever this was not possible for all wavelengths, we completed the values using the VizieR photometry tool on the SIMBAD database[24] (Ochsenbein et al., 2000). The impact of such very low resolution data for the standard stars will be discussed in section 4.3.2.

The standard stars used for the absolute reflectivity calibration of Jupiter and Saturn were selected according to different criteria. First, the availability of a star with high resolution spectrum was considered. Second, the position of the star in the sky relative to the planet being calibrated was also considered, trying to get the standard star as close as possible to the planet, with similar air-mass at the corresponding observation

[22] http://catserver.ing.iac.es/landscape/

[23] http://irtfweb.ifa.hawaii.edu/IRrefdata/sp_catalogs.php

[24] http://simbad.u-strasbg.fr/simbad/

time. As a result of these criteria, we show in Figure 4.2 the position of the standard stars used in this work relative to Jupiter and Saturn.

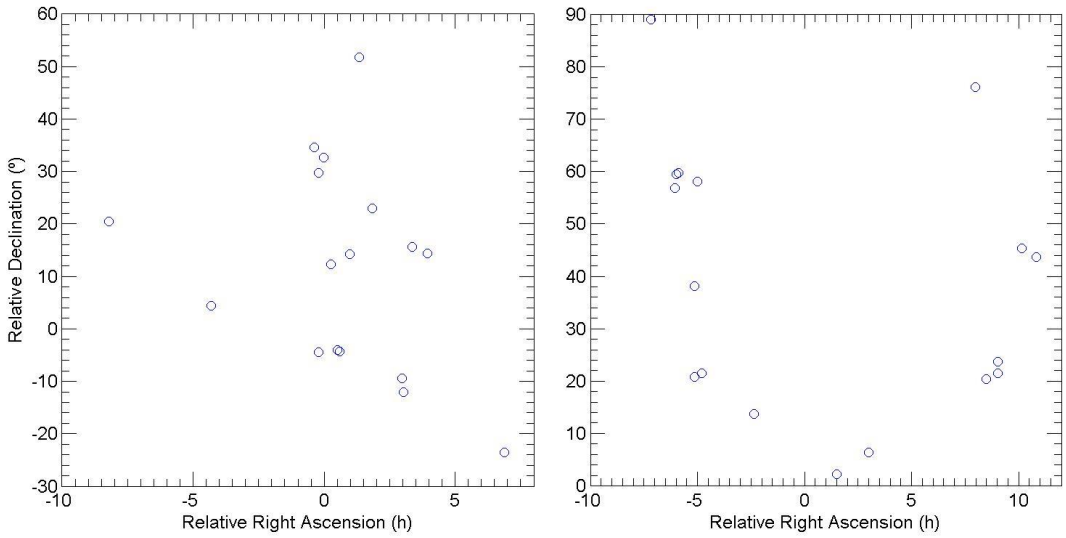

Figure 4.2. Position of the standard stars used for photometric calibration relative to Jupiter (left) and Saturn (right) positions in the sky.

4.2 Absolute Reflectivity Measurements

4.2.1 Photometric calibration

In planetary sciences, it is common to use the absolute reflectivity *I/F* of a given surface or atmosphere (Sánchez-Lavega, 2011, Ortiz et al., 1993). This quantity is defined as the ratio of surface brightness (*I*) to that of a flat Lambertian surface (*F*) where πF is the solar flux ($Wm^{-2}nm^{-1}$) at the given planetary distance. Absolute reflectivity of planetary images is computed based on a standard star image by calculating a 'calibration factor' between the known star intensity and the count rate registered, according to the following procedure.

From the image of a standard star acquired for calibration purposes we get the total number of counts ΣDN_{ST} over the star image. This image is usually the sum of *N* frames with accumulated exposure time T_{ST} (s). In order to subtract the counts from the image background, we define an area around the star, as close to it as possible, but not affected by the starlight itself. An average value of the counts rate in such a ring is then used as the background value, to be subtracted from the total counts from the star.

On the other hand, we know the star's spectrum from a database $\pi F_{ST\lambda}$ (given in $Wm^{-2}nm^{-1}$), that allows the estimation of flux detected by our equipment:

$$\pi F_{ST} = \int_{\lambda} \pi F_{ST\lambda} \cdot T(\lambda)\phi(\lambda)d\lambda \qquad (4.1)$$

being $T(\lambda)$ the filter transmittance and $\phi(\lambda)$ the instrument response (detector, optical system).

We then get the calibration factor $(IC)_\lambda$ as the ratio between star flux and counts rate registered:

$$(IC)_\lambda = \frac{\pi F_{ST}}{\left[\sum (DN_{ST})_i - \sum (DN_{BGst})_i\right]/T_{ST}} = \frac{\pi F_{ST}}{\sum C_{ST}} \qquad (4.2)$$

where ΣC_{ST} is the counts ratio from the star image (total number of counts per time unit), once the background (BG) subtracted.

This calibration factor depends on the telescope and the photometric conditions of the sky during the observations, because of its influence in the number of counts. The *IC* factor also depends on the wavelength analyzed. On the other hand, *IC* factor does not depend on the detector, optical system or even standard star used.

Once the calibration factor *IC* is calculated, and assuming we are always working in the linear part of the detector sensitivity curve, we can estimate the intensity I_{Pi} related to pixel *i* of the planetary image to be calibrated, the pixel counts being DN_{Pi} (subtracting planetary image background DN_{BGPi}) for exposure time T_P.

$$I_{Pi} = \frac{\left(DN_{Pi} - DN_{BGPi}\right)}{T_P}(IC)_\lambda = C_P \cdot (IC)_\lambda \qquad (4.3)$$

Regarding the solar flux received by the planet πF_{OP}, it can be estimated from that received on Earth πF_O and the planet distance *D* to the Sun with respect to Earth-Sun distance, i.e. in Astronomical Units. Here we use the solar spectrum given by Colina et al. (1996).

$$\pi F_{OP} = \left(\frac{1}{D}\right)^2 \pi F_O \qquad (4.4)$$

In order to estimate planetary intensity received on Earth independently from the planetary disk portion represented by the pixel, we divide I_{Pi} by the squared image scale θ arcsec/pixel. This is the solid angle per pixel approximation used by Chanover et al., 1996) shown in Figure 4.3.

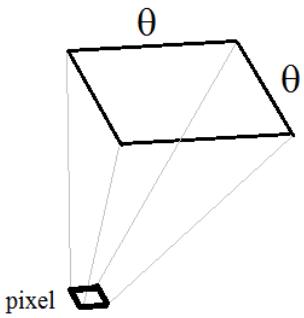

Figure 4.3. Solid angle per pixel for image scale θ.

On the other hand, the solar flux on the planet $\pi F_{OP}/\pi$ is also given per steradian, so the reflectivity calculated as the dimensionless ratio *I/F* is therefore:

$$\left(\frac{I}{F}\right)_0 = \frac{I_{Pi}/\theta^2}{\left(\pi F_O / D^2\right)/\pi} \qquad (4.5)$$

Since solar flux detected πF_O is estimated from solar spectrum in a similar way as described for star flux πF_{ST} above described, we can finally retrieve reflectivity as:

$$\left(\frac{I}{F}\right)_0 = \pi \frac{D^2}{\theta^2} \frac{C_P}{\sum C_{ST}} \frac{\int_\lambda \pi F_{ST\lambda} \cdot T(\lambda)\phi(\lambda)d\lambda}{\int_\lambda \pi F_{O\lambda} \cdot T(\lambda)\phi(\lambda)d\lambda} \qquad (4.6)$$

If star and planet images were taken with different air-mass values *X*, this has to be compensated considering an intensity exponential decay law and from the extinction coefficient κ_λ (in stellar magnitudes per air mass), from what we finally get the usual expression used for absolute reflectivity estimation for each planetary image pixel:

$$\left(\frac{I}{F}\right) = \pi \frac{D^2}{\theta^2} \frac{C_P}{\sum C_{ST}} \frac{\int_\lambda \pi F_{ST\lambda} \cdot T(\lambda)\phi(\lambda)d\lambda}{\int_\lambda \pi F_{O\lambda} \cdot T(\lambda)\phi(\lambda)d\lambda} e^{\frac{k_\lambda}{2.5}(X_P - X_{ST})} \quad (4.7)$$

This expression allows a planet image be converted from digital counts rate into absolute reflectivity *I/F* by using a standard star's intensity spectrum as reference.

4.2.2 Image acquisition and processing

The calibration process begins with the capture of the sequence of frames of the science object (planet or calibration star) that is used to build the final image. This requires appropriate exposure times for each filter in order to get a good signal to noise ratio within the detector's linear regime, while being fast enough to perform lucky imaging at least for the wider filters. Images are then processed with PLAYLIST (described in chapter 3), obtaining the planetary photometric images in FITS format containing double precision real numbers that represent the total digital counts per second for each pixel.

Figure 4.4 toFigure **4.7** show such photometric images of Jupiter and Saturn for different *PlanetCam* filters in both VIS and SWIR channels processed with PLAYLIST. These images preserve photometric information but can be high-pass filtered to show faint structures and study dynamics (see for instance Hueso et al., 2017b). All the *PlanetCam* filters are given by its short name and effective wavelength in nanometers for narrow filters (full details can be found in chapter 2, Mendikoa et al., 2016). VIS channel includes filters U, Vio, B, V, R, M1 (619), C1 (635), M2 (727), C2 (750), M3 (890) and C3 (935), while SWIR channel includes YC (1090), YM (1160), V1 (1190), V2 (1220), JC (1275), JM (1375), V3 (1435), HC (1570), HM (1650), J and H. Figure 4.4 shows photometric images of Jupiter taken with *PlanetCam2* configuration at the 2.2-m telescope at Calar Alto observatory (March 2016) for absolute reflectivity calibration with VIS channel, while Figure 4.5 shows those corresponding to SWIR channel. Figure 4.6 shows photometric images of Saturn taken with *PlanetCam2* at the 2.2-m telescope at Calar Alto observatory (May 2016) for absolute reflectivity calibration with VIS channel. Figure 4.7 shows Saturn images in the SWIR channel

where image saturation at the rings in some filters does not affect the atmosphere photometric analysis.

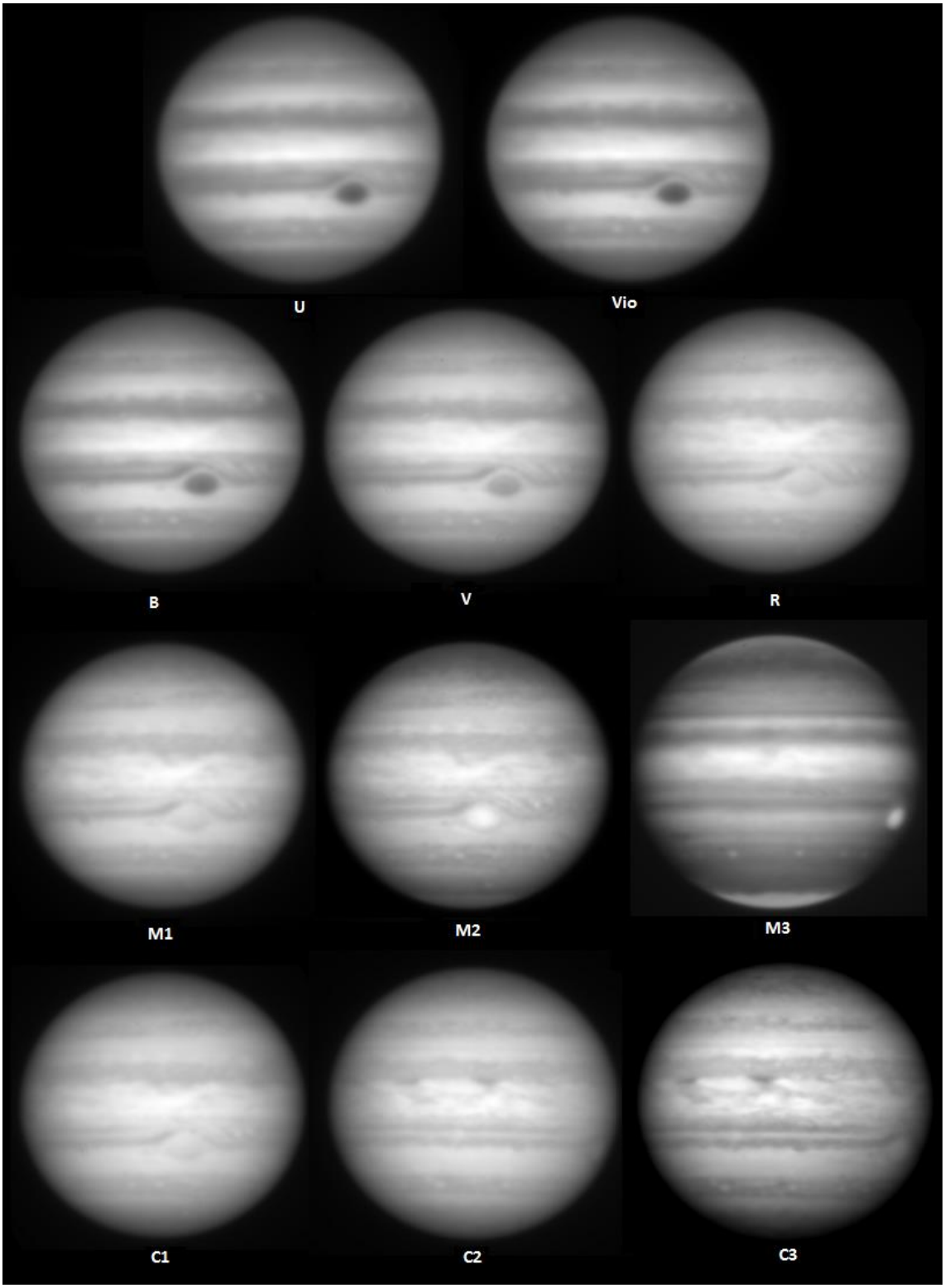

Figure 4.4. Photometric images of Jupiter with *PlanetCam* VIS channel filters (March 3rd, 2016).

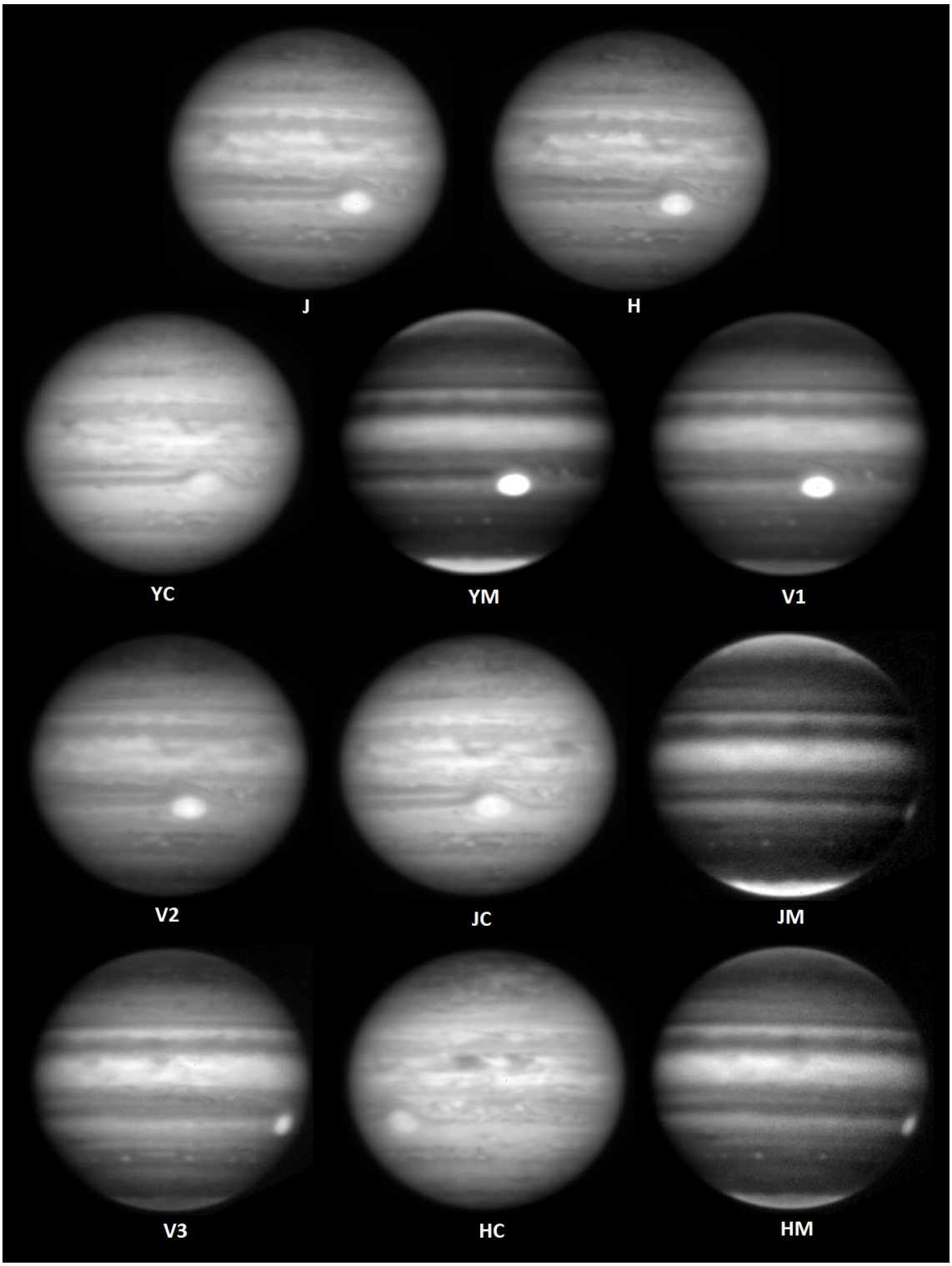

Figure 4.5. Photometric images of Jupiter with *PlanetCam* SWIR channel filters (March 3rd, 2016).

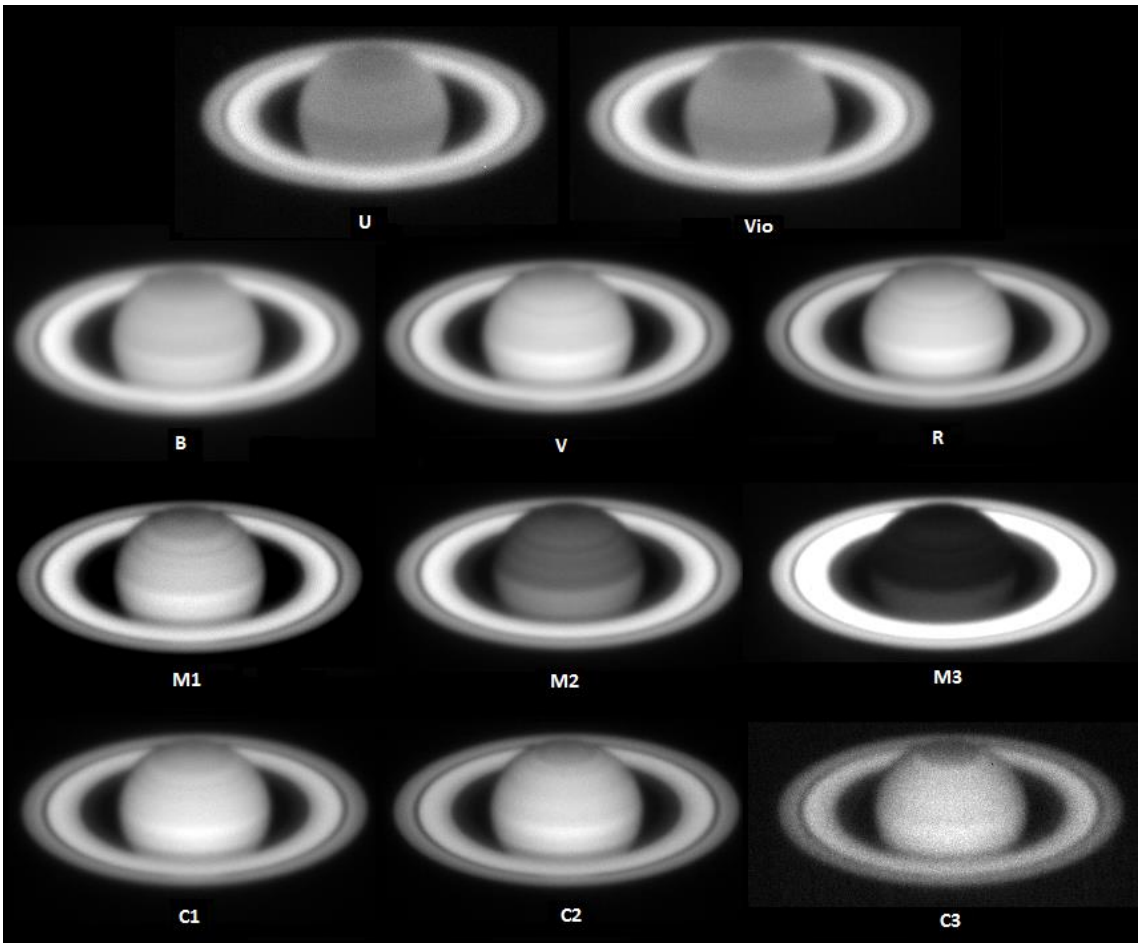

Figure 4.6. Photometric images of Saturn in *PlanetCam* VIS channel filters (May 20th, 2016).

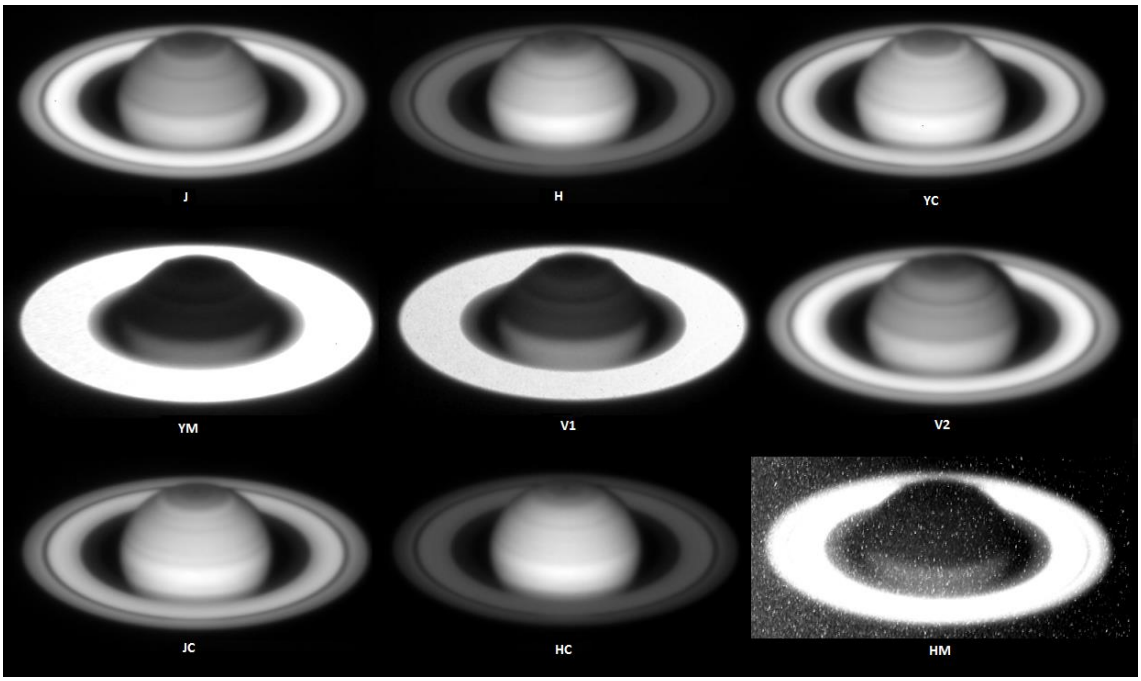

Figure 4.7. Photometric images of Saturn in *PlanetCam* SWIR channel filters (May 20th, 2016). The HM image is also affected by water absorption on Earth's atmosphere and requires acquisitions with high-gains resulting in a level of noise that cannot be fully subtracted from the dark current files.

4.3 Results

Following equation 4.7 we have photometrically calibrated Jupiter and Saturn images, computing *I/F* values for each pixel on the images. Absolute reflectivity *I/F* North-South scans along central or sub-observer meridian (i.e. *I/F* vs. latitude) will be shown for all available filters at 1º spatial resolution for each observation campaign, using different calibration standard stars as detailed in Table 4.1. Because of the zonal banding in the giant planets, this method is well suited to compare spatial and temporal reflectivity changes in different spectral regions as will be discussed in chapter 5. Mean *I/F* scan is obtained for each filter and observation campaign from planetographic latitude -80º to +80º. Figure 4.8 to Figure **4.11** show the mean absolute reflectivity for each filter, including the standard deviation from the analysis of different image series in each campaign. The error sources are mainly due to image navigation and the uncertainties in the calibration as it will be discussed in section 4.3.2. The mean *I/F* scans from some campaigns were omitted when its latitudinally averaged deviation from the overall mean *I/F* scan was higher than the standard deviation at all latitudes. After this filtering, the overall mean *I/F* scans and standard deviations were recomputed resulting in the latitudinal scans shown in Figure 4.8 to Figure **4.11**, and are tabulated in Appendix A1.

The empirical Minnaert law for diffuse reflection (Minnaert, 1941) has been used to determine the *I/F* variation with the scattering angles μ and μ_0 (Sánchez-Lavega, 2011):

$$(I/F)(\mu,\mu_0) = (I/F)_0\,\mu_0^k\mu^{(k-1)} \qquad (4.8)$$

where $(I/F)_0$ represents the absolute reflectivity for nadir viewing and k is the limb darkening coefficient. In this way, images can be corrected from limb-darkening effects and photometric results from the central meridian can be extended to other longitudes. The absolute reflectivity and Minnaert coefficients mean values (from observations from 2012 to 2016) for each latitude and *PlanetCam* filter are presented in the form of tables in the Appendix A2. These values can be of interest in order to estimate the phase light curves for extrasolar Jupiter and Saturn-like planets (Dyudina et al., 2005).

4.3.1 Absolute Reflectivity values

Jupiter mean absolute reflectivity *I/F* values along its central meridian (not using images with the Great Red Spot close to it) from observational campaigns between December 2012 and May 2016 (Figure 4.8) are determined with different levels of uncertainty at different wavelengths. We calculate the latitudinal *I/F* deviation from the mean for each filter from the ensemble of valid observations campaigns. For some filters only 3 campaigns provided valid data, while for others our sample grows to 5 campaigns. In the visible channel the overall uncertainties considering the mean of standard deviations from all latitudes are, for the filters represented in Figure 4.8, the following: UV (3 campaigns; 16%), Vio (3; 18%), B (5; 23%), V (4; 16%), M1 (3; 20%), C1 (3; 20%), M2 (3; 11%), C2 (3; 20%), M3 (5; 18%), C3 (3; 18%). It is worth to say that these uncertainty values include, among different causes discussed in section 4.3.2, possible physical changes due to planetary atmosphere temporal evolution, discussed in chapter 5.

In a similar way, we show in Figure 4.9 the overall mean absolute reflectivity and associated uncertainty for SWIR filters corresponding to observation runs between March 2015 and July 2016. Filters JM and V3 are affected by telluric water absorption, while the HM filter is affected by the SWIR detector sensitivity cut-off (Mendikoa et al., 2016) and therefore are not included in this figure. The number of campaigns considered and average uncertainties for these filters are as follows: YC (4; 24%), YM (4; 19%), V1 (4; 12%), V2 (3; 22%), JC (4; 18%), HC (4; 11%).

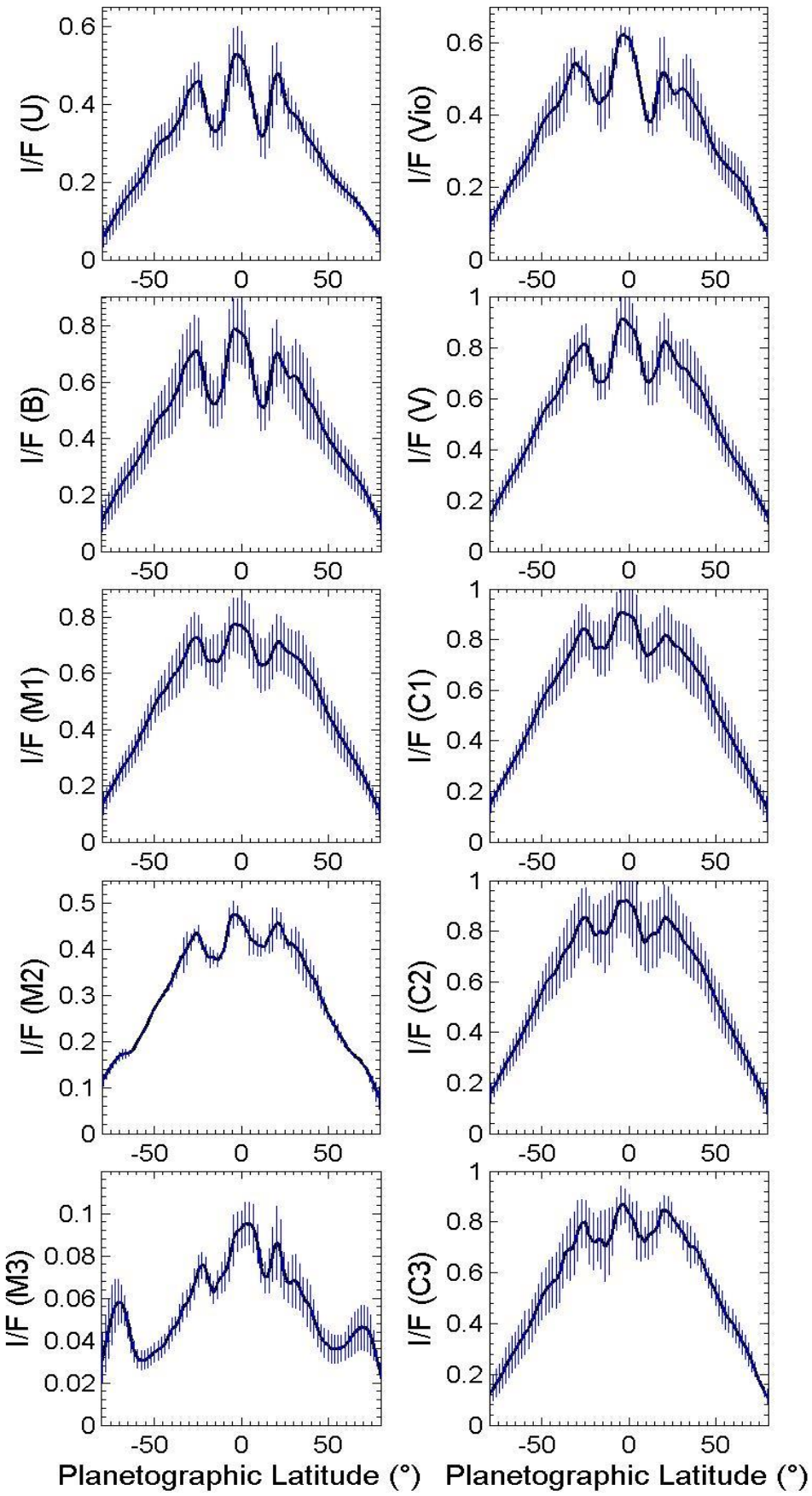

Figure 4.8. Jupiter mean absolute reflectivity at the central meridian in VIS channel filters.

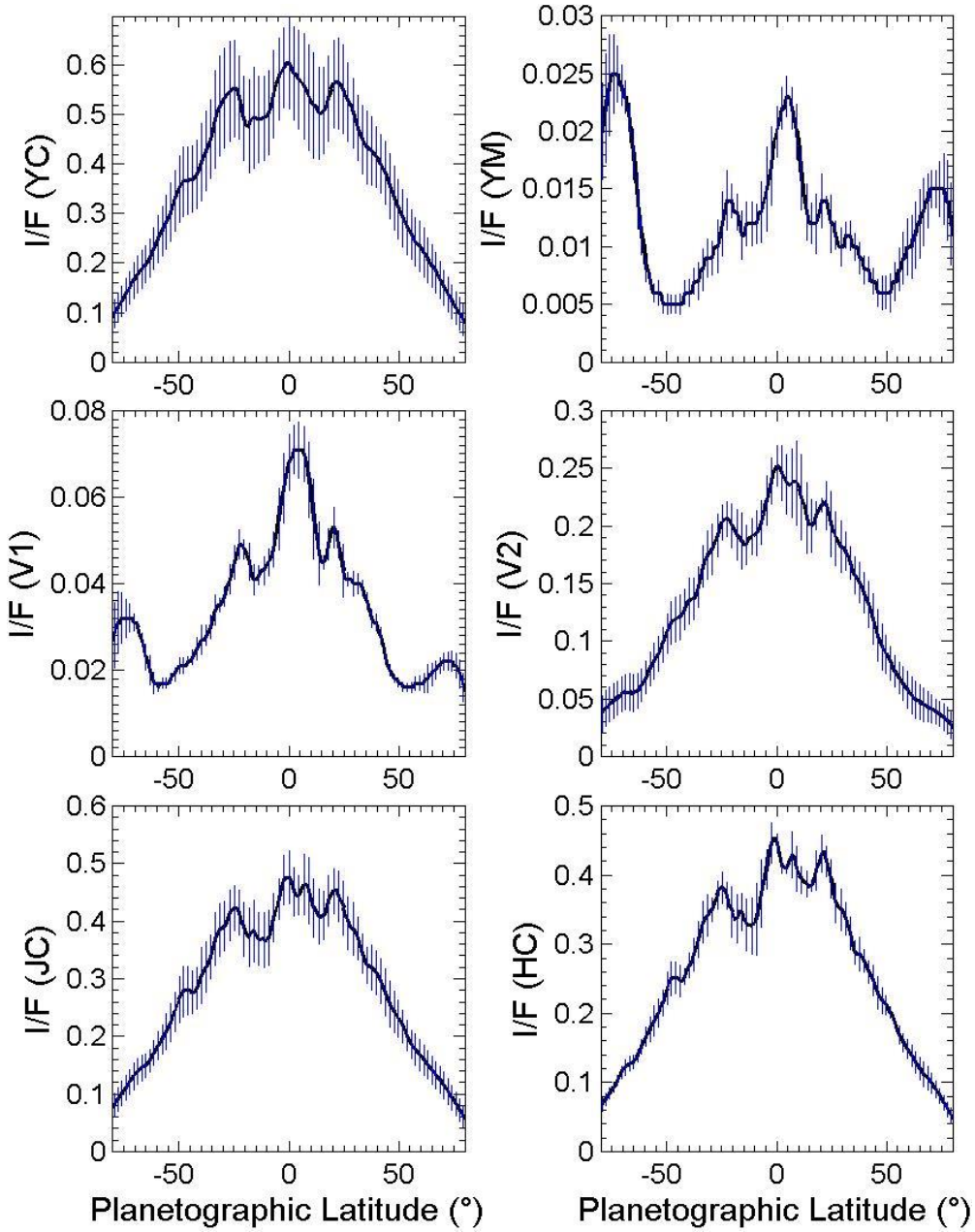

Figure 4.9. Jupiter mean absolute reflectivity at the central meridian in SWIR channel filters.

We show the overall mean absolute reflectivity at the central meridian of Saturn and its associated uncertainty in Figure 4.10 for the filters in the VIS channel. Note that Saturn's rings cover part of the disk of the planet preventing to observe the southern hemisphere. Latitudinal values here shown are limited to the northern hemisphere where the influence of Saturn rings is negligible. Our results correspond to observation campaigns run from April 2013 to May 2016. The number of campaigns considered and average uncertainties for these filters are: UV (5; 12%), Vio (4; 13%), B (4; 10%), V (4; 12%), M1 (3; 11%), C1 (4; 16%), M2 (4; 9%), C2 (3; 12%), M3 (3; 23%), C3 (2; 24%).

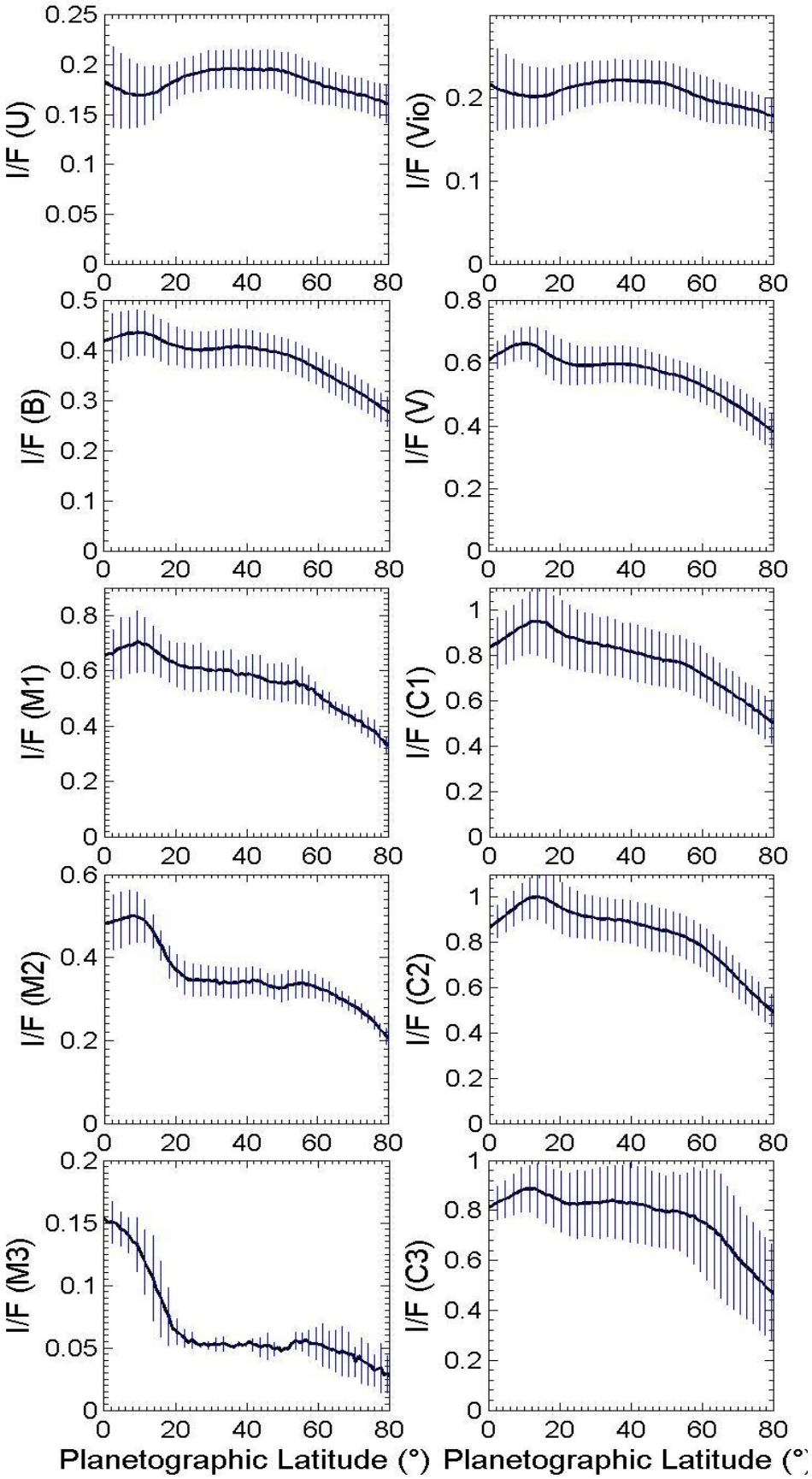

Figure 4.10. Saturn mean absolute reflectivity at the central meridian in VIS channel filters.

Similar results for the filters available in the SWIR channel are shown in Figure 4.11 and they correspond to observations acquired between May 2015 and July 2016. The number of campaigns considered and average uncertainty for these filters are: YC (4; 7%), YM (4; 12%), V1 (4; 17%), V2 (3; 11%), JC (3; 3%), HC (4; 6%).

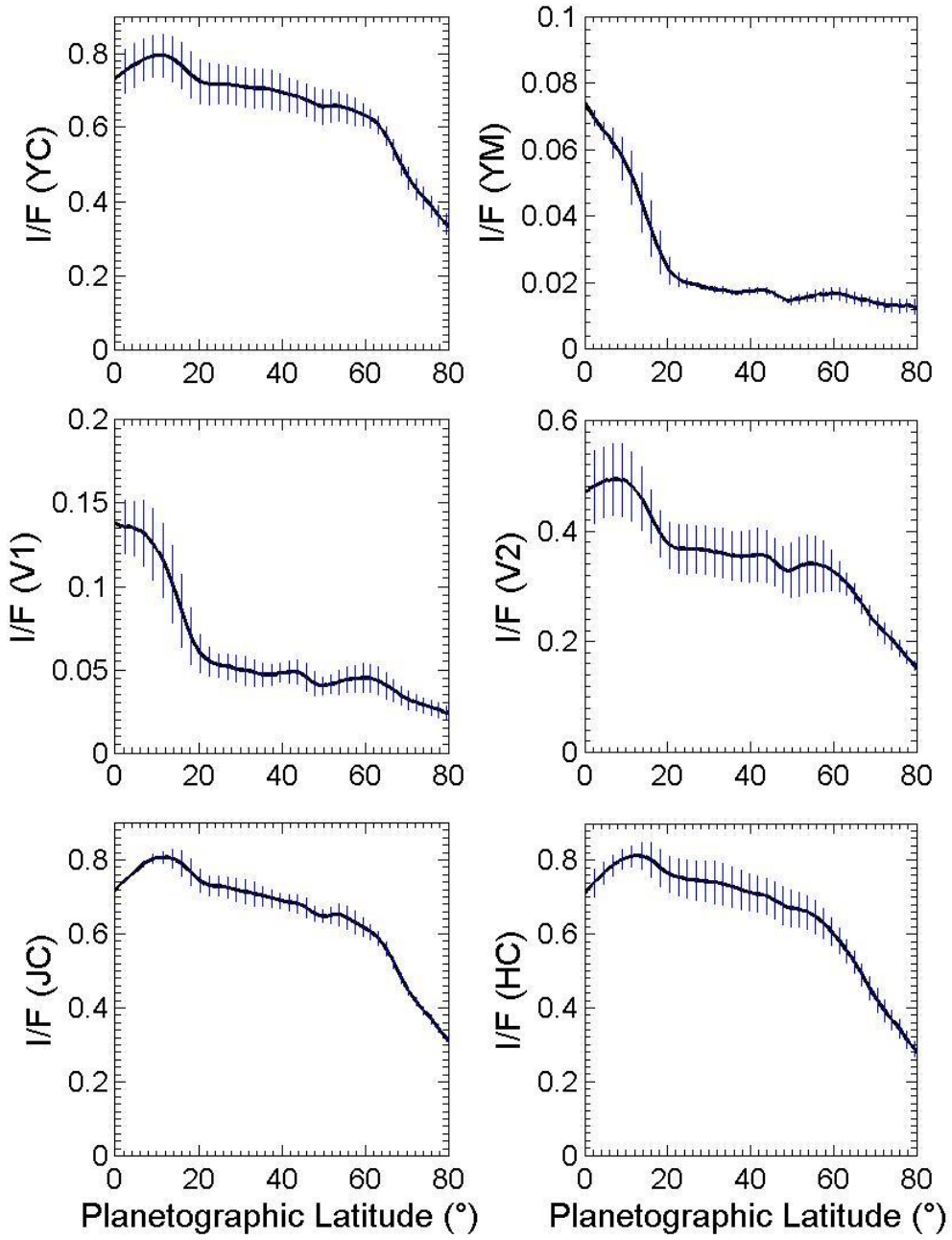

Figure 4.11. Saturn mean absolute reflectivity at the central meridian in SWIR channel filters.

4.3.2 Uncertainty sources

There are several sources of uncertainty and variability in the retrieved *I/F* mean values at each latitude: the intrinsic uncertainty in the calibration procedure itself, uncertainty in the determination of the latitudes of each pixel due to small inaccuracies in the planet navigation, variations of the reflectivity at different longitudes on particular bands and, finally, possible temporal changes in the reflectivity of some planet bands observed on different epochs.

The uncertainty on *I/F* produced by the image calibration procedure can be estimated from the errors in the different parameters appearing in *I/F* expression (equation 4.7) in section 4.2.1. In previous sections we gave an estimation of the calibration values dispersion of up to around 20%. Comparing count rates for a standard star with the same telescope and optics at different observation nights but similar air-mass, variations of 1 to 10% can be found, and rarely higher. While most of the error can be attributed to the photometrical conditions along the observing run for the planet and calibration star (sub-section A), other sources include detector noise (particularly important for some filters in deep methane absorption bands in the SWIR channel resulting in very low signals, such as the HM filter) and uncertainties in the knowledge of the spectrum of the standard star used in each case.

Fluctuations in flat-fielding and dark current subtraction can affect count rates for planet and standard star. However, these variations are well below those due to Earth atmospheric conditions (transparency, seeing). However, such instrumental sources of uncertainties rarely account for more than 2% of the signal (see chapter 3, Mendikoa et al., 2016). Extinction coefficients at Calar Alto Observatory are regularly monitored (Sanchez S.F. et al. 2007) and they imply a relative error of around 5% (sub-section B). In order to minimize errors from atmospheric extinction, the standard stars were usually observed at elevations with differences below 0.3 air masses to the elevation of the planet.

Spectral data available for the standard stars also contain a certain degree of inaccuracy that contributes to the total calibration error. In particular, for some standard stars their calibrated flux was only available at low spectral resolution for some wavelength ranges. This could imply significant calibration errors for narrow filters where spectral bands are not properly resolved in the spectrum of the standard star. As

an example, for star HD19445 different spectrum sources were compared (Isaac Newton Group, SIMBAD, X-Shooter[25]) including some synthetic models based on Kurucz (Castelli et al., 1997) and BT-Nextgen[26] (Allard et al., 2012). For visible filters, the total star flux showed a variation of around 15% depending on the stellar parameters assumed (sub-section C).

Uncertainties introduced from inaccuracies in the planet navigation can be estimated after examining results with different navigations of the same planetary image. Our tests show that the uncertainty on the width of a band can be around 10% (rarely up to 20%) and the latitudinal uncertainty in the position of the maximum brightness of a particular zone can be around 1º. This has to be considered when comparing planet reflectivity from different images at given latitude (sub-section D).

In addition, it has to be taken into account that the different *I/F* scans correspond always to the central meridian, but, due to the rotation of the planet, every scan corresponds to a different planetary longitude, and given that planetary bands have fluctuations in their albedo edges and that they may include discrete features (spots, vortices and other meteorological structures), the band width and reflectivity may vary. As in the disk navigation issue, uncertainty in bands width due to these variations have been estimated to be ~ 10% and positions in around 1º, by analyzing several *I/F* vs. latitude scans at different longitudes in the same navigated image (sub-section E).

Finally, variations in *I/F* scans can also be due to intrinsic changes of the planet reflectivity over time at particular bands in Jupiter (Pérez-Hoyos et al., 2012) or over large regions in Saturn as seasonal variations proceed (Smith et al., 1982; Sánchez-Lavega et al., 1993). Characterizing real global or local color variations in Jupiter and Saturn clouds is a key scientific area and relevant results from *PlanetCam* will be discussed in chapter 5 after artificial sources of variations and uncertainties have been appropriately constrained.

In summary, these uncertainty sources contribute to an overall systematic uncertainty that has been estimated to be around 10-20% in absolute reflectivity and much lower (possibly below 2%) in relative photometry. Not perfectly photometric

[25] http://xsl.u-strasbg.fr/

[26] http://svo2.cab.inta-csic.es/theory/newov/index.php?model=bt-nextgen-agss2009

conditions are the main cause responsible for this level of uncertainty, while the contribution of other sources, while having a minor impact, cannot be fully discarded.

The following sub-sections provide a more detailed quantitative analysis of the above mentioned uncertainty sources in absolute reflectivity calibration, including the justification of the uncertainty estimations given.

A. Uncertainty from the sky photometric conditions

In order to estimate the uncertainty due to the variable sky photometric conditions, a test has been done by comparing the number of counts of the same standard star in different observation nights, for a given gain mode and optical configuration and with a similar air mass.

The following Tables 4.2 to 4.5 show the counts rate *ΣDN/s* summed over the standard star image for each filter. The air mass at the time of the image acquisition and total exposure time is also shown. By comparing the counts rate at two different nights, the %variation in counts rate is given with respect to the mean value for each filter.

The star counts show variations of 1 to 10%, and in few cases higher values have been observed. Although small part of this is due to different air masses in both nights, it shows actual variations in the sky photometric conditions, and therefore the importance of acquiring images of the calibration standard star the same night the planet is observed.

Table 4.2. HD19445 at CAHA 1.23m with *PlanetCam1* (December 14/15, 2013).

	December 14			December 15			
Filter	**AirMass**	**T(s)**	**ΣDN/s**	**AirMass**	**T(s)**	**ΣDN/s**	**%var**
U	1.02	600	11176	1.02	150	8575	**26.3**
Vio	1.02	600	43327	1.02	100	39541	**9.1**
B	1.02	100	171520	1.02	100	167901	**2.1**
V	1.02	100	430955	1.02	100	438480	**1.7**
R	1.02	100	828576	1.02	100	832616	**0.5**
W21	1.02	100	1619070	1.02	100	1719310	**6.0**
I	1.02	100	533550	1.02	100	569202	**6.5**
M3	1.02	600	7570	1.02	150	7757	**2.4**

Table 4.3. HD173638 at CAHA 2.2m with *PlanetCam2*-VIS (July 10/11, 2015).

	July 10			July 11			
Filter	**AirMass**	**T(s)**	**ΣDN/s**	**AirMass**	**T(s)**	**ΣDN/s**	**%var**
U	2.40	30	5	2.30	30	4.32	**1.4**
Vio	2.40	36	17	2.30	36	15.57	**3.1**
B	2.40	7.2	262	2.30	7.2	229	**0.2**
V	2.40	1.2	871	2.30	3.6	885	**1.0**
R	2.40	0.48	1488	2.30	3.6	1231	**1.6**
M1	2.40	18	74	2.30	18	58	**1.7**
C1	2.40	18	74	2.30	18	58	**1.8**
M2	2.40	18	44	2.30	18	41	**0.3**
C2	2.40	18	46	2.30	18	48	**16.3**
M3	2.40	18	23	2.30	18	23	**32.2**
C3	2.40	30	3.66	2.30	30	2.75	**14.1**

Table 4.4. HD102870 at CAHA 2.2m with *PlanetCam2*-SWIR (July 2/4, 2016).

	July 2			July 4			
Filter	**AirMass**	**T(s)**	**ΣDN/s**	**AirMass**	**T(s)**	**ΣDN/s**	**%var**
J	2.13	1.28	1226318	2.50	2.55	1386310	**12.2**
H	2.13	1.28	942751	2.50	2.55	1038891	**9.7**
YC	2.13	1.50	229300	2.50	2.55	250748	**8.9**
YM	2.13	3.00	174134	2.50	4.50	196475	**12.0**
V1	2.13	3.00	114314	2.50	4.50	127129	**10.6**
V2	2.13	1.50	308119	2.50	3.00	348543	**12.3**
JC	2.13	1.50	281405	2.50	3.00	321228	**13.2**
HC	2.13	1.50	212214	2.50	4.50	235847	**10.5**

Table 4.5. HD124850 at CAHA 2.2m with *PlanetCam2*-SWIR (July 2/4, 2016).

	July 2			July 4			
Filter	**AirMass**	**T(s)**	**ΣDN/s**	**AirMass**	**T(s)**	**ΣDN/s**	**%var**
J	1.60	1.28	897280	1.85	2.55	968049	**7.6**
H	1.60	1.28	666305	1.85	2.55	718059	**7.5**
YC	1.60	3.00	162680	1.85	9.00	172652	**5.9**
YM	1.60	3.00	134194	1.85	9.00	140328	**4.4**
V1	1.60	3.00	80672	1.85	9.00	84360	**4.4**
V2	1.60	1.50	213863	1.85	9.00	234246	**9.1**
JC	1.60	1.50	191554	1.85	9.00	211963	**10.1**
HC	1.60	1.50	139653	1.85	9.00	152313	**8.7**

B. Uncertainty in the extinction coefficients

Reference values for extinction coefficients at Calar Alto observatory for different wavelengths are available as shown in Table 4.6, yet real extinction coefficient values in an observation night can differ from these values. In order to estimate the uncertainty in absolute reflectivity calculations due to this problem, the number of counts for a given standard star was measured in the same night at different positions corresponding to different air mass values.

In particular, HD102870 was observed at two different positions from Calar Alto 2.2m telescope with *PlanetCam2*. Table 4.7 presents the air mass, total exposure time and counts rate from these two tests and an estimation of the extinction coefficient *K* from them, given by the expression: $K = [2.5/(X'-X)]\ ln(\Sigma DN\ /\Sigma DN')$, where *X* is the air mass and ΣDN the corresponding counts rate summed over the star image. *PlanetCam* filters in wavelengths comparable to those with available reference values for extinction coefficient have been considered.

Table 4.6. Extinction coefficients at Calar Alto

Wavelength (nm)	κ_λ **Summer** (mag)	κ_λ **Winter** (mag)
380	0.505±0.126	0.375±0.034
436	0.324±0.057	0.223±0.022
500	0.216±0.049	0.144±0.010
671	0.109±0.034	0.055±0.005
880	0.065±0.017	0.024±0.001
1020	0.049±0.019	0.014±0.002

Source: *The night-sky at the CAHA observatory* (SF Sanchez et al.,2007)

Table 4.7. Extinction coefficient *K* estimated from *PlanetCam* observations

	Test 1			Test 2			
Filter	**AirMass**	**T(s)**	**ΣDN/s**	**AirMass**	**T(s)**	**ΣDN/s**	**K**
Vio	1.31	150	79386	1.74	18	71055	**0.64**
B	1.31	3000	999389	1.74	180	963305	**0.21**
M1	1.31	600	140719	1.74	90	133018	**0.33**
C1	1.31	600	170344	1.74	90	160056	**0.36**
M2	1.31	600	103231	1.74	90	95931	**0.43**
YC	1.31	15000	264604	1.74	15000	246300	**0.42**

Comparing these estimated *K* coefficients with those from Calar Alto reference in comparable wavelengths, we can estimate the expected influence of these different *K* values in the absolute reflectivity *I/F* calculations through the exponential factor

exp[k(X'-X)/2.5] in the *I/F* expression (equation 4.7). Assuming an air-mass difference *(X'-X)* between standard star and planet of 0.3, it can be seen that this exponential factor can account up to 5% in the reflectivity uncertainty.

A more exhaustive analysis should be done in order to experimentally determine the extinction coefficient, yet this brief study gives an estimation of the uncertainty in the absolute reflectivity calculations due to the use of reference values of extinction coefficient.

C. Uncertainty from the source of the standard star spectrum

The low spectral resolution for some standard stars also contributes to errors in absolute reflectivity calibration. In order to make an estimation of the uncertainty in absolute reflectivity calibration due to this factor, different spectrum sources for HD19445 were compared (Isaac Newton Group, SIMBAD, X-Shooter) as well as some synthetic models based on Kurucz (Castelli et al., 1997) and BT-Nextgen (Allard et al., 2012), as shown in Figure 4.12. Synthetic models spectra were scaled in order to make them coincident with ING observed spectra at 700nm and thus avoid systematic uncertainties.

According to *I/F* expression 4.7 the star intensity spectrum must be integrated over the filter transmittance and instrument response functions. This was done for each *PlanetCam2* visible filter and all the standard stars. The total star flux showed a variation between 1% and 20% depending on the filter considered (Table 4.8). Considering this uncertainty source, it would be advisable to promote a calibration campaign with simultaneous medium- to high- resolution spectra taken with another instrument for some selected stars.

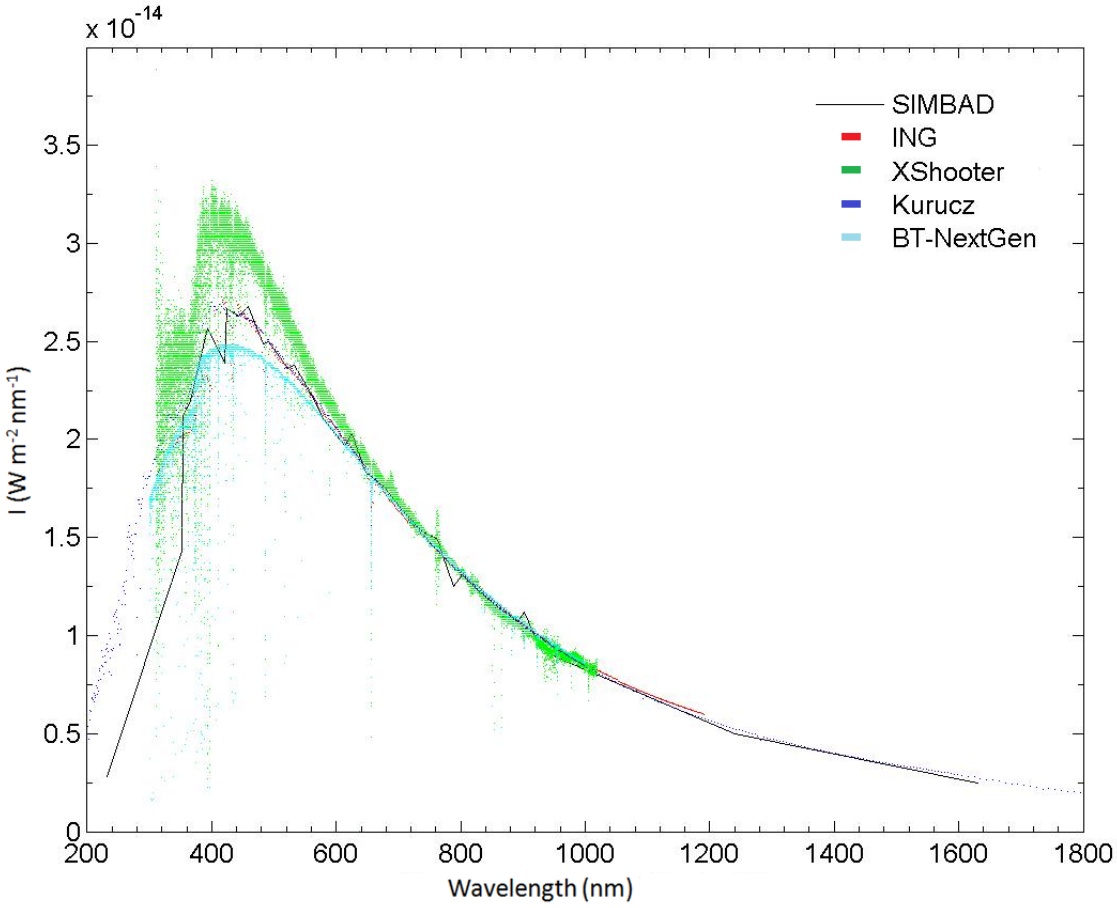

Figure 4.12. Spectrum of HD19445 from different sources.

Table 4.8. HD19445 flux integrated over *PlanetCam2* VIS filters for different spectrum sources.

Filter (PCam 2-VIS)	λ_{eff} (nm)	HD19445 I (W m^{-2})					Mean	Max-Min	%Err
		ING	SIMBAD	XSHOOTER	Bt-Nextgen	Kurucz			
U	378.42	7.44E-14	7.73E-14	8.78E-14	7.36E-14	7.97E-14	7.86E-14	1.41E-14	**19.0**
Vio	388.56	1.34E-13	1.40E-13	1.59E-13	1.31E-13	1.43E-13	1.41E-13	2.75E-14	**19.5**
B	456.77	6.29E-13	6.38E-13	7.22E-13	6.02E-13	6.41E-13	6.46E-13	1.20E-13	**18.6**
V	542.77	9.14E-13	9.18E-13	9.84E-13	8.89E-13	9.18E-13	9.25E-13	9.47E-14	**10.2**
R	640.98	1.04E-12	1.05E-12	1.06E-12	1.04E-12	1.05E-12	1.05E-12	2.10E-14	**2.0**
M1	619.32	4.58E-14	4.63E-14	4.68E-14	4.51E-14	4.57E-14	4.59E-14	1.72E-15	**3.7**
C1	635.25	4.94E-14	5.02E-14	-	4.90E-14	4.95E-14	4.95E-14	1.15E-15	**2.3**
M2	727.31	3.35E-14	3.38E-14	3.39E-14	3.37E-14	3.36E-14	3.37E-14	3.59E-16	**1.1**
C2	749.83	3.14E-14	3.21E-14	3.16E-14	3.15E-14	3.14E-14	3.16E-14	7.42E-16	**2.3**
M3	890.78	1.23E-14	1.23E-14	1.22E-14	1.24E-14	1.22E-14	1.23E-14	2.11E-16	**1.7**
C3	935.56	6.45E-15	6.16E-15	6.13E-15	6.49E-15	6.40E-15	6.33E-15	3.63E-16	**5.7**
VC	980.75	5.43E-15	5.18E-15	5.41E-15	5.45E-15	5.37E-15	5.37E-15	2.71E-16	**5.0**

D. Uncertainty from planetary image navigation

Uncertainties introduced from inaccuracies in the planet navigation can be estimated by performing different navigations of the same planetary image. In order to estimate the uncertainty in the band widths and maximum or minimum position determination due to planetary disk navigation, a Jupiter unprocessed photometric image was repeatedly navigated with LAIA software[27], and several zones and belts (Figure 4.13) analyzed.

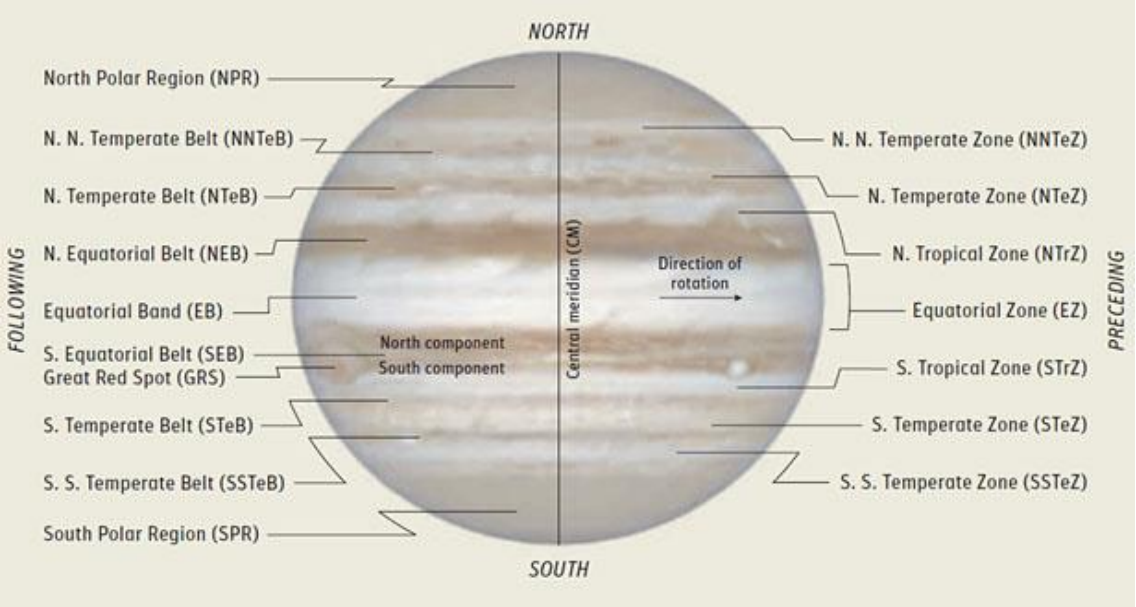

Figure 4.13. Jupiter's belts and zones (Sky&Telescope, 2004)

Figure 4.14 shows the central meridian of four navigations of the same Jupiter photometric image in YC filter without any further image processing, taken at Calar Alto 2.2m telescope with *PlanetCam* (March 3rd, 2016). The width and position of several bands have been analyzed (Table 4.9 to Table 4.11), in particular the following three:

- Belt A between planetographic latitudes from -14º to -30º (SEB) shows a mean width of 8.61º with an uncertainty of 1.1º, i.e. 12.76%. Band minimum position mean latitude is -18.71º with an uncertainty of 1.12º.
- Zone B between planetographic latitudes from -10º to -20º in SEB shows a mean width of 6.18º with an uncertainty of 1.12º, i.e. 18.05%. Maximum position mean latitude is -15.91º with an uncertainty of 0º.

[27] http://www.astrogea.org/soft/laia/laia.htm (downloadable from http://www.ajax.ehu.es/)

- Belt C between planetographic latitudes from -5º to +20º (NEB) shows a mean width of 22.42º with an uncertainty of 1.12º, i.e. 4.98%. Minimum position mean latitude is +7.42º with an uncertainty of 1.14º.

This analysis shows that mean uncertainty due to image navigation in band width estimation is around 10% and a mean uncertainty in band minimum or maximum position is around 1º.

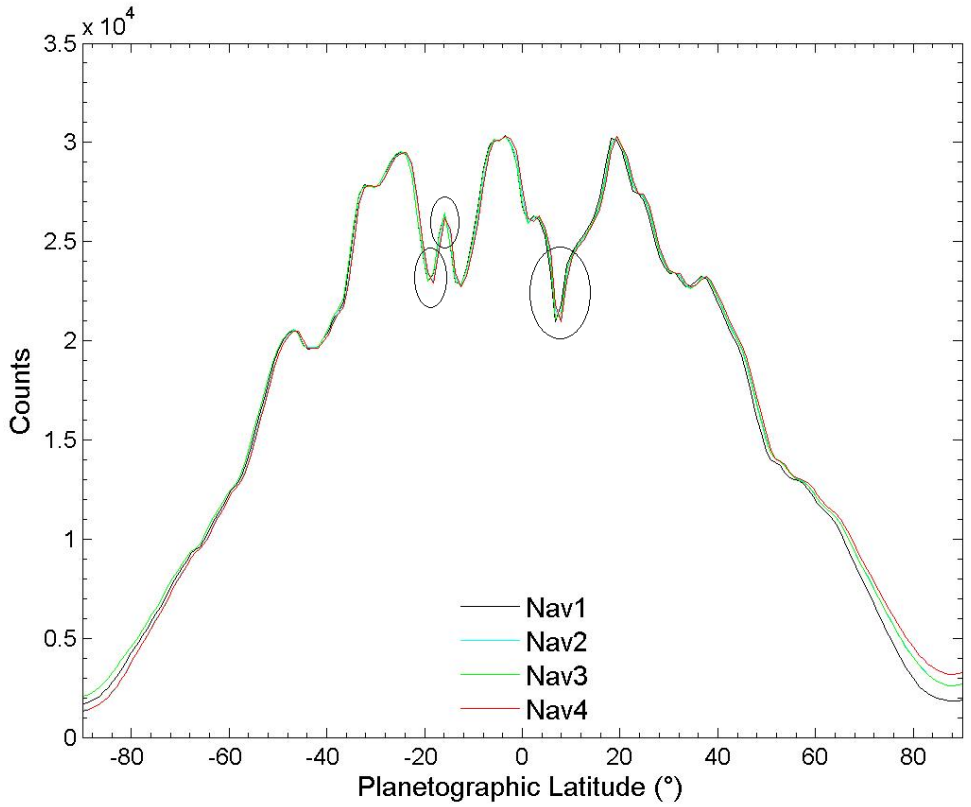

Figure 4.14. Central meridian of different navigations of a same Jupiter YC filter unprocessed photometric image

Table 4.9. Jupiter belt A width and position from four navigations of YC filter image

A.	**Belt between Latitudes -30°/-14° PG**			
	Navigation 1	Navigation 2	Navigation 3	Navigation 4
Belt Width				
DN Max left	29499	29483	29529	29494
DN Max right	26424	26295	26423	26213
Lat Max left (°)	-24.80	-24.80	-24.80	-23.70
Lat Max right (°)	-15.91	-15.91	-15.91	-15.91
Band Width (°)	**8.88**	**8.88**	**8.88**	**7.79**
Minimum position				
DN Min band	23003	23020	23021	22929
Lat Min band (°)	**-19.27**	**-18.15**	**-19.27**	**-18.15**

Table 4.10. Jupiter zone B width and position from four navigations of YC filter image

B.	**Zone between Latitudes -10°/-20° PG**			
	Navigation 1	Navigation 2	Navigation 3	Navigation 4
Zone Width				
DN Min left	23003	23020	23021	22929
DN Min right	22825	22745	22802	22713
Lat Min left (°)	-19.27	-18.15	-19.27	-18.15
Lat Min right (°)	-12.53	-12.53	-12.53	-12.53
Band Width (°)	**6.74**	**5.62**	**6.74**	**5.62**
Minimum position				
DN Max band	26424	26295	26423	26213
Lat Max band (°)	**-15.91**	**-15.91**	**-15.91**	**-15.91**

Table 4.11. Jupiter belt C width and position from four navigations of YC filter image

C.	**Belt between Latitudes -5°/+20° PG**			
	Navigation 1	Navigation 2	Navigation 3	Navigation 4
Belt Width				
DN Max left	30366	30301	30300	30310
DN Max right	30201	30298	30253	30308
Lat Max left (°)	-3.43	-3.43	-3.43	-3.43
Lat Max right (°)	18.15	19.27	19.27	19.27
Band Width (°)	**21.58**	**22.70**	**22.70**	**22.70**
Minimum position				
DN Min band	20937	21097	21118	20956
Lat Min band (°)	**6.85**	**7.99**	**6.85**	**7.99**

A similar test has been done with a M3 image. Figure 4.15 shows the central meridian of four navigations of a Jupiter photometric image in M3 filter without any further image processing, also corresponding to an observation at Calar Alto 2.2m telescope with *PlanetCam* (March 3rd 2016). The width and position of several bands have been analyzed as presented in Table 4.12 to Table 4.14:

- Zone D between planetographic latitudes from 10º to 30º (NTrZ) shows a mean width of 10.28º with an uncertainty of 1.09º, i.e. 10.64%. Maximum position mean latitude is 20.38º in all navigations.
- Belt E between planetographic latitudes from -10º to -25º (SEB) shows a mean width of 10.06º in all cases. Minimum position mean latitude is -16.19º with an uncertainty of 1.12º.
- central Zone F between planetographic latitudes from -15º to +15º (EZ) shows a mean width of 30.98º with an uncertainty of 1.12º, i.e. 3.62%. Maximum position mean latitude is +1.43º with an uncertainty of 1.14º.

This analysis shows that mean uncertainty in band width estimation is around 5% and a mean uncertainty in band minimum or maximum position is around 1º.

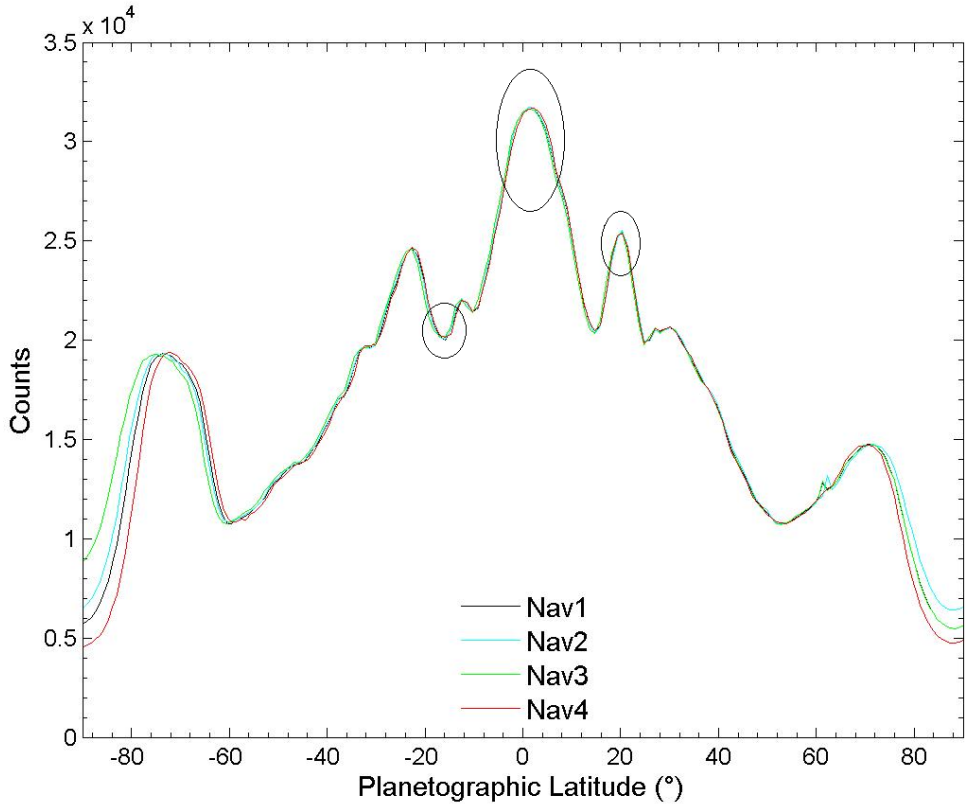

Figure 4.15. Central meridian of different navigations of a same Jupiter M3 filter unprocessed photometric image.

Table 4.12. Jupiter zone D width and position from four navigations of M3 filter image

	D. Zone between Latitudes 10°/30° PG			
	Navigation 1	Navigation 2	Navigation 3	Navigation 4
Zone Width				
DN Min left	20328	20344	20326	20496
DN Min right	19939	19952	19751	19843
Lat Min left (°)	14.79	14.79	14.79	14.79
Lat Min right (°)	24.80	25.89	24.80	24.80
Band Width (°)	**10.01**	**11.10**	**10.01**	**10.01**
Minimum position				
DN Max band	25529	25514	25419	25402
Lat Max band (°)	**20.38**	**20.38**	**20.38**	**20.38**

Table 4.13. Jupiter belt E width and position from four navigations of M3 filter image

E.	**Belt between Latitudes -10°/-25° PG**			
	Navigation 1	Navigation 2	Navigation 3	Navigation 4
Belt Width				
DN Max left	24643	24664	24578	24673
DN Max right	22082	22104	22060	22007
Lat Max left (°)	-22.60	-22.60	-22.60	-22.60
Lat Max right (°)	-12.53	-12.53	-12.53	-12.53
Band Width (°)	**10.06**	**10.06**	**10.06**	**10.06**
Minimum position				
DN Min band	20024	20057	20181	20164
Lat Min band (°)	**-15.91**	**-15.91**	**-17.03**	**-15.91**

Table 4.14. Jupiter zone F width and position from four navigations of M3 filter image

F.	**Zone between Latitudes -15°/+15° PG**			
	Navigation 1	Navigation 2	Navigation 3	Navigation 4
Zone Width				
DN Max left	20024	20057	20181	20164
DN Max right	20328	20344	20326	20496
Lat Max left (°)	-15.91	-15.91	-17.03	-15.91
Lat Max right (°)	14.79	14.79	14.79	14.79
Band Width (°)	**30.70**	**30.70**	**31.82**	**30.70**
Minimum position				
DN Min band	31722	31734	31662	31669
Lat Min band (°)	**1.14**	**1.14**	**1.14**	**2.29**

These tests show that the uncertainty due to planetary disk navigation of a band width can be around 5-10% and the latitudinal uncertainty in the position of the maximum/minimum brightness of a particular band can be around 1º. These are typical values for both VIS and SWIR unprocessed photometric images but of course processed images acquired under very good seeing conditions (<0.7'') largely minimize these errors.

E. Uncertainty from different planetary meridians

The different *I/F* scans correspond to a different planetary longitude, so in order to estimate the uncertainty in bands width and latitudinal position, the same Jupiter images in YC and M3 filters have been analyzed. Figure 4.16 shows several North-South scans at different longitudes between -45º and +45º of the same Jupiter unprocessed photometric navigated image to avoid navigation errors) in YC filter.

The width and position of several bands have been analyzed as presented in Table 4.15 and Table 4.16, where the counts DN and position of band extremes (left and right) are indicated. Results from the bands analyzed can be summarized as follows:

- Belt A between planetographic latitudes from -30º to -14º (SEB) shows a mean width of 9.04º with an uncertainty of 1.06º, i.e. 11.8%. Minimum position mean latitude is -19.43º with an uncertainty of 1.11º.
- Zone B between planetographic latitudes from -10º to -20º in SEB shows a mean width of 6.25º with an uncertainty of 1.13º, i.e. 18.1%. Maximum position mean latitude is -16.07º with an uncertainty of 1.12º. Note that this band is not clearly recognized at all longitudes.

This analysis shows that mean uncertainty in band width estimation is around 10-20% and a mean uncertainty in band minimum or maximum position is around 1º.

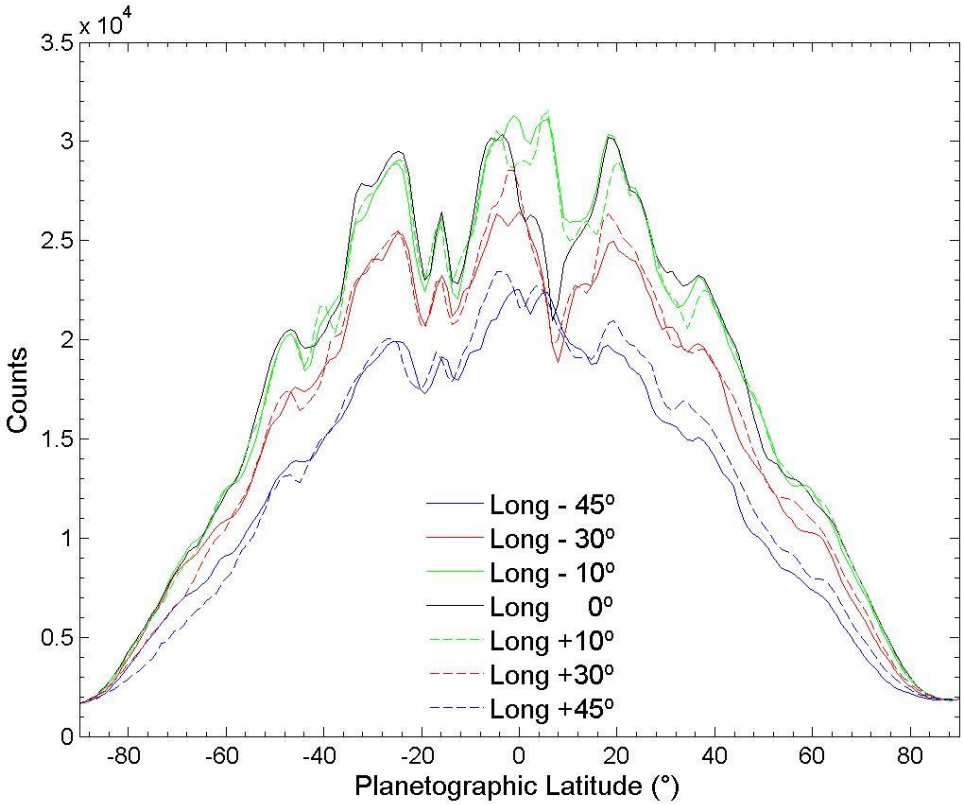

Figure 4.16. North-South scans at different longitudes of Jupiter YC filter photometric image

Table 4.15. Jupiter bands width and positions at different longitudes of the YC filter image

A.	**Belt between Latitudes -30°/-14° PG**						
Longitude (º)	-45º	-30º	-10º	0º	10º	30º	45º
Belt Width							
DN Max left	19924	25384	28864	29499	29084	25481	20045
DN Max right	19164	23253	26157	26424	25660	23014	19368
Lat Max left (°)	-24.80	-24.80	-24.80	-24.80	-24.80	-24.80	-26.98
Lat Max right (°)	-15.91	-15.91	-15.91	-15.91	-15.91	-15.91	-17.03
Band Width (°)	**8.88**	**8.88**	**8.88**	**8.88**	**8.88**	**8.88**	**9.95**
Minimum position							
DN Min band	17297	20739	22419	23003	22977	20578	17468
Lat Min band (°)	**-19.27**	**-19.27**	**-19.27**	**-19.27**	**-19.27**	**-19.27**	**-20.38**

Table 4.16. Jupiter bands width and positions at different longitudes of the YC filter image

B.	**Zone between Latitudes -10°/-20° PG**						
Longitude (º)	-45º	-30º	-10º	0º	10º	30º	45º
Zone Width							
DN Min left	17936	21211	22047	22825	22813	20789	17836
DN Min right	17297	20739	22419	23003	22977	20578	17468
Lat Min left (°)	-12.53	-13.66	-12.53	-12.53	-13.66	-13.66	-13.66
Lat Min right (°)	-19.27	-19.27	-19.27	-19.27	-19.27	-19.27	-20.38
Band Width (°)	**6.74**	**5.61**	**6.74**	**6.74**	**5.61**	**5.61**	**6.72**
Maximum position							
DN Max band	19164	23253	26157	26424	25660	23014	19368
Lat Max band (°)	**-15.91**	**-15.91**	**-15.91**	**-15.91**	**-15.91**	**-15.91**	**-17.03**

Figure 4.17 shows several North-South scans at different longitudes between -45º and +45º of a Jupiter unprocessed photometric navigated image in M3 filter. The width and position of the bands analyzed are presented in Table 4.17 and Table 4.18, and summarized as follows:

- Zone D between planetographic latitudes from 10º to 30º (NTrZ) shows a mean width of 10.65º with an uncertainty of 1.13º, i.e. 10.6%. Maximum position mean latitude is 20.38º in all cases.
- Belt E between planetographic latitudes from -10º to -25º (SEB) shows a mean width of 10.73º with an uncertainty of 1.16º, i.e. 10.8%. Minimum position mean latitude is -16.07º with an uncertainty of 1.12º.

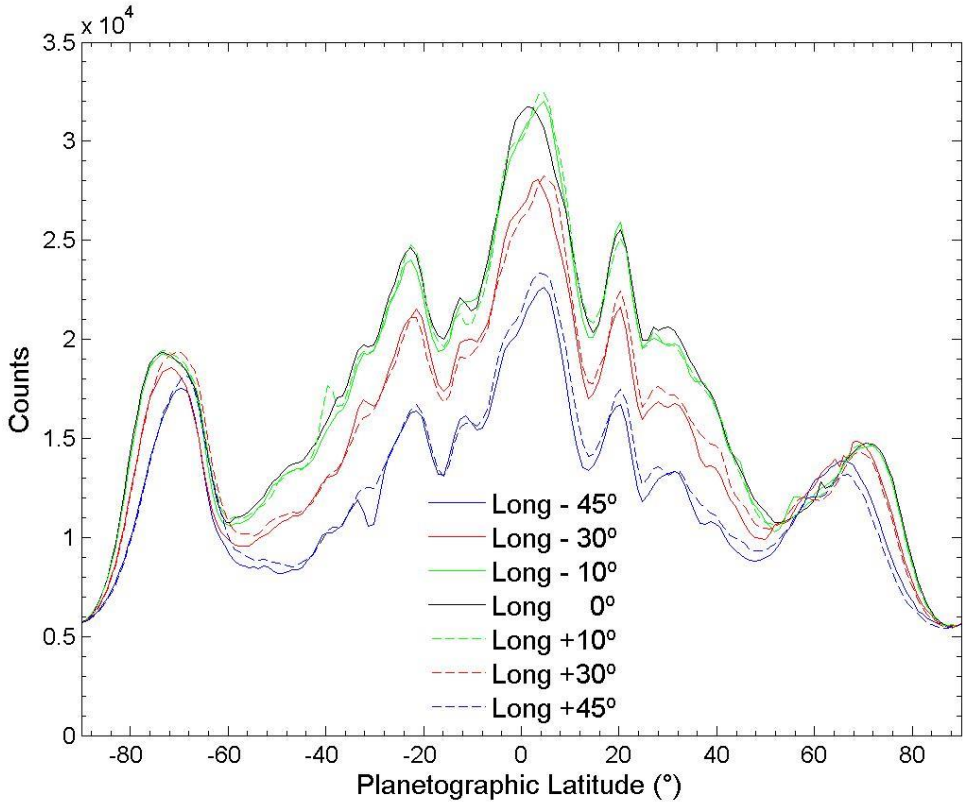

Figure 4.17. North-South scans at different longitudes of Jupiter M3 filter photometric image

Table 4.17. Jupiter zone D width and positions at different longitudes of the M3 filter image

	D. Zone between Latitudes 10°/30° PG						
Longitude (º)	-45º	-30º	-10º	0º	10º	30º	45º
Zone Width							
DN Min left	13377	16998	20089	20328	20791	17779	14089
DN Min right	11802	15961	19575	19939	19519	16563	12647
Lat Min left (°)	13.66	13.66	13.66	14.79	14.79	14.79	13.66
Lat Min right (°)	24.80	24.80	24.80	24.80	24.80	24.80	24.80
Band Width (°)	**11.14**	**11.14**	**11.14**	**10.01**	**10.01**	**10.01**	**11.14**
Maximum position							
DN Max band	16736	21631	25900	25529	25118	22454	17481
Lat Max band (°)	**20.38**	**20.38**	**20.38**	**20.38**	**20.38**	**20.38**	**20.38**

Table 4.18. Jupiter belt E width and positions at different longitudes of the M3 filter image

	E. Belt between Latitudes -10°/-25° PG						
Longitude (º)	-45º	-30º	-10º	0º	10º	30º	45º
Belt Width							
DN Max left	16135	20021	21929	22082	21276	19218	15785
DN Max right	16361	21513	24002	24643	24783	21102	16705
Lat Max left (°)	-11.40	-10.26	-11.40	-12.53	-12.53	-10.26	-10.26
Lat Max right (°)	-21.49	-21.49	-22.60	-22.60	-22.60	-21.49	-21.49
Band Width (°)	**10.09**	**11.22**	**11.20**	**10.06**	**10.06**	**11.22**	**11.22**
Minimum position							
DN Min band	13137	17385	19394	20024	19619	16811	13111
Lat Min band (°)	**-15.91**	**-15.91**	**-17.03**	**-15.91**	**-15.91**	**-15.91**	**-15.91**

This test shows that the uncertainty of a band width can be around 10-20% and the latitudinal uncertainty in the position of the maximum/minimum brightness of a particular band can be around 1º as we consider different planet meridians in an unprocessed photometric image. Again, this uncertainty can be highly reduced for processed images acquired under good seeing conditions.

4.4 Discussion

4.4.1 Absolute Reflectivity comparison with reference values

The mean Jupiter reflectivity central meridian scans (Figure 4.8 and 4.9) have been compared to available reference values from the literature (Chanover et al., 1996; de Pater et al.; 2010; see Figure 4.18 to 4.20). Ground-based calibrated observations presented by Chanover et al. (1996) and HST calibrated images obtained in February 2016 (as part of the Outer Planets Atmospheres Legacy -OPAL- program; Simon et al., 2015) constitute excellent sources of comparison for our Jupiter data in the visible. For the SWIR spectral range there are very few reference values of Jupiter's reflectivity available in the literature. We compare our *I/F* scans to values obtained by de Pater (2010) that used filters comparable to those used in *PlanetCam* SWIR. When there was no perfect match between filters wavelength, the nearest ones were used. The differences in reflectivity between our data and the reference values may be caused by real changes in the cloud structure or in the optical properties of haze particles but part of them could be due to the calibration uncertainty. In general differences above a 10% uncertainty can be assigned to real changes in the hazes and upper Jovian cloud as in particular when compared the reflectivity scans obtained in July 1994 by Chanover et al. (1996) and our *PlanetCam* data obtained about 20 years later.

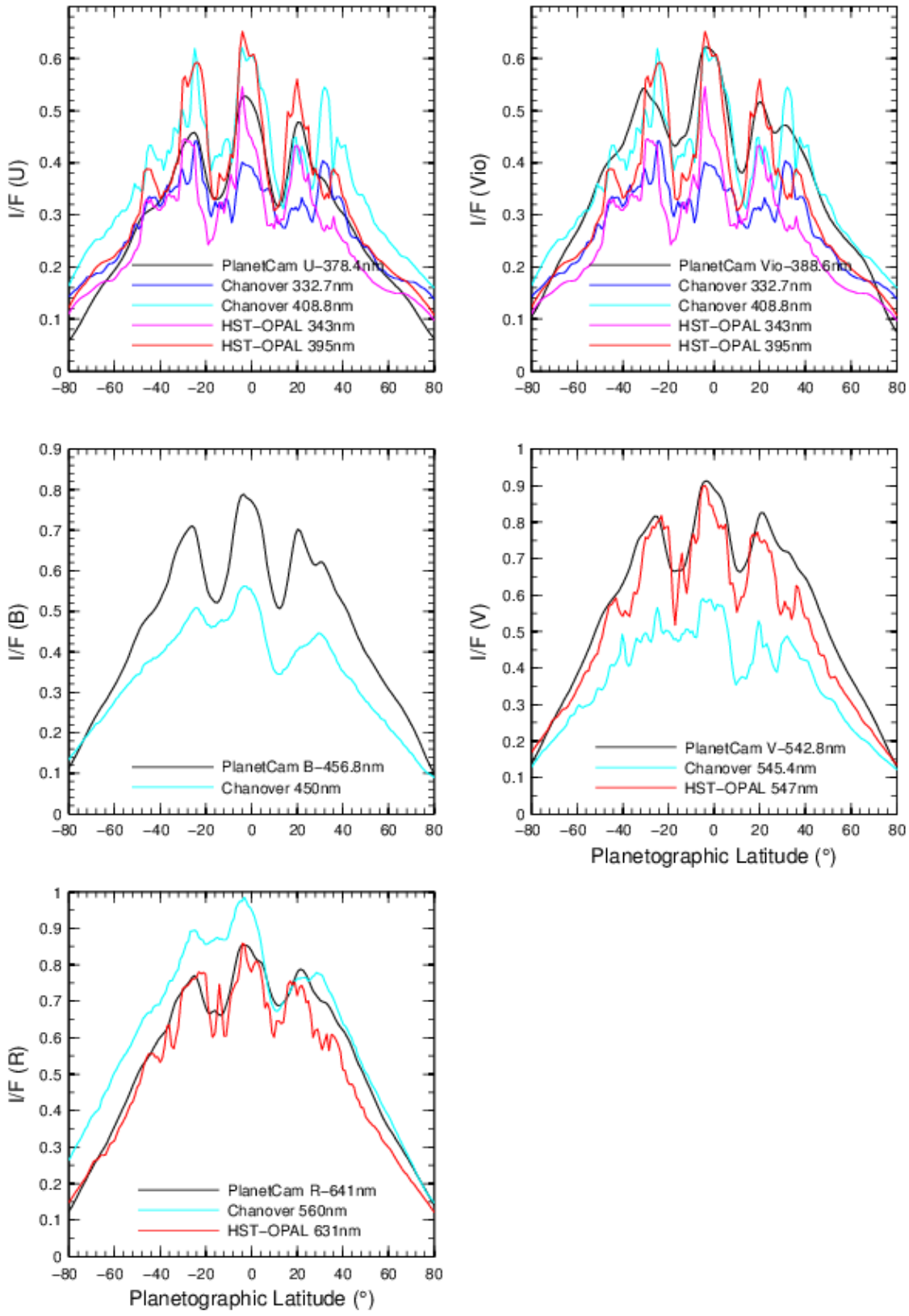

Figure 4.18. Jupiter mean absolute reflectivity North-South scans from *PlanetCam* VIS U, Vio, B, V and R filters compared to similar wavelength reference values from Chanover et al. (1996) and HST-OPAL (Simon et al., 2015).

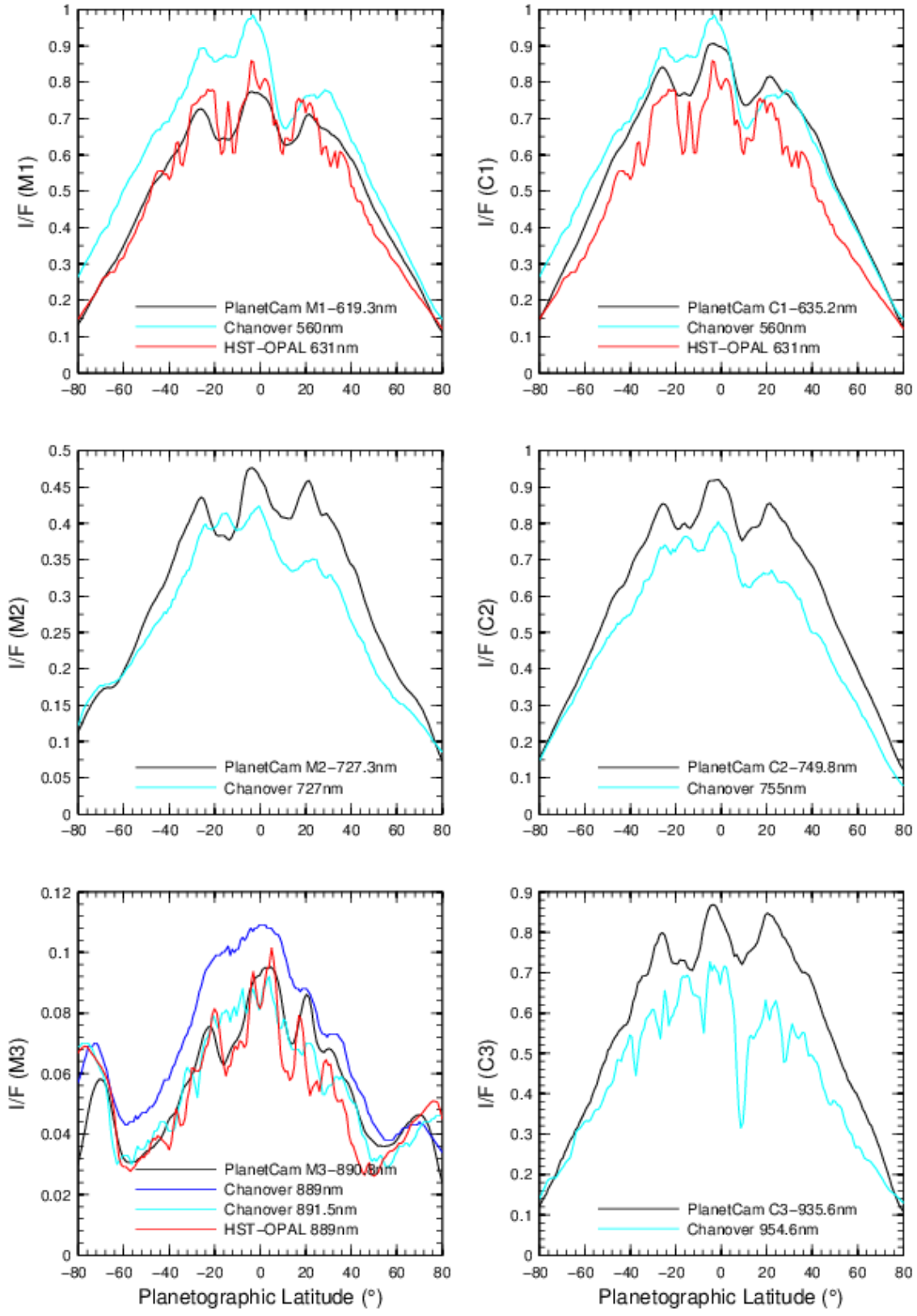

Figure 4.19. Jupiter mean absolute reflectivity North-South scans from *PlanetCam* VIS methane and continuum filters compared to similar wavelength reference values from Chanover et al. (1996) and HST-OPAL (Simon et al., 2015).

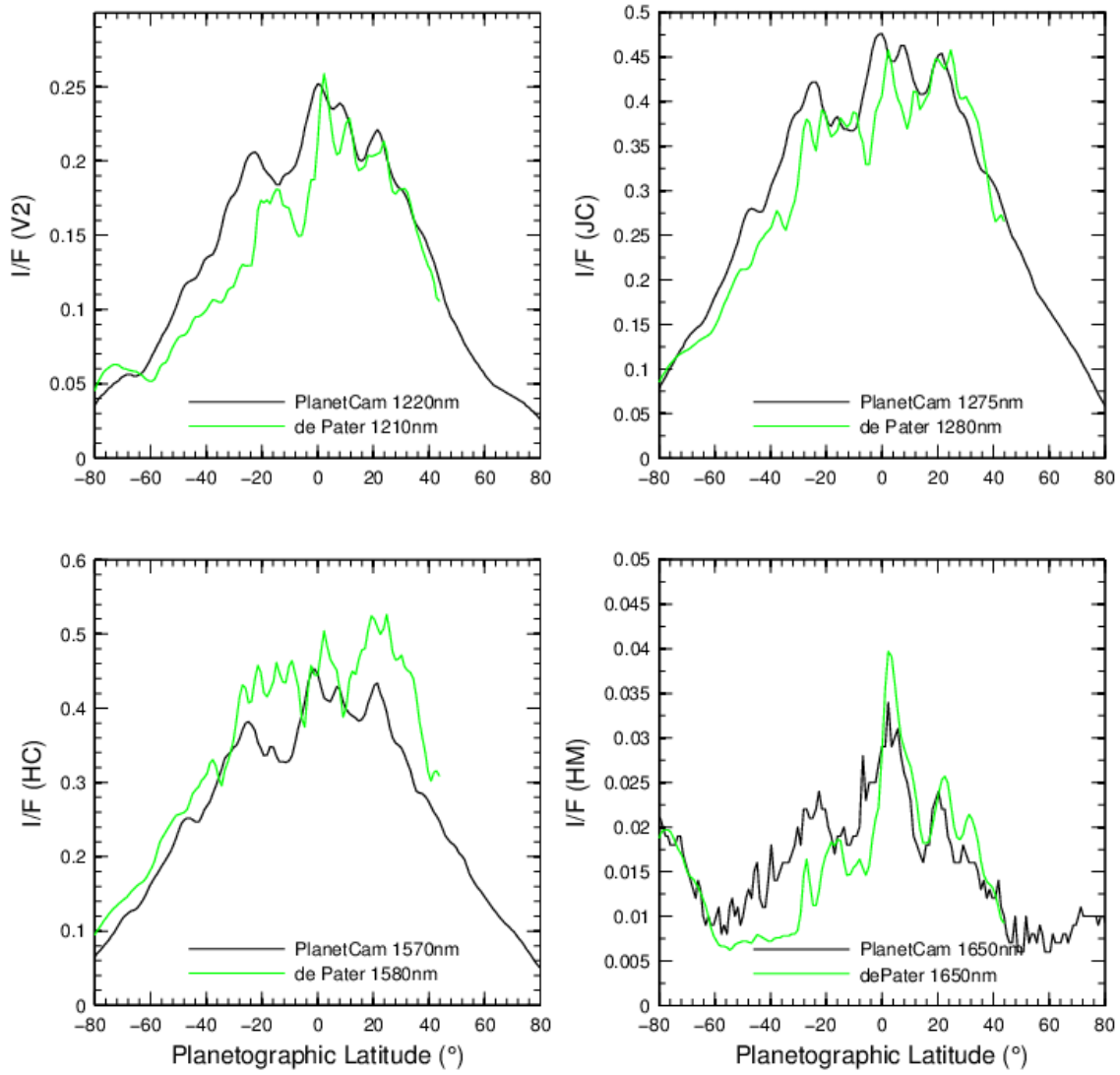

Figure 4.20. Jupiter mean absolute reflectivity North-South scans from *PlanetCam* SWIR filters compared to similar wavelength reference values from de Pater et al. (2010).

Regarding Saturn, HST observations obtained in July 2015 are used as reference. Figure 4.21 and 4.22 show a comparison of the central meridian scans corresponding to the nearest filters to *PlanetCam* from mean scans from April 2013 to May 2016.

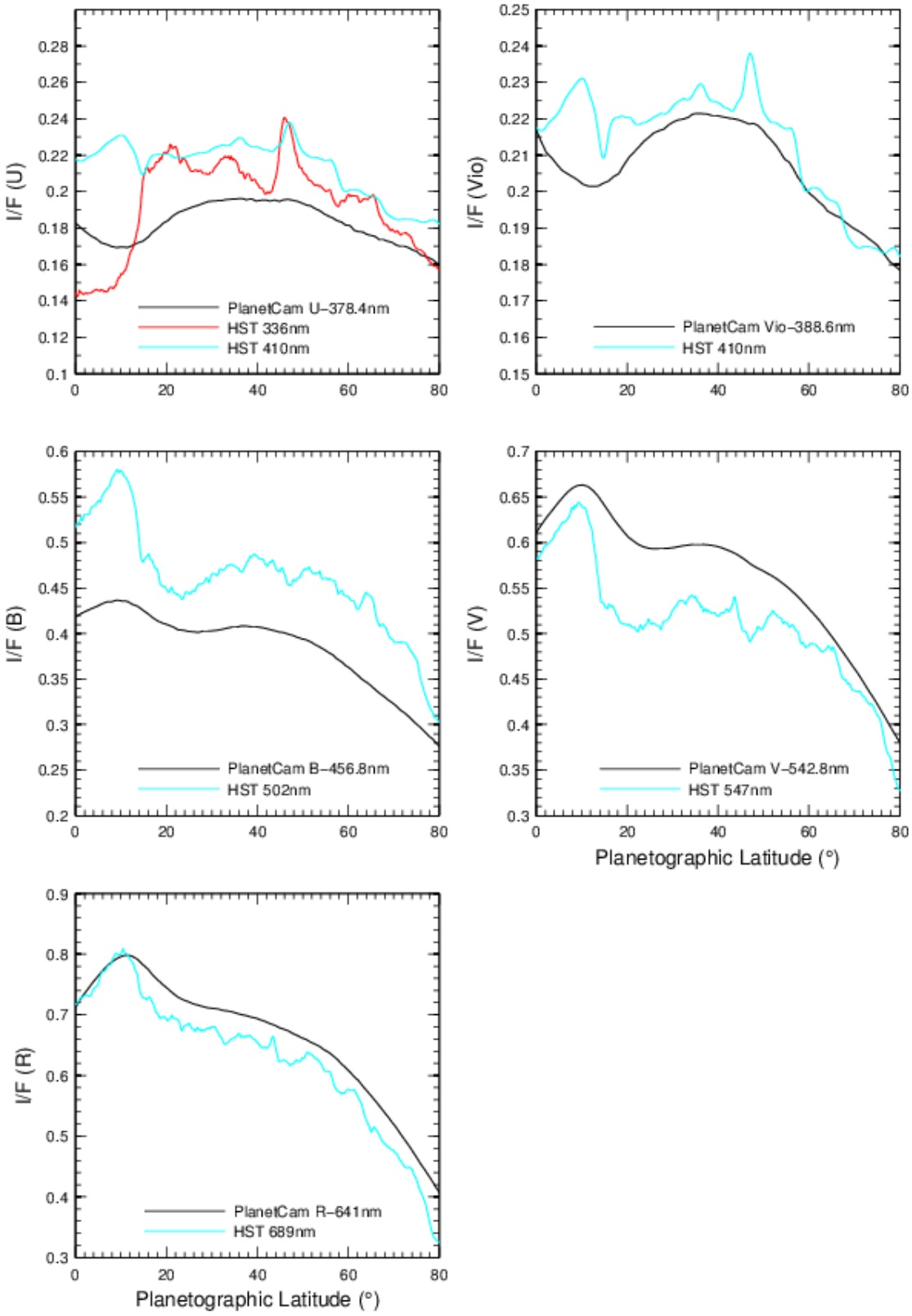

Figure 4.21. Saturn mean absolute reflectivity North-South scans from *PlanetCam* VIS U, Vio, B, V and R filters compared to similar wavelength reference values from HST images.

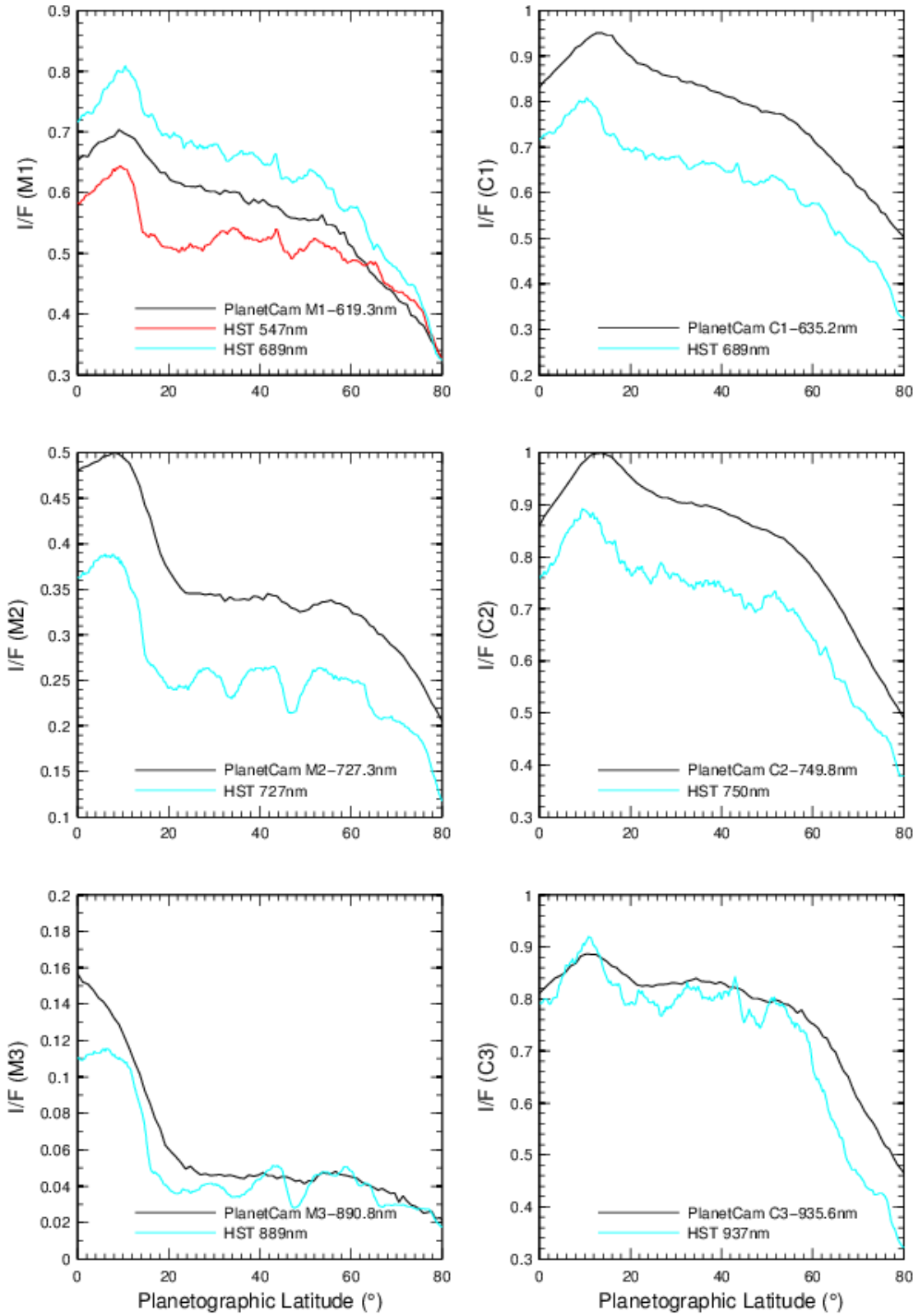

Figure 4.22. Saturn mean absolute reflectivity North-South scans from *PlanetCam* VIS methane and continuum filters compared to similar wavelength reference values from HST images.

4.4.2 Albedo

Jupiter

The full disk geometric albedo for the visual spectral range is shown in Figure 4.23 and is compared to reference values from July 1995 (ESO; Karkoschka, 1998) and February 2016 (HST/OPAL; Simon et al., 2015). The agreement is good for most cases, although small deviations are found at the wavelengths of the filters: U, M2 and C3.

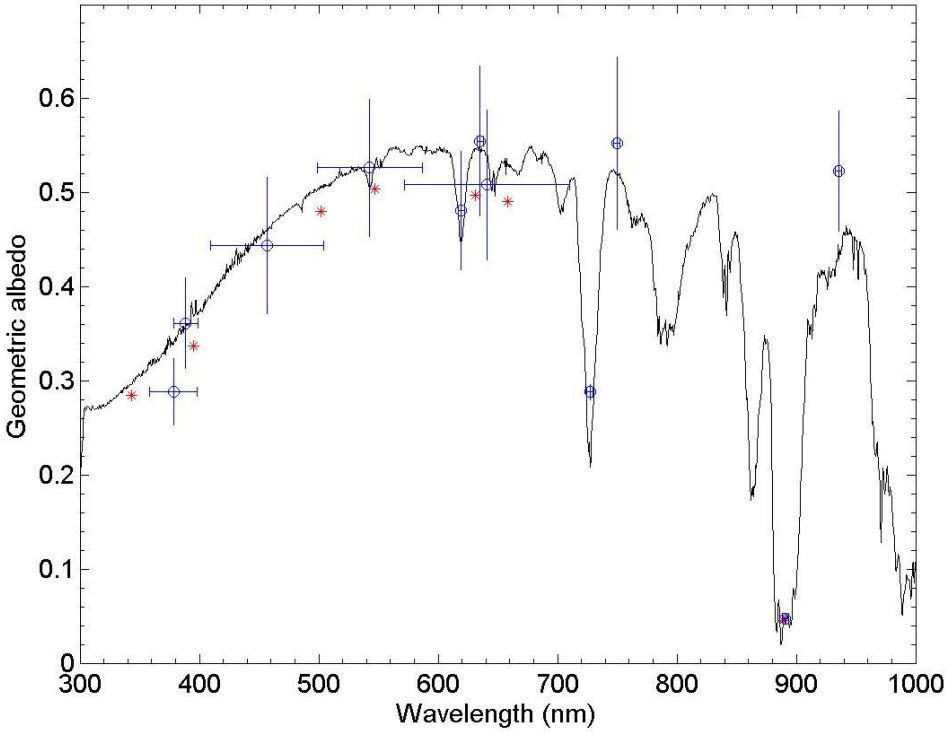

Figure 4.23. Jupiter geometric albedo from *PlanetCam* VIS observations (blue dots) compared to reference values from ground-based observations in July 1995 (Karkoschka, 1998) (black line) and February 2016 HST/OPAL data (Simon et al., 2015) (red dots). Horizontal bars account for the width (FWHM) of each filter, while vertical error bars indicate the uncertainty in the photometric calibration.

Jupiter albedo in the SWIR spectral range is shown in Figure 4.24. In this case, only the central part of the disk has been considered (reflectivity from latitudes -20º to +20º) allowing compare our results with those from Clark & McCord (1979). Again a reasonable agreement is found between both sets of values.

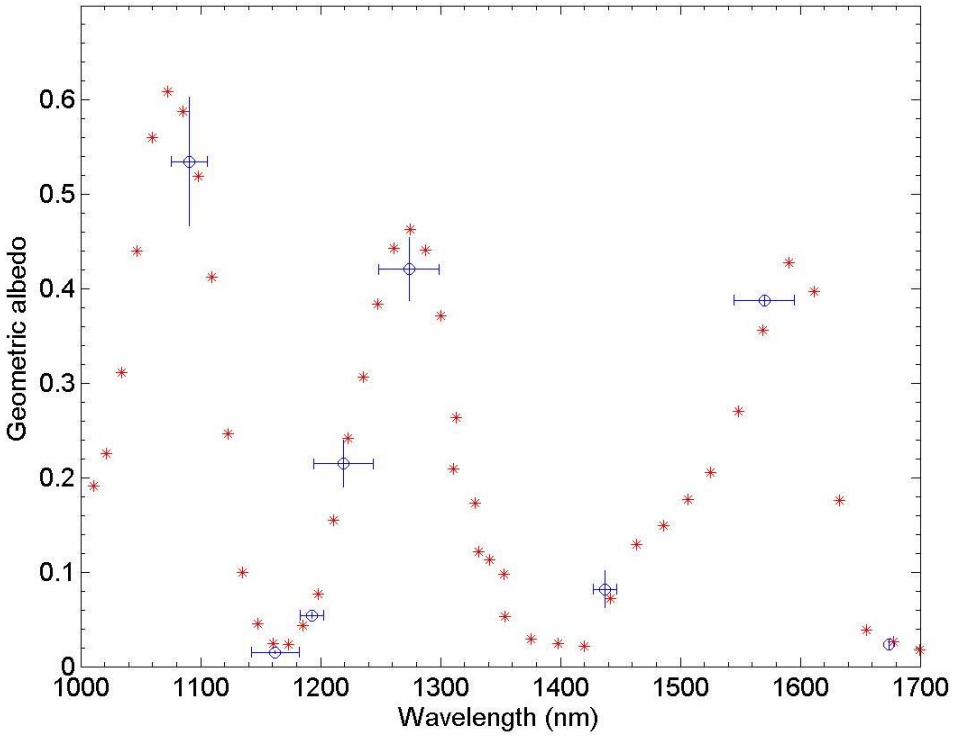

Figure 4.24. Jupiter albedo (disk centre) from *PlanetCam* SWIR observations (blue dots) compared to reference data of November 1976 (Clark & McCord, 1979) (red dots) values. *PlanetCam* albedo in filter YM-1160 is 0.015 (0.024 in Clark & McCord).

Saturn

Saturn overall mean geometric albedo from *PlanetCam* campaigns is shown in Figure 4.25 and is compared to ground-based data obtained in July 1995 (Karkoschka, 1998) and recent HST July 2015 observations (Sánchez-Lavega et al., 2016). Because of the viewing angle geometry only the northern hemisphere can be studied (see Figure 4.6 and 4.7). Our results are comparable to those retrieved from HST photometry, while there are some differences when compared to values from Karkoschka (1998) which were obtained at Saturn's equinox showing intrinsic brightness differences produced by seasonal changes in the hazes and clouds (Pérez-Hoyos et al., 2005) as well as by the different viewing/illumination geometry.

Similarly to Jupiter, Saturn's SWIR albedo measurements were calculated only for the central part of the disk (latitudes from -20º to +20º) and were compared to data from Clark & McCord (1979) (Figure 4.26). Note that this time the comparison is closer than in the VIS case, given the similar seasonal situation of the planet at both epochs since sub-solar latitude of Saturn was around -17º at the time of Clark & McCord

observations in 1977, and between +17º and +25º for *PlanetCam* observations (2012-2016), while it was around 0º by the time of Karkoschka observations in 1995.

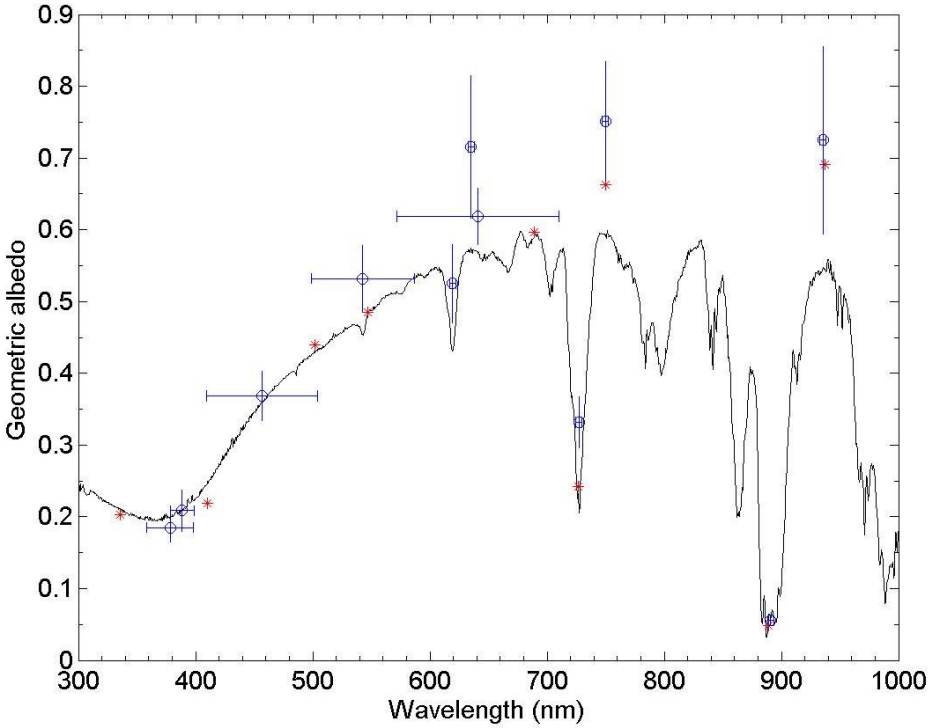

Figure 4.25. Saturn geometric albedo from *PlanetCam* VIS observations (blue dots) compared to reference results of July 1995 (Karkoschka, 1998) (black line) and HST in July 2015 (Sánchez-Lavega et al., 2015) (red dots).

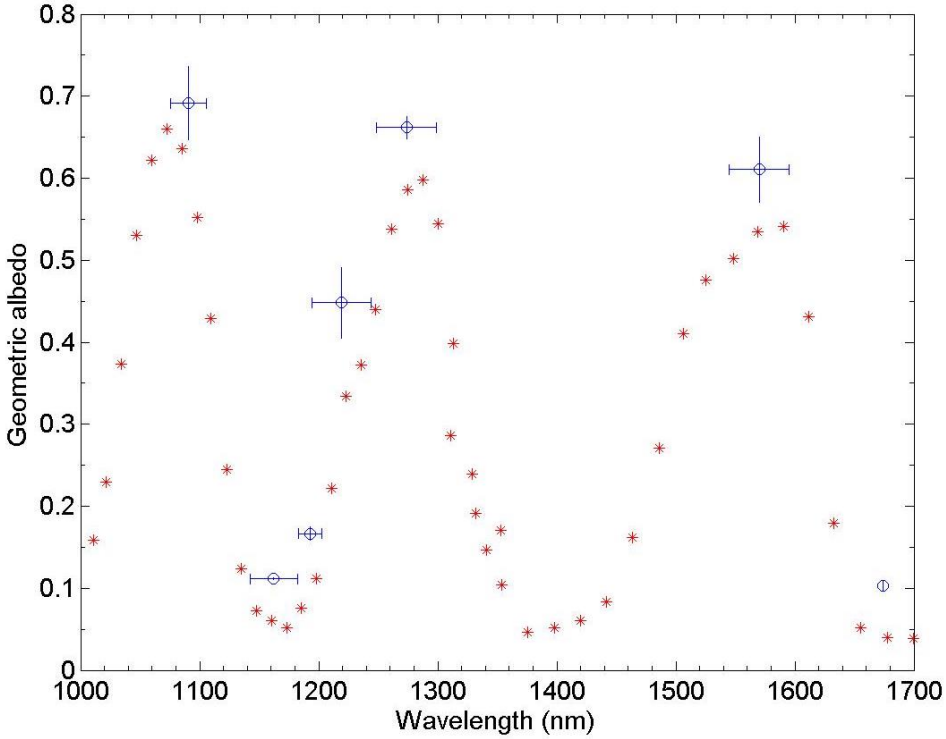

Figure 4.26. Saturn geometric albedo from *PlanetCam* SWIR observations (blue dots) compared to reference data of February 1977 (Clark & McCord, 1979) values (red dots).

Chapter 5

SCIENTIFIC APPLICATIONS OF PLANETCAM FOR SOLAR SYSTEM OBJECTS

5.1 Introduction

The main goal of *PlanetCam* is the study of Solar System bodies, in particular the cloud structure and atmospheric dynamics. However, other Solar System objects like satellites, comets or asteroids, and even extra Solar System events like exoplanetary transits or rapid evolving phenomena like Gamma Ray Burst (GRB) can also be addressed. In principle, any astronomical observation that requires high spatial resolution and/or high temporal cadence can be observed with *PlanetCam*, provided that the incoming flux is enough for the sensitivity of our camera.

We show in Table 5.1 the maximum resolution (km) achievable for the different planets in diffraction limited images at Calar Alto 1.23m and 2.2m telescopes for the spectral limits of *PlanetCam*, 380nm and 1700nm. Obviously, the seeing will hamper those values, since it is only partially compensated by the lucky imaging technique. Planets are supposed to be at their minimum distance from Earth, except Venus, supposed at 45º elongation where is usually observed.

Table 5.1. Maximum achievable resolution (km) of *PlanetCam* at CAHA 1.23m and 2.2m telescopes for different planets (diffraction limited).

	Venus	**Mars**	**Jupiter**	**Saturn**	**Uranus**	**Neptune**
CAHA 1.23m						
380nm	39	21	226	479	1037	1624
1700nm	177	96	1009	2144	4641	7265
CAHA 2.2m						
380nm	22	12	126	268	580	908
1700nm	99	54	564	1199	2595	4062

Solar system planets cyclically vary its size and phase when observed from Earth. This is particularly remarkable in the case of Venus, as shown in Figure 5.1, while in the case of outer planets the phase changes are not so apparent, yet the size variations can be clearly seen like in the case of Mars (Figure 5.2). Although Jupiter shows remarkable change in apparent size, giant planets show in general very little size and phase variations, yet in the case of Saturn rings orientation significantly change as shown in Figure 5.3. The *PlanetCam* observation campaigns covering the period 2012-2017 therefore showed remarkable differences in Venus and Mars, but little variations in Saturn rings positions.

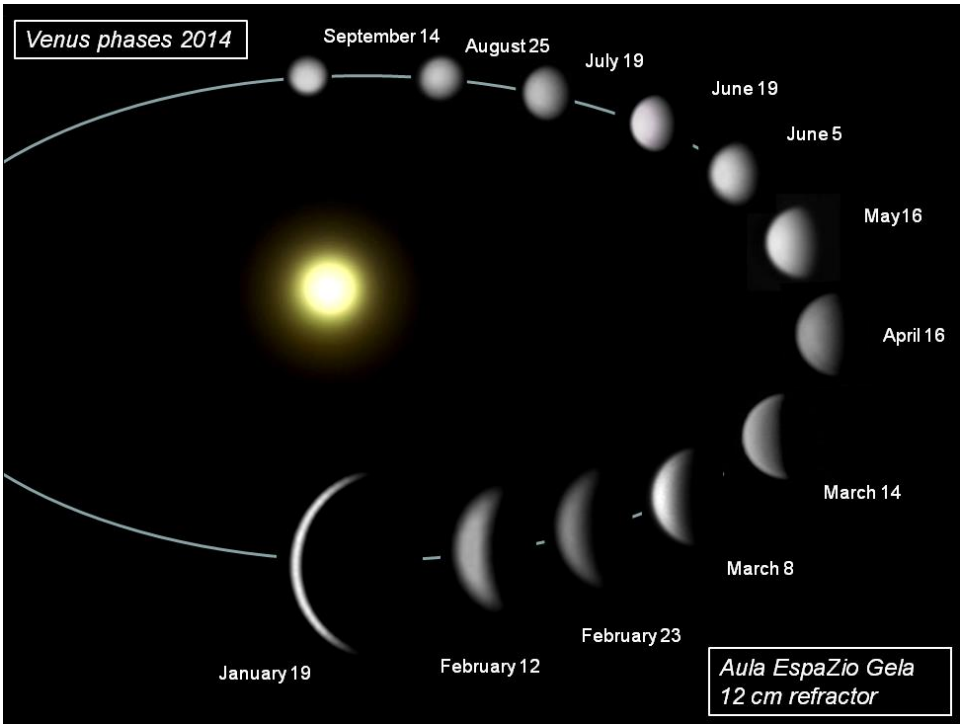

Figure 5.1. Venus phases from Earth in 2014 (Aula Espazio observatory, UPV/EHU, Bilbao)

Figure 5.2. Mars phases from Earth in 2016[28]

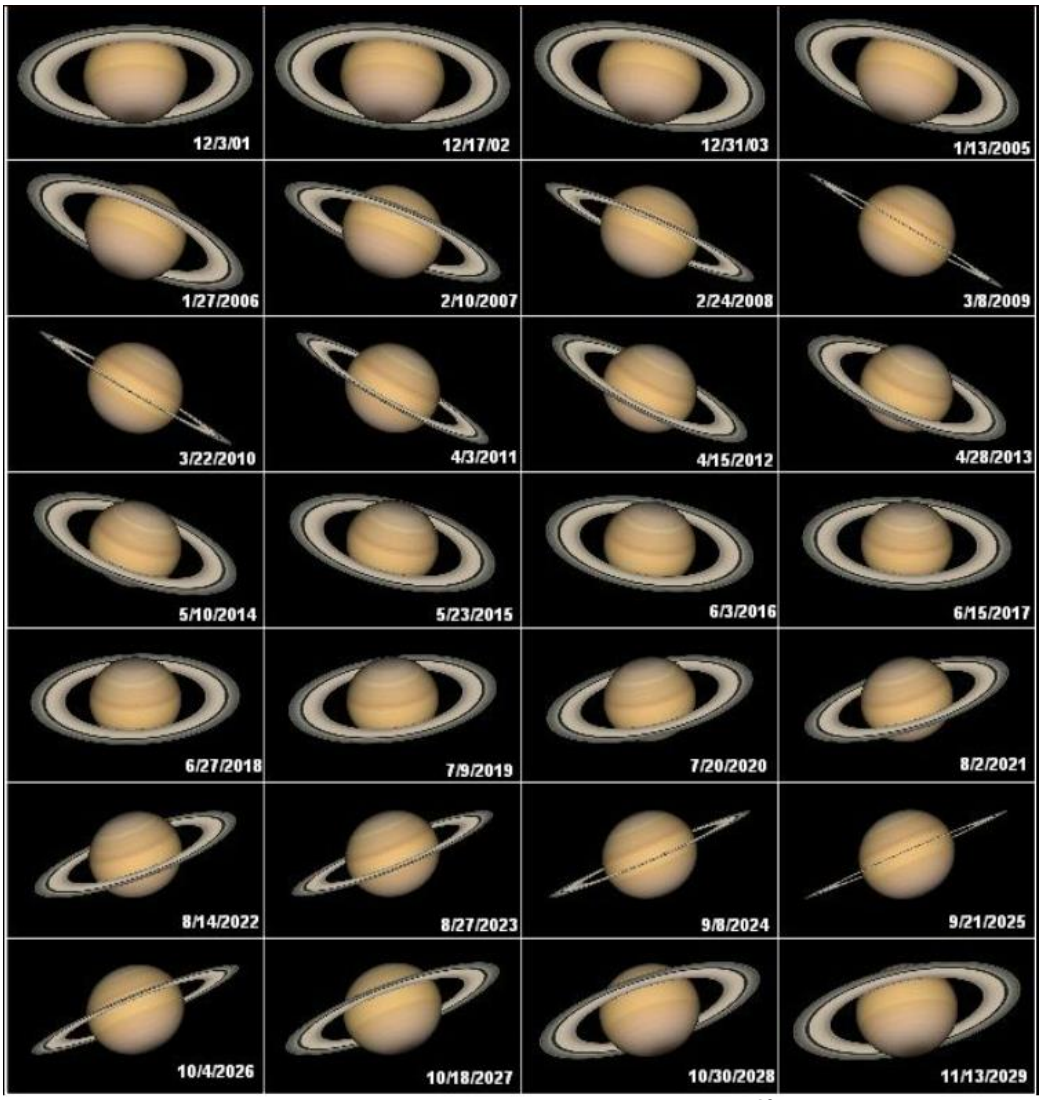

Figure 5.3. Saturn oppositions from 2001 to 2029[29]

Imaging of the planets at different wavelengths allows study the aerosol and cloud properties, meteorological phenomena, measurement of global winds and assessments of the spatial and temporal scales of evolution. Absolute radiometric calibration using standard stars allows obtaining the spectral and spatial dependence of the reflectivity across the planetary disk (from center-to-limb or north-south scans)

[28] http://earthsky.org/tonight/smallest-martian-phase-on-september-13

[29] https://en.wikiversity.org/wiki/Saturn#/media/

and/or for particular features (Sánchez-Lavega, 2011; Mendikoa et al., 2017). Modeling of the absolute reflectivity allows retrieving the cloud and aerosol vertical distribution and their optical properties (Hansen and Travis, 1984; Pérez-Hoyos et al., 2005, 2009, 2012; West et al., 2009; Karkochka and Tomasko, 2010; Ortiz et al., 1996). In what follows we describe in more detail the specific research topics with *PlanetCam* for the different planets, while the following sections describe some of the scientific works performed so far for each planet based on *PlanetCam* images.

Venus

Imaging Venus at high resolution in the VIS and SWIR spectral ranges (0.38-1.7μm) provides scientific information on the atmosphere and surface of the planet. This allows study the cloud structure and atmospheric dynamics in Venus day side at the wavelengths of interest in the VIS (UV,890-980 nm) and SWIR channels (in the CO_2 band and adjacent continuums). The night side of Venus can also be observed (SWIR range) for surface and lower atmospheric phenomena. Because of the small tilt of Venus rotation axis with respect to the orbital plane and ecliptic, the latitude range of Venus observable from Earth is from 60°N to 60°S.

The research topics that can be addressed with *PlanetCam* are the following (Schubert, 1983, Sánchez-Lavega et al., 2016; Peralta et al., 2017):

(1) Cloud morphology in the 380-410 nm spectral range is sensitive to the upper cloud (altitude z = 65-70 km) in Venus daytime. Thus, it is possible to study the Y- and Psi- horizontal wave, dark equatorial band, equatorial cellular convection and other phenomena with sizes above 200 km.

(2) Cloud morphology in the 890-980nm spectral range is sensitive to the base of the upper cloud (altitude 60 km) in Venus day side, this way we can analyze the banding and other phenomena with sizes above 200 km.

(3) Cloud morphology in the 1.05, 1.22 and 1.43 μm CO_2 absorption bands show sensitivity to scattered light (without UV-absorption) in the upper cloud (altitude 65-70 km) in Venus day side. Images in these bands have not been previously studied in detail so far (Sánchez-Lavega et al., 2016) and as long as *PlanetCam* allows search for new cloud morphology in these spectral bands, it can provide very useful information on Venus clouds.

(4) Tracking of the motions of the cloud features in the three previous spectral cases using sequences separated by a temporal interval of 2-3 hrs and at intervals of 4-8 days, allows retrieving the zonal wind velocity in day side and phase velocity for waves at different altitudes as sensed at different wavelengths (Sánchez-Lavega et al., 2016).

(5) Cloud structure from radiative transfer modeling of the above images at the different wavelengths calibrated in absolute radiance.

(6) Searching for features on the Venus nightside, aiming to detect in the SWIR spectral range (Peralta et al., 2017): surface topographic features with possible emissivity changes and control of the effects of the lower clouds (wavelengths: 1.05, 1.09, 1.16, 1.19 μm); airglow maps from molecular oxygen at 95km (wavelength 1.275 μm by comparison with 1.275 μm continuum- image); deep cloud morphology and motions at 45-50 km (wavelength 1.57 and 1.65 μm).

Cloud tracking at the upper clouds can be performed with wind errors of 10 m/s at about 50 km/pixel resolution at the CAHA 2.2 m telescope in the 380 nm wavelength, 15 m/s at about 100 km/pixel resolution at 980 nm, and 30 m/s at about 850 km/pixel resolution at 1.43 μm, taking into account the pixel size of the two detectors for visible and SWIR ranges. With this resolution ranges, *PlanetCam* observations took part in the international campaign by Japanese Space Agency (JAXA) to support Akatsuki mission, currently in orbit around Venus since December 2015.

Mars

It is well known that in the thin atmosphere of Mars H_2O and CO_2 ice clouds forms at different latitudes and seasons (Maättänen, A. et al., 2013) that can occupy a large horizontal extension and reach in some cases quite high altitudes in the atmosphere, even reaching 100 km above the surface. In addition dust “clouds” lifted from the surface can also reach 60 km (Heavens, N. G. et al., 2011) but, before 2015, there was no clue of higher structures (plumes) in Mars above 100 km. Sánchez-Lavega et al. (2015) reported the observation of a high-altitude plume reaching 200-250 km altitude at its most active moment, which defies our current understanding of Mars atmosphere and represents a challenge to the commonly accepted General Circulation Models of the red planet.

In spite of having several spacecrafts in orbit around Mars, their cameras and other instruments usually have not a complete visibility of the planetary disk or they do it at particular geometries that depends on the orbit,, thus not allowing the detection of this kind of phenomenon. High-resolution amateur images can, to some extent, fill this gap, yet they do not usually cover a broad wavelength range as required by radiative transfer models in order to constrain the nature and properties of the observed cloud. For example, the shortwave infrared spectral range (J and H bands) have not been used before for monitoring Mars dust load but it is a potential tool for limb dust events as those produced in ”rocket dust storms” (see e.g. Spiga et al., 2013). All these phenomena have an ample range of variability, both spatial and temporal, according the seasonal insolation cycle.

The reflectivity data obtained from *PlanetCam* can be used to perform radiative transfer modeling to assess the capability of this kind of observations to characterize the optical properties of the aerosols (clouds and dust), their density (optical depth) and size. Currently these analysis aim to help studies with VMC camera onboard Mars Express on which the GCP team is directly involved. In addition, this kind of analysis will be employed in the future to support with ground-based observations the meteorological and dust measurements to be performed in 2021 by instruments RMD (onboard rover Exomars2020, ESA) and MEDA (onboard rover Mars2020, NASA) in both missions with the participation of the GCP team.

Moreover, a continued observational program using *PlanetCam* is able to support the following research areas for Mars:

(1) To determine the absolute reflectivity of the clouds regularly seen at Mars, looking for the spectral differences between H_2O and CO_2 ice clouds, and dust). Particularly interesting is the yellow-red wavelengths to capture the dust and in the UV-violet spectral region to capture the ice clouds.

(2) To determine the behavior of clouds at SWIR spectral range where no observations are usually performed from the ground.

(3) To investigate the presence of high-altitude plumes at the limb of the planet.

(4) To explore the possibility to introduce simple color indexes that allow us to distinguish and classify the different kind of features we see on Mars (albedo surface features, polar caps, clouds and dust).

(5) To study the development and seasonal behavior of dynamical phenomena like: (a) Condensate clouds generated by orography, baroclinic cyclones, waves, etc.; (b) Regional and global dust storms; (c) Evolution (growth and regression) of the seasonal dependent polar caps ice deposits and their relationship with pressure changes measured in situ by the operative rovers.

Jupiter

Jupiter's size and distance from Earth makes it a perfect choice for ground-based observation as it provides the best available information on the atmospheric dynamics of a giant planet in rapid rotation. Jupiter shows a very active and extreme atmosphere, with strong East-West (zonal) winds that are remarkably stable in time although with some variability in jet peak. The way in which such zonal winds are sustained is unknown at the moment, in particular regarding the strongest equatorial jet. Any of the numerical models currently available require an observational database on a regular basis. On the other hand, the transient phenomena that periodically disturb the planet are very interesting tools to understand the general dynamics via the dynamical simulation.

There are three main research areas that can be addressed by ground-based observations of giant planets at high resolution:

(1) Zonal wind profile at a given date, particularly interesting at Jupiter in view of its variability and the attainable spatial resolution

(2) Vertical distribution of the upper clouds and hazes that can be modeled from observations in the near-infrared methane bands. The multiwavelength coverage of *PlanetCam* allows a radiative transfer modeling including a wide altitude range from upper stratosphere to the middle troposphere.

(3) Study of the Jupiter meteorology, including storms, vortices, waves, and transient phenomena at various time and spatial scales. Particularly important the tracking of major planetary-scale changes that affect some bands of the planet.

Fast acquisitions to retrieve diffraction-limited images in the broad band filters available in *PlanetCam* can be used for dynamics, while longer exposures in narrow filters at methane bands and adjacent continuums (and near-UV wavelengths) are required for vertical cloud structure analysis and dynamics of the upper hazes. The

observations of the upper hazes in the deep absorption bands can be retrieved from observations at the CAHA 2.2m telescope because of the low reflectivity in the UV and in the CH_4 absorption bands, particularly in the SWIR wavelengths. Jupiter in the 1-1.6 μm wavelength range (J and H bands) is particularly interesting since the effect of small aerosols (less than 1 μm) in the upper troposphere is still present and, combined with the strong methane absorption bands at these wavelengths is possible to perform an altimetry impossible to attain by other means.

On the other hand, ground-based observations with *PlanetCam*, with high-resolution imaging using Lucky Imaging from the near-UV to H-band, can also support scientific missions like NASA's Juno, in orbit around the planet since July, 2016. Juno has limited imaging capabilities and thus relies on ground-based observations in order to provide context information for its instruments. The capabilities of *PlanetCam* at short wave infrared wavelengths will fill a gap in the expected follow-up from ground-based observatories.

Saturn

Saturn's spectrum is dominated by methane absorption bands and therefore *PlanetCam* is able to retrieve information from atmospheric levels located from the stratosphere at a few milibar down to the upper troposphere, at roughly 1-2 bar level where the cloud deck, putatively formed by ammonia ice (West et al., 2009), is expected. While at methane continuums the planet is bright, the received flux is orders of magnitude lower at the deep methane bands.

In the case of Saturn, the detection of spot activity in 2015 subjected to rapid motions in the Equatorial Zone (Sánchez-Lavega et al., 2016) is a point of high interest that needs to be surveyed complementing the view from Cassini spacecraft at low phase angles. Convective storm activity in some periods and major atmospheric disturbances nicknamed "Great White Spot" (GWS) phenomenon are also a key point for *Planetcam* studies (Sanchez-Lavega et al., 2011, 2013). Other disturbances, as the one that occurred close to polar latitudes in 2015 (del Río-Gaztelurrutia et al., 2017) could be another important scientific target. As of this writing, the Cassini mission was orbiting the planet but the spacecraft had entered into its final polar orbit and no global context

observations were going to be produced any longer following the "Gran Finale" on September 15th, 2017. This means that context observations provided by ground-based telescopes were required by the mission in the following months. Moreover, once Cassini mission is over, ground-based observations are the only source of information for this planet.

Our observations, coupled to those from Cassini, allow to determine the short and long term behavior (annual, seasonal cycle) of clouds and aerosols and the changing solar heat deposition and its influence on upper troposphere and stratosphere dynamics under the seasonal ring shadowing and polar nights at Equator and polar regions.

Uranus / Neptune

PlanetCam also allows imaging the much dimmer planets Uranus and Neptune. Both planets show recursive but random atmospheric activity that can be observed at the methane absorption bands as bright spots (Sromovsky et al., 2012). Uranus storm activity is more scarce than Neptune one but can reach a high degree of intensity as occurred in 2012-15 (Sromovsky et al., 2015; de Pater et al., 2015), thus requiring a continuous survey. Because of its large orbital tilt, seasonal changes in the cloud and hazes structure are observed and this requires a long term survey to understand the altitude sensitivity and mechanisms operating under extreme changing insolation.

Neptune displays both an episodic and continuous cloud activity whose analysis requires high-resolution photometrically calibrated observations to determine its nature and evolution (Fitzpatrick et al., 2013). The search for spot activity, photometry and spot tracking for wind measurements allows characterize the long-term meteorology of the planet. This includes the characterization of the cloud and aerosol properties from multi-wavelength photometry on stellar calibrated images, for what high spectral and spatial resolution is required. The role of *PlanetCam* in such observations has been demonstrated for example in Hueso et al. (2017).

5.2 Venus

Venus has been imaged at CAHA 1.23 m and 2.2 m telescopes with *PlanetCam*, mainly with the UV, Violet and methane band filters to detect clouds at different altitude levels above surface (Peralta et al., 2017; Sánchez-Lavega et al., 2008, 2016). Figure 5.4 shows the cloud morphology at the two spectral ranges and altitude levels sampled: the upper cloud (65-70 km, U and Vio filters) and the base of the upper cloud (60 km, M3 890 nm), while Figure 5.5 shows optical depth and extinction estimation of Venus atmosphere (Sánchez-Lavega et al., 2016) for these altitude values and several wavelength values relevant to *PlanetCam*.

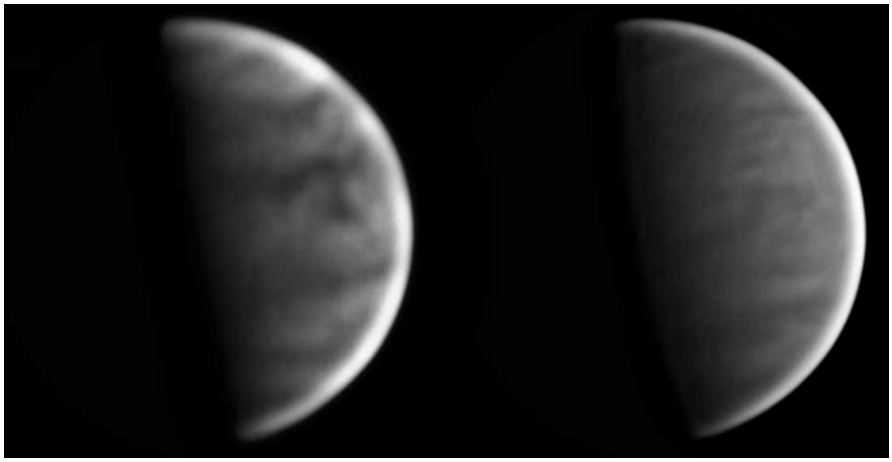

Figure 5.4. Venus on *PlanetCam1* at the CAHA 2.2m telescope observed in April 7th 2014. Left: U and Vio filters combined into a single image. Right: M3 filter (890 nm). Images were acquired at 05:22 UT (left) and 05:33 UT (right). The planet diameter is 20.9'' and the observations were acquired with an elevation of 21º and a phase angle of 82º. High-resolution images were built from the best 30% of three acquisitions (U: 300 frames of 0.5 s; Vio: 500 frames of 0.05s; M3: 2000 frames of 0.05s) and were high-pass filtered to show the cloud details. From Sánchez-Lavega et al. (2016).

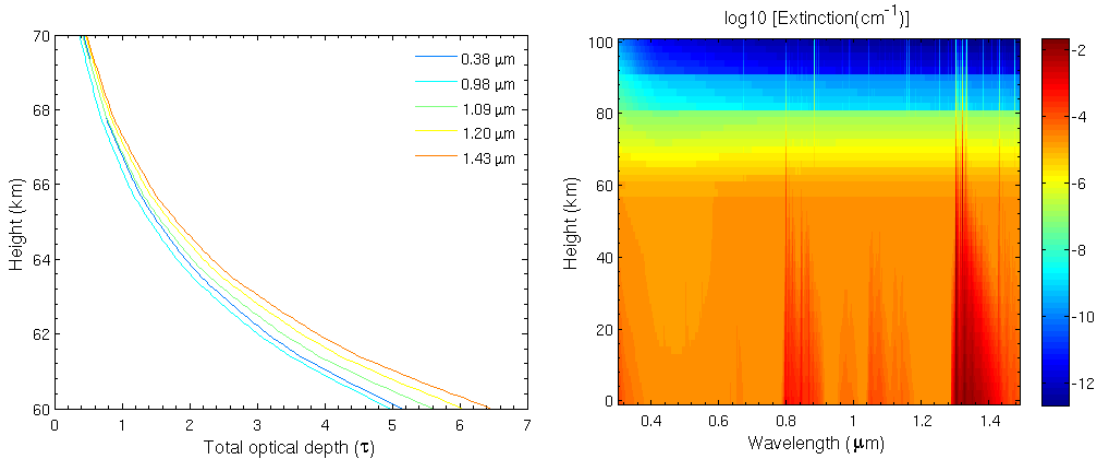

Figure 5.5. Venus atmosphere optical depth and extinction estimations

These images contribute to the analysis of Venus clouds and waves variability at different altitude levels, which can be tracked from images obtained by space missions flybys, like those from Mariner 10, Pioneer-Venus, Galileo, Mesenger and Venus Express. Between Venus Express end of mission in November 2014 and Akatsuki mission from December 2015 (Nakamura et al. 2007, 2011, 2014), only ground-based images from Earth were available. The angular proximity of Venus to the Sun allows to obtain ground-based images only when the planet is close to its maximum elongation at around 48º, having Venus' disk half illuminated, yet the lucky imaging technique allows high-resolution imaging with small telescopes and therefore image Venus during almost its whole orbit.

The evolution of clouds, morphology and motions in Venus daytime side are studied through images in the ultraviolet (UV)–violet (0.38–0.42 μm) as well as near-infrared (NIR: 0.9–0.97 μm) spectral ranges where clouds at two altitude levels can be observed. Venus images obtained with *PlanetCam* at CAHA 2.2m telescope in December 2015 provided valuable information about the status of Venus clouds and waves just before the Akatsuki mission.

Figure 5.6 shows the Venus dayside reflected spectrum with the following main features: UV aerosol absorption (300–450 nm) and CO2 absorption bands at 1.05, 1.2–1.35, and 1.435 μm. Figure 5.7 shows the aspect of Venus at different wavelengths from December 2015 *PlanetCam* images.

These *PlanetCam* images show a low spatial resolution due to the low maximum elevation of the planet at sunrise (26°), but they clearly show the different cloud morphologies depending on the wavelengths, as a consequence of the scattering and absorption properties of the upper cloud. At 380 nm we sense the morphology at altitudes of 65–70 km as traced by the mixture of the unknown UV aerosol absorber and the clouds (Figure 5.7 up-left). In the narrowband at 890 nm and in the broadband 725–950 nm filters (Figure 5.7 lower) we sense the cloud morphology at the base of the upper cloud (altitude ~60 km; Belton et al. 1991; Sánchez-Lavega et al. 2008). In the 1.435 μm CO_2 absorption band (Figure 5.7 up-right), the cloud morphology differs from that of the previous cases. The vertically integrated extinction within this band indicates that we also sense at this wavelength the upper cloud at 65–70 km, but the difference with the UV is that there is very little aerosol absorption and the brightness contrast in

the clouds originates from small differences in altitude and in the scattering behavior of the cloud particles. We measured a relative brightness contrast between features ~10% in the UV (380–410 nm) decreasing to about 5% in the NIR (750–950 nm) and SWIR (1.435 μm CO_2 band ranges).

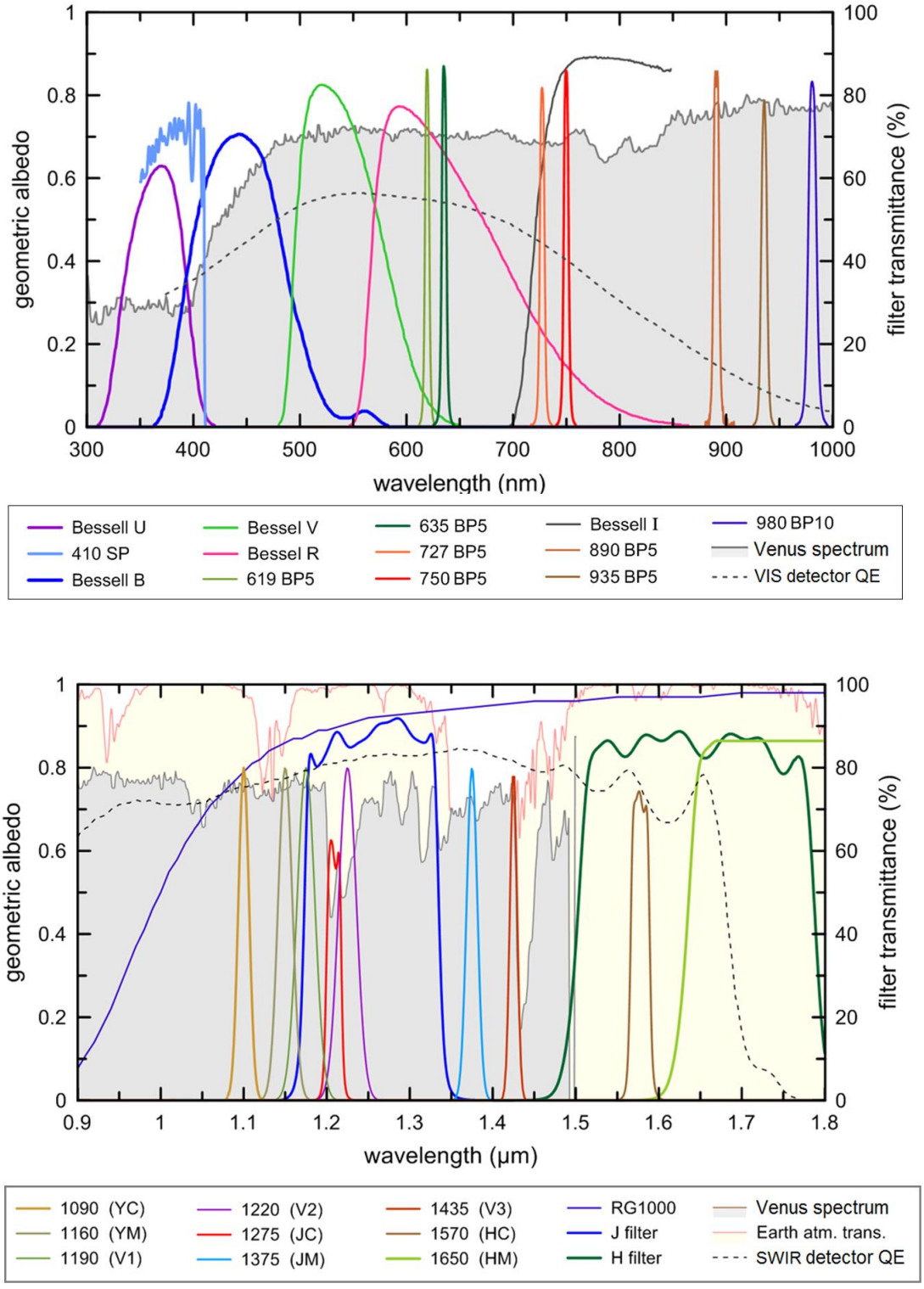

Figure 5.6. Venus spectrum represented with *PlanetCam* filters and detectors in both VIS and SWIR channels.

These images have been compared with others in the UV from different public databases taken by amateur astronomers covering both elongation periods from April to December 2015 (Sánchez-Lavega et al. 2016). The main conclusion of this analysis is that the observed dynamical state of Venus upper cloud differed in April–June from October–December when the Akatsuki Venus Orbital Insertion (VOI) took place. During the VOI, the dynamical regime was dominated by the development of planetary-scale waves typical of the Venus atmosphere at the cloud top level (Y-horizontal, C-reversed, and ψ-horizontal waves) formed by long tilted streaks and banding with complex interactions between them. Part of this difference between both observing periods can be attributed to Local Time observing conditions: afternoon hemisphere and more unstable upper cloud layer (eastern elongation) and morning with more stable conditions (western elongation).

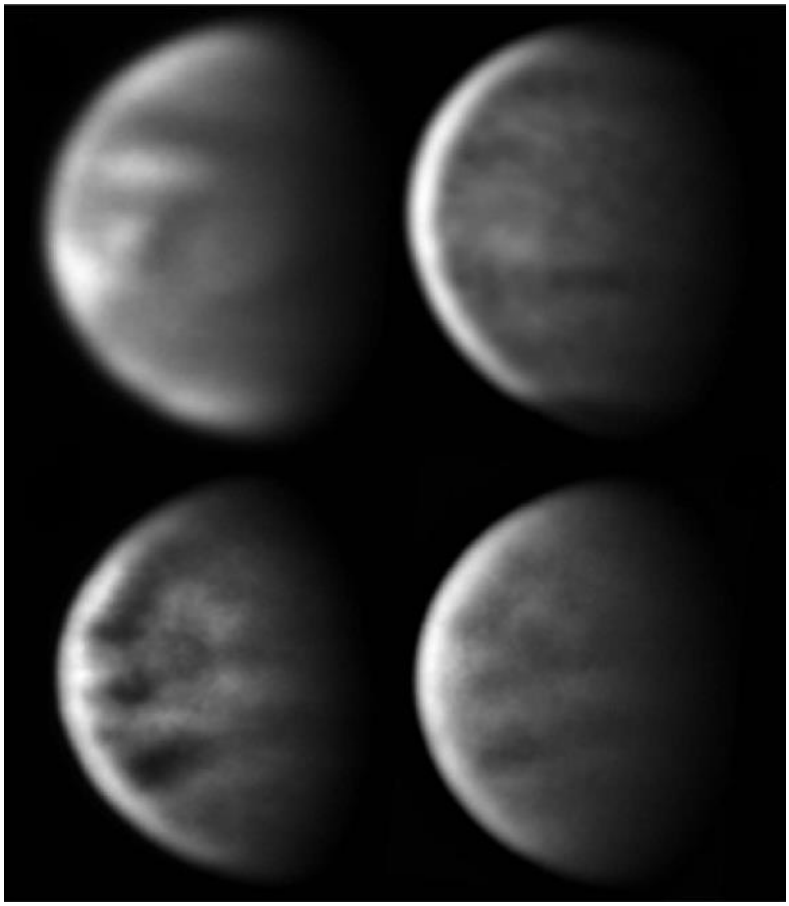

Figure 5.7. *PlanetCam* images obtained with the 2.2 m Calar Alto Obs. telescope on December 30th 2015, at wavelengths: (up-left) 380 nm (06:35 UT); (up-right) 1.435 μm (06:54 UT); (low-left) 890 nm (06:56 UT); (low-right) 725–950 nm (06:50 UT) (Sánchez-Lavega et al. 2016).

The U–Vio images obtained along the two elongation periods in 2015 were also used for cloud tracking and zonal velocity measurements. Our velocity measurements agree at lower latitudes with results from older missions (Schubert 1983), Doppler wind measurements (Machado et al. 2012, 2014), and the mean profiles from data obtained over a decade by the VMC and VIRTIS instruments on board VEx (Sánchez-Lavega et al. 2008; Khatuntsev et al. 2013; Hueso et al. 2015), as shown in Figure 5.8. The higher discrepancies found for higher latitudes might be attributable to the sporadic changes in the poleward decay of the winds also found in some orbits of VEx mission and in the difficulty in target identification at these latitudes. The zonal wind velocity retrieved from cloud tracking in the latitude range from 50°N to 50°S agrees in general with previous wind retrievals, although deviations are found. These deviations might be attributable to motions of global-scale waves apparent on the cloud tops and the solar tide (Hueso et al. 2015).

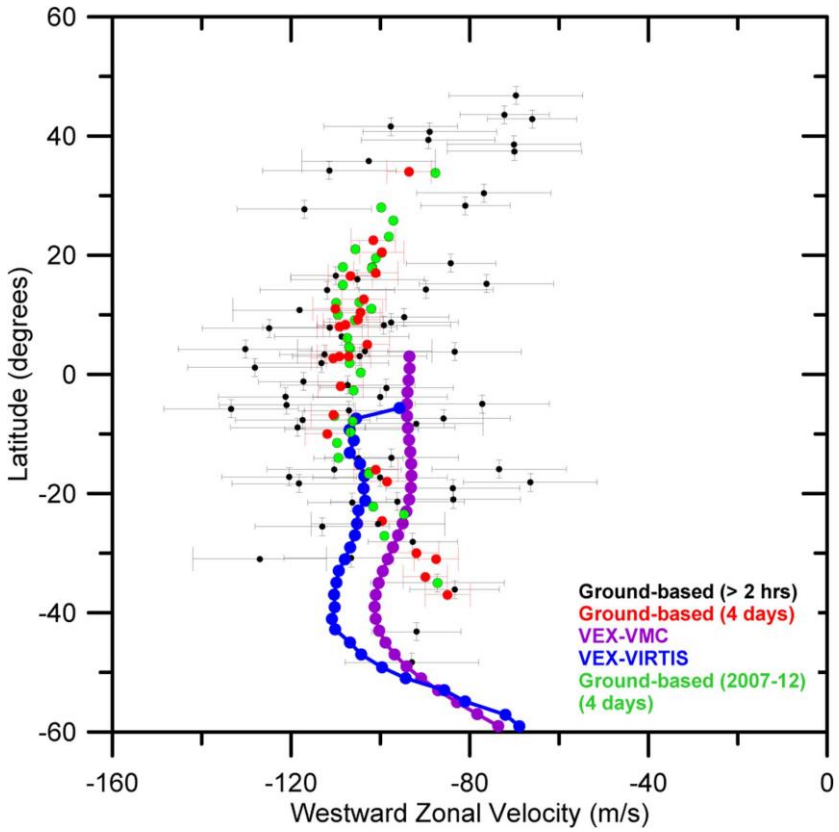

Figure 5.8. Venus zonal wind velocity profile from cloud tracking in UV–violet images. Data are from periods 2015 April–May and October–December: short-term tracking (2–6 hr; black dots), long-term tracking (4 days; red dots). Additional data for 2007–2012 is included (green dots). For comparison we show the average wind profiles obtained with VEx instruments VMC (violet; Khatuntsev et al. 2013) and VIRTIS (blue; Hueso et al. 2015) and representative of the 2006–2012 period. (Sánchez-Lavega et al. 2016).

5.3 Mars

Mars has also been imaged with *PlanetCam* at selected wavelengths, for example during the 2014 opposition. The aim was to look for the capabilities of the camera to capture surface details and atmospheric phenomena (dust and clouds). Figure 5.9 shows *PlanetCam1* images where such features are well detected and easily identifiable. Particularly interesting is the U-Vio spectral region to capture the ice clouds (both water and carbon dioxide) and the yellow-red wavelengths to capture the dust. In particular the development of the so-called "tropical cloud belt" was nicely captured in the ultraviolet. Figure 5.10 shows *PlanetCam2* images from both VIS and SWIR channels. The albedo marks on the Martian surface become conspicuous at the near-IR wavelengths allowing track reported reflectivity changes at the surface following regional dust storms. This figure also shows in the UV the presence of clouds and an extended polar cap. As it has been commented before, the detection of high-altitude plumes (Sánchez-Lavega et al., 2015) with small-sized telescopes opens a very interesting scientific case for *PlanetCam* observations of Mars. In particular, the wavelength range of the instrument would help to discriminate between dust and ice clouds. This is a kind of study difficult to be planned for limb observations with orbiting spacecrafts due to the time delay in planned spacecraft schedule and unpredictable and rapid occurrence of the events. Ground-based imaging is here essential.

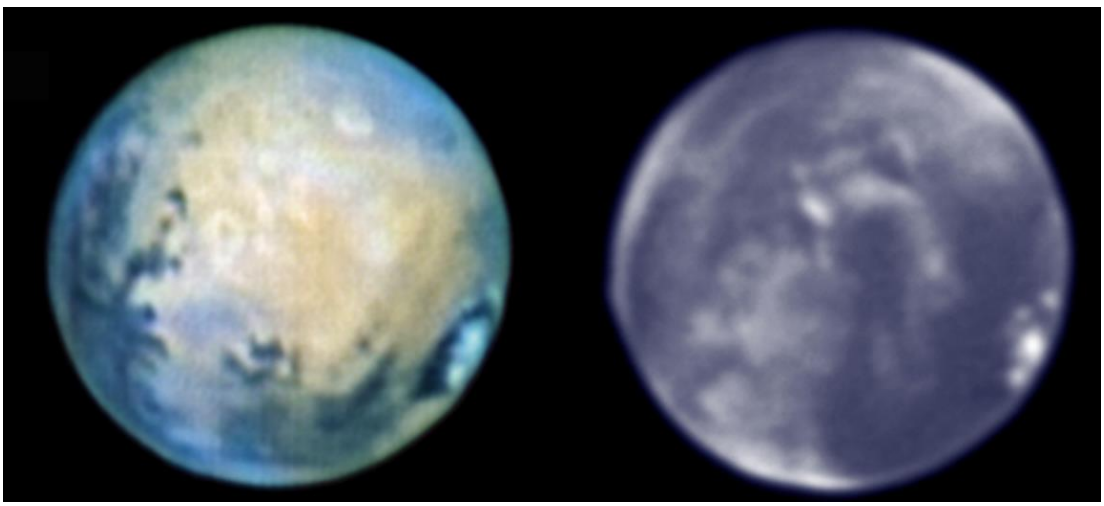

Figure 5.9. Mars imaged by *PlanetCam1* at the 2.2m telescope observed in April 7th 2014 (L_s = 113º; MY 32). Left panel: Color composition using Red, Green and Blue filters and a luminosity layer from observations in a red filter acquired at 00:06 UT; Right panel: U observation acquired at 00:39 UT. The planet diameter is 15.0'' and the observations were acquired with an elevation of 47º and a phase angle of 82º. High-resolution images were built from the best 30% of the original observations (Wratten21: 1000 frames of 1 ms; U: 200 frames of 2.0s) and were high-pass filtered to show the surface and cloud details.

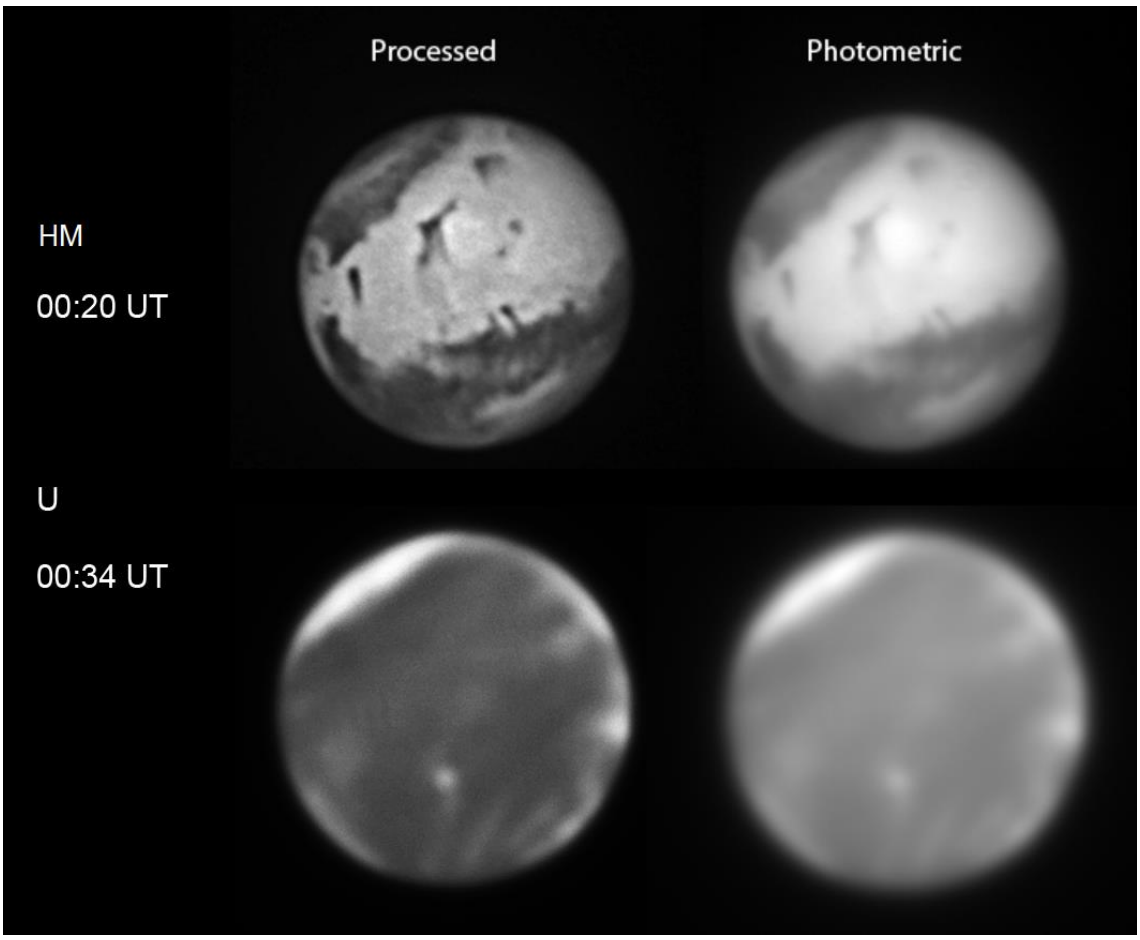

Figure 5.10. Mars imaged by *PlanetCam2* at the 2.2m telescope observed in May 17th 2016 (L_s = 343º; MY 32) in both SWIR channel HM filter (up) and VIS channel U filter (down). Both photometric and further processed images are shown for comparison of resolution achieved.

5.4 Jupiter

5.4.1 Jupiter in time and wavelength

The giant and icy planets are the primary candidates for *PlanetCam*. High-resolution imaging in visible and SWIR allows tracking a large number of dynamical phenomena as well as determining the global motions (wind field structure) at different altitude levels, and study the structure and properties of the cloud cover. Most observing campaigns with *PlanetCam* have been focused on Jupiter and Saturn at their oppositions, when apparent size is the biggest and the planet is the brightest, making the ideal case for lucky imaging. Figure 5.11 shows a typical sequence of Jupiter stacked into a RVB (Red, Green, Blue) color composite. The figure also illustrates the spatial resolution attained with lucky imaging observations (left panel) and the additional processing that is generally required to extract high-resolution information. Images without processing can be calibrated and used to retrieve the vertical cloud structure. Images processed with a variety of image processing techniques are generally required for dynamic studies. Atmospheric features smaller than 0.4" are routinely resolved. High-contrast small features are resolved easier than low-contrast features of the same size.

Figure 5.12 shows a series of Jupiter images taken in the same night with filters sensitive to different absorbing agents (aerosols and methane gas), Rayleigh scattering, thus sounding different altitude levels in the atmosphere. These series were photometrically calibrated using standard stars. Figure 5.13 shows two high resolution images of Jupiter taken at close wavelengths (890 nm methane absorption, filter M3, band and 950 nm approximately, filter C3) that sense very different altitude levels in the atmosphere. The image series obtained in the SWIR channel of *PlanetCam2* on Jupiter are shown in Figure 5.14. Some wavelengths are affected by water absorption on Earth's atmosphere (Figure 2.17), but careful calibration of the narrow band filters between 1090 and 1570 nm that involve methane bands and their adjacent continuum, can be used to retrieve in detail the cloud vertical structure at different latitudes. The filter RG1000 and those at the J and H bands are well suited for high resolution imaging.

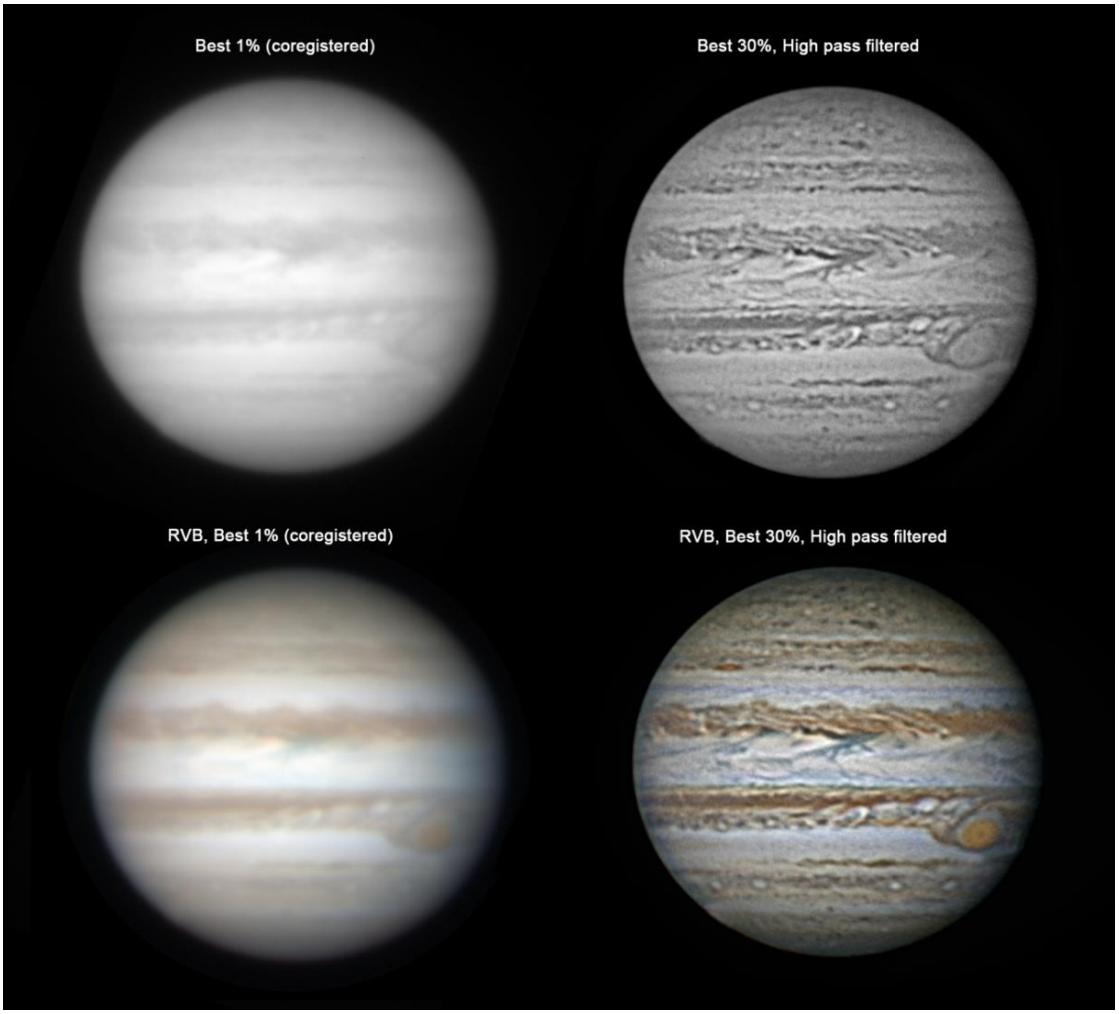

Figure 5.11. Jupiter on *PlanetCam2* at the 2.2m telescope observed on December 11th 2014 at 01:09 UT. Top: Image acquired with a Red filter. Bottom: Color image from R, V, B filters. Top left: Photometric image built from co-registering the best 1% of all frames. Top right: Image built from co-registering the best 30% of all frames and using high-pass filters to increase the visibility of atmospheric cloud features. Bottom left: Photometric color image from the best 1% of all frames. Bottom right: Color composition from the best 30% of R, V, B images using a combination of high-pass filters to enhance the visibility of atmospheric features. The planet diameter is 41.0'' and the observations were acquired with an elevation of 40º and a phase angle of 9.6º. North is up and West to the left. Frame exposure times are 0.05 s and typically 500-1500 frames are acquired in sequence.

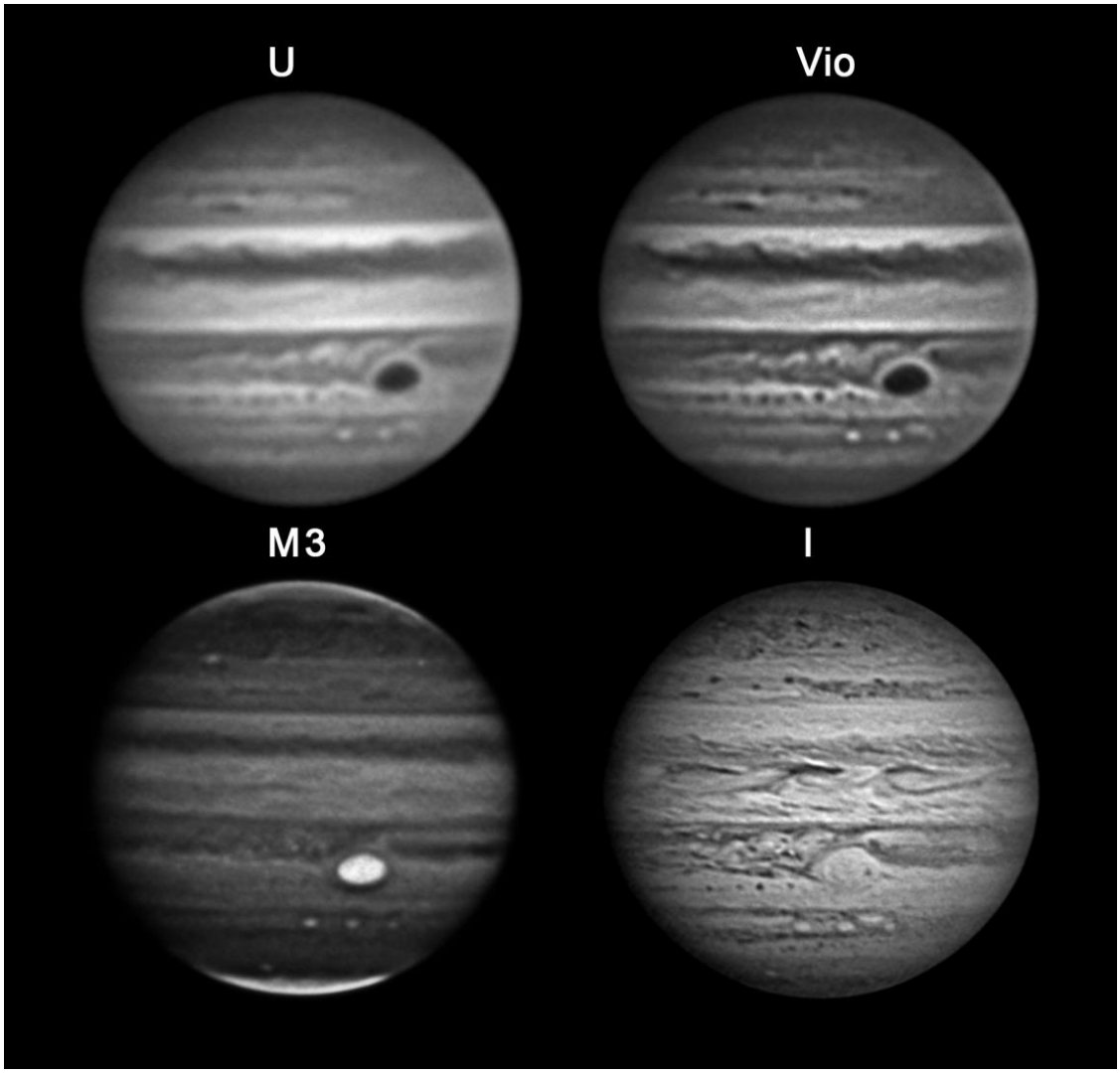

Figure 5.12. Jupiter on *PlanetCam1* at the 2.2m telescope observed on April 6th 2014 at 22:43 UT (UV), 22:11 UT (I) 22:25 UT (M3) 22:39 UT (Vio). All images have been built from co-registering the best 30% of all frames and using high-pass filters to increase the visibility of atmospheric cloud features. The planet diameter is 37.9" and the observations were acquired with an elevation of 32º and a phase angle of 11º. North is up and West to the left. Frame exposure times vary from 0.05 s in I filter to 5 s in M3.

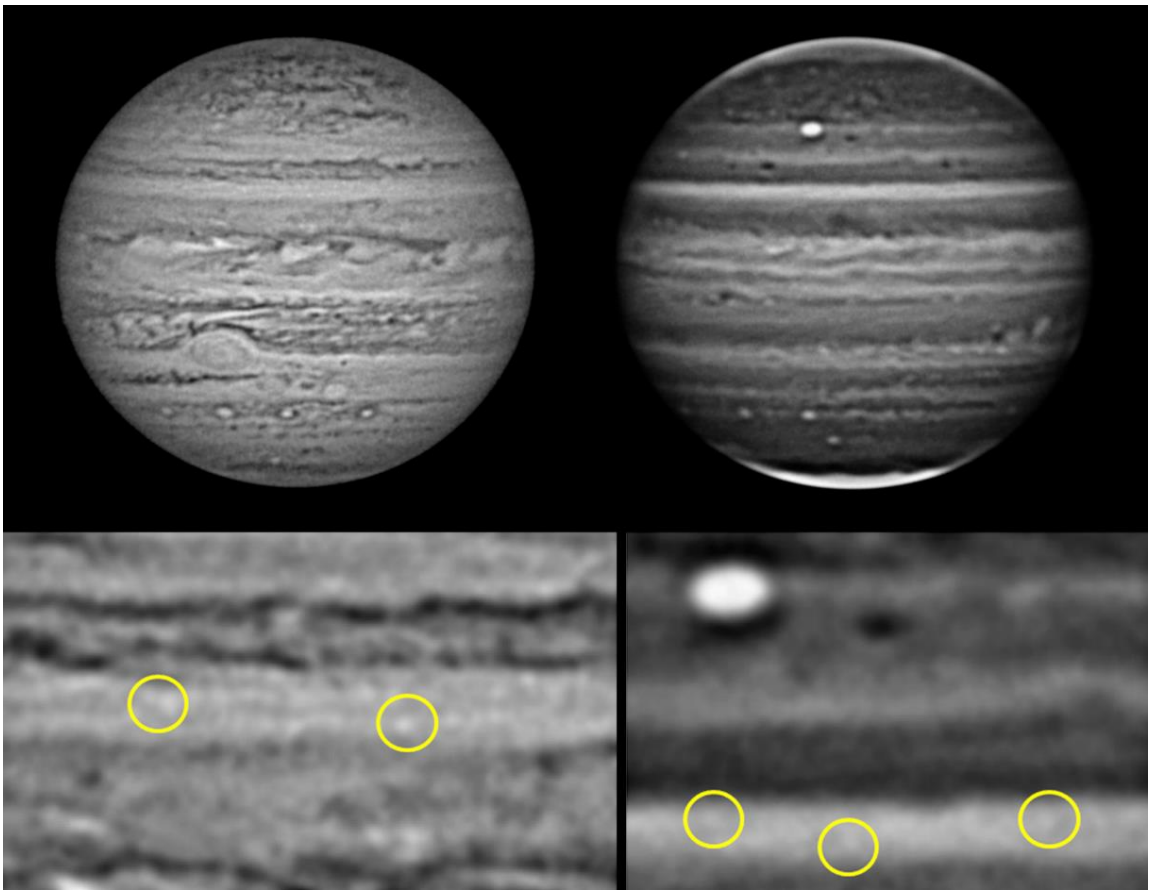

Figure 5.13. Jupiter on *PlanetCam1* at the 2.2m telescope observed on December 3rd 2012 on I filter at 19:53 UT (left) and on a M3 filter at 22:37 UT (right). Images have been built from co-registering the best 30% of all frames and using high-pass filters to increase the visibility of atmospheric cloud features. The planet diameter is 48.5'' and the observations were acquired with an elevation of 36º and 66º respectively and a phase angle of 0.2º. North is up and West to the left. In the lower part a zoomed area of each image is shown with selected (circled) small features having a size of 0.30-0.35 arcsec at the resolution limit of the instrument. Frame exposure times are 0.05 s in the I filter and 10 s in M3.

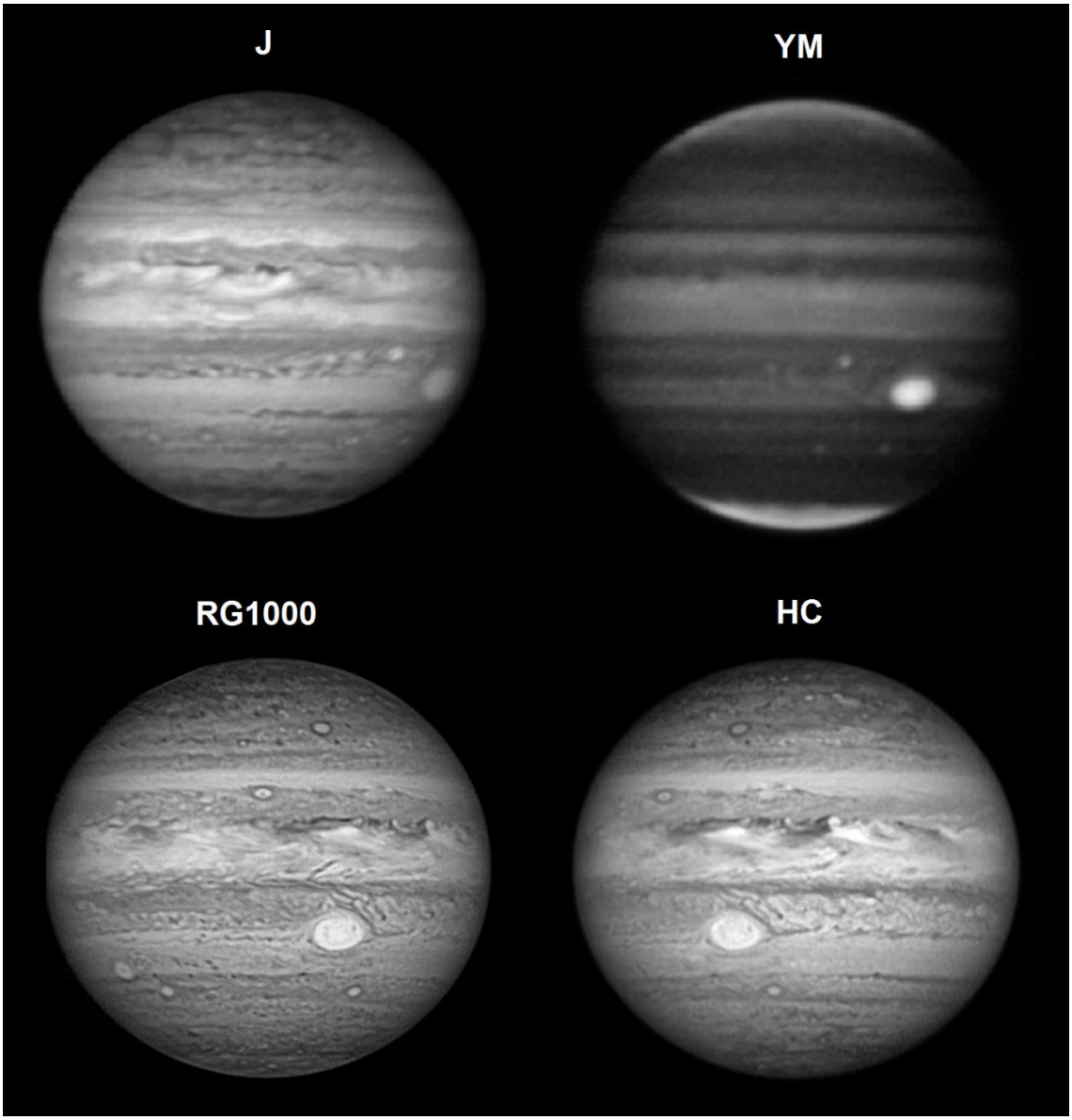

Figure 5.14. Jupiter on *PlanetCam2* at the 2.2m telescope in several SWIR filters observed December 11th 2014 (filters J and YM) and on March 30th 2017 (filters RG1000 and HC with additional unsharp mask processing by Josep M. Gomez-Forrellad). Images were built from co-registering the best 1% in bright wide filters (J, HC, RG1000) to all frames in dark methane filter (YM) and using high-pass filters to increase the visibility of atmospheric cloud features.

5.4.2 Jupiter temporal changes in Absolute Reflectivity

The temporal evolution of the properties of the cloud cover of Jupiter and Saturn can be analyzed comparing absolute reflectivity *I/F* scans obtained in different observing campaigns. A key issue in this analysis is to estimate the uncertainty values from the different sources as described in chapter 4, so that the observed variations can be clearly attributed to physical atmospheric variations over time rather than to systematic or random photometric errors.

In order to minimize the uncertainty in absolute reflectivity calibration, the different *I/F* scans have been scaled so that they all are compared to the overall mean geometric albedo. Thus, we assume that full disk geometric albedo is constant over the four years of *PlanetCam* observations. As long as this assumption is valid, and the other uncertainty sources related to image navigation (particularly remarkable at high latitudes) and belt/zone width variations along the whole longitudes are controlled, the remaining variations between the different observing campaigns can be interpreted as caused by temporal changes in the cloud cover of these planets.

Figure 5.15 to Figure 5.17 show the Jupiter central meridian reflectivity evolution of the belts and zones from December 2012 to May 2016 in the Northern hemisphere (those for full disk can be found in Appendix 3), where some changes are remarkable. In the violet (Vio) filter we observe at 20º planetographic latitude that the reflectivity increases from a peak *I/F* of 0.41 in December 2012 to 0.64 in April 2014, decreasing down to 0.56 in March 2016. We can also compare these *I/F* peak values to the averaged reference value of 0.55, so a variation of up to 40% can be observed in this spectral band. We estimate that the uncertainties due to the error sources above discussed can be of the order of 10%.

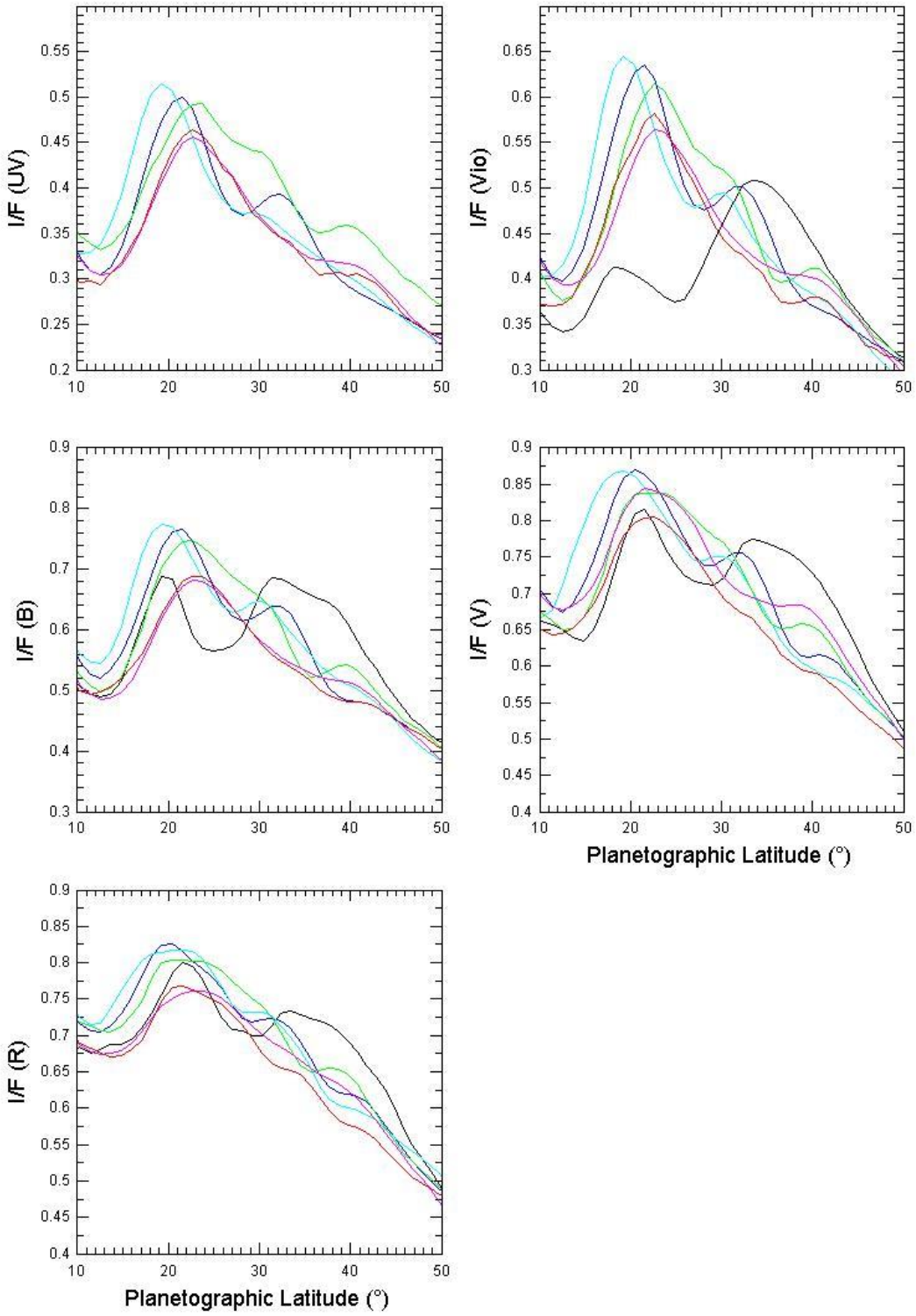

Figure 5.15. Jupiter absolute reflectivity evolution in northern hemisphere detail in VIS channel U, Vio, B, V and R filters (black corresponds to December 2012, blue to December 2013, cyan to April 2014, green to March 2015, magenta to March 2016, red to May2016).

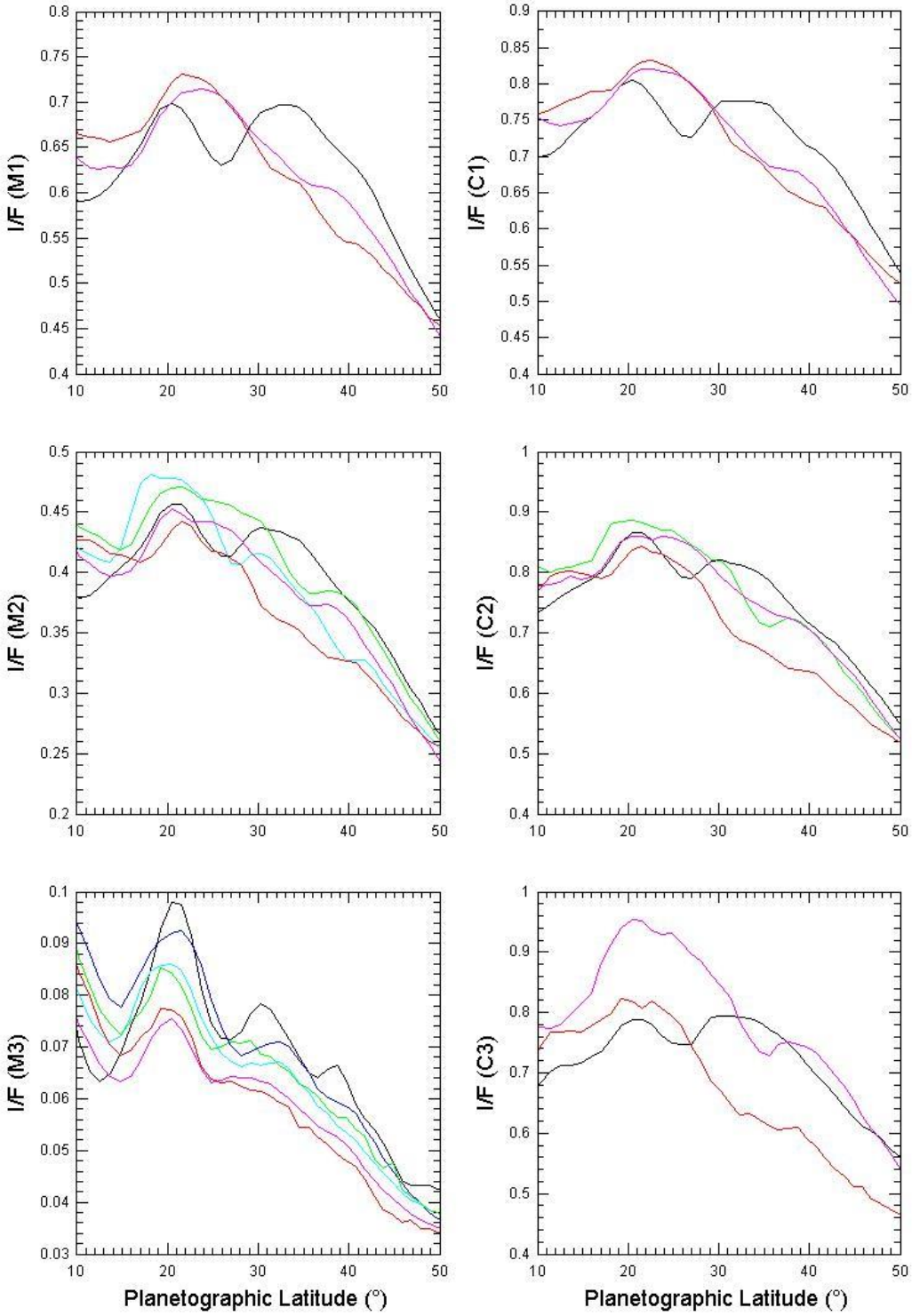

Figure 5.16. Jupiter absolute reflectivity evolution in northern hemisphere detail in VIS channel methane and continuum filters (black corresponds to December 2012, blue to December 2013, cyan to April 2014, green to March 2015, magenta to March 2016, red to May2016).

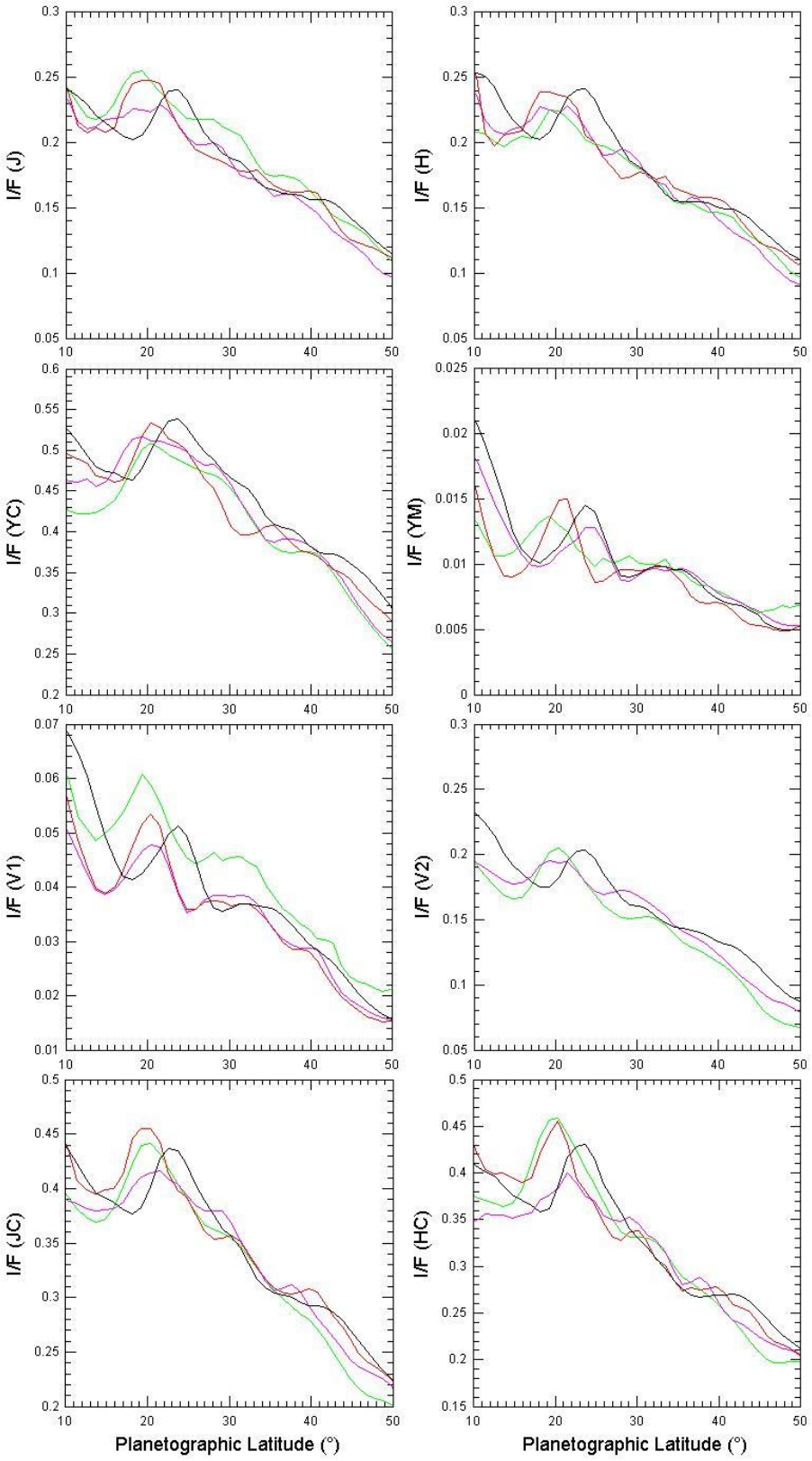

Figure 5.17. Jupiter absolute reflectivity evolution in northern hemisphere detail in SWIR filters (black corresponds to December 2012, blue to December 2013, cyan to April 2014, green to March 2015, magenta to March 2016, red to May2016).

Similar variations can be observed in the blue (B) filter, where I/F peak at latitude +20º varies from 0.69 in Dec 2012 (0.98 times the average of this peak in B filter) to 0.77 in April 2014 (being 1.1 the global average) and back to 0.68 in March 2016 (being 0.97 the global average). Note that a dark belt at planetographic latitude +25º present in December 2012 vanishes in the following years (Figure 5.18).

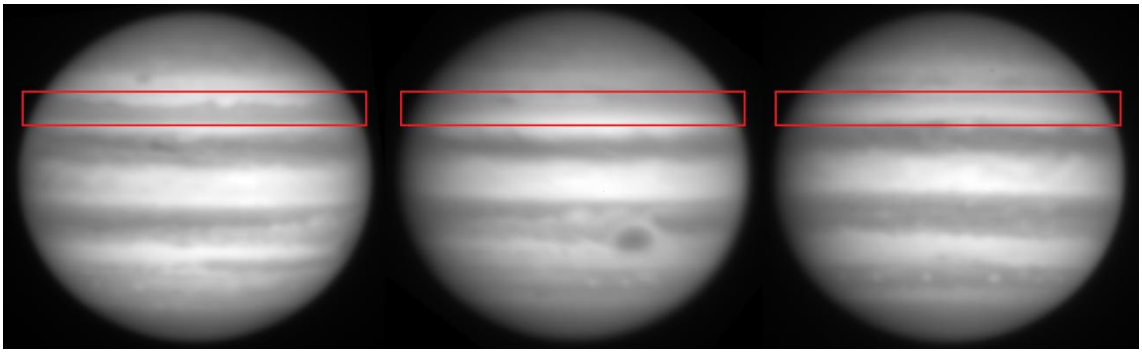

Figure 5.18. Temporal evolution of dark band at latitude 25º in Jupiter B filter (from left to right: December 2012, April 2014, May 2016).

The reflectivity in the methane band filters shows the opposite behavior at these latitudes. The *I/F* scans in M3 show a peak at latitude +20º continuously decreasing from 0.098 in Dec 2012 (1.14 times the average) to 0.086 in April 2014 (1.00 times the average) and 0.075 in March 2016 (0.87 the average), i.e. a total reflectivity decrease of 27% from the average. A smaller variation can be seen in the 2º wide band at latitude around 45º, with a variation of 10% with respect to the four-year average at that latitude. The nearby continuum filter C3 does not show any of these reflectivity values decreases, suggesting altitude variations in the top of a haze layer. On the other hand, variations over the time at this latitude are also seen in the continuum filter HC changing from 0.46 in March 2015 (1.09 times the average) to 0.40 in March 2016 (0.95 the average). Ongoing analysis of these data and their interpretation in terms of radiative transfer models will be presented in the following section.

5.4.3 Radiative Transfer modeling

From a radiative transfer model of photometrically calibrated images, some information can be retrieved about the vertical structure of Jupiter atmosphere. Such exercise was performed on *PlanetCam* images in the context of the changes observed in the North Temperate Belt (NTB) in 2016. The result of this study is presented in Sánchez-Lavega et al. 2017, and other cases of study are under development and will be presented elsewhere.

Outbreak events can provide information on the atmospheric dynamics and cloud and aerosol behavior over the pressure range in altitude from 0.01 to 5 bar. The NTB Disturbance (NTBD) occurs in the most intense jet of Jupiter at 23.5ºN It starts with an initial single or multiple convective outbreak seen as a bright spot (a "plume") close to the jet peak that interacts with the wind sheared background flow leading to a disturbance formed by multiple dark irregular spots and filaments that propagates relative to the outbreak source, encircling the whole latitude in one to three months, finally generating a new low albedo band (a belt) Rogers, 1995; Sánchez-Lavega et al., 1991, 2008). The jet peak velocity ranges from ~135 to 175 m/s, where this variability could be intrinsic or related to the different altitudes of the tracers, coupled to a possible vertical wind shear. The jet gradually accelerates before a NTBD outbreak, until it reaches almost the speed of the subsequent plumes (Rogers et al., 2006; Sanchez-Lavega et al., 2008). The 2016 outbreak was exceptional since four plumes were active in generating the disturbance whereas in the last two well studied events in 1990 and 2007 there were two plumes. In addition, this eruption took place shortly before the Juno spacecraft perijove-2 (PJ2) on October 19. For the study of this specific outbreak in 2016 (Sánchez-Lavega et al., 2017) images from different sources taken at different dates and covering different wavelengths were used and analyzed, including images from Hubble Space Telescope (HST), JUNO mission and *PlanetCam*.

Hubble Space Telescope (HST) maps of the cloud morphology obtained on February 9-10, 2016 showed that northward of the jet peak in a conspicuous narrow band from latitudes 24.5°± 0.2° to 25.5°± 0.4°, the reflectivity at 275 nm was high relative to surroundings, but it was low in the 890 nm methane absorption band (OPAL program, Simon et al. 2015). This suggests that this narrow band was a region depleted

in high-altitude aerosols, with UV brightness due to Rayleigh scattering and methane-band darkness due to gas absorption.

We performed a preliminary analysis of photometrically calibrated *PlanetCam* images obtained before the outbreak on May 19th 2016 using nine filters from the UV (378 nm) to three near-infrared methane absorption bands (M2 - 727nm, M3 - 890nm, YM - 1162 μm) and their adjacent continuums (Figure 5.19).

For the analysis of the *PlanetCam* images, we used the radiative transfer and retrieval suite NEMESIS, developed by Irwin et al. (2008). We computed correlated-k tables for methane absorption at the *PlanetCam* filters used here: UV, VIO, B, M1, M2, M3, YM, C1, C2, C3 and YC. The k-tables were based on the updated methane absorption coefficients given by Karkoschka and Tomasko (2010). The atmosphere is assumed to be plane-parallel and the radiative-transfer solver is based on the doubling-adding technique. We tried to fit the observed reflectivity at 5 selected locations on the disk, thus fitting both the spatial and spectral behavior of the absolute reflectivity. We used as free parameters the optical thickness of the stratospheric haze (assumed to be located between 10 and 60 mbar) and the lower ammonia cloud (assumed to be at the ammonia condensation level). For the tropospheric haze we used a more detailed description with the following free parameters: base pressure, maximum abundance and scale height, as well as particle size (a log-normal distribution assumed) and imaginary refractive index. Best-fitting results pointed to a small scale height of just 1.5+/-1.0 km and particle size of 0.7+/-0.1 μm. Imaginary refractive indexes at shortest wavelengths are around 0.012+/-0.006, while they are below 0.005 for NIR wavelengths. The stratospheric haze optical depth was found to be less than $5x10^{-4}$.

Radiative-transfer models for February 2016 PlanetCam images show a particle-free stratosphere and upper troposphere with a haze deck located at 370±100 mbar with optical thickness of $\tau_{haze} = 3.8 \pm 0.6$, above a cloud ($\tau_{cloud} = 6.0 \pm 2.0$) assumed to be located at the ammonia condensation level (~ 700 mbar).

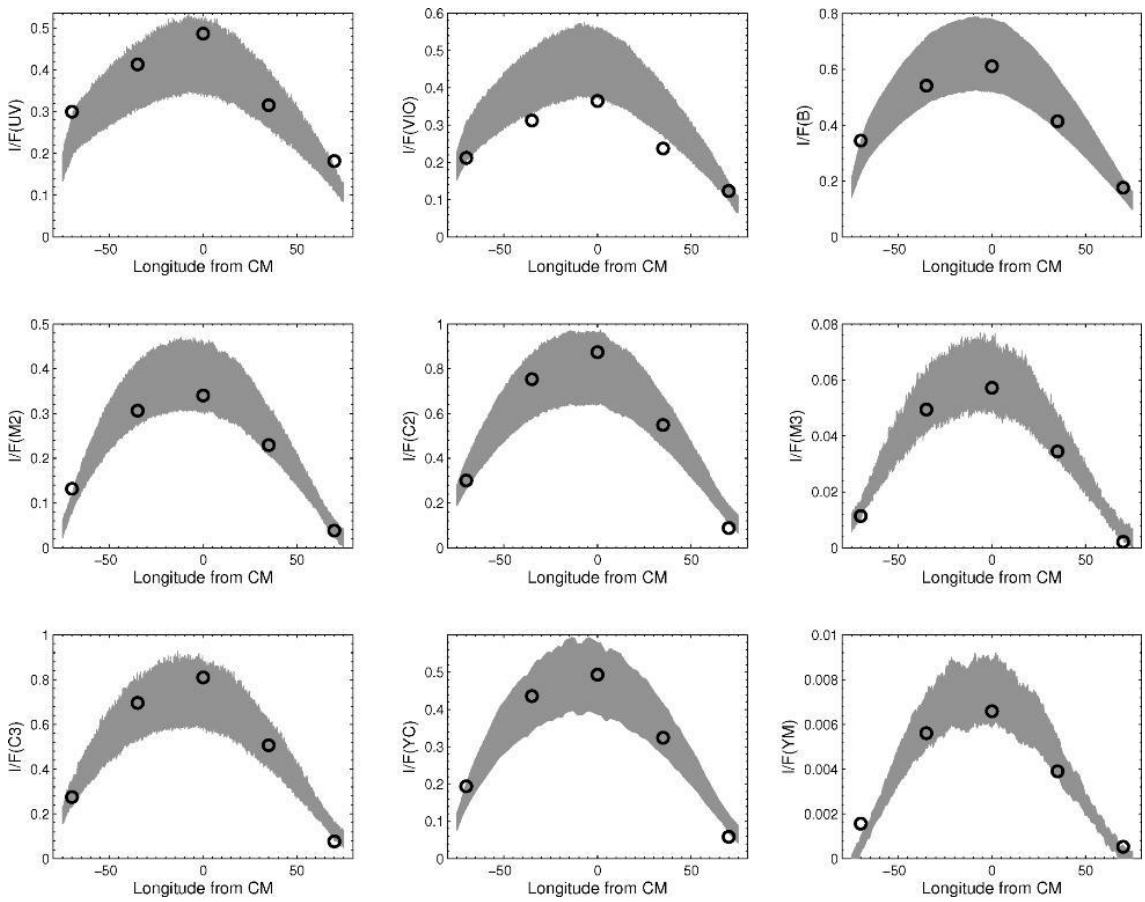

Figure 5.19. This figure shows the absolute reflectivity of *PlanetCam* observations (May 19th 2016) at nine filters with their corresponding error bars (grey areas) and the best-fit models (black circles) at the five locations modeled over the disk at the latitude of the NTB (23.5ºN) before the outbreak. (Sánchez-Lavega et al., 2017).

5.4.4 Cloud morphology and Zonal Wind studies

Jupiter global winds are zonal and alternate in latitude between eastward and westward forming a system of nearly constant jet streams that interacts with vortices, turbulent regions, convective storms and atmospheric waves (Ingersoll et al., 2004). Transient events, like convective disturbances, often develop quickly (Sánchez-Lavega and Gómez, 1996; Sánchez-Lavega et al., 2008) and large scale changes occurring over a few months drastically change the optical properties of bands and belts (Fletcher et al., 2011; Pérez-Hoyos et al., 2012) affecting the wind system in the disturbance latitude. Data acquired in the time domain are needed to understand the evolution of meteorological features in the planet. Atmospheric dynamics at the troposphere also

have implications for the interpretation of observations of the deep atmosphere (de Pater et al., 2016; Li et al., 2016).

The general state of Jupiter's atmosphere over 2016 (cloud morphology, large wave systems, polar regions and global winds) has been analyzed with *PlanetCam* images among others, in order to present the context of Juno's perijove 1 (PJ1) observations obtained by the MWR, JIRAM and JunoCam instruments on August 2016. The result of this study is presented in Hueso et al. 2017.

Images from *PlanetCam* based on lucky imaging technique with additional sharpen processing can improve the spatial resolution over the seeing by a factor of 3-4 while long exposures are used in narrow band filters sampling methane absorption bands. Images in the visible can provide spatial resolutions of around 0.05-0.1'' (200-350 km over Jupiter at opposition) while in the case of SWIR channel spatial resolutions of 0.09-0.2'' (300-700 km) are achieved. Non-sharpened images retain the photometric information and can be calibrated with observations of spectrophotometric standard stars and enable the study of the vertical distribution of clouds and hazes and the spatial distribution of colors, as it has been already presented in the previous section. Four Jupiter observing campaigns were performed with *PlanetCam* from December 2015 to July 2016, including images from July 4 about 7 hours before Juno's orbit insertion. Figure 5.20 shows some images from these observations.

Most of Jupiter's cloud systems from December 2015 to August 2016 are very similar to those observed over 2014-2015 and described from HST observations (Simon et al., 2015). No major disturbances were observed except for a moderate expansion of the North Equatorial Belt (NEB) from 17°N to 21°N that started in 2015 (Fletcher et al., 2016; Orton et al. 20016).

(i) Great Red Spot (GRS)

The Great Red Spot (GRS) maintained an intense orange coloration observed since 2014, several photometric color compositions of the planet from PlanetCam observations show indistinguishable colors in the GRS throughout 2016. PlanetCam, amateur and HST observations show the GRS with a visual longitudinal size of 14.5±0.2° and a latitudinal size of 10.2±0.2°. This is slightly larger than reported values

over 2015 from HST images with a longitudinal size of 13.9° and a latitudinal size of 9.7° (Simon et al., 2015). The difference could be due to different measuring methods (we define the size of the GRS as the apparent size of the dark oval in blue wavelength images; our measurements for the GRS size over HST images in 2015 is 13.9±0.2° and 10.2±0.2°). Amateur and PlanetCam images over December 2015 to July 2016 show a constant size within an uncertainty of 0.2° implying that the diminishing size of the GRS over the last decades (Simon et al., 2014) may have reached a stable configuration.

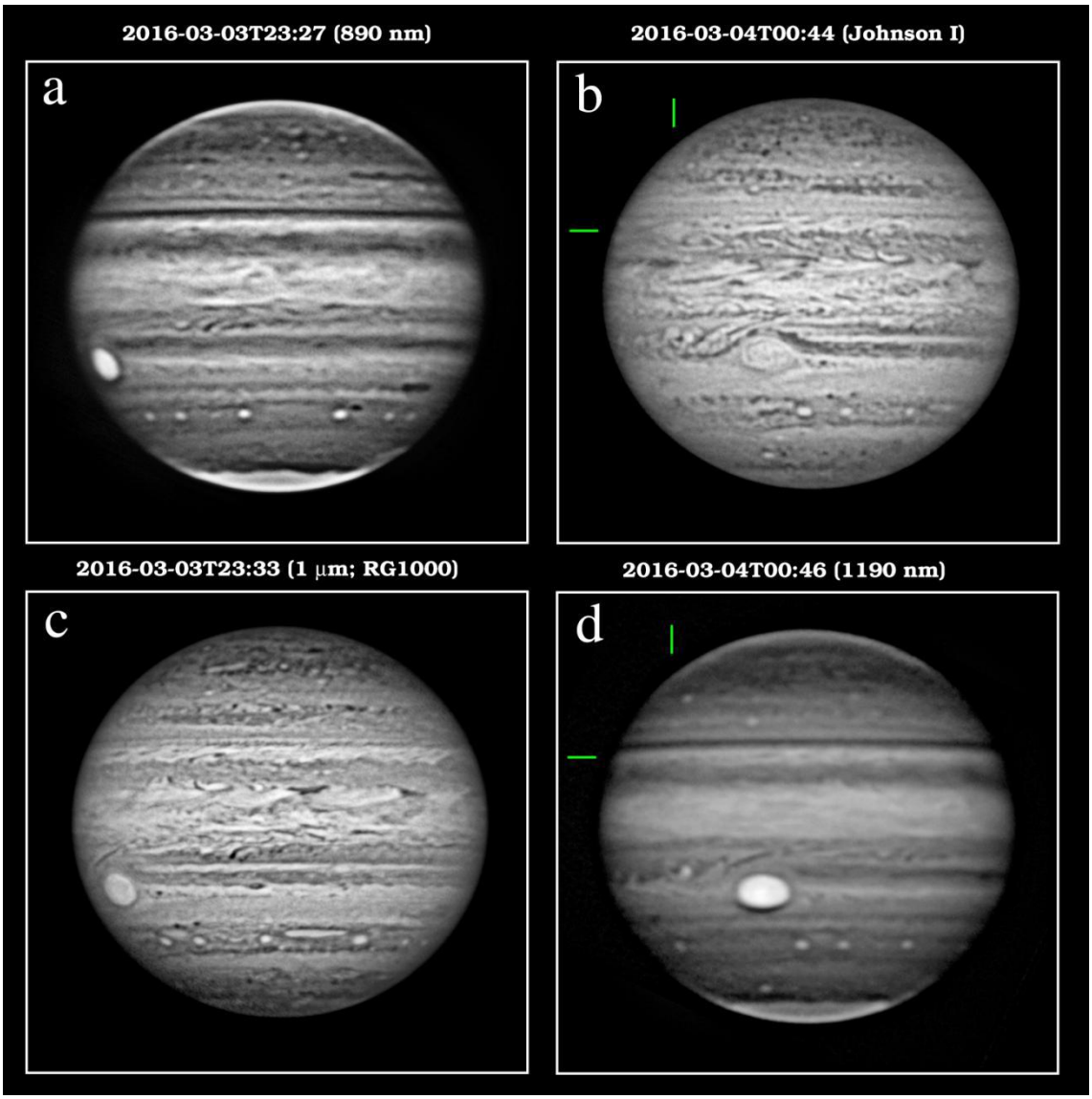

Figure 5.20. *PlanetCam* observations close to Jupiter opposition. (a) 890 nm; (b) Johnson I (wide-band filter at 806 nm); (c) 1.0-1.7 μm filter (RG1000); (d) 1190 nm. Images at 890 and 1190 nm are strongly sensitive to methane absorption and provide views of the upper hazes. Images in Johnson I and the 1.0-1.7 μm filter (RG1000) are weakly sensitive to methane absorption and show details up to the polar regions. A North Tropical Oval later discussed is highlighted in (b) and (d). (Hueso et al., 2017).

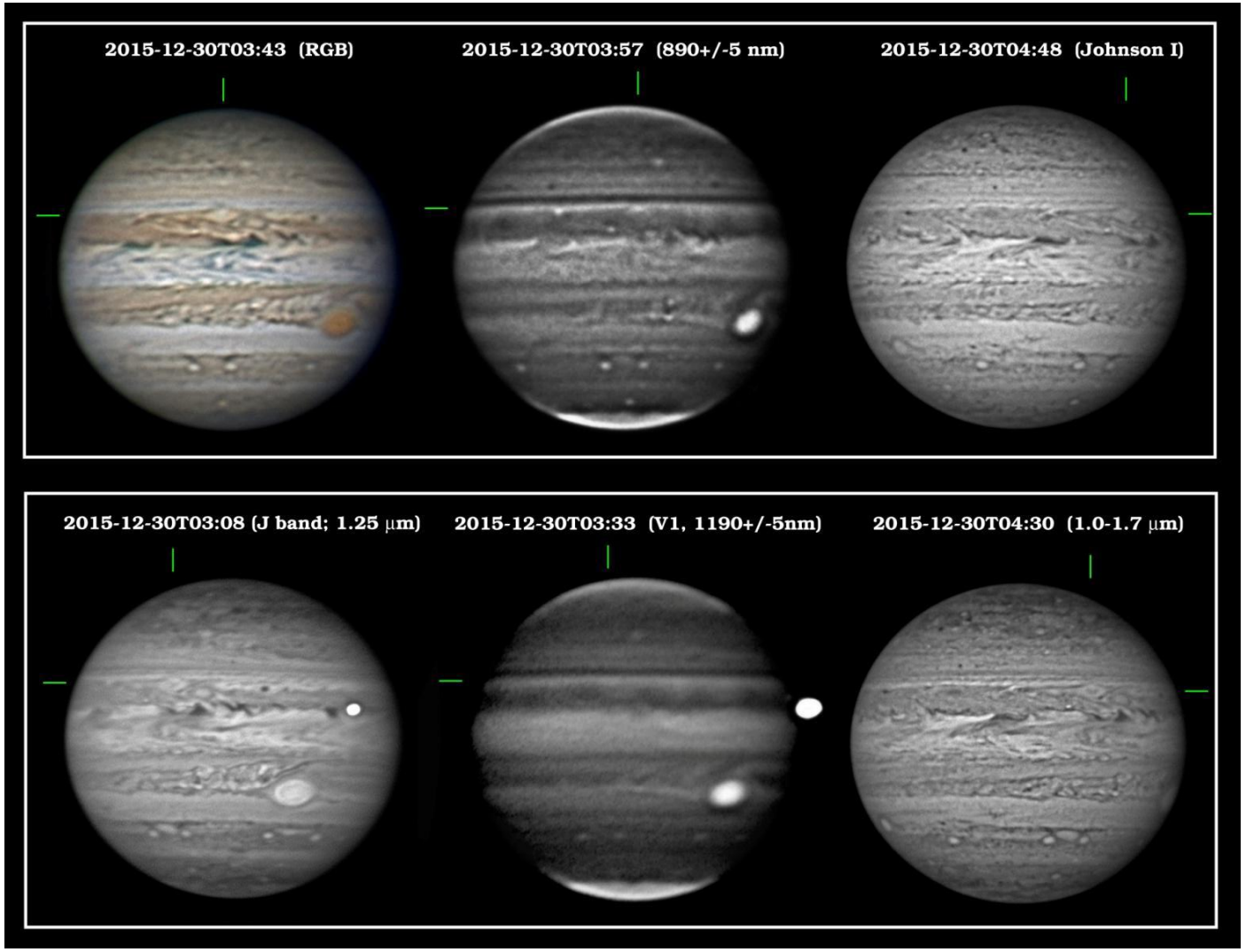

Figure 5.21. *PlanetCam* observations on December 2015 in several filters of VIS channel (upper row) and SWIR channel (lower row). Hi-pass filter processing has been performed. NTrO position is highlighted with green lines. Images in 890nm and 1160nm filters, very sensitive to methane absorption, suggests slightly higher altitude of the red ring around the vortex, not covered by high haze.

(ii) Polar regions

Figure 5.22 shows polar projections from *Planetcam* observations in March and May 2016 in methane absorption bands that are sensitive to the high altitude hazes that cover both poles. The South hemisphere is covered by a homogeneous haze layer that extends from the pole to mean planetographic latitudes -67º±0.5º and is limited by an undulating pattern with varying amplitude in latitude from 1.5 to 2.5º±0.4º. The wavenumber of this pattern is N=12 ±1 in March 2016 (the ±1 uncertainty arises from a coverage of only 320º in longitude) and N=13 in May 2016 without uncertainties from global maps. The north polar projections show similar hazes limited at different latitudes by undulating patterns. The most remarkable system is located at a mean planetographic latitude of +59º and the undulating pattern has amplitudes of 4.0º with wavenumber N=4-5. Other wave systems are visible in sectors of the North polar projection at a mean latitude of +51º, yet their wave number and phase speed cannot be quantified due to the lower contrast of the images, the superposition of different waves at different latitudes and limited latitudinal coverage.

These wave systems were reported from Voyager 1 images in 1979 (Sánchez-Lavega et al. 1998) and HST images in 1993 and 1994, with average phase speed around 2 m/s implying that the different wave systems can be explained as planetary Rossby waves. Later analyses of HST and Cassini ISS also showed very similar characteristics and small phase speeds for the different wave systems (Vincent et al., 2000; Li et al., 2006; Barrado-Izagirre et al., 2008). Our current determination of the global wave number for the south polar wave system extends these properties from 1979 to 2016 showing that it is a very stable structure surviving at least 4 Jovian years.

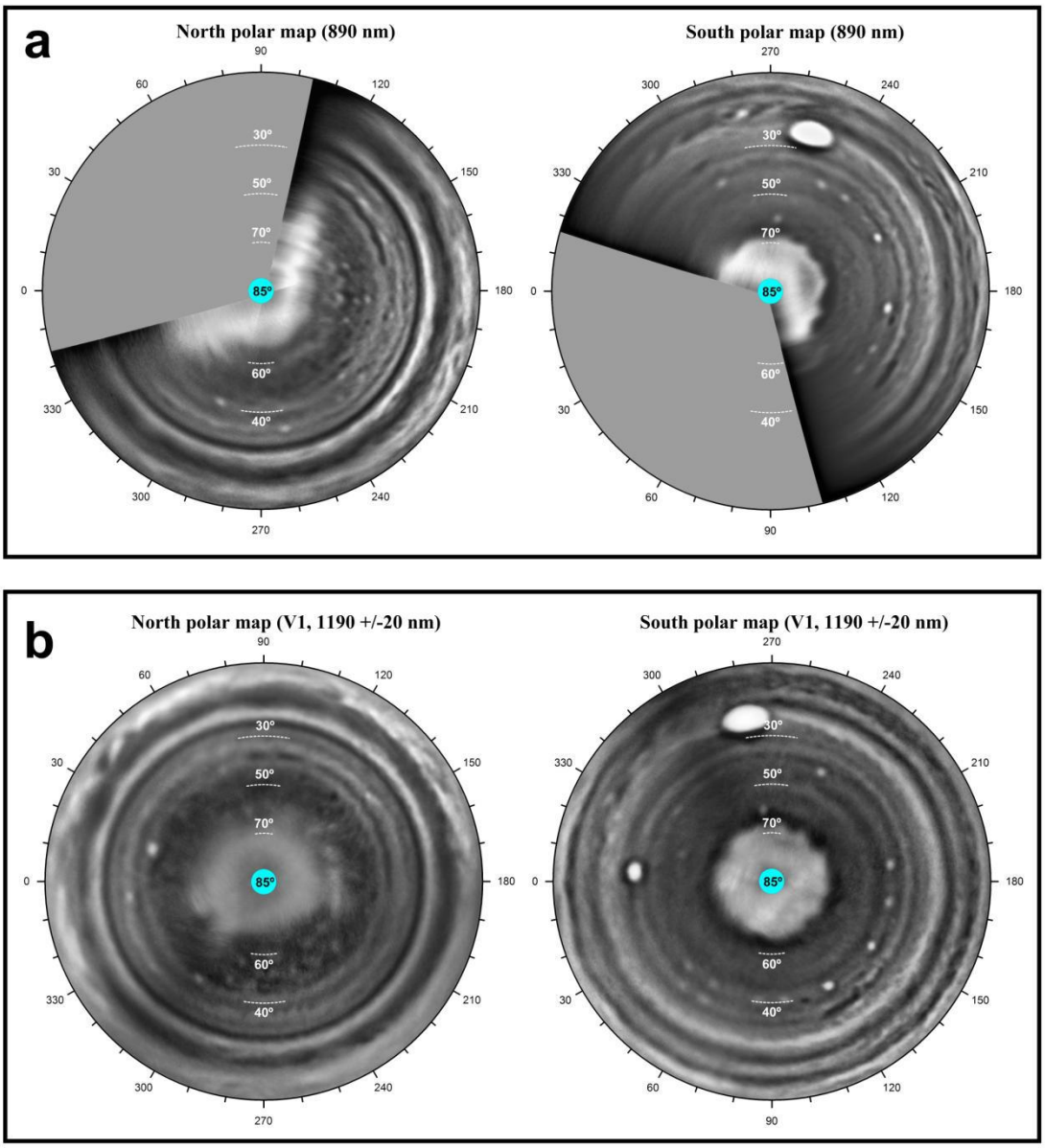

Figure 5.22. Stereographic polar projections of both poles in strong methane absorption bands. (a) March 3 and 4 2016 in 890 nm; (b) May 17 to 19 2016 in 1190 nm. Longitudes are displayed so that rotation is clockwise in the North hemisphere and anticlockwise in the South hemisphere. (Hueso et al., 2017).

PlanetCam images in narrow infrared (750±5 nm, 935±5 nm) and in wide filters in the SWIR channel (1.0-1.7 μm) probe the upper cloud and provide spatially resolved images of the upper latitudes. Figure 5.23 shows polar projections of the planet in March 2016 and July 2016. Compact features, probably small vortices, can be seen up to latitudes +73° and -76°. South polar vortices at -70° seem distributed similarly to the crests and through of the South polar wave observed in the upper hazes. The number and distribution of vortices from 60° to 73° suggests that vortices locate homogeneously

in area in the polar regions. We cannot extend this conclusion beyond 73° due to the worse image quality at higher latitudes.

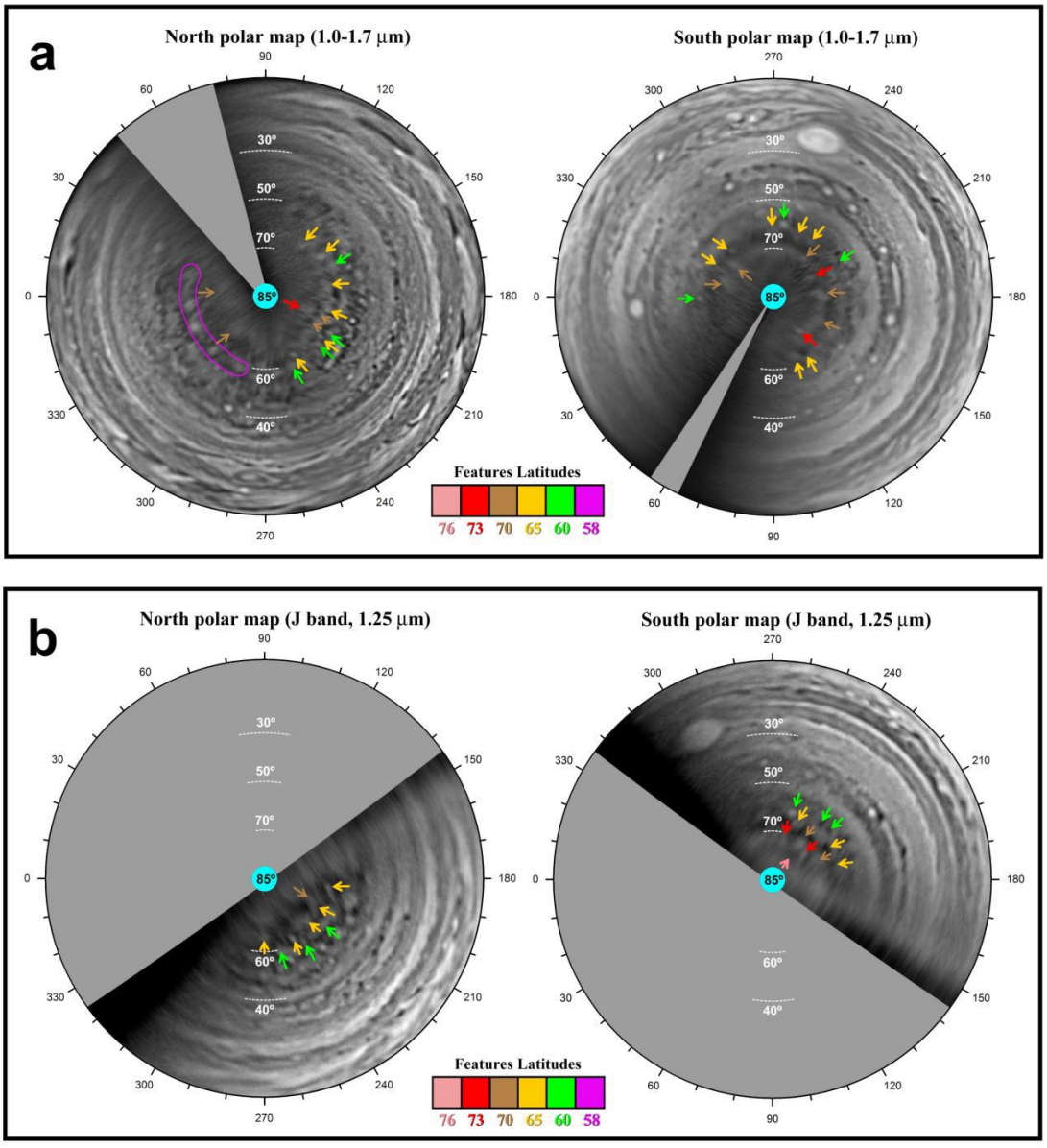

Figure 5.23. Stereographic polar projections of both poles at broad filters in long wavelengths. (a) March 3 and 4 2016 integrating light from 1.0 to 1.7 μm, a chain of vortices at latitude 58° is highlighted; (b) July 4 in band J (1.25 μm) partially sensitive to methane absorption but able to uncover part of the lower clouds. Colored arrows indicate compact features at latitudes higher than 60°, probably vortices. (Hueso et al., 2017).

(iii) Zonal winds

A global zonal wind profile has been done (Figure 5.24) selecting 26 image pairs separated in time from one to a few Jupiter rotations using amateur observations, images from *PlanetCam* dataset and from the Pic du Midi 1m telescope. Images were cylindrically projected, limb-darkened corrected and compared using image correlation algorithms. We obtained 23,820 measurements from planetographic latitudes -68.5° to 70.3°. The mean value of the standard deviation of measurements for latitude bins of 0.1° is around 7.5 m/s.

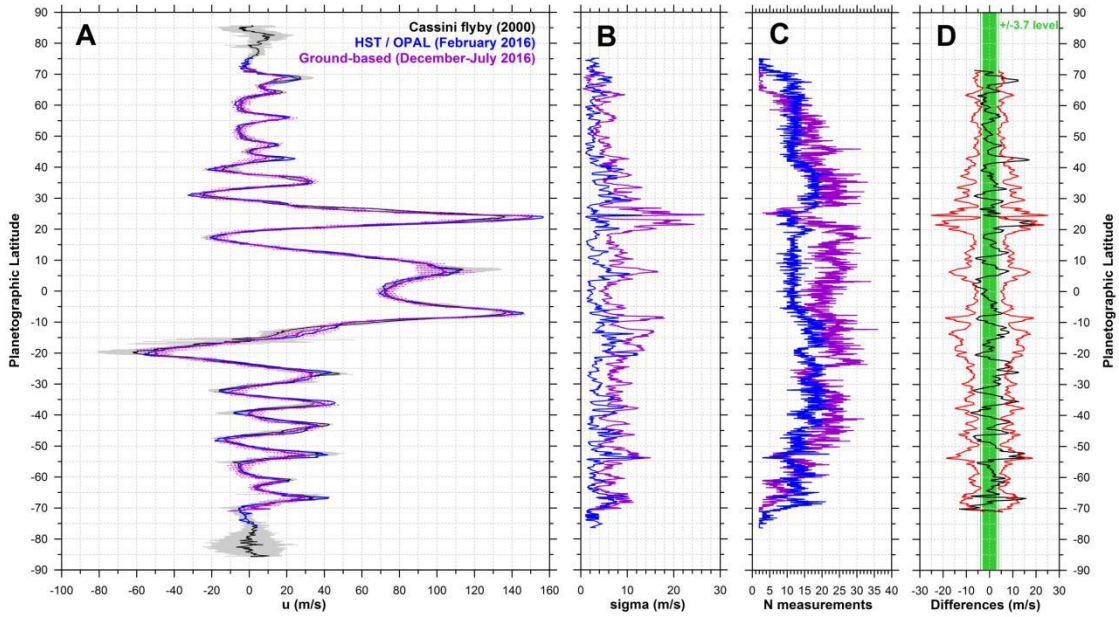

Figure 5.24. Jupiter zonal winds in 2016. (A) Zonal winds from HST images in the F631 filter (blue) compared with zonal winds from ground-based observations (magenta) together with a reference zonal wind profile from Cassini in 2000 (black with grey error bar). (B) Standard deviations of the 2016 HST (blue) and ground-based (magenta) data. (C) Number of measurements per latitudinal bin of 0.1° for both datasets (HST in blue; ground-based in magenta). (D) Differences between both 2016 profiles (black) are generally below the measurement noise level from HST of ±3.7 m/s (green). Standard deviations of the zonal wind differences are shown with red lines showing that differences are below the combined measurement noise. (Hueso et al., 2017).

From this analysis we can conclude that *Planetcam* observations of the polar regions at filters not sensitive to methane absorption provide dynamical context to the high resolution polar observations of JunoCam (Orton et al., 2017). Finally to say that our study of the evolution of the NEB dark projections over 2016 provide temporal context to JIRAM observations of the equatorial hot spots (Hueso et al., 2017).

5.5 Saturn

5.5.1 Saturn in time and wavelength

Saturn has been imaged at a variety of wavelengths with *PlanetCam*. Figure 5.25 shows some processed images from SWIR channel, while Figure 5.26 shows some image compositions mainly from VIS channel images. The main goal here is to complement Cassini ISS observations (Porco et al., 2004) in order to survey for large-scale dynamical phenomena and to study the vertical cloud structure and their long-term changes from photometrically calibrated images. SWIR images at maximum optical amplification are able to resolve most bands on the planets and details such as the north polar hexagon and polar vortex.

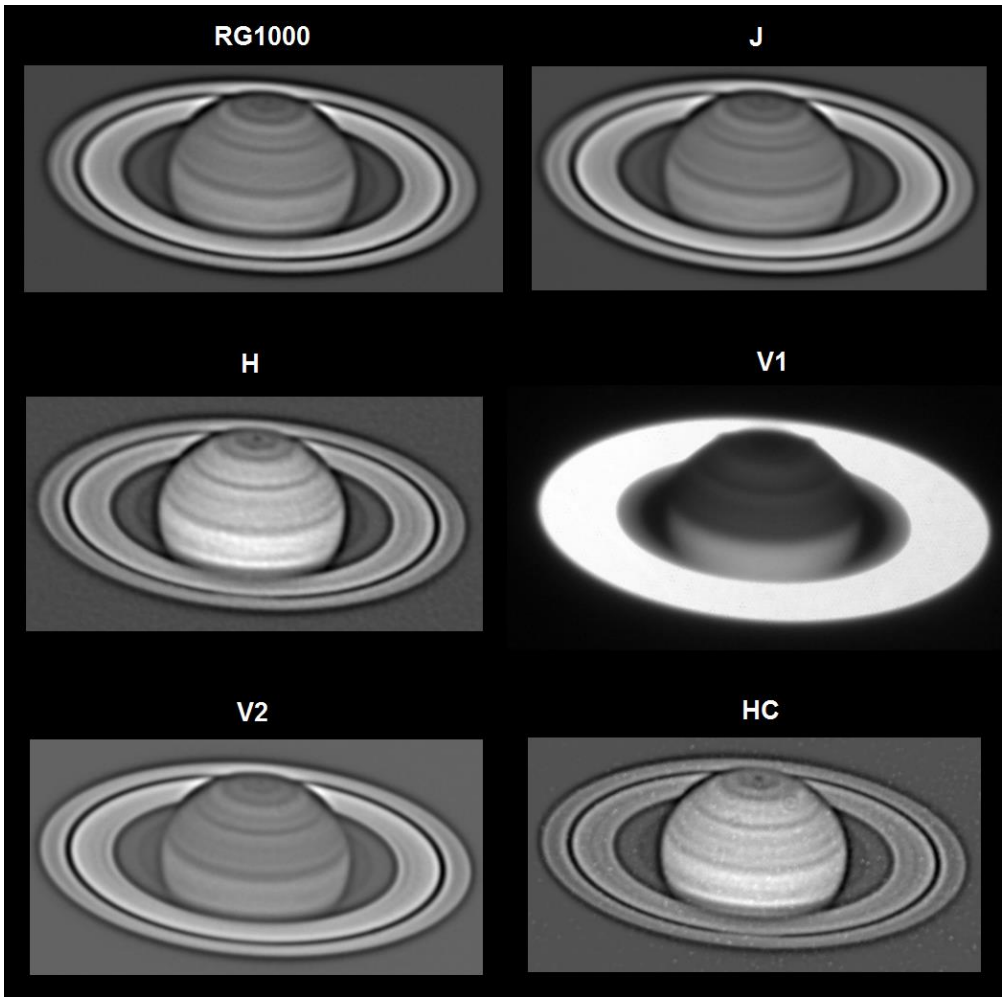

Figure 5.25. *PlanetCam2-SWIR* processed images from observations at 2.2m telescope on May 19th 2016. Wide filters RG1000, J and H allow short lucky imaging exposure times, while methane V1 filter needed up to 2s. Images were built from co-registering of the best 1% in widest filters (RG1000, J, H) to all frames in dark methane filter (V1), and further processing with high-pass filters to visualize atmospheric features.

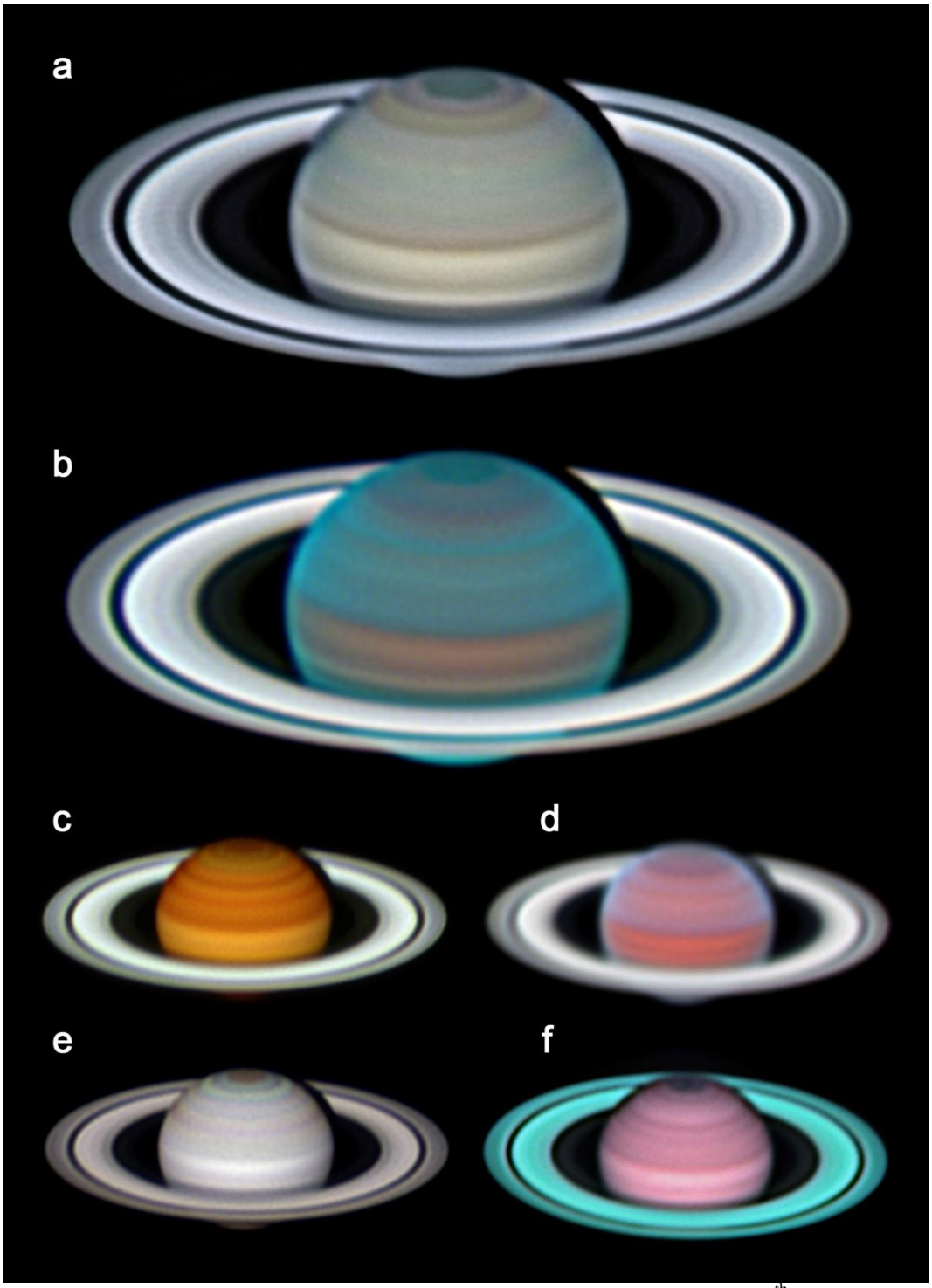

Figure 5.26. *PlanetCam1* observations of Saturn at the 2.2m on April 6th 2014 at maximum magnification (a, b) and minimum magnification on 2014-07-22 (c, d, e) compared with *PlanetCam2-SWIR* observations on May 22nd 2015 on the 2.2m telescope (f). (a) Color image from R, V, B filters sensitive to the upper clouds. (b) Color image from M2-Vio-U images sensitive to the upper hazes. (c) M1, M2, M3 color image, (d) B-Vio-U color image, (e) C1, C2, C3 color image. (f) H, J, RG1000 SWIR color image. All images have been processed from co-registering a selection of the best frames and using high-pass filters to increase the visibility of atmospheric cloud features Saturn equatorial diameter is 18.3'', on panels a and b and 18.6'' on panels c, d and e and 18.5'' on panel f. North is up and West to the left. Most observations were acquired with Saturn at an approximate elevation of 32º. Frame exposure times vary from 0.01 s to 5 s in different filters.

5.5.2 Saturn temporal changes in Absolute Reflectivity

In Figure 5.27 to Figure 5.29 we show the spectral reflectivity scans for the ring-free from projection in the northern hemisphere under the viewing geometry of the period 2013-2016. Similar considerations have to be done as described in the case of Jupiter regarding the different possible sources of the yearly averaged variations. The most remarkable differences we detect among these campaigns occur between the brightest part near the equator and the polar zones. In addition, smaller variations in some specific belts and zones can be observed.

Globally Saturn's Northern Hemisphere showed variations of its temporal reflectivity along the observing period (4-years) in particular at visual wavelengths, in agreement with previous observations (Pérez-Hoyos et al., 2006; West et al., 2009). Temporal variability at different latitudes is detected in particular in the blue filter, probably related to changes in the upper aerosol haze layers (stratospheric and tropospheric) sensitive to short wavelength absorption (Pérez-Hoyos et al., 2005, 2016). The Equatorial Zone (0° to +20°) and the polar area (+60° to +90°) are the regions where most of the reflectivity temporal variability is seen. Changes in the blue and red filters can reach up to 30% relative to the mean values. Curiously, the variability is much less pronounced in the SWIR channel, while changes around 5% can also be detected for example at the filter V2. A study of the origin of this variability will be performed and presented elsewhere.

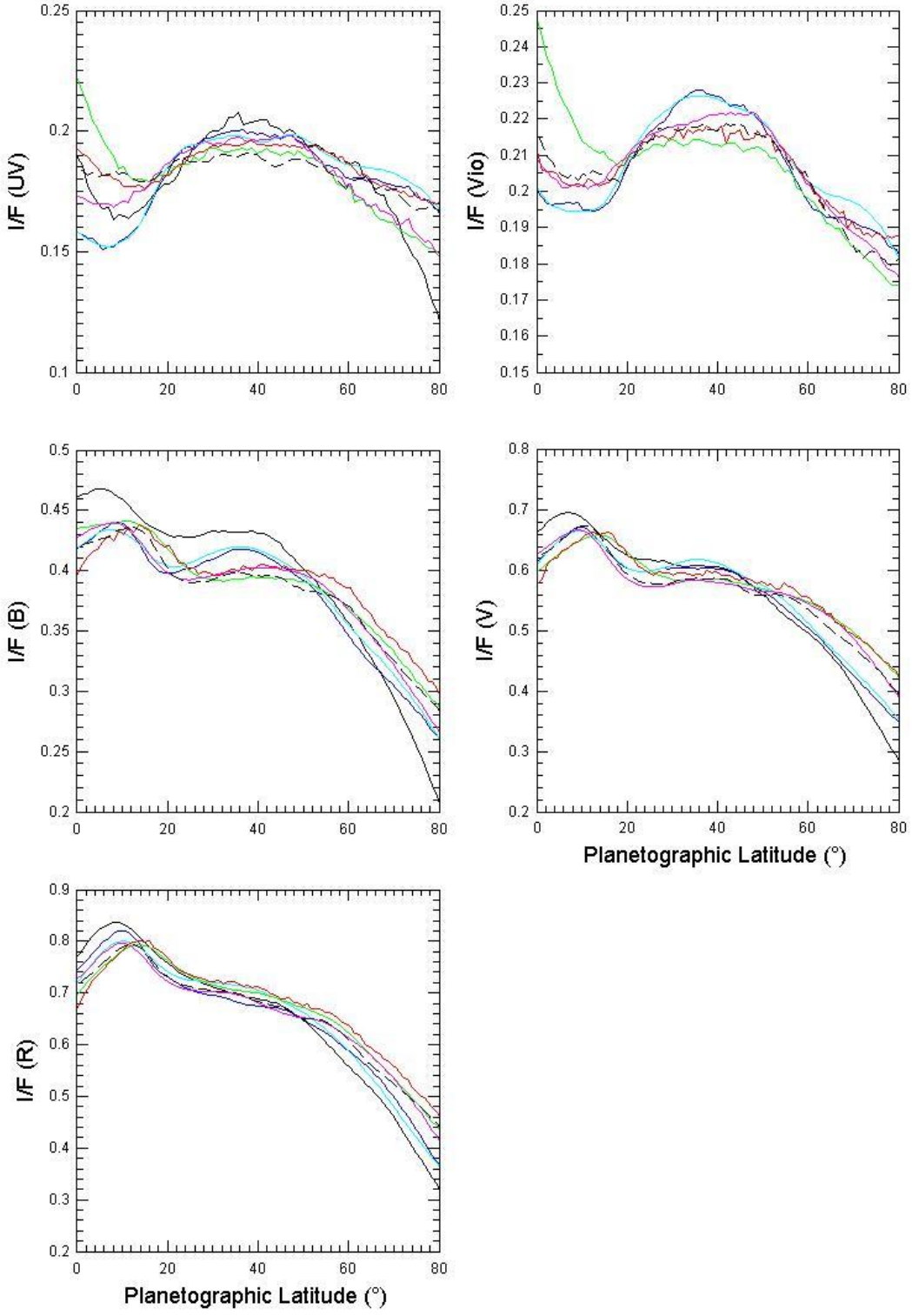

Figure 5.27. Temporal absolute reflectivity North-South scans of Saturn Northern hemisphere at selected wavelengths for the period from April 2013 to May 2016 in VIS filters U, Vio, B, V and R (black corresponds to April 2013, blue to April 2014, cyan to July 2014, green to May 2015, magenta to July 2015, red to March 2016; black dashed to May2016 and blue dashed to July 2016).

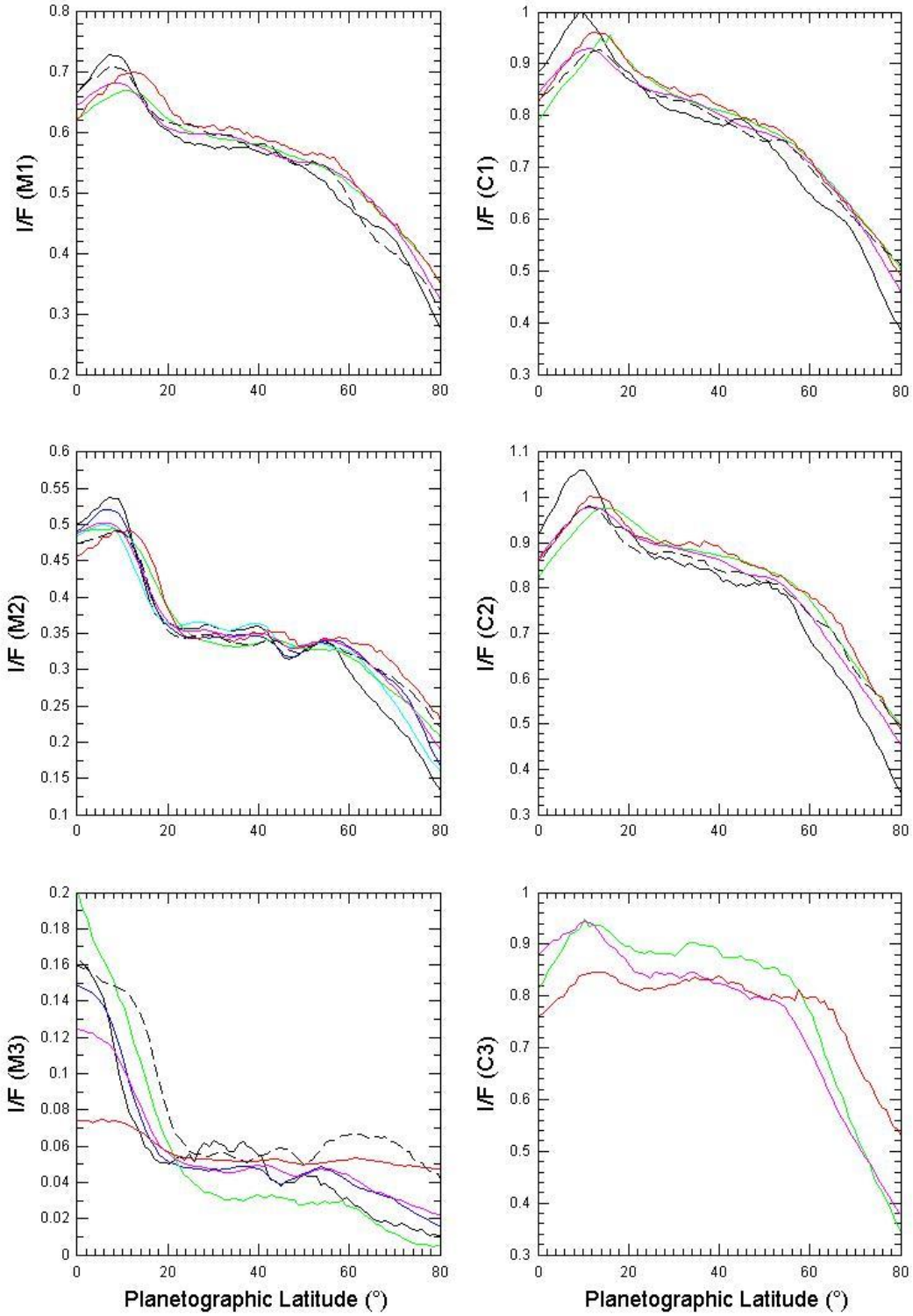

Figure 5.28. Temporal absolute reflectivity for North-South scans of Saturn Northern hemisphere at selected wavelengths for the period from April 2013 to May 2016 in VIS methane and continuum filters (black corresponds to April 2013, blue to April 2014, cyan to July 2014, green to May 2015, magenta to July 2015, red to March 2016; black dashed to May2016 and blue dashed to July 2016).

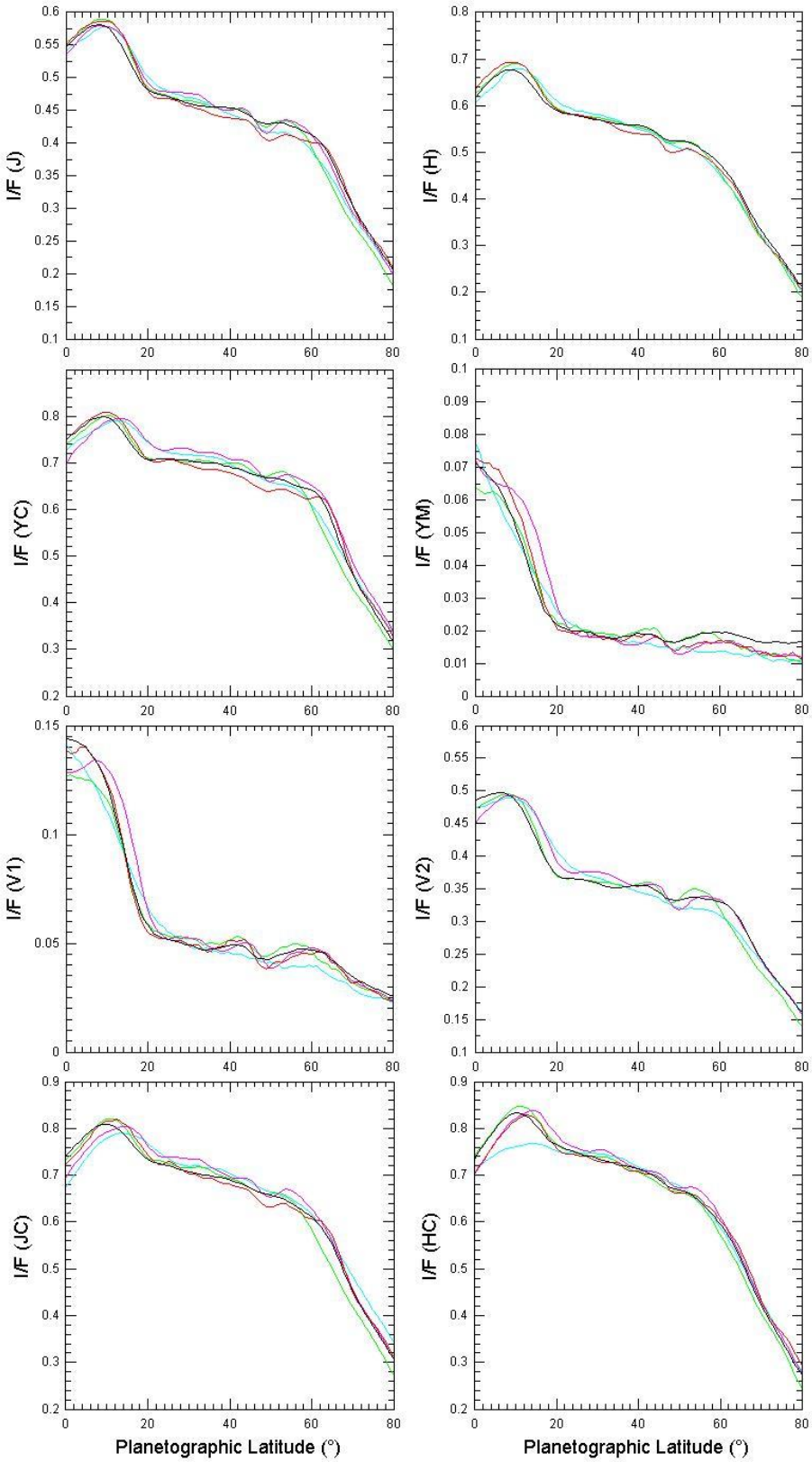

Figure 5.29. Temporal absolute reflectivity North-South scans of Saturn Northern hemisphere at selected wavelengths for the period from April 2013 to May 2016 in SWIR filters (black corresponds to April 2013, blue to April 2014, cyan to July 2014, green to May 2015, magenta to July 2015, red to March 2016; black dashed to May2016 and blue dashed to July 2016).

5.5.3 Atmospheric dynamics

PlanetCam images have also been used for several studies on Saturn atmospheric dynamics. First the motion of the polar Hexagon wave has been analyzed, and proposed to be a proxy to the undefined Saturn's rotation period. Second, Saturn's equatorial jet structure was analyzed through measurements on a rapidly moving equatorial storm.

(i) Steady motion of Saturn's hexagon

Images from Voyager 1 and 2 flybys in 1980 and 1981 showed a hexagonal feature at planetocentric latitude 75° N enclosing a strong eastward jet with peak speed of 120m/s (Godfrey, 1988). The same feature was later observed in 1990–1995 with ground-based telescopes and the Hubble Space Telescope (Sánchez-Lavega et al., 1993; Caldwell et al., 1993). The north polar region was not reobserved until 2007–2008 when Composite Infrared Spectrometer and visual and infrared mapping spectrometer instruments onboard the Cassini spacecraft revealed the hexagon in Saturn's night both in the temperature field (Fletcher et al., 2008) and in the cloud opacity at 5 μm (Baines et al., 2009).

The long-term motion of Saturn's North pole hexagon and the structure of its associated eastward jet has now been analyzed using images from Cassini, *PlanetCam* and other ground-based sources. This analysis is reported in Sánchez-Lavega et al 2014.

(ii) Equatorial jet structure

Saturn zonal wind system is similar to Jupiter's one and show few temporal changes since the first detailed measurements in 1979–1980 (Del Genio et al., 2009). One exception is Saturn's broad equatorial jet that extends from planetographic latitudes ~35N to 35 S reaching eastward peak velocities ~450–500 m/s (Sánchez-Lavega et al., 2000; Garcia-Melendo et al., 2011). The velocity field that traces the equatorial jet is much more complex than at other latitudes, showing a vertical structure and temporal variability that have been so far not well-characterized, since a key part of the measurements at different altitudes were obtained in different epochs. The Equatorial jets of Jupiter and Saturn are particularly relevant to atmospheric dynamics because of their eastward flow (contrary to the equatorial westward flows that occur in other

rapidly rotating planets, as Earth, Mars, Uranus and Neptune) and because of their intensity (Saturn Equatorial peak velocities reach ~one-third of the sound speed). The origin of Jupiter's and Saturn's jets is not well understood, and it is an open issue whether they are deep or shallow in vertical extent and if they have deep or shallow forcing sources, or a mixture of both (solar heating, internal energy and latent heat release). Distinguishing between these possibilities requires a good characterization of the energy balance in the atmosphere, a quantification of the contribution of each of the above sources to forcing, a precise determination of the wind field, and knowledge of the structure of the deep atmosphere by gravity field measurement.

We have analyzed (Sánchez-Lavega et al. 2016) the vertical structure and temporal variability of the Saturn's Equatorial jet. Using ground-based and Hubble Space Telescope (HST) images obtained in 2015 in the visual range, we were able to measure wind speeds using cloud tracking at three different altitude levels in the peak of the Equatorial jet between latitudes ~20N and 20S. The altitude of the tracers was retrieved using radiative transfer modeling, based on HST images, of the spectral and geometrical dependence of the absolute reflectivity across the equatorial zone. By combining these wind measurements and altitude determinations with those previously reported during the last three decades, we constrain the temporal variability of the jet at different altitudes from 1980 to present, encompassing more than one Saturn's year (29.5 years).

Ground-based observations of Saturn obtained during the first half of 2015 showed the presence of a remarkable white spot (WS) at red wavelengths (approx 610–950 nm) in the Equatorial Zone (planetographic latitude 6ºN). The spot was easily detected by observers using telescopes in the range of 25–40 cm in diameter contributing to the PVOL database of planetary images and with *PlanetCam* on the 2.2m telescope at Calar Alto Observatory (Figure 5.30a). Its motion, tracked from April to October, revealed a steady linear drift in longitude relative to the rotating reference frame System III with a rapid zonal velocity of u=447±1m/s (Figure 5.30b).

Our results indicate that Saturn's broad Equatorial jet, spanning from ~35N to 35S, has a central peak (from latitudes ~10N to 10S) that has an intense vertical wind shear in its upper cloud and haze layers (from the tropopause at ~0.06 bar to the upper

cloud at ~1–2 bar) and that has experienced temporal variability in the velocity of the upper cloud and haze levels.

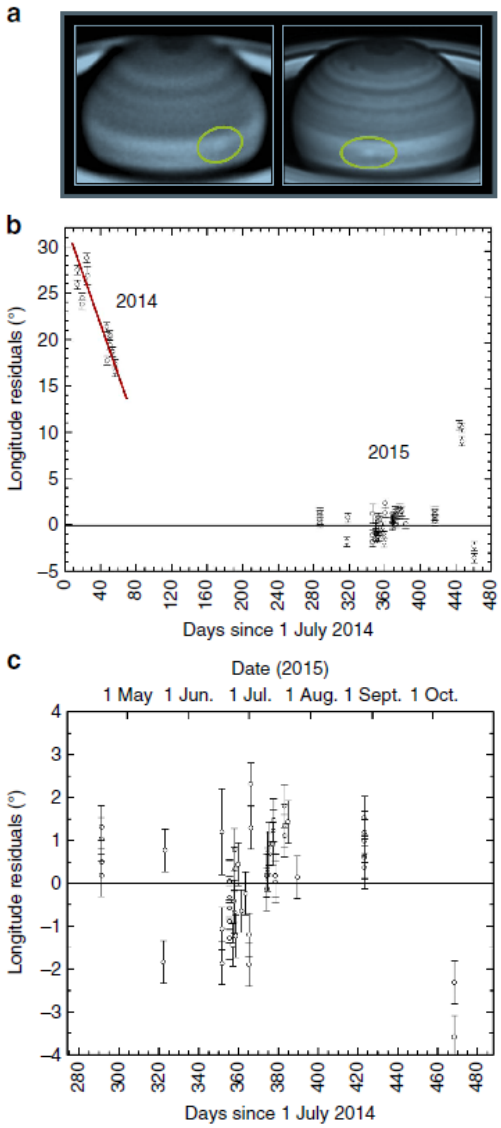

Figure 5.30. Ground-based images and motion of Saturn's white spot in 2014–2015. (a) June 21 (left, Aula EspaZio 28 cm telescope, wavelength 615–950 nm) and July 13 (right, *PlanetCam* at the 2.2m telescope Calar Alto Observatory, 750–950nm); (b) Residuals in the longitude position of spots measured relative to a reference system rotating with a period of 10 h 11 min 26.3 s (horizontal black continuous line), found from the mean zonal drift of white spot between 18 April and 12 October 2015 (-37.05 per day in System III or u=447 m/s). (c) Detail of the residuals in longitude measured in 2015. The error bar of each individual longitude measurement is given by the image resolution at the location of the spot in the disk (typically 1º). (Sánchez-Lavega et al. 2016).

5.6 Uranus and Neptune

Imaging of Uranus and Neptune in methane bands in the visible and SWIR channels is not straightforward but it allows detecting the major cloud features and tracking their motions to infer winds (Sromovsky et al., 2012; de Pater et al., 2014). Additionally calibrated images can be used to infer the cloud vertical structure in the planet and its long-term changes.

(i) Uranus

Uranus, with size around 3.6'' and apparent magnitude 5.78, was also imaged with *PlanetCam*. Figure 5.31 and Figure 5.32 show *PlanetCam1* and *PlanetCam2* images of Uranus in both channels from Calar Alto 2.2m telescope in several filters. The infrared filters RG1000, J and H shows nicely the presence of high altitude hazes surrounding the northern pole and extending up to mid-latitudes. No discrete features were captured during the different campaigns.

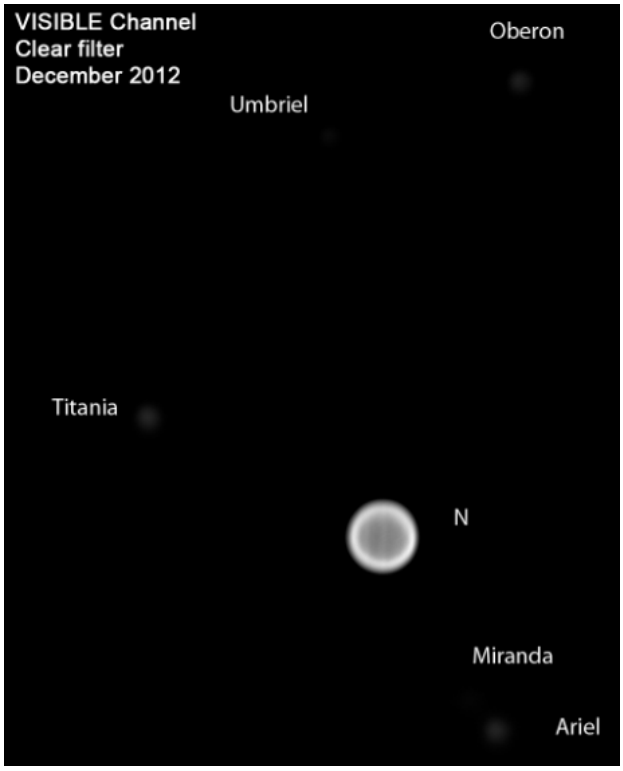

Figure 5.31. Uranus with *PlanetCam1* at Calar Alto 2.2m telescope (December 2012). Some satellites can be recognized.

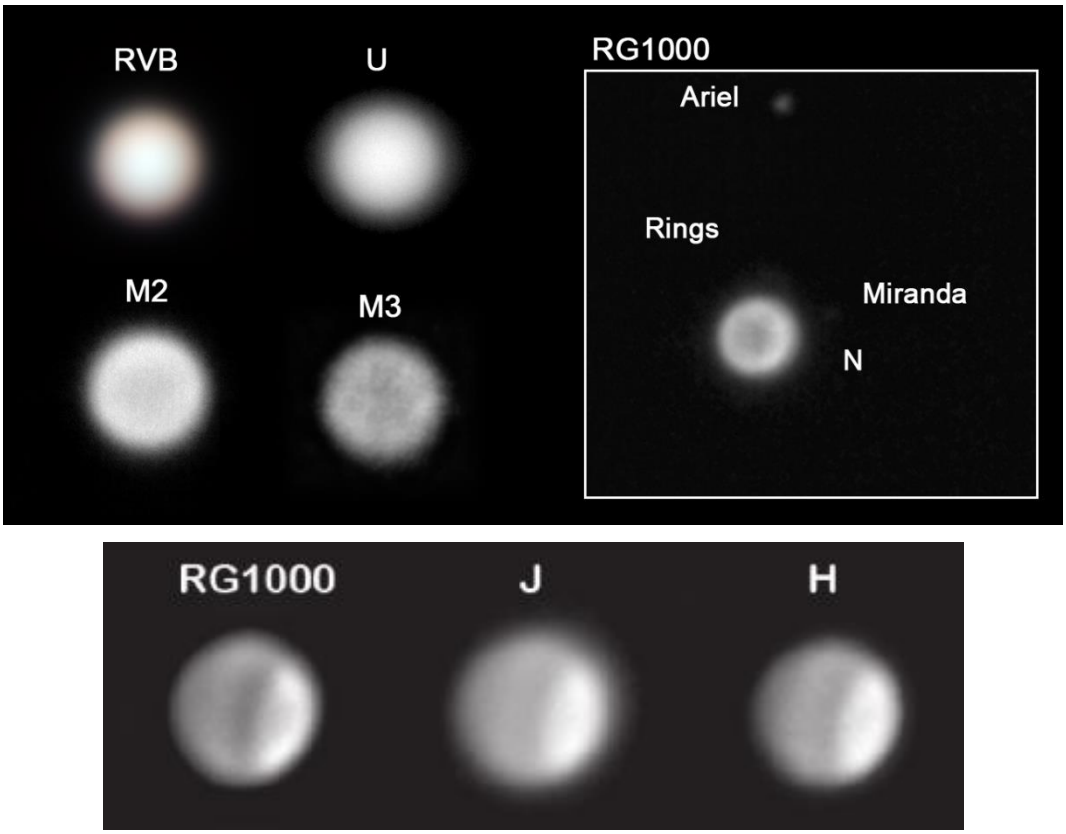

Figure 5.32. Uranus images at Calar Alto 2.2m telescope with *PlanetCam2* in December 2014 (up) with a variety of VIS filters and in RG1000 filter, frame exposure times vary from 0.2 to 2 s in the RG1000 filter and up to 120 s in the M3 filter. SWIR channel wide filters RG100, J and H clearly showing Uranus atmosphere bands in July 2015 (down).

(ii) Neptune

Neptune, with size around 2.3'' and apparent magnitude 7.8, has also been imaged, and *PlanetCam* observations of Neptune from Calar Alto in 2014-2016 have been used to analyze the size and drift rates of bright features, as well as zonal winds profiles, as reported in Hueso et al. (2017). Additional images have been used for this analysis, provided by telescopes with diameters from 28 cm (amateur size) to 10-m (Keck II telescope), including data from HST, performing a long-term tracking of the brightest atmospheric features.

Neptune shows rapidly varying cloud activity, zonal bands that change over the years, long-lived dark ovals and sporadic clouds around them. Neptune's global circulation is dominated by a broad retrograde westward equatorial jet with a peak velocity of 350 m/s that diminishes at higher latitudes until it gives way to pro-grade winds from mid-latitudes to the South Pole in a narrower eastward jet with a peak velocity of +300 m/s at -74°S (Sánchez-Lavega et al., 2017).

A bright feature was observed from January 2015 and nearly continuously from July to December 2015 in observations with telescopes in the 2-10-m class and in images from amateur astronomers. *PlanetCam* images ware taken at visible and near-infrared wavelengths on 13 and 14 July, and on October 10 with the 2.2-m telescope at Calar Alto Observatory. In July 13, 2015 a bright atmospheric feature at mid-latitudes was easily observed, called 2015-A. Figure 5.33 shows a selection of observations in those filters where the bright feature can be observed or even dominates the brightness of the planet. Observations at shorter wavelengths including blue filters, or in the visible, but at wavelengths without methane absorption bands, showed a bland planet without atmospheric features. Images in Figure 5.33 have not been processed after stacking retaining the real contrast of the features. The contrast of the bright features varied strongly in different image filters and intensified in those with methane absorption like the 890 nm strong absorption band. The contrast peaked in the J (1.25 μm) and H (1.65 μm) bands where the bright feature alone accounted for 28 and 40% of the total light coming from the planet suggesting high cloud tops.

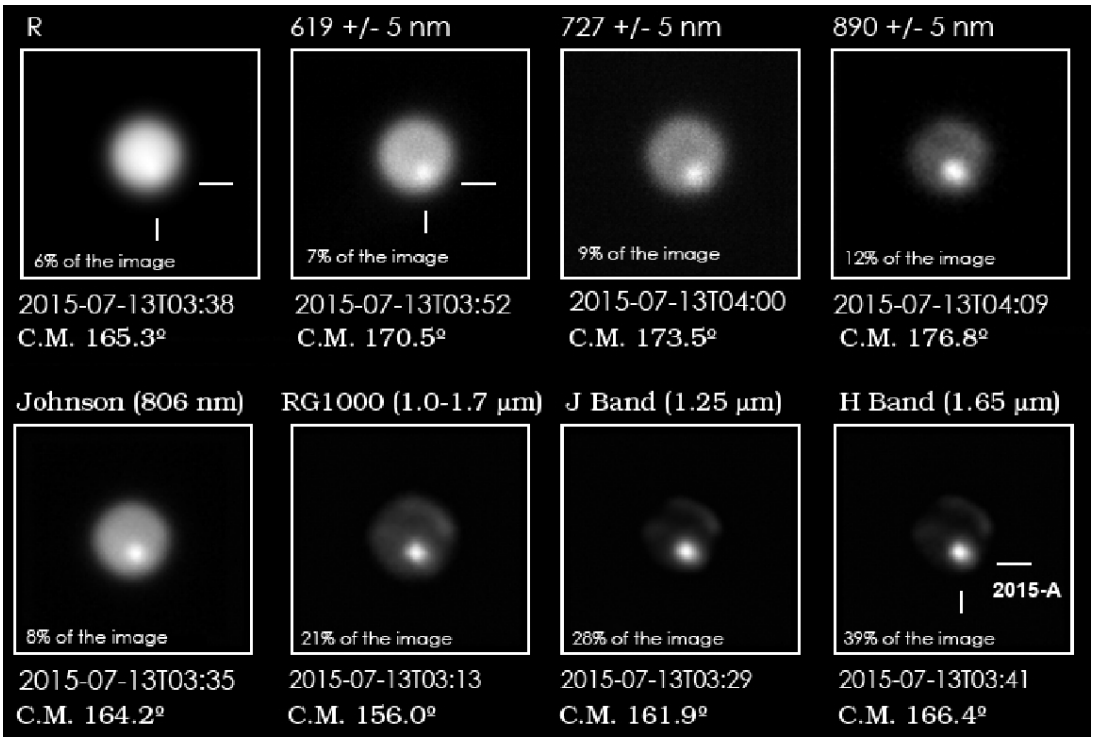

Figure 5.33. *PlanetCam2* observations of a bright feature in Neptune in 2015 from Calar Alto. Images cover the longitudinal range from 240° (West limb) to 75° (East limb) at the latitude of the bright feature. Percentages in the insets indicate the comparative brightness of the feature with respect to the full planet. The relative brightness and contrast of this atmospheric feature increased at spectral regions progressively dominated by methane absorption. North is up and West is to the left with the planet tilted. (Hueso et al., 2017).

Figure 5.34 shows the other side of the planet observed the following night. While several other atmospheric features are observed, their relative contrast with the rest of the planet is lower in all cases than in the bright feature observed the previous day at comparable wavelengths. Besides the regular structure of the South mid-latitudes belt, a North tropical bright feature and a South polar cloud are observable in this side of the planet.

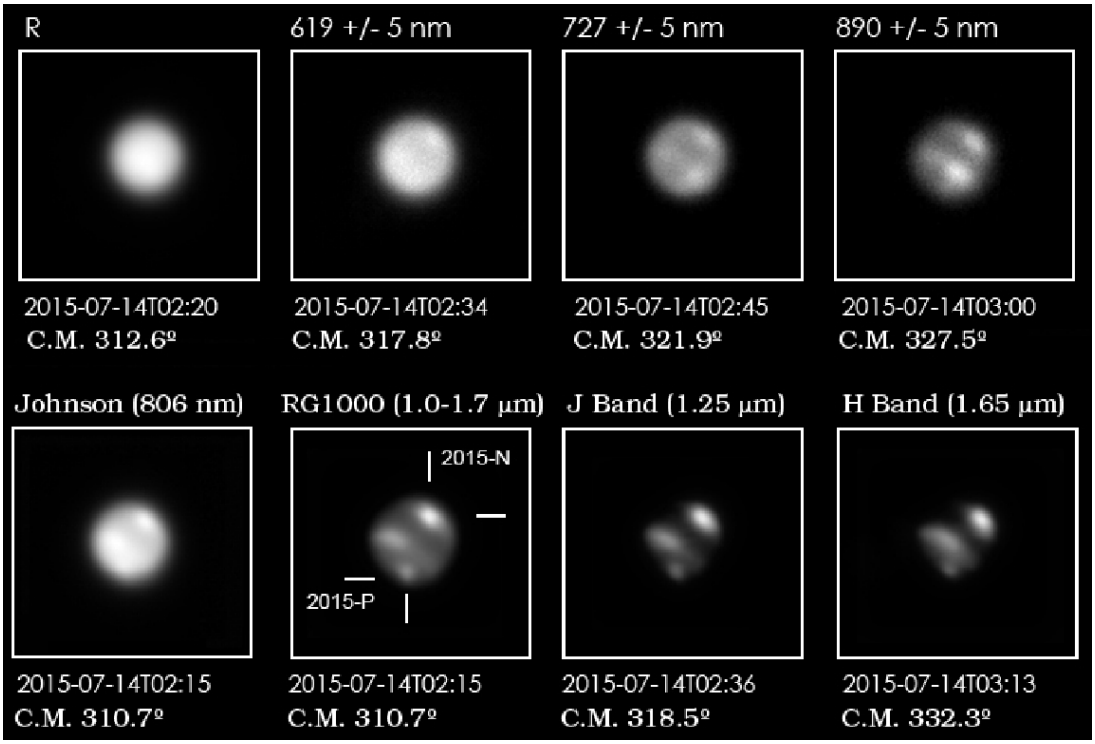

Figure 5.34. *PlanetCam2* observations of Neptune in 2015 from Calar Alto. These observations were acquired one day after those in Figure 5 showing the other side of the planet. Images cover the longitudinal range from 45° (West limb) to 230° (East limb) at the latitude of the bright feature. Atmospheric features, especially in the South mid-latitudes belt of clouds, have significantly less contrast than the bright feature observed the previous night. Other observations in nearby wavelengths and short wavelengths without methane absorption failed to show any atmospheric feature in the planet. Orientation is like in Figure 5.33. Features also visible in later observations in the North (2015-N) and South (2015-P) hemispheres are labeled in one of the panels. (Hueso et al., 2017).

Calar Alto, Keck, and HST observations show that a single bright feature was present in Neptune's mid southern latitudes from July to September 2015. Using data from July to November from large telescopes together with a selection of outstanding amateur images in November 2015 allows to obtain an unambiguous fit to the data with a westward drift rate of 24.48±0.03°/day for the spot 2015-A bright feature (Figure 5.35 up), or -94 ± 3 m/s, which is about 30 m/s slower than the zonal winds measured at the

time of the Voyager 2 flyby. The fit is unique due to the high number of observations and short time difference between many of them and the small error in the drift rate comes from the long time span of the observations (153 days). The planetographic latitude of the feature from the ensemble of measurements gives a value of -40.1±1.6° (Figure 5.35 down).

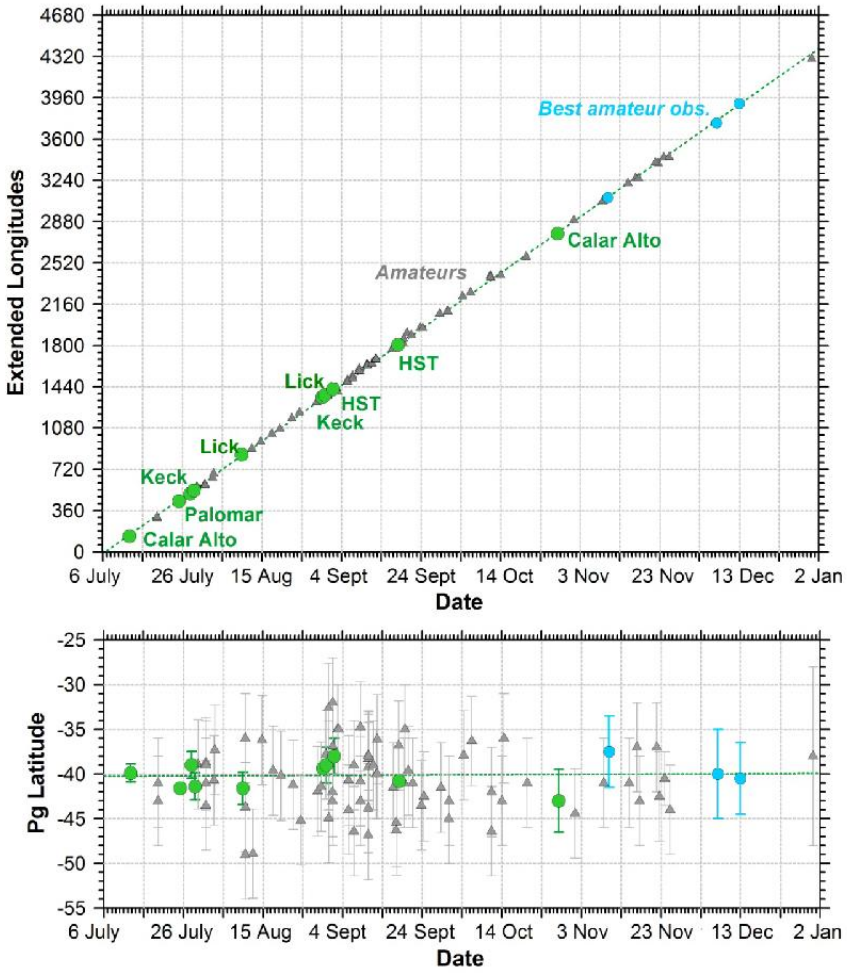

Figure 5.35. Global tracking of spot 2015-A. Up: Longitudes of all bright features as a function of time. Extended longitudes are shown correcting for the number of feature rotations around the planet. Measurements from large telescopes are marked as large green circles and amateur observations are showed with triangles. Amateur observations of outstanding quality selected after the last observations with large telescopes are shown with blue circles and are also used for the longitude time fit. Down: Planetographic latitudes of the centroid of the bright feature. (Hueso et al., 2016).

5.7 Other Objects

The asteroids Ceres and Vesta, the Galilean satellites, and the satellite Titan are small objects but with a measureable size at high resolution accessible to *PlanetCam*. As an example in Figure 5.36 we show an image of asteroid Ceres obtained with *PlanetCam1* at CAHA 2.2m using the maximum amplification where its disk of 0.8" can be measured. We also show an image of Jupiter's satellite Ganymede (1.65" in diameter) taken with *PlanetCam1* at the 1.5 m TCS telescope at Teide Observatory. Several surface details can be distinguished that correspond well with those predicted from known surface maps of the satellite. The lowest resolved details have a size of 0.2-0.3 arcsec.

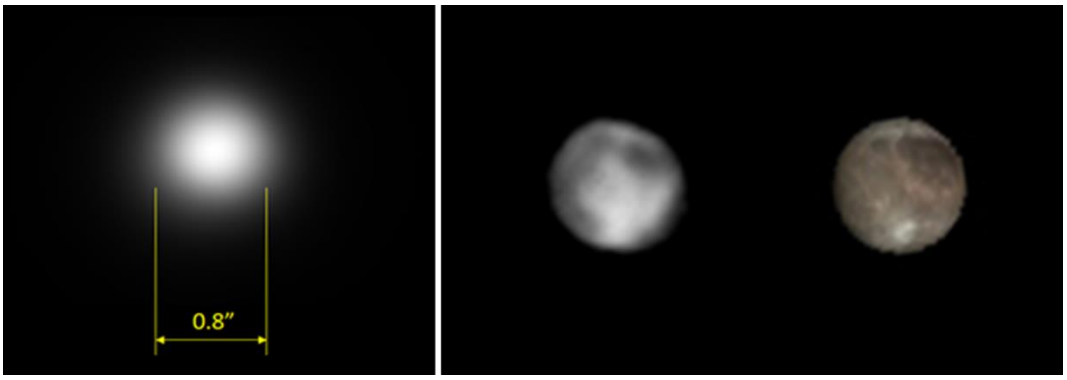

Figure 5.36. Left: The disk of the asteroid Ceres with *PlanetCam1* at the CAHA 2.2m telescope and maximum amplification (barlow x4) obtained on April 5th 2014. Analysis of 1000 frames with exposure times of 0.1 s. Right: PlanetCam1 observation of Ganymede acquired with the TCS 1.5m telescope on January 17th 2013 at 20:56 UT at high amplification (barlow x2). The image has been processed with Lucy-Richardson deconvolution over a stacking of the best 1% frames from a 300 frames sequence with individual exposure times 0.01 s. Details in Ganymede are compared with the expected details in the surface simulated with the WinJupos software. Ganymede disk is 1.65'' with an apparent magnitude of 4.81 and the observation was run at an elevation angle of 78º. North is up and West to the left. Surface features on Ganymede with a size of 0.15 arcsec can be resolved.

PlanetCam can also be used in studies of other astronomical objects outside the Solar System. We present the results of two astronomical events that require careful temporal resolution. Figure 5.37 shows a transiting curve for the extrasolar planet WASP 43b in the I band, an ultra-short period (0.81347753 days, Gillon et al., 2012) hot Jupiter orbiting the K7 dwarf star GSC 05490-00141 (Hellier et al, 2011). The host star is a quite red object with a V magnitude of 12.4 and a (V-I) = 1.3 mag. The exoplanet transit has a depth of ~ 0.03 and lasted ~70 minutes at optical wavelengths.

The data shown in Figure 5.37 were obtained for a transit on December 12, 2013, for 60-second individual exposures obtained with PlanetCam1 attached to the 1.23 m telescope at Calar Alto Observatory. Average scatter is ~2 mmag, showing that under photometric conditions it is possible to reach high precision data.

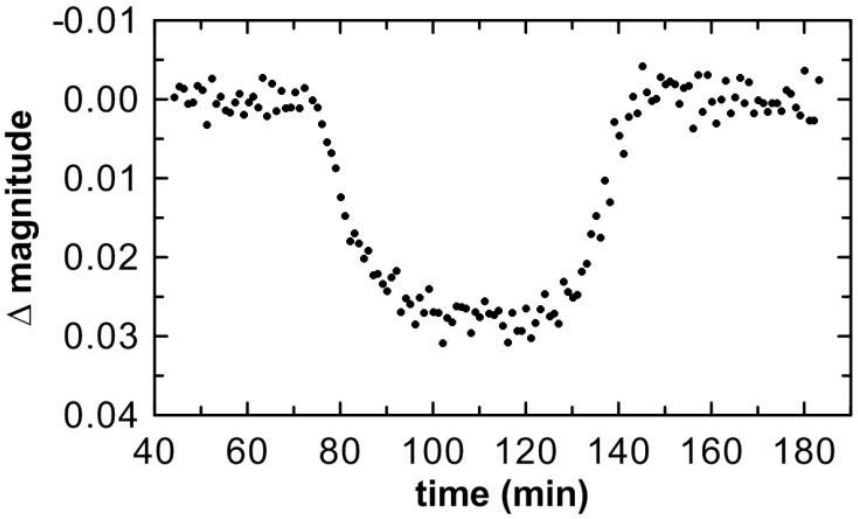

Figure 5.37. WASP-43b transit in the I band captured with *PlanetCam1* attached to the 1.23m telescope at Calar Alto Observatory. Instrumental non-standard magnitudes are given for an arbitrary zero magnitude reference point. Light-curve trend is mostly due to air mass variation between 1.56 and 1.51. Photometric data was extracted using a synthetic aperture procedure.

The second event is the detection and photometric measurements of a Gamma Ray Burst (GRB) event that was observed about one hour after its discovery. The object was GRB 130418A (Gorosabel et al., 2013) and we performed photometry in I band of its optical afterglow using *PlanetCam1* at the 1.23 m CAHA telescope (Figure 5.38). We show the light curve evolution until de GRB reached a limit magnitude $I \sim 17.5$,it must be noted that, due to its rapid response, PlanetCam operating at the 1.23m telescope provided the first photometric data for this event, which is an essential piece of information to characterize the afterglow of the Gamma Ray Bursts.

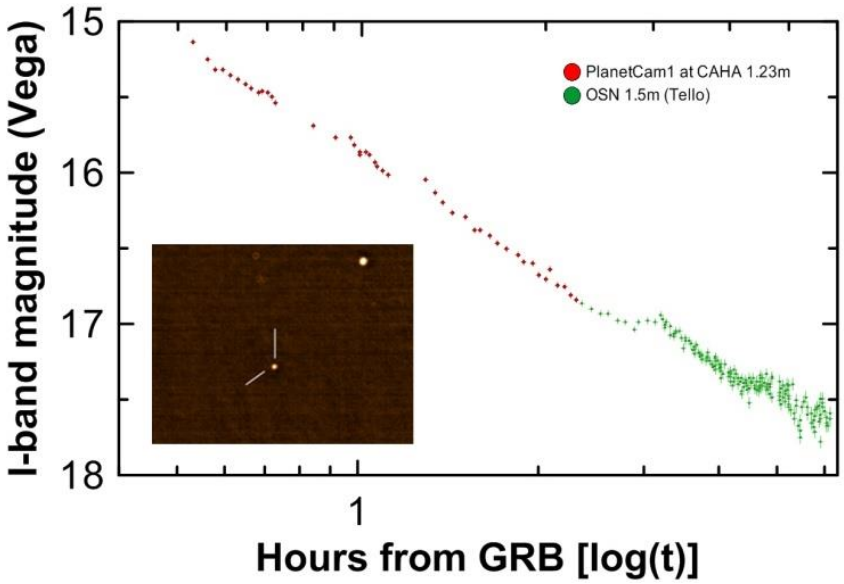

Figure 5.38. Photometric curve of Gamma Ray Burst GRB 130418A in I band detected with *PlanetCam1* at 1.23m CAHA telescope with a total exposure time of 2145.25s (left) and from Tello et al. (2013) at the 1.5m telescope at the Observatory of Sierra Nevada (right), showing a good agreement between both instruments. The inset shows an image of the object.

Chapter 6

CONCLUSIONS AND FUTURE PROSPECTS

6.1 Conclusions

PlanetCam is a relatively simple and low cost astronomical camera for simultaneous imaging of Solar System objects at high spatial resolution in the Visible and SWIR spectral ranges (0.38 – 1.7 μm) based on the lucky imaging technique, and including filters selected for their interest in planetary studies. The instrument is currently fully operative and works in two different configurations, *PlanetCam1* Visible channel camera that can be mounted in several telescopes, and the dual channel Visible and SWIR camera *PlanetCam2*, which is now currently at Calar Alto Observatory. In addition, a specific on purpose pipeline is available for *PlanetCam* image processing. While *PlanetCam* detectors are based on current technology that provides the best combination for the relevant parameters required, it has been designed in a way that allows an easy substitution of the detector as soon as new technology becomes available. This modular design has been thoroughly described in Chapters 1 and 2 of this Thesis and published in Mendikoa et al. 2016 and Sanchez-Lavega et al. 2012.

Regarding *PlanetCam* characterization and calibration, the main conclusions can be summarized as follows:

- *PlanetCam* radiometric performance has been characterized in laboratory and its astronomic performance tested at several telescopes, in particular 1.23m and 2.2m telescopes at Calar Alto observatory. Radiometric performance characterization included the linearity of both detectors together with the

quantum efficiency response of the visible channel detector, not provided by the manufacturer below 400nm, as well as image uniformity and stability. Astronomic performance characterization included an estimation of resolution achievable for contrasted features of around 0.3" and identification of limiting magnitudes for different configurations. This characterization of the instrument has been presented in Chapters 3 and 4 and in Mendikoa et al. (2016).

- Absolute photometric calibration of *PlanetCam* has been performed with images of Jupiter and Saturn. In addition, spatially resolved absolute reflectivity values of Jupiter and Saturn are provided over four years of observation campaigns and in a wide wavelength range at specific filters of planetary interest for the study of the cloud structures of both planets from the ultraviolet to short near infrared wavelengths. Spatial resolution of these photometric images, with no further processing, reaches values of up to 0.5", with typical values of around 1". From all this work, *PlanetCam* is providing a long baseline of absolutely calibrated observations of Jupiter and Saturn with at least 2-3 observation campaigns each year, having been determined using a wide range of standard stars. Although the precision of these measurements depends on wavelength, it was found that a precision of the order of 10-20% can be achieved in the determination of *I/F* values, having also been done an analysis of the main uncertainty sources, as shown in Chapter 4 and in Mendikoa et al. (2017).
- The photometric calibration has been validated through a comparison with published data available in the literature. Photometrically calibrated images or albedo values of giant planets are scarce in the scientific literature and the capability to determine the absolute reflectivity of Jupiter and Saturn in different years can contribute with relevant data to this field. Minnaert coefficients, useful to characterize the reflectivity of giant planets' atmospheres under different viewing angles, have also been estimated for Jupiter and Saturn, which can also be of interest for the study of starlight reflection on exoplanetary atmospheres as well.

The instrument has been successfully used in different telescopes including *Calar Alto* 1.23m and 2.2m telescopes, 1m planetary dedicated telescope at *Pic du Midi* Observatory, and at the 1.5 m TCS telescope at *Teide Observatory*, and has proven to be suitable not only for Solar System planetary atmosphere studies but also for other Solar system targets, as summarized in the following paragraphs:

- Imaging *Venus* at high resolution in the *PlanetCam* VIS and SWIR spectral ranges allows scientific research on the atmosphere and surface of the planet. In particular, the cloud structure and atmospheric dynamics in Venus day side can be studied using UV and 890-980 nm VIS filters as well as the SWIR filters in the CO_2 band and adjacent continuums, while the night side can also be observed in the SWIR range for surface and lower atmospheric phenomena analysis. Venus images obtained with *PlanetCam* at CAHA 2.2m telescope in December 2015 provided valuable information about the status of Venus clouds and waves just before the Akatsuki mission (Sánchez-Lavega et al. 2016).
- Regarding *Mars*, *PlanetCam* observations are able to support different research areas, determining the absolute reflectivity of the clouds looking for the spectral differences between H_2O-, CO_2-ice clouds, and dust. The behavior of clouds at SWIR spectral range, where no ground-based observations are usually performed, can also be studied. The presence of high-altitude plumes at the limb of the planet can also be investigated as well as different kind of features we see on our planet images. We plan to use *PlanetCam* in forthcoming oppositions to support the regular observations performed with the Visual Monitoring Camera (VMC) onboard Mars Express under ESA support on which our team is involved.
- As for Giants planets, absolute reflectivity North-South scans along the central meridian of Jupiter and Saturn for each spectral filter show temporal changes in the upper aerosol haze layers along the period studied (2012-2016), some of which have been identified and discussed. Relative changes in reflectivity were detected and estimated in around 5-10% when assuming the invariability of the geometric albedo of the planet at a given wavelength.
- The high spatial resolution provided by the lucky-imaging method allows follow the spectrally dependent reflectivity changes in belts and zones, but

also in specific features like the Great Red Spot, ovals and other cyclones, anticyclones and storms in Jupiter and Saturn.

- The main specific research areas for *Jupiter* where *PlanetCam* can make significant contributions are to study the variability of zonal wind profiles, vertical distribution of the upper clouds and hazes, and the study of the Jupiter meteorology where major planetary-scale changes that affect some bands of the planet can be tracked.

    - It was performed a preliminary analysis of photometrically calibrated *PlanetCam* images obtained before the NTBD outbreak on May 19th 2016 using nine filters from the UV to three near-infrared methane absorption bands and their adjacent continuums. For the analysis of these *PlanetCam* images radiative transfer model was done in order to analyze the atmosphere vertical structure. In addition, four Jupiter observing campaigns were performed with *PlanetCam* from December 2015 to July 2016, including images from July 4, about 7 hours before Juno's orbit insertion. These images show a constant size of the Great Red Spot within an uncertainty of 0.2° implying that its diminishing size over the last decades may have reached a stable configuration. Polar projections of the images of March 2016 and July 2016 show compact features, probably small vortices, up to latitudes +73° and -76°. The number and distribution of vortices from 60° to 73° suggests that vortices locate homogeneously in the polar regions. From this analysis we conclude that *PlanetCam* observations of the polar regions at filters not sensitive to methane absorption provide dynamical context to the high resolution polar observations of JunoCam (Sánchez-Lavega et al. 2017).

    - A global Jupiter zonal wind profile was also done based on images from *PlanetCam* among others, with measurements from planetographic latitudes -68.5° to 70.3°. The mean value of the standard deviation of measurements for latitude bins of 0.1° was found to be around 7.5 m/s, which is an excellent indication of the typical uncertainty that is possible to attain using *PlanetCam* for future studies (Hueso et al. 2017).

- Based on *PlanetCam* images we are also able to retrieve information from *Saturn*'s atmospheric levels located from the stratosphere at a few mili-bar down to the upper troposphere at roughly 1-2 bar level where the cloud deck is expected. In the case of Saturn, the detection of atmospheric activity in 2015, in the form of compact spots under rapid motions in the Equatorial Zone is a point of high interest that needs to be surveyed complementing the view from Cassini spacecraft at low phase angles. Convective storm activity in some periods and major atmospheric disturbances are also a key point for *PlanetCam* studies. Our observations, coupled to those from Cassini, allow determine the short and long term behavior of clouds and aerosols and the changing solar heat deposition and its influence on upper troposphere and stratosphere dynamics under the seasonal ring shadowing and polar nights at Equator and polar regions. *PlanetCam* images have been used for several studies on Saturn atmospheric dynamics. First, the motion of the polar Hexagon wave has been analyzed and proposed to be a proxy to the undefined Saturn's rotation period (Sánchez-Lavega et al 2014). Second, Saturn's equatorial jet structure was analyzed through measurements on a rapidly moving equatorial storm (Sánchez-Lavega et al 2016). Ground-based observations of Saturn obtained during the first half of 2015 showed the presence of a remarkable white spot (WS) at red wavelengths in the Equatorial Zone. The spot was easily detected with *PlanetCam* on the 2.2m telescope at Calar Alto Observatory. Our results indicated that Saturn's broad Equatorial jet, spanning from ~35N to 35S, has a central peak from latitudes ~10N to 10S that has an intense vertical wind shear in its upper cloud and haze layers, from the tropopause at ~ 0.06 bar to the upper cloud at ~ 1–2 bar, and that has experienced temporal variability in the velocity of the upper cloud and haze levels.

- *Uranus* was also imaged by *PlanetCam*, and in particular the infrared filters RG1000, J and H show the presence of high altitude hazes surrounding the northern pole and extending up to mid-latitudes. This demonstrated the capability of *PlanetCam* to work with the icy giants, although no systematic study of this planet has been performed yet.

- *Neptune* images by *PlanetCam* also contributed to the search for spot activity, photometry and spot tracking for wind measurements allowing characterize the long-term meteorology of the planet. Images from Calar Alto in 2014-2016 were used to analyze the size and drift rates of bright features, as well as zonal winds profiles. In July 2015 a bright atmospheric feature at mid-latitudes was easily observed with *PlanetCam* and these images, among others from different observatories, allowed obtain a fit to the data with a westward drift rate of 24.48±0.03°/day for this spot bright feature, or -94 ± 3 m/s, which is about 30 m/s slower than the zonal winds measured at the time of the Voyager 2 flyby. The planetographic latitude of the feature from the ensemble of measurements provided a value estimation of -40.1±1.6° (Hueso et al. 2017).
- Finally, *PlanetCam* has also been used to the study of other astronomical objects outside the Solar System (Mendikoa et al. 2016). A transiting curve for the *extrasolar* planet WASP 43b, an ultra-short period hot Jupiter orbiting the K7 dwarf star GSC 05490-00141, was obtained in December 2013. This exoplanet transit has a depth of ~ 0.03 magnitudes and lasted ~70 minutes at optical wavelengths, and average scatter was found to be ~2 mmag, showing that under photometric conditions we can reach high precision data. In addition, the detection and photometric measurements of the afterglow *Gamma Ray Burst GRB 130418A* event was observed about one hour after its discovery. Its light curve evolution was obtained until the GRB reached a limit magnitude $I \sim 17.5$. Due to its rapid response *PlanetCam* provided the first photometric data for this event. These are exploratory ideas that provide other scenarios for the use of the instrument. So far we have collaborated under request from other teams interested in high spatial resolution at high temporal rates. Although not presented in this Thesis, we have also explored the observation of bright galactic nuclei, debris disks among young stars and structure of cometary nucleus and coma.

6.2 Future Prospects

Some of the results here presented will be further analyzed in future works in terms of a radiation transfer model in order to retrieve information related to the vertical structure of Jupiter's and Saturn's cloud systems. In particular, a detailed study of the photometry of *PlanetCam* images before the Juno orbital insertion and the subsequent radiative transfer modeling will be completed in the near future.

In general, the reflectivity data obtained from *PlanetCam* can be used to perform radiative transfer models in order to assess the capability of this kind of observations to characterize the optical properties of the aerosols (clouds and dust), their density (optical depth) and size. Currently these analyses aim to support studies with VMC camera onboard Mars Express in which the *Grupo de Ciencias Planetarias* (GCP) team is directly involved. In addition, this kind of analysis will be employed in the future to support with ground-based observations the meteorological and dust measurements to be performed in 2021 by instruments RMD (onboard rover Exomars2020, ESA) and MEDA (onboard rover Mars2020, NASA), both missions participated by the GCP team as well.

On the other hand, ground-based observations with *PlanetCam*, with high-resolution imaging using Lucky Imaging from the near-UV to H-band, is also expected to support scientific missions like NASA's Juno, in orbit around the planet since July, 2016. Juno has limited imaging capabilities and thus relies on ground-based observations in order to provide context information for its instruments. The capabilities of *PlanetCam* at short wave infrared wavelengths will fill a gap in the expected follow-up from ground-based observatories, as already demonstrated with our publications.

Our database of planetary calibrated images is expected to be enlarged with additional observations in the future. We expect that these observations will continue to support space mission such as Akatsuki at Venus, Mars Reconnaissance Orbiter, Mars Express and Exomars at Mars as already mentioned, Juno at Jupiter and to contribute to the legacy of the Cassini mission. The long-term observations will serve to cover the study of those planets where no space missions are expected in the near future as for Saturn, after Cassini Grand Finale in September 2017, as well as Uranus and Neptune.

References

Allard et al. (2012). RSPTA.370.2765A

ANDOR™ Technology, Neo sCMOS, brochure (2012)

Baines K.H., Momary T.W., Fletcher L.N., Showman A.P., Roos-Serote M., Brown R.H., Buratti B.J., Clark R.N. and Nicholson P.D. (2009). *Saturn's north polar cyclone and hexagon at depth revealed by Cassini/VIMS*. Planet. Space Sci., 57, 1671–1681

Barrado-Izagirre N., Rojas J.F., Hueso R., Sánchez-Lavega A., Colas F., Dauvergne J.L., Peach D. and the IOPW Team (2013). *Jupiter's zonal winds and their variability studied with small-size telescopes*. Astronomy & Astrophysics, 2013, 554, A74, d.o.i.: 10.1051/0004-6361/201321201

Barrado-Izagirre N., Legarreta J., Sánchez-Lavega A., Hueso R., Pérez-Hoyos S., Rojas J.F. and Mendikoa I. (2015). A *long-lived and color changing oval on Jupiter's NTrZ (at 19°N)*. Abstract P41B-2068 presented at 2010 Fall Meeting, AGU, San Francisco, USA

Belton M.J.S. et al. (1991). *Images from Galileo of the Venus cloud deck*. Science 253, 1531–1536

Bergstralh J.T., Orton G.S., Diner D.J., Baines K.H., Neff J.S. and Allen M.A. (1981). *Spatially resolved absolute spectrophotometry of Saturn: 3390 to 8080 Å*. Icarus, 46, 27-39

Caldwell J., Benoit T., Hua X.M., Barnet C.D. and Westphal J.A. (1993). *An observed drift of Saturn's Polar Spot by HST*. Science, 260, 326–329

Castelli et al. (1997). A&A.318,841C

Cochran W.D. (1982). *Spatially resolved reflectivities of Saturn - 3000-6000 A*. Astron. J., 87, 718-723

Chanover N.J., Kuehn D.M., Banfield D., Momary T., Beebe R.F., Baines K.H., Nicholson P.D., Simon A.A. and Murrell A.S. (1996). *Absolute Reflectivity Spectra of Jupiter: 0.25-3.5 Micrometers*. Icarus, 121, 351-360

Clark R.N. and McCord T.B. (1979). *Jupiter and Saturn: near infrared spectral albedos*. Icarus 40, 180-188

Del Genio A.D., Achterberg R.K., Baines K.H., Flasar F.M., Read P.L., Sánchez-Lavega A. and Showman A.P. *Saturn Atmospheric Structure and Dynamics* (2009). Ch.6 of *Saturn after Cassini-Huygens*. M. Dougherty, L. Esposito and T. Krimigis (edt.), Springer-Verlag, pp. 113-159. ISBN 978-1-4020-9217-6

De Pater I. et al. *A multi-wavelength study of the 2009 impact on Jupiter: Comparison of high resolution images from Gemini, Keck and HST* (2010). Icarus 210
De Pater I., Sromovsky L., Fry P.M., Hammel H.B., Baranec C. and Sayanagi K. (2015). *Record-breaking storm activity on Uranus in 2014*. Icarus, 252, 121-128

De Pater I., Sault R.J., Butler B., De Boer D. and Wong M.H. (2016). *Peering through Jupiter's clouds with radio spectral imaging*. Science, 352(6290), 1198–1201, doi:10.1126/science.aaf2210

Dyudina U.A., Sackett P.D., Bayliss D.D.R., Seager S., Porco, C.C., Throop H.B. and Done L. (2005). *Phase light curves for extrasolar Jupiters and Saturns*. The Astrophysical Journal, 618m 973-986

Fletcher L. N. et al. (2008), *Temperature and Composition of Saturn's Polar Hot Spots and Hexagon*. Science, 319, 79–81

Fletcher L.N. et al. (2011). Science, 332, 1413

Fletcher L.N., Orton G.S., Greathouse T.K., Sinclair J., Giles R., Irwin P., Rogers J.and Encrenaz T. (2016). *Jupiter's thermal structure on the eve of Juno's arrival and an NEB expansion event*. EGU2016-13076

Fitzpatrick et al. (2013). *Dispersion in Neptunes zonal wind velocities from NIR Keck AO observations in July 2009*. Astrophysics and Space Science, doi: 10.1007/s10509-013-1737-2

Fried D.L. (1965). Statistics *of a geometrical representation of wave-front distortion*. J. Opt. Soc. Am., 55, 1427-35

García-Melendo E. et al. (2009). *The Jovian anticyclone BA: I.Motions and interaction with the GRS from observations and non-linear simulations*. Icarus 203, 486–498

García-Melendo E., Sánchez-Lavega A., Rojas J.F., Pérez-Hoyos S. and Hueso R. (2009). *Vertical shears in Saturn's eastward jets at cloud level*. Icarus 201, 818–820

García-Melendo E., Sánchez-Lavega A., Legarreta J., Perez-Hoyos S. and Hueso R. (2010). *A strong high altitude narrow jet detected at Saturn's Equator*. Geophysical Research Letters, 37, L22204

García-Melendo E., Pérez-Hoyos S., Sánchez-Lavega A. and Hueso R. (2011). *Saturn's zonal wind profile in 2004 - 2009 from Cassini ISS images and its long-term variability*. Icarus, 215, 62-74

Gérard J.C., Saglam A., Piccioni G., Drossart P., Cox C., Erard S., Hueso R. and Sánchez-Lavega A. (2008). *The distribution of the O_2 infrared nightglow observed with VIRTIS on board Venus Express*. Geophysical Research Letters 35

Gillon M., Triaud A.H., Fortney J.J., Demory B.O., Jehin E., Lendl M., Magain P., Kabath P., Queloz D., Alonso R., Anderson D.R., Collier Cameron A., Fumel A., Hebb L., Hellier C., Lanotte A., Maxted P.F., Mowlavi N. and Smalley B. (2012). *The TRAPPIST survey of southern transiting planets. I. Thirty eclipses of the ultra-short period planet WASP-43 b*. Astronomy & Astrophysics, 542, A4. doi: 10.1051/0004-6361/201218817

Godfrey D. A. (1988). *A hexagonal feature around Saturn's north pole*. Icarus, 76, 335–356

Gonzalez R.C. and Woods R.E. (2008). *Digital Image Processing* (3rd ed.; Englewood Cliffs, NJ: Prentice-Hall)

Gorosabel J., Perez-Hoyos S., Mendikoa I., Sanchez-Lavega A., Hueso R., Rojas J.F. and de Ugarte Postigo A. (2013). GCN Circular #14378

Grant-Smith A. (2010). *An examination of Selective Imaging techniques*. MSc.Thesis, MacQuarie University, Sidney, Australia

Hammel H.B., Wong M.H., Clarke J.T., de Pater I., Fletcher L.N., Hueso R., Noll K., Orton G.S., Pérez-Hoyos S., Sánchez-Lavega A., Simon-Miller A.A. and Yanamandra-Fisher P.A. (2010). *Jupiter after the 2009 impact: Hubble Space Telescope imaging of the impact-generated debris and its temporal evolution*. The Astrophysical Journal Letters, 715, 2, L155

Hardy J. W. (2000). *Adaptive optics for astronomical telescopes*. Physics today vol. 53, no. 4, p. 69

Heavens N.G. et al. (2011). *The vertical distribution of dust in the Martian atmosphere during northern spring and summer: observations by the Mars Climate Sounder and analysis of zonal average vertical dust profiles*. J. Geophys. Res. Planets 116, E04003

Helbert J., Müller N., Kostama P., Marinangeli L., Piccioni G. and Drossart, P. (2008). *Surface brightness variations seen by VIRTIS on Venus Express and implications for the evolution of the Lada Terra region, Venus*. Geophysical Research Letters, 35, 11, L11201

Hellier C., Anderson D.R., Collier Cameron A., Gillon M., Jehin E., Lendl M., Maxted P.F.L., Pepe F., Pollacco D., Queloz D., Ségransan D., Smalley B., Smith A.M.S., Southworth J., Triaud A. H. M., Udry S., and West R.G. (2011). *WASP-43b: the*

closest-orbiting hot Jupiter. Astronomy & Astrophysics, 535, L7, doi: 10.1051/0004-6361/201117081

Hormuth F. (2007). *AstraLux: High Angular Resolution Astronomywith an Electron Multiplying CCD*. Diploma thesis in Physics, Faculty of Physics and Astronomy, University of Heidelberg, Germany

Hormuth F., Hippler S., Brandner W., Wagner K. and Henning T. (2008). *AstraLux: the Calar Alto lucky-imaging camera*. Proc. SPIE 7014, Ground-based and Airborne Instrumentation for Astronomy II, 701448 (July 11, 2008), doi:10.1117/12.787384

Hubbard W. B. (1999). *Gravitational Signature of Jupiter's Deep Zonal Flows*. Icarus 137, 357–359

Hueso R. et al. (2008). *Morphology and Dynamics of Venus Oxygen Airglow from Venus Express/VIRTIS observations*. J. Geophys. Res.-Planets 113, E00B02

Hueso R., Legarreta J., García-Melendo E., Sánchez-Lavega A. and Pérez-Hoyos S. (2009). *The Jovian anticyclone BA: II. Circulation and interaction with the zonal jets*. Icarus, 203, 499-515

Hueso R. et al. (2010). *The international outer planets watch atmospheres node database of giant planets images*. Planet. Space Sci. 58, 1152–1159

Hueso R., Wesley A., Go C., Pérez-Hoyos S., Wong M.H., Fletcher L.N., Sánchez-Lavega A., Boslough M.B.E., de Pater I., Orton G.S., Simon-Miller A.A., Djorgovski S.G., Edwards M.L., Hammel H.B., Clarke J.T., Noll K.S. and Yanamandra-Fishe P.A. (2010). *First Earth-based detection of a Superbolide on Jupiter*. The Astrophysical Journal Letters, 721, 2, L129

Hueso R., Pérez-Hoyos S., Sánchez-Lavega A., Wesley A., Hall G., Go C., Tachikawa M., Aoki K., Ichimaru M., Pond J.W.T., Korycansky D.G., Palotai C., Chappell G., Rebeli N., Harrington J., Delcroix M., Wong M., de Pater I., Fletcher L.N., Hammel H., Orton G.S., Tabe I., Watanabe J. and Moreno J.C. (2013). *Impact flux on Jupiter: From superbolides to large-scale collisions*. Astronomy and Astrophysics, 560, A55

Hueso, R., Peralta, J., Garate-Lopez, I., et al. Six years of Venus winds at the upper cloud level from UV, visible and near infrared observations from VIRTIS on Venus Express. Planetary and Space Science, Volumes 113–114, 2015, Pages 78–99

Hueso R., Sánchez-Lavega A., Iñurrigarro P., Rojas J.F., Pérez-Hoyos S., Mendikoa I., Gómez-Forrellad J.M., Go C., Peach D., Colas F. and Vedovato M. (2017). *Jupiter cloud morphology and zonal winds from ground based observations before and during Juno's first perijove*. Geophysical Research Letters, Special Section (Early Results: Juno at Jupiter), doi: 10.1002/2017GL073444

Hueso R. et al. (2017). *Neptune long-lived atmospheric features in 2013-2015 from small (28 cm) and large (10 m) telescopes*. ICARUS (in press)

Ingersoll A.P., Dowling T.E., Gierasch P.J., Orton G.S., Read P.L., Sanchez-Lavega A., Showman A.P., Simon-Miller A.A. and Vasavada A.R. (2004). *Dynamics of Jupiter's Atmosphere.* Ch. 6 in *Jupiter: The Planet, Satellites & Magnetosphere* (eds. F. Bagenal, W. McKinnon, T. Dowling), Cambridge University Press, pp 105-128. ISBN-13: 978-0521035453

Irwin P.G.J. (2003). *Giant Planets of Our Solar System*. Springer & Praxis, Chichester, U. K, pp. 197–246

Karkoschka E. (1998). *Methane, ammonia and temperature measurements of the jovian planets and Titan from CCD-spectrophotometry*. Icarus 133, 134–146

Karkoschka E. and Tomasko M.G. (2010). *Methane absorption coefficients for the jovian planets from laboratory, Huygens, and HST data*. Icarus 205, 674–694

Khatuntsev I.V. et al. (2013). *Cloud level winds from the Venus Express Monitoring Camera imaging*. Icarus, Volume 226, Issue 1, Pages 140–158

Law N.M., Mackay C.D. and Baldwin L.E. (2005). *Lucky Imaging: High Angular Resolution Imaging in the Visible from the Ground*. Astronomy & Astrophysics 446, 739 – 745

Law N.M. (2006). *Lucky-imaging: diffraction-limited astronomy from the ground in the visible*. Ph.D. Thesis, Cambridge University, Cambridge, UK

Lelievre G., Nieto J.L., Thouvenot E., Salmon D. and Llebaria A. (1988). *Very high resolution imaging using sub-pupil apertures, recentering and selection of short exposures*. Astronomy and Astrophysics, 200(July), 301–311

Li L. et al. (2011). *Equatorial winds on Saturn and the stratospheric oscillation*. Nat. Geosci. 4, 750–752

Li C., Ingersoll A.P. and Janssen M.A. (2016). *Retrievals of atmospheric parameters from radiances obtained by the Juno microwave radiometer*. Abstract P33C-2167 presented at 2010 Fall Meeting, AGU, San Francisco, USA

López López R. (2012). *Diseño, construcción y desarrollo de un sistema limitado por difracción para telescopios terrestres: FastCam*. Ph.D. Thesis, Universidade de Vigo, Vigo, Spain

Lucy L.B. (1974). *An iterative technique for the rectification of observed distributions*. Astronomical Journal, 79, 745–754

Maättänen A. et al. (2013). *A complete climatology of the aerosol vertical distribution on Mars from MEx/SPICAM UV solar occultations*. Icarus 223, 892-941

Machado P. (2012). *Mapping zonal winds at Venus's cloud tops from ground-based Doppler velocimetry*. Icarus, Volume 221, Issue 1, Pages 248–261

Machado P., Widemann Th., Luz D. and Peralta J. (2014). *Wind circulation regimes at Venus' cloud tops: Ground-based Doppler velocimetry using CFHT/ESPaDOnS and comparison with simultaneous cloud tracking measurements using VEx/VIRTIS in February 2011*. Icarus, Volume 243, Pages 249–263

Mackay C. et al. (2016). *AOLI: near-diffraction limited imaging in the visible on large ground-based telescopes*. Proc. SPIE 9908, Ground-based and Airborne Instrumentation for Astronomy VI, 99080M (2016), doi: 10.1117/12.2230900

Mendikoa I., Sánchez-Lavega A., Pérez-Hoyos S., Hueso R., Rojas J.F., Aceituno J., Aceituno F., Murga G., De Bilbao L. and García-Melendo E. (2016). *PlanetCam UPV/EHU: A Two-channel Lucky Imaging Camera for Solar System Studies in the Spectral Range 0.38–1.7μm*. Publications of the Astronomical Society of the Pacific, 128, doi: 10.1088/1538-3873/128/961/035002

Mendikoa I., Sánchez-Lavega A., Pérez-Hoyos S., Hueso R., Rojas J.F., and López-Santiago J. (2017). *Temporal and spatial variations of Jupiter's and Saturn's absolute reflectivity from 0.38 to 1.7 μm using PlanetCam-UPV/EHU* (2017). Astronomy & Astrophysics (submitted)

Minnaert, M. (1941), ApJ, 93, 403

Mousis O. et al. (2014). *Instrumental Methods for Professional and Amateur Collaborations in Planetary Astronomy*. Experimental Astronomy, 38, 91-191

Nakamura M. et al. (2007). *Planet-C: Venus Climate Orbiter mission of Japan*. Planetary and Space Science, Volume 55, Issue 12, Pages 1831–1842

Nakamura M. et al. (2011). *Overview of Venus orbiter, Akatsuki*. Earth, Planets and Space, Volume 63, Issue 5, pp 443–457

Nakamura M. et al. (2014). *Return to Venus of the Japanese Venus Climate Orbiter AKATSUKI*. Acta Astronautica, Volume 93, Pages 384–389

Ochsenbein F., Bauer P. and Marcout J. (2000). *The VizieR database of astronomical catalogues*. Astronomy & Astrophysics, Supplement Series 143, 23 – 32

Ordoñez-Etxebarria I., Hueso R., Sánchez-Lavega A. and Pérez-Hoyos S. *Spatial distribution of Jovian clouds, hazes and colors from Cassini ISS multi-spectral images*. Icarus (submitted).

Ortiz J.L., Moreno F. and Molina A. (1993). *Absolutely Calibrated CCD Images of Saturn at Methane Band and Continuum Wavelengths During its 1991 Opposition*. Journal of Geophysical Research 98, E2, 3053 – 3063

Ortiz J.L., Moreno F. and Molina A. (1996). *Saturn 1991-1993: Clouds and hazes.* Icarus, Volume 119, Issue 1, Pages 53-66

Orton G.S. et al. (2016), *Activity in Jupiter's northern hemisphere before the Juno Mission: Waves associated with the North Equatorial Belt and relation to expansion phase*. DPS meeting 48, id.501.09

Orton G. S. et al. (2017). *The first close-up images of Jupiter's polar regions: results from the Juno mission JunoCam instrument*. Geophysical Research Letters 44, doi:10.1002/2016GL072443

Parker D.C., Beish J.D., Troiani D.M., Joyce D.P. and Hernandez C.E. (1999). *Telescopic observations of Mars, 1996-1997: Results of the Marswatch program*. Icarus 138, 3–19

Peralta J., Hueso R. and Sánchez-Lavega A. (2007). *A reanalysis of Venus winds at two cloud levels from Galileo SSI images*. Icarus, 190, 469-477

Peralta J., Joo Lee Y., McGouldrick K., Sagawa H., Sanchez-Lavega A., Imamura T., Widemann T. and Nakamura M. (2017). *Overview of useful spectral regions for Venus: an update to encourage observations complementary to the Akatsuki mission*. Icarus, 288, 235-239

Pérez-Hoyos S., Sánchez-Lavega A., French R.G. and Rojas J.F. (2005). *Saturn's cloud structure and temporal evolution from ten years of Hubble Space Telescope images (1994–2003)*. Icarus 176, 155–174

Pérez-Hoyos S. and Sánchez-Lavega A. (2006). *On the vertical wind shears of Saturn's Equatorial Jet at cloud level*. Icarus 180, 161–175

Pérez-Hoyos S., Sánchez-Lavega A., Hueso R., García-Melendo E. and Legarreta J. (2009). *The Jovian anticyclone BA: III. Aerosol properties and color change*. Icarus 203, 516–530

Pérez-Hoyos S., Sanz-Requena J.F., Barrado-Izagirre N., Rojas J.F. and Sánchez-Lavega A. (2012). *The 2009-10 Fade of Jupiter's South Equatorial Belt: vertical cloud structure models and zonal winds from visible imaging*. Icarus, 217, 256-271

Pérez-Hoyos, S., García-Muñoz, A., Sánchez-Lavega, A., Holsclaw, G., & McClintock, W. M. 2013. Analysis of MESSENGER/MASCS data during second Venus flyby. European Planetary Science Congress (Göttingen: Copernicus), EPSC2013-156

Pérez-Hoyos S., Sanz-Requena J.F., Sánchez-Lavega A., Irwin P.G.J. and Smith A. (2016). *Saturn's tropospheric particles phase function and spatial distribution from Cassini ISS 2010–11 observations*. Icarus, 277, 1-18

Porco C.C. et al. (2004). *Cassini imaging science: Instrument characteristics and anticipated scientific investigations at Saturn*. Space Sci. Rev.,115, 363–497

Porco C.C. et al. (2005). *Cassini imaging science: initial results on Saturn's atmosphere*. Science 307, 1243–1247

Qiu P., Mao Y.N., Lu X.M., Xiang E., Jian X.J. (2012). *Evaluation of a scientific CMOS camera for astronomical observations*. Research in Astronomy and Astrophysics, 13, 615, doi:10.1088/1674-4527/13/5/012

Rayner J.T., Cushing M.C. and Vacca W.D. (2009). *The Infrared Telescope Facility (IRTF) Spectral Library: Cool Stars*. The Astrophysical Journal Supplement Series 185, 289 – 432

Richardson W.H. (1972). *Bayesian-Based Iterative Method of Image Restoration*. JOSA, 62, 55-59

Rogers J.H. (1995). *The Giant Planet Jupiter*. Ch.7, pp. 101–110, Cambridge Univ. Press, Cambridge, UK

Sanchez S.F. et al. (2007). *The night-sky at the CAHA observatory*. doi: 10.1086/522378. https://arxiv.org/abs/0709.0813v1

Sánchez Lavega A., Colas F., Lecacheux J., Laques P., Miyazaki I. and Parker D. (1991). *The Great White Spot and disturbances in Saturn's equatorial atmosphere during 1990*. Nature, 353, 397 - 401

Sánchez Lavega A., Miyazaki I., Parker D., Laques P. and Lecacheux J. (1991). *A disturbance in Jupiter's high-speed North Temperate jet during 1990*. Icarus, 94, 92 - 97

Sánchez-Lavega A., Lecacheaux J., Colas, F. and Laques, P. (1993). J. Geophys. Res., 98, 18857

Sánchez-Lavega A. et al. (1996), Science, 271, 631.

Sanchez-Lavega A., Rojas J.F. and Sada P.V. (2000). *Saturn's zonal winds at cloud level*. Icarus 147, 405–420

Sánchez-Lavega A., Pérez-Hoyos S., Rojas J.F., Hueso R. and French R.G. (2003). *A strong decrease in Saturn's equatorial jet at cloud level*. Nature 423, 623–625

Sanchez-Lavega, A., Hueso, R. & Pe´rez-Hoyos., S. The three-dimensional structure of Saturn's equatorial jet at cloud level. Icarus 187, 510–519 (2007)

Sánchez-Lavega A., Hueso R., Piccioni G., Drossart P., Peralta J., Pérez-Hoyos S., Wilson C.F., Taylor F.W., Baines K.H., Luz D., Erard S. and Lebonnois S. (2008). *Variable winds on Venus mapped in three dimensions*. Geophysical Research Letters, 35, L13204, doi:10.1029/2008GL033817

Sánchez-Lavega A., Orton G.S., Hueso R., García-Melendo E., Pérez-Hoyos S., Simon-Miller A., Rojas J.F., Gomez J.M., Yanamandra-Fisher P., Fletcher L., Joels J., Kemerer J., Hora J., Karkoschka E., de Pater I., Wong M.H., Marcus P.S., Pinilla-Alonso N., Carvalho F., Go C., Parker D., Salway M., Valimberti M., Wesley A. and Pujic Z.

(2008). *Depth of a strong jovian jet from a planetary-scale disturbance driven by storms*. Nature, 451, 437-440

Sánchez-Lavega A., Wesley A., Orton G., Hueso R., Perez-Hoyos S., Fletcher L.N., Yanamandra-Fisher P., Legarreta J., de Pater I., Hammel H., Simon-Miller A., Gomez-Forrellad J.M., Ortiz J.L., García-Melendo E., Puetter R.C. and Chodas P. (2010). *The impact of a large object on Jupiter in 2009 July*. The Astrophysical Journal Letters, 715, 2, L150

Sánchez-Lavega A. et al. (2011). *Deep winds beneath Saturn's upper clouds from a seasonal long-lived planetary-scale storm*. Nature 475, 71-74; doi:10.1038/nature10203

Sánchez-Lavega A. (2011). *An Introduction to Planetary Atmospheres*. Taylor-Francis, CRC Press Boca Raton, USA

Sánchez-Lavega et al. (2012). *PlanetCam UPV/EHU: a simultaneous visible and near infrared lucky-imaging camera to study solar system objects*. Ground-based and Airborne Instrumentation for Astronomy IV, edited by Ian S. McLean, Suzanne K. Ramsay, Hideki Takami, Proc. of SPIE Vol. 8446, 84467X1-X9, doi: 10.1117/12.926149

Sánchez-Lavega A. et al. (2011). *Long-term evolution of the aerosol debris cloud produced by the 2009 impact on Jupiter*. Icarus, 214, 462-476

Sánchez-Lavega A., del Río-Gaztelurrutia T., Hueso R., Gómez-Forrellad J.M., Sanz-Requena J.F., Legarreta J., García-Melendo E., Colas F., Lecacheux J., Fletcher L.N., Barrado-Navascués D., Parker D. and the International Outer PlanetWatch Team (2011). *Deep winds beneath Saturn's upper clouds from a seasonal long-lived planetary-scale storm*. Nature, 475, 71-74, doi: 10.1038/nature10203

Sánchez-Lavega A., Legarreta J., García-Melendo E., Hueso R., Pérez-Hoyos S., Gómez-Forrellad J.M., Fletcher L.N., Orton G.S., Simon-Miller A., Chanover N., Irwin P., Tanga P. and Cecconi M. (2013). *Colors of Jupiter's large anticyclones and the interaction of a Tropical Red Oval with the Great Red Spot in 2008*. J. Geophys. Res. 118, 1-21

Sánchez-Lavega A., del Río-Gaztelurrutia T., Hueso R., Pérez-Hoyos S., García-Melendo E., Antuñano A., Mendikoa I., Rojas J.F., Lillo J., Barrado-Navascués D., Gomez-Forrellad J.M., Go C., Peach D., Barry T., Milika D.P., Nicholas P. and Wesley A. (2014). *The long-term steady motion of Saturn's hexagon and the stability of its enclosed jet stream under seasonal changes*. Geophysical Research Letters, 41, 1425-1431

Sánchez-Lavega A., Pérez-Hoyos S., Hueso R., del Río-Gaztelurrutia T. and Oleaga A. (2014). *The Aula EspaZio Gela and the Master of Space Science & Technology in the Universidad del País Vasco (University of the Basque Country)*. Eur. J. Eng. Educ. 39, 518–526

Sánchez-Lavega et al. (2015). *An extremely high-altitude plume seen at Mars morning terminator*. Nature 518, 525-528

Sánchez-Lavega A., García Muñoz A., García-Melendo E., Pérez-Hoyos S., Gómez-Forrellad J.M., Pellier C., Delcroix M., López-Valverde M.A., González-Galindo F., Jaeschke W., Parker D., Phillips J. and Peach D. (2015). *An extremely high altitude plume seen at Mars morning terminator*. Nature, 518, 525- 528

Sánchez-Lavega A. et al. (2016). *An Enduring rapidly moving storm as a guide to Saturn's equatorial jet complex structure*. Nature Communications, 7:13262, doi: 10.1038/NCOMMS13262

Sanchez-Lavega A. et al. (2016). *Venus cloud morphology and motions from long-term ground-based observations*. International Venus Scientific Conference, 7-11 April, Oxford, UK

Sánchez-Lavega A., Peralta J., Gomez-Forrellad J.M., Hueso R., Pérez-Hoyos S., Mendikoa I., Rojas J.F., Horinouchi T., Lee Y.J. and Watanabe S. (2016). *Venus cloud morphology and motions from ground-based images at the time of the Akatsuki orbit insertion*. Astrophysical Journal Letters, 833 L7, 7pp

Sánchez-Lavega A., Rogers J.H., Orton G.S., García-Melendo E., Legarreta J., Colas F., Dauvergne J.L., Hueso R., Rojas J.F., Pérez-Hoyos S., Mendikoa I., Iñurrigarro P., Gomez-Forrellad J.M., Momary T., Hansen C.J., Eichstaedt G., Miles P. and Wesley A. (2017). *A planetary-scale disturbance in the most intense Jovian atmospheric jet from JunoCam and ground-based observations*. Geophysical Research Letters, Special Section (Early Results: Juno at Jupiter), doi: 10.1002/2017GL073421

Sanz-Requena J.F., Pérez-Hoyos S., Sánchez-Lavega A., del Río-Gaztelurrutia T., Barrado-Navascués D., Colas F., Lecacheux J. and Parker D. (2012). *Cloud structure of Saturn's Storm from ground-based visual imaging*. Icarus, 219, 142-149

Schubert G. (1983). *General Circulation and the Dynamical State of the Venus Atmosphere*, in Venus I, edts. D. M. Hunten, L. Colin, T. M. Donahue, V. I. Moroz, University of Arizona Press, Tucson, pp. 681-765

Simon-Miller A.A., Banfield D. and Gierasch P.J. (2001a). *An HST study of Jovian chromophores*. Icarus, 149, 94–106

Simon-Miller A.A., Banfield D. and Gierasch P.J. (2001b). *Color and the vertical structure in Jupiter's belts, zones, and weather systems*. Icarus 154, 459–474.

Simon-Miller A.A., Carlson R.W. and Sanchez-Lavega A. (2015). *Spectral Comparison and Stability of Red Regions on Jupiter*. J. Geophys. Res.

Simon-Miller A.A., Wong M.H. and Orton G.S. (2015). *First results from the Hubble OPAL Program: Jupiter in 2015*. ApJL, 812(1), id55, 8, doi: 10.1088/0004-637X/812/1/55

Smith B. A. et al. (1982), Science, 215, 504

Smith W.J. (2000). *Modern Optical Engineering*, McGraw-Hill, Third edition

Souchay J., Feissel-Vernier M. (eds.) (2006). *The International Celestial Reference System and Frame*. IERS Technical Note, N. 34, Verlag des Bundesamts für Kartographie und Geodäsie, Frankfurt am Main

Spiga A. et al. (2013). *Rocket dust storm and detached dust layers in the Martian atmosphere*. Journal of Geophys. Res., 118, 746-767

Sromovsky L.A., Hammel H.B., de Pater I., Fry P.M., Rages K.A., Showalter M.R., Merline W.J., Tamblyn P., Neyman C., Margot J.L., Fang J., Colas F., Dauvergne J.L., Gomez-Forrellad J.M., Hueso R., Sanchez-Lavega A., Stallard T. (2012). *Episodic bright and dark spots on Uranus*. Icarus, 220, 6-22

Sromovsky L.A. et al. (2013). *Saturns Great Storm of 20102011: Evidence for ammonia and water ices from analysis of VIMS spectra*. Icarus, 226, 402-418

Sromovsky L.A., de Pater I., Fry P.M., Hammel H.B., Marcus P. (2015). *High S/N Keck and Gemini AO imaging of Uranus during 2012-2014: New cloud patterns, increasing activity, and improved wind measurements*. Icarus, 258, 192-223

Strycker P.D., Chanover N.J., Simon-Miller A.A., Banfield D. and Gierasch P.J. (2011). *Jovian chromophore characteristics from multispectral HST images*. Icarus, 215, 552–583

Tello J.C., Sanchez-Ramirez R., Gorosabel J., Aceituno F. and Castro-Tirado A. (2013). *GRB130418A: OSN 1.5m fading afterglow detection*. GCN # 14385.

Titov D. V., Markiewicz W. J., Ignatiev N.I., Song L., Limay S.S., Sanchez-Lavega A., Almeida M., Roatsch T., Matz K.D., Scholten F., Crisp D., Esposito L.W., Hviid S.F., Jaumann R., Kelle H.U. and Moissl R. (2012). *Morphology of the cloud tops as observed by the Venus Express Monitoring Camera*. Icarus, 217, 682-701

Travis L.D. (1978). *Nature of the atmospheric dynamics on Venus from power spectrum analysis of Mariner 10 images*. J. Atmos. Sci. 35, 1584–1595

Vasavada A. R. and Showman A.P. (2005). *Jovian atmospheric dynamics: an update after Galileo and Cassini*. Rep. Prog. Phys. 68, 1935–1996

Vincent M.B., Chanover N.J., Beebe R.F., Huber L. (2005). *Calibration of the Infrared Telescope Facility National Science Foundation Camera Jupiter Galileo Data Set*. Publications of the Astronomical Society of the Pacific, 117, 1129-1143

Washington Visual Double Star Catalog (WDS), (2014). http://ad.usno.navy.mil/proj/WDS/

West R.A. and Tomasko M.G. (1980). *Spatially resolved methane band photometry of Jupiter. III - Cloud vertical structures for several axisymmetric bands and the Great Red Spot*. Icarus 41, 278–292

West R.A. (1982). *Spatially resolved methane band photometry of Saturn: I. Absolute reflectivity and center-to-limb variations in the 6190-, 7250-, and 8900-A bands*. Icarus 51, 51–64

West R.A., Sato M., Hart H., Lane A.L., Hord C.W., Simmons K.E., Esposito L.W., Coffeen D.L. and Pomphrey R.B. (1983). *Photometry and polarimetry of Saturn at 2640 and 7500 A*. J. Geophys. Res. 88, 8679–8697

West R.A. (1983). *Spatially resolved methane band photometry of Saturn: II. Cloud structure models at four latitudes*. Icarus 53, 301–309

West R.A., Baines K.H., Karkoschka E. and Sánchez-Lavega A. (2009). *Clouds and Aerosols in Saturn's Atmosphere*. Ch.7 in *Saturn after Cassini-Huygens*. M. Dougherty, L. Esposito and T. Krimigis (edt.), Springer-Verlag, pp. 161-179

West R.A. et al. (2010). *Insight calibration of the Cassini imaging science sub-system cameras*. Planetary and Space Science, 58, 1475-1488

Appendix

A1. PlanetCam mean I/F-latitude in VIS/SWIR filters for Jupiter and Saturn

A2. Minnaert Coefficients $(I/F)_0$ and k

A3. Absolute reflectivity of Jupiter from December 2012 to July 2016 in both VIS and SWIR channels

A4. Observation campaigns with PlanetCam

A5. List of Publications

A1. PlanetCam mean I/F-latitude in VIS/SWIR filters for Jupiter and Saturn

Jupiter - VIS

Lat PC (°)	(I/F) UV	(I/F) Vio	(I/F) B	(I/F) V	(I/F) R	(I/F) M1	(I/F) C1	(I/F) M2	(I/F) C2	(I/F) M3	(I/F) C3	Lat PG (°)
-80.00	0.052	0.098	0.103	0.127	0.111	0.123	0.135	0.105	0.141	0.026	0.113	-81.23
-79.00	0.056	0.103	0.110	0.135	0.119	0.130	0.143	0.111	0.150	0.029	0.118	-80.35
-78.00	0.061	0.108	0.117	0.144	0.128	0.139	0.152	0.116	0.160	0.032	0.126	-79.47
-77.00	0.066	0.115	0.126	0.154	0.138	0.147	0.162	0.122	0.170	0.035	0.135	-78.58
-76.00	0.072	0.121	0.135	0.164	0.148	0.157	0.173	0.128	0.181	0.039	0.145	-77.70
-75.00	0.078	0.128	0.145	0.174	0.158	0.167	0.184	0.135	0.192	0.042	0.152	-76.81
-74.00	0.084	0.136	0.154	0.186	0.169	0.178	0.196	0.140	0.203	0.045	0.166	-75.92
-73.00	0.091	0.143	0.165	0.197	0.180	0.189	0.208	0.145	0.215	0.049	0.174	-75.03
-72.00	0.098	0.152	0.175	0.209	0.191	0.199	0.219	0.151	0.228	0.052	0.183	-74.14
-71.00	0.106	0.160	0.186	0.221	0.202	0.210	0.232	0.156	0.240	0.054	0.193	-73.24
-70.00	0.113	0.169	0.196	0.233	0.213	0.220	0.244	0.160	0.252	0.056	0.203	-72.34
-69.00	0.120	0.177	0.206	0.244	0.224	0.231	0.256	0.164	0.264	0.057	0.220	-71.44
-68.00	0.127	0.186	0.216	0.255	0.234	0.241	0.267	0.167	0.276	0.058	0.235	-70.54
-67.00	0.134	0.194	0.226	0.267	0.245	0.250	0.279	0.170	0.287	0.058	0.241	-69.63
-66.00	0.141	0.202	0.235	0.277	0.255	0.260	0.290	0.172	0.298	0.057	0.255	-68.72
-65.00	0.148	0.210	0.244	0.288	0.265	0.269	0.302	0.173	0.310	0.056	0.265	-67.81
-64.00	0.154	0.218	0.253	0.298	0.274	0.279	0.312	0.174	0.320	0.054	0.279	-66.90
-63.00	0.160	0.225	0.261	0.309	0.284	0.286	0.323	0.174	0.330	0.051	0.288	-65.98
-62.00	0.165	0.232	0.269	0.319	0.293	0.295	0.335	0.174	0.342	0.047	0.295	-65.06
-61.00	0.171	0.239	0.277	0.329	0.303	0.303	0.345	0.176	0.353	0.044	0.310	-64.14
-60.00	0.176	0.245	0.285	0.340	0.313	0.312	0.357	0.179	0.366	0.040	0.317	-63.21
-59.00	0.181	0.252	0.293	0.352	0.325	0.323	0.370	0.182	0.379	0.037	0.328	-62.28
-58.00	0.186	0.259	0.303	0.364	0.338	0.333	0.384	0.188	0.391	0.035	0.339	-61.34
-57.00	0.191	0.265	0.312	0.376	0.351	0.344	0.398	0.194	0.404	0.033	0.350	-60.41
-56.00	0.197	0.272	0.321	0.389	0.363	0.357	0.412	0.200	0.417	0.031	0.362	-59.46
-55.00	0.203	0.281	0.331	0.401	0.376	0.369	0.427	0.206	0.430	0.031	0.371	-58.52
-54.00	0.209	0.289	0.342	0.414	0.389	0.382	0.440	0.213	0.444	0.031	0.379	-57.57
-53.00	0.216	0.298	0.352	0.428	0.402	0.394	0.454	0.219	0.457	0.031	0.397	-56.61
-52.00	0.223	0.308	0.364	0.442	0.414	0.406	0.468	0.225	0.471	0.031	0.411	-55.66
-51.00	0.232	0.319	0.376	0.456	0.427	0.420	0.482	0.233	0.486	0.031	0.422	-54.69
-50.00	0.240	0.329	0.389	0.471	0.441	0.432	0.497	0.241	0.499	0.032	0.442	-53.73
-49.00	0.250	0.340	0.403	0.487	0.456	0.446	0.512	0.249	0.513	0.032	0.460	-52.76
-48.00	0.260	0.352	0.418	0.503	0.471	0.459	0.526	0.257	0.530	0.033	0.473	-51.78
-47.00	0.271	0.363	0.432	0.520	0.487	0.472	0.542	0.265	0.545	0.034	0.484	-50.80
-46.00	0.281	0.374	0.445	0.535	0.500	0.486	0.557	0.272	0.562	0.034	0.508	-49.82
-45.00	0.289	0.384	0.457	0.548	0.512	0.499	0.572	0.279	0.578	0.035	0.514	-48.83
-44.00	0.297	0.392	0.467	0.559	0.523	0.511	0.586	0.286	0.592	0.035	0.528	-47.83
-43.00	0.302	0.399	0.475	0.569	0.531	0.521	0.598	0.291	0.603	0.036	0.539	-46.84
-42.00	0.306	0.404	0.482	0.579	0.541	0.527	0.609	0.296	0.612	0.037	0.546	-45.83
-41.00	0.308	0.409	0.488	0.586	0.551	0.534	0.616	0.302	0.620	0.037	0.556	-44.83
-40.00	0.311	0.413	0.494	0.594	0.561	0.541	0.625	0.308	0.625	0.038	0.561	-43.81
-39.00	0.314	0.418	0.501	0.602	0.572	0.549	0.634	0.312	0.631	0.040	0.568	-42.80
-38.00	0.318	0.423	0.510	0.611	0.584	0.561	0.645	0.319	0.643	0.042	0.570	-41.78
-37.00	0.323	0.429	0.519	0.622	0.594	0.575	0.658	0.326	0.658	0.044	0.579	-40.75
-36.00	0.329	0.437	0.532	0.635	0.603	0.585	0.673	0.335	0.677	0.045	0.601	-39.72
-35.00	0.336	0.450	0.544	0.648	0.610	0.596	0.685	0.344	0.695	0.046	0.628	-38.68
-34.00	0.343	0.463	0.556	0.664	0.618	0.601	0.697	0.353	0.708	0.047	0.645	-37.64
-33.00	0.350	0.476	0.572	0.682	0.630	0.609	0.708	0.364	0.720	0.048	0.675	-36.60
-32.00	0.361	0.490	0.594	0.705	0.650	0.620	0.722	0.374	0.729	0.051	0.680	-35.54
-31.00	0.375	0.504	0.619	0.729	0.675	0.632	0.733	0.381	0.738	0.053	0.692	-34.49
-30.00	0.390	0.520	0.641	0.748	0.696	0.645	0.747	0.388	0.749	0.056	0.692	-33.43
-29.00	0.405	0.534	0.656	0.760	0.709	0.662	0.762	0.396	0.762	0.057	0.696	-32.37
-28.00	0.419	0.543	0.668	0.767	0.718	0.677	0.776	0.402	0.780	0.058	0.715	-31.30
-27.00	0.430	0.542	0.680	0.776	0.728	0.694	0.795	0.410	0.799	0.059	0.736	-30.22
-26.00	0.438	0.534	0.690	0.787	0.738	0.707	0.810	0.416	0.814	0.061	0.766	-29.15
-25.00	0.444	0.526	0.699	0.798	0.746	0.718	0.824	0.425	0.831	0.063	0.775	-28.07
-24.00	0.452	0.520	0.707	0.809	0.755	0.725	0.837	0.432	0.845	0.067	0.794	-26.98
-23.00	0.457	0.515	0.711	0.816	0.766	0.727	0.842	0.436	0.854	0.070	0.799	-25.89
-22.00	0.458	0.509	0.704	0.815	0.770	0.722	0.837	0.434	0.853	0.073	0.792	-24.80
-21.00	0.451	0.499	0.681	0.800	0.760	0.713	0.828	0.425	0.844	0.074	0.771	-23.70
-20.00	0.434	0.486	0.649	0.774	0.740	0.700	0.814	0.412	0.828	0.075	0.744	-22.60
-19.00	0.410	0.469	0.614	0.739	0.713	0.679	0.796	0.401	0.808	0.076	0.725	-21.49
-18.00	0.384	0.455	0.579	0.703	0.688	0.657	0.778	0.391	0.791	0.073	0.723	-20.38
-17.00	0.361	0.444	0.552	0.677	0.671	0.644	0.764	0.384	0.784	0.070	0.721	-19.27
-16.00	0.345	0.435	0.537	0.666	0.665	0.640	0.763	0.383	0.786	0.066	0.732	-18.15
-15.00	0.335	0.431	0.529	0.665	0.672	0.644	0.768	0.383	0.796	0.064	0.730	-17.03
-14.00	0.331	0.436	0.522	0.668	0.675	0.647	0.770	0.384	0.800	0.063	0.729	-15.91
-13.00	0.331	0.445	0.522	0.667	0.667	0.643	0.765	0.379	0.790	0.065	0.713	-14.79
-12.00	0.333	0.449	0.531	0.671	0.661	0.641	0.763	0.377	0.786	0.067	0.707	-13.66
-11.00	0.340	0.452	0.546	0.684	0.665	0.647	0.772	0.380	0.796	0.068	0.705	-12.53
-10.00	0.353	0.464	0.569	0.712	0.682	0.660	0.789	0.388	0.809	0.070	0.723	-11.40
-9.00	0.372	0.488	0.597	0.745	0.705	0.674	0.806	0.396	0.822	0.071	0.739	-10.26
-8.00	0.397	0.518	0.636	0.778	0.733	0.693	0.825	0.411	0.839	0.073	0.763	-9.13
-7.00	0.430	0.550	0.684	0.818	0.767	0.716	0.852	0.435	0.865	0.075	0.803	-7.99
-6.00	0.467	0.582	0.730	0.862	0.805	0.744	0.882	0.459	0.893	0.078	0.831	-6.85
-5.00	0.499	0.606	0.765	0.894	0.835	0.764	0.900	0.472	0.913	0.083	0.854	-5.71
-4.00	0.520	0.619	0.784	0.909	0.851	0.772	0.905	0.476	0.918	0.087	0.866	-4.57
-3.00	0.528	0.622	0.789	0.913	0.854	0.774	0.906	0.476	0.918	0.090	0.868	-3.43
-2.00	0.527	0.620	0.782	0.910	0.854	0.770	0.903	0.474	0.920	0.091	0.864	-2.29
-1.00	0.523	0.616	0.777	0.901	0.849	0.771	0.899	0.469	0.920	0.092	0.849	-1.14
0.00	0.517	0.611	0.772	0.891	0.839	0.768	0.897	0.462	0.911	0.093	0.833	0.00

Lat PC (°)	(I/F) UV	(I/F) Vio	(I/F) B	(I/F) V	(I/F) R	(I/F) M1	(I/F) C1	(I/F) M2	(I/F) C2	(I/F) M3	(I/F) C3	Lat PG (°)
0.00	0.517	0.611	0.772	0.891	0.839	0.768	0.897	0.462	0.911	0.093	0.833	0.00
1.00	0.507	0.601	0.764	0.883	0.825	0.761	0.892	0.457	0.901	0.094	0.821	1.14
2.00	0.494	0.584	0.752	0.875	0.813	0.756	0.887	0.450	0.896	0.095	0.803	2.29
3.00	0.476	0.563	0.733	0.862	0.810	0.748	0.876	0.438	0.882	0.095	0.790	3.43
4.00	0.453	0.536	0.703	0.838	0.805	0.733	0.850	0.427	0.856	0.095	0.768	4.57
5.00	0.426	0.504	0.662	0.804	0.786	0.711	0.816	0.421	0.821	0.094	0.740	5.71
6.00	0.396	0.469	0.616	0.759	0.759	0.687	0.786	0.418	0.792	0.093	0.745	6.85
7.00	0.367	0.436	0.578	0.715	0.730	0.665	0.763	0.414	0.766	0.090	0.730	7.99
8.00	0.342	0.409	0.549	0.683	0.711	0.645	0.744	0.409	0.752	0.086	0.720	9.13
9.00	0.325	0.391	0.525	0.667	0.697	0.630	0.736	0.408	0.761	0.080	0.731	10.26
10.00	0.316	0.381	0.510	0.663	0.688	0.627	0.737	0.407	0.774	0.075	0.747	11.40
11.00	0.318	0.381	0.507	0.671	0.688	0.629	0.742	0.407	0.782	0.072	0.752	12.53
12.00	0.329	0.389	0.516	0.682	0.693	0.631	0.751	0.406	0.789	0.070	0.758	13.66
13.00	0.350	0.410	0.540	0.697	0.702	0.637	0.759	0.414	0.789	0.070	0.764	14.79
14.00	0.381	0.440	0.577	0.719	0.713	0.645	0.767	0.424	0.791	0.073	0.775	15.91
15.00	0.415	0.474	0.617	0.747	0.729	0.656	0.775	0.435	0.797	0.077	0.797	17.03
16.00	0.445	0.501	0.656	0.780	0.747	0.675	0.785	0.443	0.814	0.081	0.817	18.15
17.00	0.467	0.514	0.689	0.807	0.766	0.694	0.801	0.450	0.837	0.084	0.841	19.27
18.00	0.478	0.517	0.703	0.825	0.782	0.708	0.814	0.457	0.853	0.086	0.847	20.38
19.00	0.477	0.511	0.697	0.826	0.788	0.712	0.817	0.459	0.856	0.085	0.842	21.49
20.00	0.465	0.497	0.679	0.815	0.785	0.706	0.812	0.452	0.846	0.081	0.839	22.60
21.00	0.444	0.482	0.662	0.798	0.776	0.699	0.802	0.441	0.839	0.075	0.827	23.70
22.00	0.421	0.468	0.645	0.781	0.761	0.689	0.793	0.429	0.827	0.071	0.818	24.80
23.00	0.402	0.458	0.630	0.764	0.745	0.680	0.781	0.419	0.816	0.068	0.807	25.89
24.00	0.389	0.457	0.618	0.749	0.729	0.674	0.773	0.411	0.808	0.067	0.789	26.98
25.00	0.380	0.462	0.613	0.737	0.719	0.672	0.770	0.412	0.803	0.067	0.785	28.07
26.00	0.375	0.468	0.617	0.728	0.709	0.668	0.766	0.414	0.791	0.068	0.773	29.15
27.00	0.373	0.472	0.622	0.722	0.702	0.664	0.759	0.409	0.776	0.068	0.763	30.22
28.00	0.369	0.473	0.620	0.720	0.698	0.656	0.746	0.404	0.761	0.068	0.748	31.30
29.00	0.364	0.470	0.611	0.718	0.697	0.653	0.739	0.400	0.752	0.067	0.730	32.37
30.00	0.355	0.464	0.598	0.711	0.691	0.648	0.731	0.394	0.744	0.065	0.722	33.43
31.00	0.344	0.456	0.584	0.699	0.681	0.642	0.724	0.388	0.736	0.062	0.709	34.49
32.00	0.334	0.447	0.568	0.686	0.668	0.631	0.713	0.379	0.725	0.060	0.700	35.54
33.00	0.324	0.439	0.554	0.674	0.654	0.620	0.703	0.370	0.714	0.059	0.701	36.60
34.00	0.316	0.430	0.542	0.665	0.642	0.610	0.692	0.359	0.702	0.058	0.697	37.64
35.00	0.310	0.421	0.533	0.657	0.631	0.600	0.684	0.351	0.693	0.057	0.692	38.68
36.00	0.304	0.412	0.524	0.650	0.623	0.591	0.674	0.344	0.685	0.055	0.677	39.72
37.00	0.299	0.403	0.514	0.640	0.615	0.583	0.667	0.341	0.675	0.053	0.663	40.75
38.00	0.293	0.392	0.504	0.627	0.604	0.573	0.657	0.336	0.661	0.050	0.646	41.78
39.00	0.285	0.380	0.491	0.613	0.592	0.559	0.641	0.327	0.647	0.048	0.627	42.80
40.00	0.277	0.368	0.476	0.598	0.577	0.543	0.626	0.317	0.632	0.045	0.612	43.81
41.00	0.269	0.355	0.462	0.581	0.560	0.527	0.609	0.306	0.616	0.043	0.592	44.83
42.00	0.261	0.343	0.447	0.564	0.543	0.512	0.591	0.295	0.600	0.041	0.580	45.83
43.00	0.252	0.331	0.435	0.549	0.529	0.497	0.573	0.287	0.581	0.040	0.563	46.84
44.00	0.245	0.320	0.423	0.534	0.516	0.482	0.555	0.277	0.565	0.039	0.550	47.83
45.00	0.237	0.309	0.411	0.519	0.504	0.468	0.539	0.268	0.550	0.038	0.537	48.83
46.00	0.230	0.301	0.400	0.503	0.490	0.455	0.525	0.260	0.534	0.038	0.523	49.82
47.00	0.224	0.293	0.391	0.487	0.476	0.443	0.510	0.252	0.520	0.037	0.507	50.80
48.00	0.218	0.286	0.383	0.472	0.462	0.433	0.498	0.246	0.506	0.036	0.492	51.78
49.00	0.212	0.280	0.374	0.459	0.449	0.421	0.485	0.239	0.494	0.036	0.476	52.76
50.00	0.207	0.274	0.366	0.446	0.435	0.410	0.475	0.234	0.482	0.036	0.463	53.73
51.00	0.203	0.269	0.356	0.434	0.421	0.400	0.463	0.228	0.468	0.036	0.453	54.69
52.00	0.198	0.264	0.347	0.422	0.408	0.389	0.450	0.221	0.456	0.036	0.435	55.66
53.00	0.194	0.258	0.338	0.410	0.394	0.378	0.438	0.214	0.442	0.036	0.426	56.61
54.00	0.189	0.253	0.330	0.399	0.382	0.369	0.426	0.208	0.429	0.036	0.415	57.57
55.00	0.185	0.249	0.321	0.387	0.370	0.359	0.415	0.202	0.417	0.037	0.406	58.52
56.00	0.180	0.245	0.313	0.377	0.360	0.348	0.403	0.196	0.405	0.037	0.400	59.46
57.00	0.176	0.240	0.305	0.367	0.350	0.339	0.389	0.190	0.391	0.038	0.388	60.41
58.00	0.172	0.236	0.298	0.357	0.341	0.328	0.377	0.185	0.377	0.040	0.377	61.34
59.00	0.168	0.231	0.290	0.347	0.332	0.318	0.365	0.181	0.366	0.040	0.360	62.28
60.00	0.164	0.227	0.284	0.337	0.323	0.307	0.352	0.177	0.353	0.042	0.353	63.21
61.00	0.160	0.222	0.276	0.327	0.313	0.298	0.340	0.173	0.343	0.043	0.340	64.14
62.00	0.156	0.217	0.269	0.317	0.304	0.289	0.329	0.170	0.330	0.044	0.327	65.06
63.00	0.151	0.210	0.261	0.307	0.294	0.280	0.318	0.167	0.319	0.044	0.320	65.98
64.00	0.147	0.204	0.252	0.297	0.285	0.271	0.306	0.164	0.306	0.045	0.307	66.90
65.00	0.141	0.196	0.244	0.287	0.276	0.261	0.294	0.161	0.294	0.046	0.294	67.81
66.00	0.136	0.187	0.235	0.276	0.267	0.251	0.283	0.158	0.281	0.046	0.278	68.72
67.00	0.131	0.178	0.225	0.265	0.257	0.240	0.271	0.153	0.268	0.046	0.267	69.63
68.00	0.125	0.168	0.216	0.254	0.247	0.229	0.258	0.148	0.255	0.046	0.250	70.54
69.00	0.119	0.157	0.205	0.242	0.237	0.218	0.246	0.143	0.242	0.046	0.233	71.44
70.00	0.112	0.146	0.194	0.230	0.227	0.205	0.233	0.137	0.228	0.045	0.219	72.34
71.00	0.106	0.136	0.183	0.218	0.216	0.193	0.220	0.130	0.214	0.044	0.203	73.24
72.00	0.100	0.126	0.171	0.205	0.206	0.181	0.206	0.123	0.200	0.042	0.186	74.14
73.00	0.093	0.116	0.159	0.193	0.196	0.169	0.193	0.115	0.186	0.040	0.170	75.03
74.00	0.087	0.107	0.147	0.181	0.186	0.157	0.179	0.108	0.173	0.038	0.157	75.92
75.00	0.081	0.099	0.135	0.169	0.177	0.145	0.167	0.100	0.160	0.035	0.144	76.81
76.00	0.076	0.092	0.125	0.157	0.167	0.135	0.155	0.092	0.148	0.032	0.130	77.70
77.00	0.071	0.085	0.115	0.146	0.157	0.126	0.143	0.084	0.137	0.028	0.121	78.58
78.00	0.066	0.079	0.106	0.136	0.147	0.118	0.133	0.077	0.127	0.026	0.112	79.47
79.00	0.061	0.073	0.098	0.126	0.138	0.110	0.124	0.071	0.119	0.023	0.105	80.35
80.00	0.057	0.068	0.091	0.117	0.129	0.104	0.117	0.065	0.112	0.021	0.099	81.23

Jupiter - SWIR

Lat PC (°)	(I/F) J	(I/F) H	(I/F) YC	(I/F) YM	(I/F) V1	(I/F) V2	(I/F) JC	(I/F) JM	(I/F) V3	(I/F) HC	(I/F) HM	Lat PG (°)
-80.00	0.047	0.039	0.086	0.017	0.025	0.033	0.071	0.016	0.024	0.059	0.019	-81.23
-79.00	0.050	0.042	0.092	0.019	0.027	0.035	0.076	0.017	0.025	0.063	0.021	-80.35
-78.00	0.053	0.045	0.098	0.020	0.028	0.037	0.081	0.018	0.025	0.068	0.021	-79.47
-77.00	0.057	0.048	0.104	0.021	0.030	0.040	0.086	0.018	0.025	0.072	0.020	-78.58
-76.00	0.060	0.051	0.110	0.022	0.031	0.042	0.091	0.018	0.025	0.076	0.019	-77.70
-75.00	0.063	0.053	0.117	0.023	0.031	0.043	0.096	0.018	0.025	0.080	0.019	-76.81
-74.00	0.065	0.056	0.123	0.024	0.032	0.045	0.101	0.018	0.024	0.084	0.018	-75.92
-73.00	0.068	0.059	0.130	0.025	0.032	0.047	0.106	0.017	0.024	0.088	0.018	-75.03
-72.00	0.071	0.062	0.137	0.025	0.032	0.048	0.111	0.016	0.024	0.093	0.018	-74.14
-71.00	0.073	0.065	0.144	0.025	0.032	0.050	0.116	0.016	0.023	0.097	0.019	-73.24
-70.00	0.076	0.068	0.150	0.025	0.032	0.051	0.121	0.016	0.023	0.103	0.019	-72.34
-69.00	0.079	0.071	0.158	0.024	0.032	0.052	0.125	0.015	0.023	0.108	0.017	-71.44
-68.00	0.082	0.074	0.165	0.024	0.031	0.054	0.131	0.014	0.023	0.114	0.016	-70.54
-67.00	0.084	0.077	0.171	0.023	0.031	0.055	0.135	0.014	0.023	0.119	0.015	-69.63
-66.00	0.086	0.079	0.177	0.023	0.030	0.056	0.139	0.013	0.022	0.122	0.014	-68.72
-65.00	0.087	0.081	0.183	0.022	0.028	0.056	0.142	0.012	0.022	0.125	0.013	-67.81
-64.00	0.088	0.082	0.188	0.021	0.027	0.056	0.145	0.011	0.020	0.127	0.012	-66.90
-63.00	0.088	0.082	0.193	0.019	0.025	0.055	0.147	0.009	0.019	0.128	0.014	-65.98
-62.00	0.087	0.082	0.197	0.018	0.023	0.055	0.149	0.007	0.018	0.130	0.013	-65.06
-61.00	0.088	0.082	0.203	0.016	0.022	0.056	0.153	0.004	0.017	0.134	0.010	-64.14
-60.00	0.089	0.083	0.210	0.014	0.020	0.057	0.158	0.003	0.016	0.139	0.009	-63.21
-59.00	0.092	0.086	0.219	0.012	0.018	0.059	0.164	0.003	0.016	0.145	0.010	-62.28
-58.00	0.095	0.089	0.229	0.011	0.017	0.062	0.171	0.002	0.018	0.152	0.009	-61.34
-57.00	0.098	0.093	0.239	0.010	0.017	0.065	0.178	0.002	0.019	0.160	0.009	-60.41
-56.00	0.102	0.097	0.249	0.008	0.016	0.069	0.184	0.002	0.021	0.166	0.010	-59.46
-55.00	0.106	0.102	0.258	0.008	0.017	0.072	0.190	0.002	0.022	0.172	0.011	-58.52
-54.00	0.111	0.105	0.265	0.007	0.017	0.076	0.195	0.001	0.022	0.177	0.008	-57.57
-53.00	0.115	0.109	0.273	0.006	0.017	0.079	0.201	0.001	0.022	0.183	0.009	-56.61
-52.00	0.119	0.113	0.283	0.006	0.017	0.083	0.209	0.001	0.024	0.189	0.008	-55.66
-51.00	0.124	0.118	0.292	0.006	0.017	0.086	0.217	0.001	0.026	0.195	0.011	-54.69
-50.00	0.128	0.122	0.303	0.006	0.018	0.089	0.224	0.001	0.027	0.201	0.012	-53.73
-49.00	0.133	0.126	0.314	0.006	0.019	0.093	0.233	0.001	0.030	0.207	0.010	-52.76
-48.00	0.136	0.129	0.326	0.005	0.019	0.097	0.242	0.001	0.032	0.215	0.011	-51.78
-47.00	0.141	0.133	0.338	0.005	0.020	0.102	0.253	0.001	0.034	0.226	0.009	-50.80
-46.00	0.148	0.137	0.350	0.005	0.021	0.107	0.264	0.001	0.034	0.236	0.010	-49.82
-45.00	0.153	0.142	0.360	0.005	0.021	0.112	0.273	0.001	0.036	0.245	0.012	-48.83
-44.00	0.157	0.145	0.365	0.005	0.021	0.116	0.278	0.001	0.036	0.250	0.013	-47.83
-43.00	0.158	0.147	0.367	0.005	0.021	0.118	0.280	0.001	0.036	0.252	0.012	-46.84
-42.00	0.160	0.148	0.367	0.005	0.022	0.119	0.279	0.001	0.036	0.252	0.015	-45.83
-41.00	0.162	0.149	0.369	0.005	0.022	0.120	0.277	0.001	0.035	0.250	0.016	-44.83
-40.00	0.162	0.151	0.370	0.005	0.023	0.121	0.276	0.001	0.036	0.247	0.012	-43.81
-39.00	0.162	0.151	0.373	0.005	0.024	0.124	0.277	0.001	0.037	0.247	0.011	-42.80
-38.00	0.163	0.153	0.380	0.006	0.025	0.128	0.284	0.001	0.039	0.253	0.011	-41.78
-37.00	0.166	0.154	0.390	0.006	0.026	0.133	0.295	0.001	0.039	0.263	0.014	-40.75
-36.00	0.170	0.157	0.404	0.006	0.027	0.135	0.306	0.001	0.042	0.269	0.018	-39.72
-35.00	0.175	0.163	0.418	0.006	0.027	0.136	0.314	0.002	0.047	0.274	0.014	-38.68
-34.00	0.180	0.168	0.427	0.007	0.028	0.137	0.321	0.002	0.045	0.285	0.014	-37.64
-33.00	0.182	0.171	0.438	0.007	0.029	0.141	0.329	0.002	0.045	0.295	0.015	-36.60
-32.00	0.186	0.173	0.451	0.007	0.030	0.147	0.338	0.002	0.048	0.307	0.016	-35.54
-31.00	0.198	0.180	0.469	0.008	0.032	0.156	0.352	0.002	0.051	0.318	0.016	-34.49
-30.00	0.211	0.191	0.491	0.008	0.034	0.165	0.369	0.002	0.057	0.332	0.016	-33.43
-29.00	0.218	0.200	0.507	0.009	0.035	0.171	0.379	0.002	0.058	0.337	0.017	-32.37
-28.00	0.223	0.204	0.518	0.009	0.035	0.175	0.385	0.002	0.058	0.341	0.018	-31.30
-27.00	0.230	0.209	0.527	0.009	0.036	0.177	0.388	0.002	0.061	0.347	0.020	-30.22
-26.00	0.236	0.215	0.534	0.009	0.037	0.180	0.391	0.003	0.065	0.350	0.018	-29.15
-25.00	0.239	0.221	0.540	0.010	0.039	0.185	0.399	0.003	0.068	0.359	0.022	-28.07
-24.00	0.243	0.224	0.547	0.010	0.041	0.192	0.410	0.004	0.070	0.371	0.022	-26.98
-23.00	0.249	0.230	0.551	0.011	0.043	0.199	0.419	0.004	0.072	0.380	0.021	-25.89
-22.00	0.253	0.236	0.553	0.012	0.045	0.203	0.422	0.004	0.075	0.382	0.021	-24.80
-21.00	0.254	0.238	0.553	0.013	0.047	0.205	0.422	0.006	0.077	0.378	0.022	-23.70
-20.00	0.251	0.233	0.536	0.014	0.049	0.206	0.415	0.006	0.079	0.370	0.024	-22.60
-19.00	0.246	0.228	0.511	0.014	0.049	0.204	0.396	0.006	0.076	0.354	0.022	-21.49
-18.00	0.239	0.225	0.493	0.014	0.048	0.200	0.385	0.006	0.071	0.346	0.022	-20.38
-17.00	0.233	0.225	0.478	0.013	0.047	0.195	0.375	0.004	0.069	0.336	0.020	-19.27
-16.00	0.230	0.222	0.477	0.013	0.045	0.192	0.372	0.003	0.067	0.337	0.019	-18.15
-15.00	0.232	0.221	0.490	0.012	0.042	0.190	0.380	0.002	0.066	0.348	0.017	-17.03
-14.00	0.237	0.224	0.495	0.011	0.041	0.187	0.383	0.002	0.067	0.347	0.019	-15.91
-13.00	0.235	0.221	0.491	0.011	0.041	0.184	0.375	0.003	0.067	0.335	0.019	-14.79
-12.00	0.230	0.216	0.491	0.012	0.042	0.184	0.369	0.003	0.069	0.328	0.020	-13.66
-11.00	0.227	0.215	0.491	0.012	0.043	0.189	0.369	0.004	0.068	0.328	0.018	-12.53
-10.00	0.227	0.218	0.493	0.012	0.043	0.191	0.367	0.004	0.066	0.327	0.018	-11.40
-9.00	0.230	0.221	0.497	0.012	0.044	0.192	0.367	0.004	0.069	0.329	0.019	-10.26
-8.00	0.228	0.217	0.505	0.012	0.045	0.194	0.371	0.004	0.070	0.336	0.019	-9.13
-7.00	0.233	0.218	0.518	0.013	0.046	0.197	0.387	0.005	0.073	0.355	0.020	-7.99
-6.00	0.247	0.226	0.542	0.013	0.048	0.203	0.406	0.005	0.076	0.374	0.028	-6.85
-5.00	0.260	0.239	0.563	0.014	0.051	0.211	0.421	0.006	0.079	0.390	0.023	-5.71
-4.00	0.277	0.255	0.573	0.015	0.055	0.222	0.439	0.008	0.086	0.408	0.025	-4.57
-3.00	0.290	0.273	0.586	0.016	0.059	0.231	0.458	0.009	0.096	0.434	0.025	-3.43
-2.00	0.294	0.281	0.595	0.017	0.062	0.239	0.471	0.010	0.101	0.447	0.025	-2.29
-1.00	0.299	0.288	0.605	0.019	0.065	0.248	0.475	0.011	0.105	0.453	0.027	-1.14
0.00	0.299	0.294	0.605	0.020	0.068	0.252	0.476	0.012	0.108	0.446	0.029	0.00

Lat PC (°)	(I/F) J	(I/F) H	(I/F) YC	(I/F) YM	(I/F) V1	(I/F) V2	(I/F) JC	(I/F) JM	(I/F) V3	(I/F) HC	(I/F) HM	Lat PG (°)
0.00	0.299	0.294	0.605	0.020	0.068	0.252	0.476	0.012	0.108	0.446	0.029	0.00
1.00	0.290	0.286	0.594	0.021	0.069	0.251	0.468	0.013	0.106	0.430	0.029	1.14
2.00	0.280	0.272	0.584	0.022	0.071	0.246	0.451	0.013	0.106	0.414	0.034	2.29
3.00	0.279	0.267	0.580	0.022	0.071	0.241	0.445	0.014	0.107	0.411	0.029	3.43
4.00	0.276	0.265	0.572	0.023	0.071	0.236	0.445	0.013	0.108	0.409	0.030	4.57
5.00	0.278	0.268	0.565	0.023	0.071	0.235	0.452	0.013	0.106	0.418	0.031	5.71
6.00	0.282	0.269	0.558	0.022	0.070	0.237	0.463	0.012	0.100	0.429	0.028	6.85
7.00	0.280	0.268	0.547	0.021	0.068	0.239	0.463	0.010	0.094	0.426	0.026	7.99
8.00	0.281	0.269	0.535	0.020	0.064	0.237	0.453	0.008	0.087	0.409	0.025	9.13
9.00	0.274	0.266	0.526	0.018	0.060	0.232	0.437	0.006	0.079	0.399	0.023	10.26
10.00	0.261	0.257	0.519	0.016	0.055	0.225	0.423	0.005	0.071	0.393	0.019	11.40
11.00	0.253	0.248	0.514	0.014	0.051	0.217	0.414	0.003	0.070	0.390	0.018	12.53
12.00	0.250	0.240	0.504	0.013	0.047	0.207	0.408	0.003	0.067	0.387	0.017	13.66
13.00	0.251	0.240	0.504	0.012	0.045	0.201	0.408	0.003	0.065	0.383	0.016	14.79
14.00	0.253	0.239	0.509	0.012	0.045	0.200	0.410	0.004	0.068	0.385	0.018	15.91
15.00	0.256	0.239	0.517	0.012	0.046	0.202	0.418	0.005	0.075	0.392	0.018	17.03
16.00	0.260	0.245	0.534	0.012	0.049	0.209	0.435	0.006	0.084	0.407	0.022	18.15
17.00	0.261	0.251	0.552	0.013	0.052	0.214	0.445	0.007	0.087	0.419	0.023	19.27
18.00	0.262	0.254	0.563	0.014	0.053	0.218	0.452	0.008	0.087	0.431	0.024	20.38
19.00	0.268	0.260	0.567	0.014	0.052	0.221	0.454	0.008	0.083	0.434	0.022	21.49
20.00	0.267	0.256	0.564	0.014	0.049	0.218	0.443	0.006	0.075	0.420	0.022	22.60
21.00	0.260	0.249	0.560	0.013	0.046	0.211	0.434	0.004	0.070	0.409	0.019	23.70
22.00	0.251	0.240	0.552	0.012	0.043	0.202	0.423	0.003	0.064	0.395	0.018	24.80
23.00	0.243	0.230	0.537	0.012	0.041	0.195	0.407	0.003	0.063	0.375	0.016	25.89
24.00	0.238	0.226	0.526	0.011	0.041	0.189	0.396	0.003	0.065	0.360	0.016	26.98
25.00	0.236	0.222	0.519	0.010	0.041	0.185	0.389	0.003	0.065	0.353	0.016	28.07
26.00	0.230	0.215	0.504	0.010	0.040	0.182	0.386	0.003	0.063	0.350	0.018	29.15
27.00	0.222	0.208	0.488	0.010	0.040	0.181	0.380	0.003	0.061	0.346	0.017	30.22
28.00	0.215	0.201	0.473	0.011	0.040	0.178	0.370	0.003	0.059	0.337	0.016	31.30
29.00	0.208	0.194	0.462	0.011	0.040	0.174	0.356	0.003	0.056	0.326	0.016	32.37
30.00	0.201	0.187	0.451	0.011	0.039	0.168	0.343	0.003	0.055	0.316	0.016	33.43
31.00	0.194	0.179	0.440	0.010	0.037	0.161	0.332	0.003	0.053	0.300	0.015	34.49
32.00	0.190	0.176	0.435	0.010	0.036	0.157	0.324	0.003	0.050	0.288	0.013	35.54
33.00	0.190	0.178	0.431	0.010	0.034	0.154	0.321	0.003	0.048	0.286	0.014	36.60
34.00	0.189	0.176	0.427	0.009	0.032	0.151	0.319	0.002	0.046	0.285	0.012	37.64
35.00	0.185	0.172	0.421	0.009	0.031	0.147	0.315	0.003	0.046	0.281	0.013	38.68
36.00	0.180	0.167	0.415	0.008	0.031	0.142	0.310	0.002	0.043	0.276	0.012	39.72
37.00	0.176	0.164	0.410	0.008	0.029	0.137	0.304	0.002	0.039	0.268	0.012	40.75
38.00	0.171	0.160	0.401	0.008	0.028	0.132	0.296	0.002	0.037	0.260	0.014	41.78
39.00	0.164	0.155	0.392	0.007	0.026	0.126	0.286	0.002	0.035	0.255	0.011	42.80
40.00	0.159	0.149	0.383	0.007	0.023	0.119	0.276	0.002	0.033	0.248	0.010	43.81
41.00	0.154	0.144	0.370	0.007	0.021	0.112	0.266	0.002	0.030	0.238	0.008	44.83
42.00	0.148	0.137	0.356	0.006	0.020	0.105	0.256	0.002	0.027	0.229	0.007	45.83
43.00	0.142	0.131	0.344	0.006	0.019	0.100	0.248	0.002	0.024	0.223	0.007	46.84
44.00	0.134	0.123	0.332	0.006	0.018	0.095	0.243	0.002	0.023	0.219	0.010	47.83
45.00	0.128	0.117	0.320	0.006	0.018	0.092	0.237	0.002	0.020	0.216	0.006	48.83
46.00	0.122	0.114	0.309	0.006	0.017	0.089	0.231	0.002	0.021	0.212	0.006	49.82
47.00	0.119	0.111	0.299	0.006	0.017	0.085	0.224	0.002	0.019	0.205	0.006	50.80
48.00	0.115	0.108	0.290	0.006	0.016	0.081	0.217	0.002	0.018	0.201	0.010	51.78
49.00	0.112	0.105	0.282	0.007	0.016	0.077	0.210	0.002	0.018	0.196	0.007	52.76
50.00	0.108	0.102	0.274	0.007	0.016	0.074	0.202	0.002	0.016	0.186	0.008	53.73
51.00	0.105	0.100	0.266	0.007	0.016	0.071	0.193	0.003	0.017	0.176	0.008	54.69
52.00	0.103	0.098	0.258	0.008	0.016	0.068	0.186	0.003	0.017	0.169	0.007	55.66
53.00	0.101	0.094	0.249	0.008	0.016	0.065	0.181	0.003	0.017	0.163	0.009	56.61
54.00	0.097	0.091	0.243	0.009	0.017	0.063	0.177	0.004	0.018	0.158	0.008	57.57
55.00	0.095	0.089	0.238	0.009	0.017	0.060	0.173	0.004	0.016	0.154	0.006	58.52
56.00	0.093	0.088	0.234	0.010	0.017	0.058	0.168	0.004	0.015	0.149	0.006	59.46
57.00	0.092	0.086	0.228	0.010	0.017	0.055	0.164	0.004	0.015	0.144	0.006	60.41
58.00	0.090	0.084	0.221	0.010	0.017	0.053	0.159	0.004	0.015	0.139	0.008	61.34
59.00	0.088	0.082	0.214	0.011	0.018	0.051	0.155	0.004	0.016	0.134	0.007	62.28
60.00	0.086	0.079	0.206	0.011	0.018	0.049	0.151	0.005	0.016	0.129	0.007	63.21
61.00	0.084	0.078	0.200	0.012	0.019	0.048	0.146	0.005	0.015	0.125	0.007	64.14
62.00	0.082	0.077	0.194	0.012	0.019	0.047	0.141	0.006	0.017	0.120	0.008	65.06
63.00	0.081	0.075	0.188	0.013	0.020	0.046	0.137	0.006	0.016	0.116	0.008	65.98
64.00	0.078	0.073	0.181	0.013	0.020	0.045	0.133	0.007	0.016	0.112	0.007	66.90
65.00	0.076	0.071	0.173	0.014	0.021	0.044	0.128	0.008	0.017	0.109	0.008	67.81
66.00	0.074	0.068	0.166	0.014	0.021	0.043	0.124	0.008	0.018	0.106	0.009	68.72
67.00	0.071	0.065	0.158	0.015	0.022	0.042	0.120	0.008	0.018	0.102	0.009	69.63
68.00	0.068	0.061	0.150	0.015	0.022	0.041	0.115	0.009	0.018	0.099	0.010	70.54
69.00	0.065	0.058	0.143	0.015	0.022	0.040	0.110	0.009	0.018	0.094	0.011	71.44
70.00	0.062	0.055	0.136	0.015	0.022	0.039	0.104	0.010	0.018	0.090	0.010	72.34
71.00	0.059	0.052	0.129	0.015	0.022	0.038	0.099	0.010	0.018	0.086	0.010	73.24
72.00	0.056	0.050	0.122	0.015	0.022	0.037	0.094	0.010	0.018	0.081	0.010	74.14
73.00	0.053	0.047	0.116	0.015	0.021	0.035	0.088	0.010	0.017	0.076	0.010	75.03
74.00	0.050	0.044	0.109	0.015	0.021	0.034	0.083	0.010	0.016	0.071	0.010	75.92
75.00	0.047	0.041	0.103	0.014	0.020	0.032	0.077	0.010	0.016	0.066	0.010	76.81
76.00	0.044	0.039	0.097	0.014	0.019	0.031	0.072	0.009	0.015	0.061	0.009	77.70
77.00	0.041	0.036	0.090	0.013	0.018	0.029	0.067	0.009	0.013	0.056	0.010	78.58
78.00	0.039	0.033	0.085	0.012	0.016	0.027	0.062	0.009	0.012	0.052	0.010	79.47
79.00	0.036	0.030	0.079	0.011	0.015	0.025	0.057	0.008	0.011	0.048	0.009	80.35
80.00	0.034	0.028	0.074	0.011	0.014	0.024	0.053	0.007	0.010	0.044	0.009	81.23

Saturn - VIS

Lat PC (°)	(I/F) UV	(I/F) Vio	(I/F) B	(I/F) V	(I/F) R	(I/F) M1	(I/F) C1	(I/F) M2	(I/F) C2	(I/F) M3	(I/F) C3	Lat PG (°)
0.00	0.183	0.217	0.418	0.611	0.712	0.652	0.831	0.480	0.860	0.154	0.810	0.00
1.00	0.180	0.214	0.422	0.619	0.726	0.662	0.845	0.484	0.878	0.150	0.820	1.14
2.00	0.178	0.211	0.425	0.627	0.738	0.659	0.855	0.485	0.892	0.150	0.830	2.29
3.00	0.176	0.209	0.427	0.635	0.750	0.674	0.869	0.489	0.906	0.149	0.840	3.43
4.00	0.174	0.207	0.430	0.642	0.760	0.683	0.880	0.491	0.920	0.145	0.845	4.57
5.00	0.172	0.206	0.432	0.649	0.770	0.685	0.892	0.496	0.934	0.143	0.850	5.71
6.00	0.171	0.205	0.435	0.655	0.780	0.690	0.903	0.497	0.948	0.140	0.863	6.85
7.00	0.170	0.204	0.435	0.660	0.787	0.693	0.918	0.501	0.963	0.135	0.869	7.99
8.00	0.169	0.203	0.437	0.663	0.793	0.704	0.924	0.498	0.977	0.133	0.882	9.13
9.00	0.170	0.202	0.436	0.663	0.797	0.697	0.935	0.494	0.987	0.125	0.886	10.26
10.00	0.169	0.201	0.436	0.662	0.798	0.694	0.945	0.488	0.996	0.118	0.886	11.40
11.00	0.170	0.201	0.432	0.657	0.796	0.689	0.951	0.477	0.999	0.112	0.885	12.53
12.00	0.172	0.202	0.430	0.651	0.791	0.677	0.951	0.463	1.000	0.106	0.878	13.66
13.00	0.173	0.202	0.426	0.643	0.783	0.664	0.946	0.443	0.996	0.096	0.872	14.79
14.00	0.175	0.203	0.422	0.634	0.776	0.654	0.946	0.429	0.992	0.089	0.863	15.91
15.00	0.178	0.204	0.417	0.626	0.765	0.645	0.929	0.409	0.981	0.081	0.860	17.03
16.00	0.180	0.205	0.413	0.619	0.757	0.633	0.917	0.389	0.972	0.075	0.849	18.15
17.00	0.183	0.207	0.411	0.612	0.749	0.633	0.905	0.377	0.960	0.065	0.845	19.27
18.00	0.184	0.209	0.409	0.606	0.742	0.621	0.898	0.368	0.951	0.063	0.835	20.38
19.00	0.187	0.211	0.407	0.601	0.735	0.617	0.884	0.359	0.941	0.060	0.826	21.49
20.00	0.189	0.212	0.404	0.598	0.729	0.616	0.882	0.352	0.935	0.058	0.825	22.60
21.00	0.190	0.214	0.404	0.595	0.725	0.610	0.879	0.346	0.929	0.054	0.826	23.70
22.00	0.191	0.215	0.402	0.594	0.722	0.610	0.870	0.345	0.924	0.056	0.824	24.80
23.00	0.192	0.216	0.402	0.593	0.718	0.609	0.867	0.346	0.918	0.054	0.827	25.89
24.00	0.193	0.217	0.401	0.593	0.716	0.612	0.859	0.345	0.914	0.052	0.828	26.98
25.00	0.194	0.217	0.403	0.593	0.714	0.604	0.857	0.344	0.914	0.053	0.828	28.07
26.00	0.195	0.218	0.403	0.594	0.712	0.602	0.854	0.345	0.910	0.052	0.831	29.15
27.00	0.195	0.219	0.403	0.594	0.711	0.602	0.854	0.343	0.905	0.053	0.830	30.22
28.00	0.195	0.220	0.404	0.595	0.710	0.598	0.845	0.344	0.903	0.053	0.828	31.30
29.00	0.195	0.220	0.405	0.596	0.707	0.604	0.843	0.337	0.903	0.052	0.834	32.37
30.00	0.196	0.220	0.406	0.597	0.706	0.601	0.844	0.342	0.904	0.053	0.836	33.43
31.00	0.196	0.221	0.407	0.598	0.705	0.602	0.837	0.338	0.899	0.052	0.840	34.49
32.00	0.196	0.221	0.407	0.598	0.702	0.600	0.836	0.339	0.897	0.051	0.834	35.54
33.00	0.196	0.221	0.408	0.598	0.700	0.587	0.832	0.340	0.900	0.051	0.833	36.60
34.00	0.196	0.221	0.408	0.598	0.699	0.581	0.825	0.338	0.896	0.053	0.833	37.64
35.00	0.196	0.221	0.408	0.597	0.696	0.589	0.822	0.343	0.893	0.052	0.829	38.68
36.00	0.195	0.221	0.407	0.596	0.695	0.583	0.819	0.342	0.890	0.052	0.833	39.72
37.00	0.195	0.221	0.407	0.594	0.692	0.589	0.813	0.339	0.886	0.055	0.829	40.75
38.00	0.195	0.220	0.406	0.592	0.689	0.581	0.810	0.345	0.880	0.052	0.822	41.78
39.00	0.195	0.220	0.405	0.590	0.685	0.577	0.808	0.343	0.878	0.052	0.822	42.80
40.00	0.195	0.220	0.403	0.588	0.683	0.578	0.800	0.342	0.874	0.050	0.820	43.81
41.00	0.195	0.220	0.402	0.585	0.679	0.570	0.796	0.336	0.868	0.052	0.815	44.83
42.00	0.196	0.219	0.401	0.582	0.676	0.562	0.794	0.334	0.864	0.051	0.807	45.83
43.00	0.196	0.219	0.399	0.578	0.674	0.559	0.790	0.330	0.859	0.051	0.801	46.84
44.00	0.195	0.219	0.398	0.574	0.669	0.558	0.787	0.328	0.857	0.049	0.801	47.83
45.00	0.195	0.218	0.396	0.572	0.666	0.556	0.777	0.325	0.853	0.050	0.799	48.83
46.00	0.194	0.217	0.394	0.569	0.662	0.557	0.779	0.326	0.852	0.047	0.795	49.82
47.00	0.193	0.215	0.393	0.567	0.659	0.554	0.777	0.328	0.847	0.050	0.793	50.80
48.00	0.192	0.214	0.391	0.564	0.655	0.556	0.774	0.333	0.842	0.049	0.799	51.78
49.00	0.191	0.213	0.388	0.561	0.652	0.555	0.774	0.333	0.838	0.053	0.796	52.76
50.00	0.190	0.211	0.385	0.557	0.648	0.564	0.770	0.336	0.835	0.056	0.790	53.73
51.00	0.188	0.209	0.382	0.554	0.643	0.547	0.763	0.337	0.827	0.054	0.789	54.69
52.00	0.186	0.208	0.379	0.550	0.638	0.548	0.757	0.338	0.820	0.055	0.783	55.66
53.00	0.186	0.206	0.376	0.545	0.633	0.545	0.751	0.335	0.810	0.056	0.773	56.61
54.00	0.184	0.204	0.372	0.541	0.626	0.532	0.740	0.334	0.803	0.054	0.779	57.57
55.00	0.183	0.202	0.369	0.536	0.619	0.535	0.731	0.332	0.795	0.053	0.764	58.52
56.00	0.182	0.201	0.365	0.531	0.613	0.516	0.727	0.330	0.787	0.053	0.755	59.46
57.00	0.181	0.199	0.362	0.525	0.606	0.511	0.713	0.324	0.774	0.053	0.750	60.41
58.00	0.179	0.198	0.358	0.520	0.598	0.496	0.703	0.322	0.765	0.052	0.743	61.34
59.00	0.178	0.197	0.353	0.515	0.591	0.490	0.696	0.321	0.752	0.050	0.728	62.28
60.00	0.178	0.196	0.349	0.509	0.583	0.484	0.685	0.317	0.741	0.049	0.724	63.21
61.00	0.177	0.195	0.346	0.503	0.575	0.470	0.676	0.311	0.729	0.048	0.705	64.14
62.00	0.176	0.194	0.343	0.497	0.567	0.464	0.665	0.308	0.717	0.047	0.698	65.06
63.00	0.175	0.193	0.338	0.490	0.558	0.455	0.659	0.301	0.703	0.046	0.677	65.98
64.00	0.174	0.193	0.334	0.484	0.550	0.450	0.645	0.300	0.691	0.047	0.660	66.90
65.00	0.174	0.192	0.331	0.477	0.541	0.443	0.640	0.295	0.674	0.046	0.651	67.81
66.00	0.173	0.191	0.328	0.471	0.532	0.440	0.631	0.290	0.661	0.045	0.631	68.72
67.00	0.172	0.190	0.324	0.465	0.523	0.433	0.616	0.286	0.646	0.045	0.612	69.63
68.00	0.171	0.189	0.320	0.458	0.514	0.422	0.609	0.282	0.630	0.039	0.599	70.54
69.00	0.170	0.189	0.316	0.451	0.505	0.418	0.604	0.277	0.617	0.043	0.584	71.44
70.00	0.170	0.188	0.313	0.444	0.495	0.416	0.588	0.270	0.605	0.040	0.572	72.34
71.00	0.169	0.187	0.309	0.437	0.486	0.398	0.581	0.264	0.588	0.038	0.563	73.24
72.00	0.168	0.186	0.304	0.430	0.475	0.395	0.573	0.258	0.575	0.037	0.548	74.14
73.00	0.167	0.185	0.301	0.422	0.465	0.386	0.557	0.251	0.563	0.035	0.532	75.03
74.00	0.165	0.184	0.297	0.415	0.454	0.381	0.554	0.243	0.552	0.032	0.517	75.92
75.00	0.165	0.182	0.292	0.407	0.445	0.369	0.539	0.234	0.535	0.033	0.511	76.81
76.00	0.164	0.181	0.287	0.400	0.435	0.356	0.528	0.225	0.523	0.034	0.496	77.70
77.00	0.163	0.180	0.284	0.392	0.424	0.346	0.518	0.219	0.511	0.028	0.482	78.58
78.00	0.161	0.179	0.279	0.385	0.414	0.333	0.508	0.210	0.498	0.029	0.472	79.47
79.00	0.159	0.178	0.275	0.377	0.404	0.323	0.497	0.202	0.486	0.027	0.461	80.35
80.00	0.158	0.176	0.270	0.369	0.395	0.314	0.486	0.194	0.472	0.028	0.453	81.23

Saturn - SWIR

Lat PC (°)	(I/F) J	(I/F) H	(I/F) YC	(I/F) YM	(I/F) V1	(I/F) V2	(I/F) JC	(I/F) HC	(I/F) HM	Lat PG (°)
0.00	0.544	0.616	0.731	0.074	0.138	0.469	0.718	0.710	0.090	0.00
1.00	0.550	0.626	0.742	0.072	0.136	0.475	0.732	0.725	0.096	1.14
2.00	0.557	0.636	0.752	0.069	0.136	0.480	0.743	0.739	0.099	2.29
3.00	0.563	0.646	0.760	0.068	0.136	0.484	0.754	0.751	0.105	3.43
4.00	0.568	0.655	0.768	0.066	0.135	0.488	0.766	0.765	0.124	4.57
5.00	0.574	0.664	0.776	0.064	0.133	0.492	0.777	0.776	0.109	5.71
6.00	0.579	0.673	0.783	0.062	0.132	0.494	0.789	0.787	0.111	6.85
7.00	0.581	0.679	0.788	0.060	0.129	0.494	0.797	0.795	0.116	7.99
8.00	0.582	0.682	0.793	0.057	0.125	0.492	0.803	0.802	0.145	9.13
9.00	0.582	0.682	0.795	0.054	0.121	0.488	0.806	0.806	0.135	10.26
10.00	0.579	0.679	0.794	0.052	0.116	0.481	0.806	0.810	0.112	11.40
11.00	0.573	0.672	0.791	0.048	0.109	0.471	0.806	0.812	0.085	12.53
12.00	0.564	0.662	0.785	0.044	0.101	0.459	0.803	0.812	0.048	13.66
13.00	0.553	0.651	0.777	0.040	0.094	0.444	0.798	0.808	0.039	14.79
14.00	0.540	0.637	0.766	0.036	0.085	0.427	0.790	0.801	0.038	15.91
15.00	0.524	0.624	0.754	0.032	0.077	0.410	0.778	0.791	0.045	17.03
16.00	0.510	0.612	0.742	0.029	0.070	0.395	0.767	0.780	0.040	18.15
17.00	0.498	0.603	0.731	0.026	0.065	0.383	0.754	0.770	0.028	19.27
18.00	0.490	0.596	0.723	0.024	0.060	0.375	0.744	0.762	0.030	20.38
19.00	0.484	0.591	0.719	0.022	0.057	0.370	0.735	0.756	0.033	21.49
20.00	0.480	0.588	0.717	0.021	0.055	0.369	0.730	0.754	0.032	22.60
21.00	0.478	0.585	0.716	0.020	0.054	0.368	0.728	0.752	0.025	23.70
22.00	0.476	0.583	0.716	0.020	0.053	0.367	0.729	0.749	0.027	24.80
23.00	0.474	0.581	0.716	0.020	0.052	0.367	0.728	0.747	0.024	25.89
24.00	0.473	0.580	0.716	0.019	0.052	0.367	0.725	0.745	0.036	26.98
25.00	0.472	0.578	0.714	0.019	0.051	0.367	0.721	0.744	0.041	28.07
26.00	0.471	0.576	0.713	0.019	0.051	0.365	0.718	0.743	0.028	29.15
27.00	0.470	0.575	0.711	0.018	0.050	0.364	0.715	0.741	0.026	30.22
28.00	0.469	0.573	0.709	0.018	0.049	0.362	0.714	0.740	0.027	31.30
29.00	0.467	0.570	0.707	0.018	0.049	0.361	0.711	0.738	0.023	32.37
30.00	0.465	0.568	0.706	0.018	0.048	0.360	0.708	0.736	0.024	33.43
31.00	0.462	0.566	0.705	0.017	0.047	0.358	0.706	0.732	0.027	34.49
32.00	0.458	0.563	0.705	0.017	0.047	0.356	0.702	0.728	0.023	35.54
33.00	0.455	0.560	0.704	0.017	0.047	0.355	0.699	0.724	0.018	36.60
34.00	0.452	0.558	0.701	0.017	0.047	0.354	0.696	0.720	0.091	37.64
35.00	0.450	0.556	0.698	0.017	0.047	0.354	0.693	0.717	0.100	38.68
36.00	0.449	0.553	0.695	0.017	0.048	0.355	0.690	0.713	0.045	39.72
37.00	0.448	0.552	0.691	0.017	0.048	0.356	0.687	0.710	0.022	40.75
38.00	0.449	0.550	0.688	0.018	0.048	0.357	0.684	0.708	0.042	41.78
39.00	0.448	0.547	0.686	0.018	0.049	0.357	0.683	0.706	0.033	42.80
40.00	0.446	0.542	0.683	0.017	0.049	0.354	0.680	0.702	0.016	43.81
41.00	0.441	0.536	0.678	0.017	0.047	0.350	0.677	0.697	0.039	44.83
42.00	0.434	0.529	0.673	0.017	0.046	0.344	0.670	0.691	0.029	45.83
43.00	0.427	0.524	0.668	0.016	0.043	0.337	0.662	0.684	0.025	46.84
44.00	0.421	0.521	0.662	0.015	0.042	0.331	0.654	0.677	0.014	47.83
45.00	0.419	0.519	0.658	0.014	0.040	0.328	0.649	0.673	0.011	48.83
46.00	0.420	0.519	0.656	0.015	0.040	0.329	0.647	0.670	0.014	49.82
47.00	0.423	0.518	0.657	0.015	0.041	0.332	0.648	0.668	0.012	50.80
48.00	0.426	0.518	0.658	0.015	0.041	0.336	0.650	0.667	0.010	51.78
49.00	0.429	0.516	0.658	0.015	0.042	0.339	0.652	0.663	0.009	52.76
50.00	0.429	0.512	0.657	0.016	0.042	0.341	0.652	0.660	0.015	53.73
51.00	0.427	0.507	0.654	0.016	0.043	0.341	0.648	0.654	0.025	54.69
52.00	0.424	0.501	0.651	0.016	0.044	0.340	0.643	0.646	0.025	55.66
53.00	0.421	0.493	0.647	0.016	0.044	0.339	0.637	0.637	0.022	56.61
54.00	0.416	0.484	0.643	0.016	0.045	0.337	0.631	0.629	0.018	57.57
55.00	0.411	0.475	0.638	0.016	0.045	0.333	0.624	0.618	0.016	58.52
56.00	0.403	0.465	0.633	0.017	0.045	0.329	0.618	0.607	0.020	59.46
57.00	0.394	0.455	0.629	0.017	0.045	0.324	0.612	0.595	0.019	60.41
58.00	0.385	0.445	0.624	0.017	0.045	0.318	0.605	0.582	0.013	61.34
59.00	0.376	0.434	0.616	0.016	0.044	0.312	0.598	0.568	0.008	62.28
60.00	0.368	0.423	0.606	0.016	0.043	0.304	0.588	0.554	0.014	63.21
61.00	0.358	0.410	0.593	0.016	0.042	0.296	0.574	0.539	0.010	64.14
62.00	0.347	0.397	0.577	0.015	0.040	0.288	0.559	0.524	0.011	65.06
63.00	0.337	0.383	0.558	0.015	0.039	0.278	0.541	0.507	0.007	65.98
64.00	0.325	0.369	0.539	0.015	0.037	0.268	0.521	0.489	0.003	66.90
65.00	0.313	0.355	0.519	0.015	0.036	0.257	0.502	0.472	0.000	67.81
66.00	0.302	0.342	0.499	0.014	0.035	0.247	0.481	0.454	0.002	68.72
67.00	0.292	0.329	0.480	0.014	0.033	0.238	0.461	0.436	0.000	69.63
68.00	0.283	0.319	0.462	0.014	0.032	0.230	0.444	0.420	0.001	70.54
69.00	0.275	0.308	0.447	0.013	0.031	0.223	0.430	0.406	0.002	71.44
70.00	0.267	0.298	0.434	0.013	0.030	0.216	0.417	0.393	0.000	72.34
71.00	0.259	0.288	0.421	0.013	0.029	0.209	0.404	0.380	0.006	73.24
72.00	0.251	0.278	0.410	0.013	0.028	0.202	0.392	0.367	0.009	74.14
73.00	0.243	0.267	0.398	0.013	0.028	0.195	0.381	0.355	0.006	75.03
74.00	0.235	0.255	0.386	0.013	0.027	0.188	0.369	0.342	0.000	75.92
75.00	0.225	0.242	0.374	0.013	0.027	0.180	0.357	0.329	0.000	76.81
76.00	0.216	0.230	0.362	0.013	0.026	0.172	0.344	0.315	0.000	77.70
77.00	0.207	0.219	0.350	0.013	0.025	0.164	0.331	0.301	0.000	78.58
78.00	0.198	0.208	0.338	0.013	0.024	0.157	0.318	0.288	0.001	79.47
79.00	0.190	0.198	0.326	0.012	0.023	0.150	0.305	0.275	0.006	80.35
80.00	0.183	0.189	0.315	0.012	0.022	0.144	0.294	0.263	0.006	81.23

A2. Minnaert Coefficients $(I/F)_0$ and k

Minnaert $(I/F)_0$ and K coefficients for Jupiter PlanetCam VIS observations. December2012 (black), December2013 (blue), April2014 (green), March2015 (red), March2016 (cyan), May2016 (magenta). Tables provide mean values.

Jupiter $(I/F)_0$ – VIS

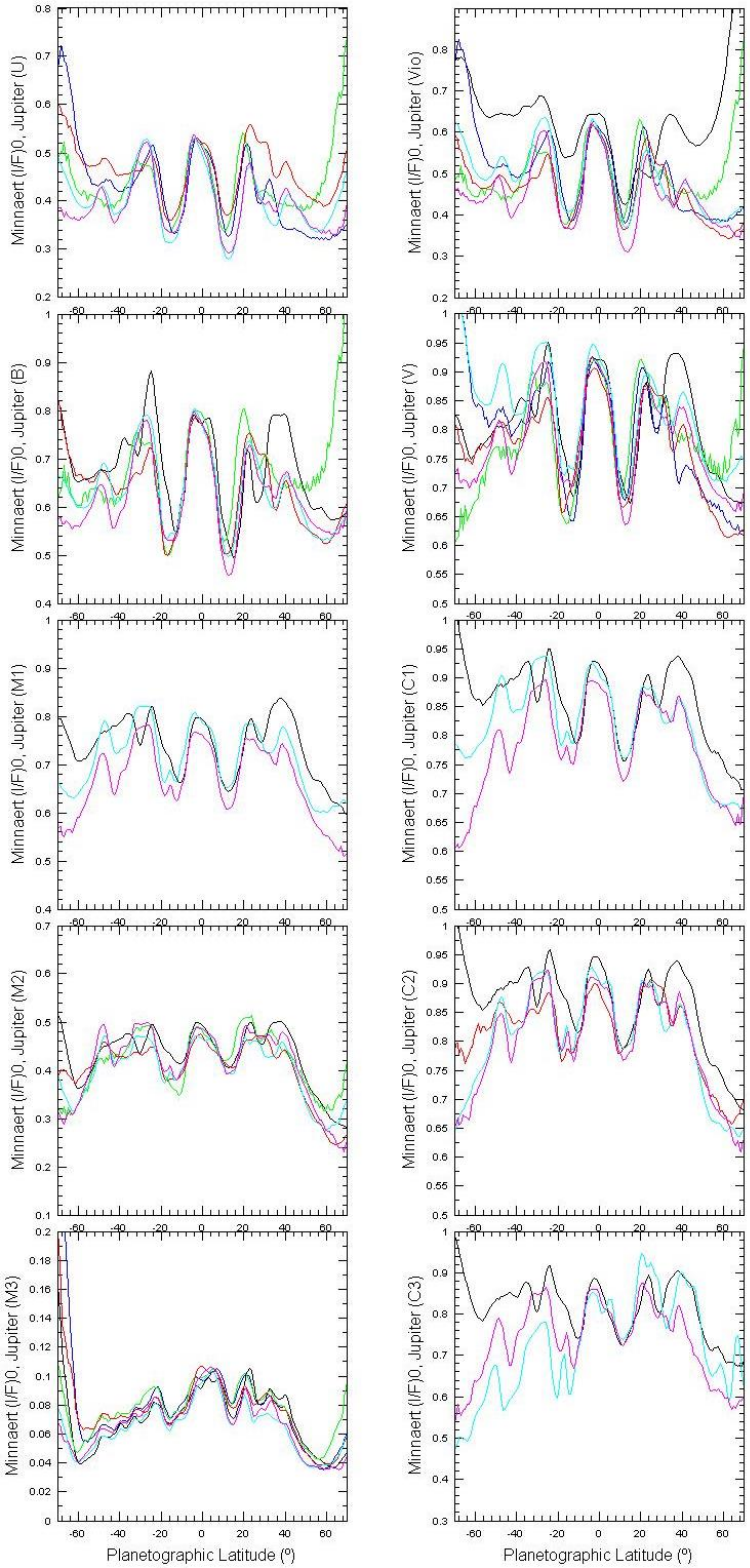

Jupiter *k* – VIS

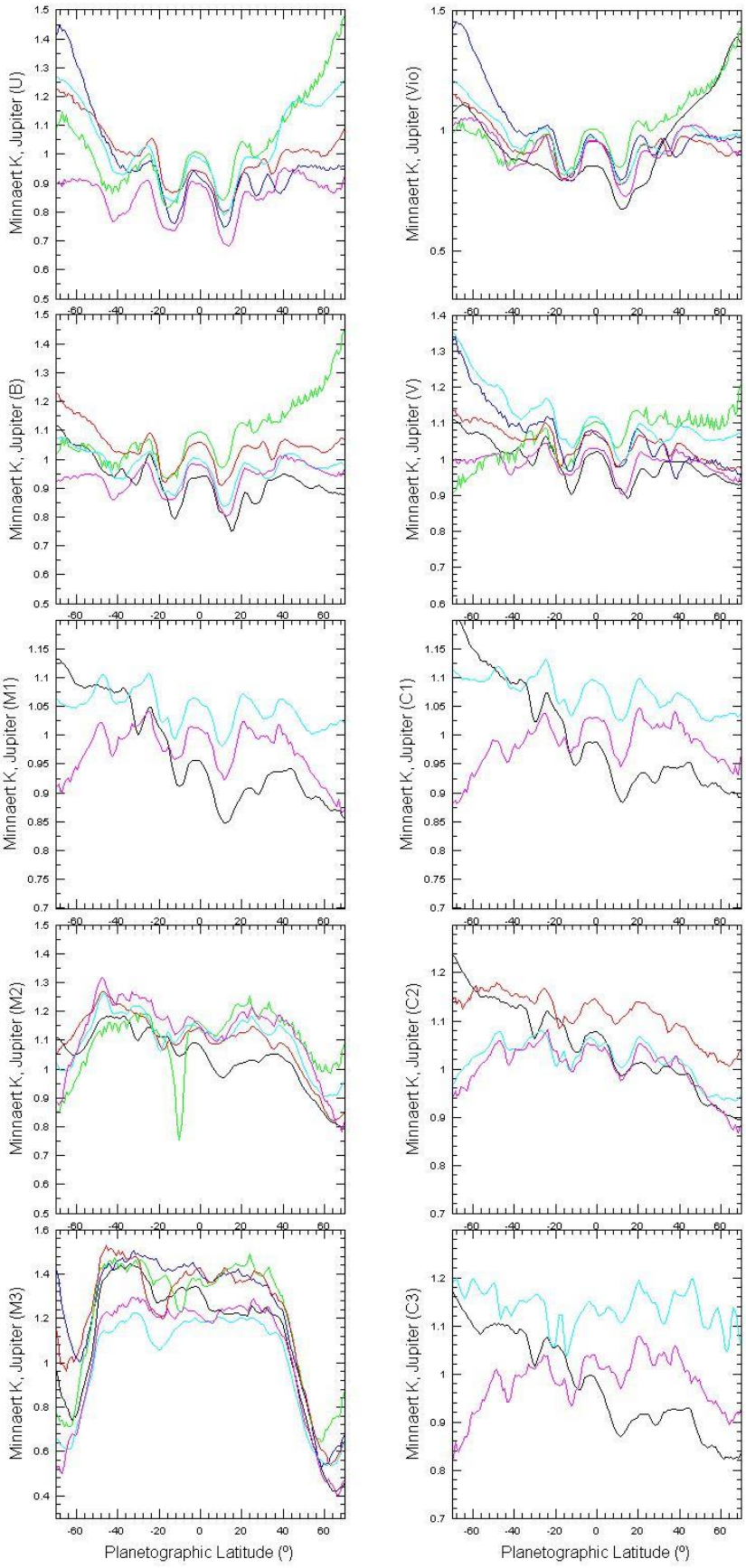

Jupiter $(I/F)_0$ – VIS

Lat PC (°)	$(I/F)_o$ UV	$(I/F)_o$ Vio	$(I/F)_o$ B	$(I/F)_o$ V	$(I/F)_o$ M1	$(I/F)_o$ C1	$(I/F)_o$ M2	$(I/F)_o$ C2	$(I/F)_o$ M3	$(I/F)_o$ C3	Lat PG (°)
-76	0.156	0.132	0.231	0.236	0.413	0.407	0.266	0.307	0.045	0.114	-77.70
-75	0.483	0.218	0.415	0.492	0.433	0.470	0.286	0.444	0.081	0.168	-76.81
-74	0.284	0.294	0.436	0.451	0.450	0.479	0.310	0.366	0.098	0.185	-75.92
-73	0.420	0.427	0.455	0.791	0.442	0.479	0.283	0.399	0.181	0.241	-75.03
-72	0.453	0.571	0.680	0.893	0.662	0.789	0.423	0.674	0.273	0.607	-74.14
-71	0.481	0.590	0.710	0.876	0.669	0.798	0.407	0.724	0.271	0.587	-73.24
-70	0.508	0.611	0.722	0.885	0.677	0.814	0.406	0.738	0.247	0.631	-72.34
-69	0.520	0.610	0.718	0.875	0.685	0.822	0.398	0.759	0.209	0.644	-71.44
-68	0.530	0.618	0.706	0.867	0.677	0.808	0.390	0.773	0.182	0.657	-70.54
-67	0.530	0.620	0.698	0.852	0.675	0.802	0.383	0.778	0.156	0.670	-69.63
-66	0.536	0.626	0.694	0.853	0.673	0.798	0.378	0.782	0.140	0.677	-68.72
-65	0.528	0.620	0.684	0.836	0.664	0.790	0.371	0.773	0.122	0.674	-67.81
-64	0.524	0.617	0.686	0.826	0.658	0.782	0.367	0.774	0.110	0.663	-66.90
-63	0.514	0.606	0.667	0.814	0.658	0.776	0.360	0.772	0.099	0.658	-65.98
-62	0.504	0.596	0.660	0.807	0.652	0.770	0.356	0.763	0.089	0.650	-65.06
-61	0.490	0.582	0.643	0.791	0.647	0.768	0.348	0.765	0.079	0.649	-64.14
-60	0.477	0.568	0.632	0.779	0.641	0.763	0.340	0.763	0.070	0.644	-63.21
-59	0.465	0.554	0.625	0.772	0.640	0.765	0.339	0.769	0.063	0.647	-62.28
-58	0.451	0.540	0.619	0.768	0.642	0.768	0.340	0.774	0.057	0.658	-61.34
-57	0.442	0.532	0.616	0.769	0.645	0.772	0.345	0.781	0.053	0.665	-60.41
-56	0.435	0.522	0.616	0.768	0.647	0.773	0.351	0.784	0.050	0.665	-59.46
-55	0.431	0.516	0.618	0.774	0.654	0.778	0.359	0.789	0.050	0.666	-58.52
-54	0.427	0.513	0.622	0.779	0.660	0.783	0.367	0.788	0.050	0.669	-57.57
-53	0.425	0.509	0.624	0.781	0.665	0.784	0.373	0.792	0.051	0.675	-56.61
-52	0.418	0.503	0.623	0.776	0.673	0.792	0.380	0.798	0.052	0.689	-55.66
-51	0.420	0.504	0.629	0.784	0.682	0.799	0.389	0.802	0.053	0.700	-54.69
-50	0.419	0.503	0.633	0.786	0.692	0.809	0.399	0.810	0.054	0.716	-53.73
-49	0.421	0.504	0.638	0.791	0.703	0.819	0.408	0.818	0.056	0.732	-52.76
-48	0.426	0.509	0.647	0.802	0.719	0.833	0.422	0.832	0.058	0.747	-51.78
-47	0.430	0.515	0.656	0.810	0.735	0.847	0.437	0.848	0.062	0.758	-50.80
-46	0.434	0.519	0.662	0.818	0.748	0.858	0.449	0.861	0.064	0.765	-49.82
-45	0.437	0.523	0.663	0.824	0.756	0.863	0.456	0.868	0.066	0.757	-48.83
-44	0.433	0.519	0.657	0.820	0.760	0.867	0.458	0.871	0.065	0.740	-47.83
-43	0.432	0.519	0.655	0.823	0.757	0.860	0.457	0.868	0.065	0.725	-46.84
-42	0.422	0.511	0.643	0.814	0.748	0.850	0.449	0.859	0.064	0.715	-45.83
-41	0.417	0.505	0.635	0.810	0.736	0.839	0.443	0.847	0.063	0.713	-44.83
-40	0.408	0.496	0.624	0.798	0.722	0.830	0.435	0.835	0.063	0.707	-43.81
-39	0.400	0.486	0.616	0.784	0.715	0.827	0.428	0.829	0.064	0.708	-42.80
-38	0.402	0.487	0.621	0.786	0.716	0.831	0.430	0.830	0.066	0.715	-41.78
-37	0.404	0.489	0.629	0.790	0.724	0.840	0.433	0.837	0.067	0.728	-40.75
-36	0.407	0.493	0.637	0.794	0.734	0.845	0.437	0.844	0.069	0.738	-39.72
-35	0.412	0.499	0.646	0.801	0.737	0.845	0.440	0.847	0.069	0.747	-38.68
-34	0.417	0.506	0.652	0.807	0.741	0.850	0.442	0.849	0.068	0.761	-37.64
-33	0.422	0.512	0.661	0.813	0.747	0.859	0.444	0.854	0.068	0.776	-36.60
-32	0.430	0.519	0.673	0.821	0.757	0.873	0.446	0.864	0.069	0.794	-35.54
-31	0.446	0.534	0.697	0.841	0.772	0.891	0.458	0.879	0.072	0.808	-34.49
-30	0.460	0.549	0.715	0.860	0.784	0.902	0.468	0.891	0.075	0.816	-33.43
-29	0.471	0.561	0.724	0.869	0.785	0.900	0.469	0.891	0.075	0.813	-32.37
-28	0.478	0.569	0.728	0.871	0.780	0.894	0.467	0.885	0.074	0.807	-31.30
-27	0.482	0.575	0.730	0.871	0.778	0.890	0.463	0.882	0.074	0.805	-30.22
-26	0.489	0.584	0.742	0.877	0.782	0.894	0.466	0.885	0.075	0.812	-29.15
-25	0.495	0.591	0.757	0.887	0.789	0.902	0.469	0.893	0.076	0.823	-28.07
-24	0.500	0.597	0.771	0.899	0.798	0.914	0.474	0.905	0.078	0.837	-26.98
-23	0.502	0.600	0.778	0.909	0.805	0.922	0.477	0.915	0.080	0.848	-25.89
-22	0.498	0.596	0.771	0.909	0.803	0.921	0.478	0.920	0.083	0.843	-24.80
-21	0.485	0.581	0.750	0.895	0.788	0.906	0.472	0.913	0.085	0.819	-23.70
-20	0.459	0.552	0.709	0.862	0.760	0.882	0.456	0.890	0.086	0.775	-22.60
-19	0.431	0.519	0.663	0.823	0.728	0.853	0.438	0.857	0.086	0.741	-21.49
-18	0.400	0.484	0.614	0.778	0.702	0.826	0.420	0.829	0.083	0.723	-20.38
-17	0.374	0.453	0.574	0.737	0.684	0.808	0.405	0.812	0.078	0.726	-19.27
-16	0.355	0.430	0.549	0.709	0.676	0.799	0.397	0.804	0.072	0.741	-18.15
-15	0.344	0.416	0.540	0.698	0.679	0.804	0.396	0.813	0.068	0.753	-17.03
-14	0.339	0.411	0.539	0.696	0.686	0.810	0.399	0.825	0.067	0.742	-15.91
-13	0.338	0.411	0.537	0.692	0.679	0.801	0.394	0.819	0.068	0.714	-14.79
-12	0.340	0.414	0.538	0.688	0.662	0.784	0.386	0.800	0.071	0.691	-13.66
-11	0.348	0.422	0.549	0.693	0.653	0.777	0.382	0.790	0.073	0.692	-12.53
-10	0.359	0.435	0.571	0.711	0.659	0.786	0.384	0.798	0.074	0.706	-11.40
-9	0.378	0.457	0.600	0.743	0.674	0.803	0.391	0.814	0.075	0.725	-10.26
-8	0.400	0.483	0.634	0.777	0.690	0.820	0.402	0.825	0.076	0.744	-9.13
-7	0.432	0.517	0.681	0.817	0.712	0.844	0.420	0.839	0.078	0.776	-7.99
-6	0.471	0.558	0.735	0.863	0.743	0.875	0.442	0.871	0.082	0.812	-6.85
-5	0.507	0.596	0.776	0.900	0.771	0.901	0.462	0.901	0.087	0.842	-5.71
-4	0.527	0.620	0.793	0.918	0.785	0.913	0.474	0.914	0.092	0.858	-4.57
-3	0.531	0.626	0.794	0.923	0.790	0.916	0.482	0.919	0.096	0.865	-3.43
-2	0.527	0.622	0.788	0.922	0.788	0.915	0.484	0.919	0.098	0.865	-2.29
-1	0.519	0.616	0.780	0.918	0.784	0.910	0.483	0.916	0.098	0.862	-1.14
0	0.512	0.609	0.774	0.911	0.780	0.905	0.480	0.910	0.099	0.847	0.00

Lat PC (°)	$(I/F)_o$ UV	$(I/F)_o$ Vio	$(I/F)_o$ B	$(I/F)_o$ V	$(I/F)_o$ M1	$(I/F)_o$ C1	$(I/F)_o$ M2	$(I/F)_o$ C2	$(I/F)_o$ M3	$(I/F)_o$ C3	Lat PG (°)
0	0.512	0.609	0.774	0.911	0.780	0.905	0.480	0.910	0.099	0.847	0.00
1	0.504	0.599	0.767	0.903	0.774	0.898	0.474	0.901	0.100	0.828	1.14
2	0.493	0.586	0.758	0.894	0.769	0.892	0.469	0.895	0.101	0.818	2.29
3	0.478	0.569	0.743	0.884	0.763	0.887	0.466	0.892	0.102	0.815	3.43
4	0.459	0.544	0.718	0.865	0.751	0.873	0.461	0.885	0.102	0.814	4.57
5	0.434	0.514	0.681	0.837	0.731	0.852	0.454	0.869	0.102	0.807	5.71
6	0.405	0.479	0.635	0.797	0.705	0.823	0.444	0.844	0.102	0.785	6.85
7	0.375	0.442	0.585	0.754	0.679	0.795	0.432	0.815	0.099	0.762	7.99
8	0.350	0.410	0.543	0.716	0.658	0.771	0.422	0.794	0.095	0.747	9.13
9	0.332	0.388	0.519	0.691	0.643	0.755	0.414	0.785	0.088	0.732	10.26
10	0.324	0.377	0.508	0.680	0.635	0.746	0.407	0.782	0.082	0.728	11.40
11	0.324	0.376	0.507	0.679	0.635	0.747	0.404	0.784	0.077	0.735	12.53
12	0.332	0.384	0.513	0.687	0.639	0.755	0.406	0.791	0.074	0.750	13.66
13	0.349	0.402	0.530	0.705	0.647	0.766	0.410	0.796	0.074	0.757	14.79
14	0.373	0.429	0.559	0.735	0.660	0.781	0.419	0.803	0.076	0.767	15.91
15	0.404	0.462	0.600	0.773	0.685	0.806	0.435	0.823	0.081	0.796	17.03
16	0.438	0.498	0.645	0.817	0.715	0.835	0.454	0.853	0.087	0.839	18.15
17	0.468	0.527	0.686	0.851	0.740	0.858	0.470	0.877	0.091	0.869	19.27
18	0.492	0.548	0.721	0.876	0.760	0.874	0.480	0.893	0.095	0.887	20.38
19	0.504	0.560	0.741	0.888	0.771	0.883	0.484	0.901	0.095	0.893	21.49
20	0.501	0.559	0.737	0.887	0.775	0.884	0.481	0.901	0.092	0.885	22.60
21	0.487	0.547	0.720	0.880	0.777	0.885	0.482	0.904	0.087	0.888	23.70
22	0.465	0.526	0.697	0.863	0.775	0.881	0.479	0.906	0.081	0.884	24.80
23	0.448	0.510	0.681	0.849	0.765	0.872	0.472	0.899	0.079	0.864	25.89
24	0.435	0.502	0.671	0.837	0.753	0.860	0.464	0.886	0.079	0.841	26.98
25	0.429	0.500	0.668	0.831	0.743	0.852	0.460	0.875	0.080	0.828	28.07
26	0.428	0.504	0.669	0.834	0.738	0.848	0.460	0.869	0.080	0.822	29.15
27	0.428	0.507	0.672	0.839	0.738	0.844	0.461	0.866	0.082	0.810	30.22
28	0.428	0.510	0.677	0.845	0.743	0.849	0.463	0.866	0.084	0.803	31.30
29	0.425	0.509	0.676	0.846	0.750	0.857	0.465	0.867	0.085	0.807	32.37
30	0.415	0.501	0.669	0.840	0.752	0.858	0.464	0.864	0.085	0.808	33.43
31	0.401	0.486	0.655	0.824	0.752	0.859	0.458	0.856	0.082	0.813	34.49
32	0.394	0.475	0.651	0.813	0.756	0.864	0.456	0.856	0.079	0.822	35.54
33	0.394	0.471	0.658	0.812	0.771	0.877	0.459	0.868	0.077	0.847	36.60
34	0.398	0.472	0.666	0.814	0.782	0.887	0.463	0.881	0.076	0.867	37.64
35	0.403	0.475	0.676	0.817	0.785	0.888	0.463	0.886	0.075	0.872	38.68
36	0.410	0.480	0.684	0.824	0.781	0.882	0.462	0.880	0.076	0.868	39.72
37	0.410	0.480	0.684	0.824	0.776	0.876	0.456	0.873	0.074	0.858	40.75
38	0.408	0.479	0.678	0.821	0.765	0.866	0.450	0.862	0.070	0.845	41.78
39	0.403	0.474	0.665	0.811	0.754	0.852	0.441	0.850	0.066	0.831	42.80
40	0.397	0.467	0.654	0.801	0.745	0.844	0.431	0.839	0.062	0.826	43.81
41	0.395	0.464	0.646	0.794	0.731	0.834	0.421	0.827	0.059	0.820	44.83
42	0.387	0.456	0.631	0.775	0.715	0.818	0.405	0.812	0.056	0.807	45.83
43	0.383	0.450	0.621	0.764	0.701	0.804	0.393	0.795	0.052	0.792	46.84
44	0.382	0.448	0.616	0.758	0.687	0.791	0.383	0.779	0.050	0.773	47.83
45	0.374	0.441	0.605	0.743	0.673	0.777	0.370	0.767	0.048	0.751	48.83
46	0.371	0.438	0.598	0.732	0.661	0.765	0.360	0.753	0.046	0.731	49.82
47	0.368	0.436	0.594	0.729	0.649	0.751	0.352	0.742	0.045	0.706	50.80
48	0.363	0.431	0.584	0.716	0.638	0.741	0.341	0.730	0.044	0.688	51.78
49	0.361	0.430	0.580	0.710	0.629	0.731	0.333	0.721	0.042	0.676	52.76
50	0.363	0.432	0.581	0.708	0.620	0.723	0.326	0.709	0.041	0.661	53.73
51	0.361	0.429	0.575	0.698	0.616	0.718	0.317	0.706	0.040	0.659	54.69
52	0.364	0.435	0.579	0.700	0.614	0.716	0.314	0.703	0.040	0.663	55.66
53	0.361	0.433	0.575	0.692	0.611	0.714	0.307	0.700	0.039	0.664	56.61
54	0.365	0.440	0.579	0.695	0.609	0.714	0.305	0.696	0.039	0.671	57.57
55	0.365	0.440	0.574	0.685	0.604	0.706	0.297	0.688	0.039	0.667	58.52
56	0.369	0.449	0.576	0.684	0.601	0.705	0.291	0.685	0.039	0.660	59.46
57	0.377	0.459	0.584	0.685	0.598	0.701	0.290	0.678	0.040	0.645	60.41
58	0.380	0.463	0.581	0.677	0.596	0.699	0.286	0.676	0.040	0.634	61.34
59	0.385	0.473	0.586	0.677	0.594	0.697	0.283	0.671	0.041	0.627	62.28
60	0.393	0.485	0.593	0.679	0.592	0.693	0.283	0.669	0.042	0.620	63.21
61	0.406	0.499	0.610	0.684	0.588	0.690	0.284	0.664	0.044	0.623	64.14
62	0.417	0.512	0.621	0.686	0.586	0.688	0.283	0.659	0.045	0.650	65.06
63	0.430	0.524	0.632	0.689	0.583	0.684	0.284	0.657	0.047	0.664	65.98
64	0.435	0.531	0.638	0.689	0.589	0.689	0.285	0.657	0.049	0.669	66.90
65	0.444	0.538	0.650	0.690	0.583	0.679	0.290	0.652	0.052	0.664	67.81
66	0.467	0.553	0.673	0.705	0.579	0.676	0.298	0.655	0.056	0.645	68.72
67	0.486	0.556	0.689	0.715	0.577	0.692	0.308	0.663	0.059	0.640	69.63
68	0.489	0.557	0.702	0.715	0.579	0.689	0.315	0.668	0.065	0.625	70.54
69	0.497	0.549	0.712	0.719	0.587	0.686	0.331	0.669	0.071	0.678	71.44
70	0.499	0.546	0.731	0.731	0.601	0.713	0.341	0.680	0.078	0.662	72.34
71	0.526	0.545	0.757	0.751	0.634	0.738	0.360	0.701	0.089	0.819	73.24

Jupiter *k* – VIS

Lat PC (°)	K (UV)	K (Vio)	K (B)	K (V)	K (M1)	K (C1)	K (M2)	K (C2)	K (M3)	K (C3)	Lat PG (°)
-76	0.404	0.330	0.384	0.363	0.663	0.634	0.477	0.470	0.261	0.298	-77.70
-75	0.759	0.507	0.646	0.601	0.675	0.671	0.647	0.729	0.470	0.399	-76.81
-74	0.666	0.568	0.656	0.590	0.686	0.676	0.673	0.571	0.485	0.452	-75.92
-73	1.020	0.873	0.721	0.888	0.681	0.675	0.705	0.663	0.825	0.522	-75.03
-72	1.105	1.096	1.043	1.132	1.035	1.075	0.997	1.016	1.077	0.959	-74.14
-71	1.137	1.114	1.066	1.140	1.038	1.078	0.992	1.048	1.066	0.966	-73.24
-70	1.160	1.134	1.079	1.152	1.041	1.084	1.000	1.056	1.045	1.017	-72.34
-69	1.172	1.135	1.079	1.148	1.044	1.086	0.994	1.066	0.998	1.041	-71.44
-68	1.180	1.141	1.075	1.144	1.037	1.077	0.987	1.072	0.955	1.053	-70.54
-67	1.182	1.145	1.072	1.137	1.035	1.074	0.984	1.074	0.906	1.064	-69.63
-66	1.189	1.153	1.073	1.139	1.036	1.073	0.982	1.077	0.879	1.071	-68.72
-65	1.186	1.151	1.069	1.132	1.029	1.068	0.981	1.072	0.843	1.068	-67.81
-64	1.187	1.156	1.076	1.131	1.026	1.064	0.989	1.074	0.825	1.058	-66.90
-63	1.185	1.151	1.067	1.124	1.031	1.063	0.996	1.076	0.816	1.055	-65.98
-62	1.182	1.150	1.067	1.124	1.030	1.061	1.011	1.071	0.814	1.051	-65.06
-61	1.174	1.143	1.058	1.116	1.029	1.061	1.016	1.073	0.815	1.052	-64.14
-60	1.166	1.136	1.052	1.109	1.025	1.057	1.018	1.072	0.811	1.052	-63.21
-59	1.159	1.129	1.049	1.105	1.026	1.059	1.027	1.077	0.810	1.058	-62.28
-58	1.147	1.119	1.046	1.102	1.027	1.059	1.036	1.079	0.816	1.068	-61.34
-57	1.139	1.113	1.043	1.101	1.028	1.060	1.049	1.085	0.826	1.074	-60.41
-56	1.131	1.104	1.042	1.099	1.026	1.057	1.060	1.085	0.849	1.070	-59.46
-55	1.126	1.098	1.043	1.100	1.030	1.058	1.075	1.089	0.882	1.067	-58.52
-54	1.119	1.093	1.045	1.103	1.033	1.059	1.090	1.087	0.918	1.064	-57.57
-53	1.112	1.085	1.045	1.101	1.033	1.056	1.100	1.089	0.961	1.061	-56.61
-52	1.094	1.071	1.038	1.093	1.037	1.059	1.109	1.091	0.985	1.067	-55.66
-51	1.089	1.065	1.040	1.096	1.041	1.060	1.123	1.091	1.027	1.067	-54.69
-50	1.076	1.052	1.037	1.093	1.044	1.063	1.140	1.093	1.060	1.074	-53.73
-49	1.062	1.039	1.031	1.090	1.048	1.064	1.151	1.095	1.098	1.080	-52.76
-48	1.050	1.028	1.027	1.090	1.054	1.068	1.171	1.101	1.154	1.088	-51.78
-47	1.037	1.017	1.021	1.087	1.061	1.072	1.192	1.106	1.218	1.092	-50.80
-46	1.023	1.005	1.013	1.085	1.067	1.074	1.208	1.111	1.274	1.100	-49.82
-45	1.012	0.996	1.005	1.082	1.069	1.073	1.222	1.112	1.320	1.094	-48.83
-44	0.992	0.979	0.992	1.073	1.070	1.073	1.226	1.115	1.339	1.080	-47.83
-43	0.987	0.974	0.990	1.076	1.066	1.066	1.232	1.112	1.353	1.070	-46.84
-42	0.965	0.957	0.977	1.065	1.061	1.060	1.222	1.105	1.358	1.065	-45.83
-41	0.959	0.950	0.972	1.066	1.053	1.055	1.221	1.098	1.360	1.070	-44.83
-40	0.943	0.934	0.962	1.057	1.041	1.048	1.209	1.090	1.363	1.061	-43.81
-39	0.922	0.916	0.948	1.043	1.034	1.044	1.194	1.085	1.358	1.056	-42.80
-38	0.922	0.913	0.950	1.047	1.033	1.045	1.195	1.084	1.368	1.055	-41.78
-37	0.917	0.910	0.951	1.046	1.036	1.050	1.194	1.087	1.369	1.065	-40.75
-36	0.914	0.906	0.953	1.045	1.043	1.052	1.195	1.091	1.376	1.073	-39.72
-35	0.917	0.909	0.960	1.049	1.043	1.049	1.202	1.090	1.378	1.074	-38.68
-34	0.921	0.912	0.962	1.051	1.044	1.050	1.204	1.091	1.383	1.080	-37.64
-33	0.919	0.911	0.963	1.049	1.044	1.052	1.201	1.091	1.371	1.080	-36.60
-32	0.917	0.908	0.961	1.045	1.046	1.054	1.190	1.090	1.366	1.079	-35.54
-31	0.931	0.917	0.975	1.053	1.049	1.060	1.196	1.094	1.384	1.077	-34.49
-30	0.941	0.925	0.981	1.060	1.051	1.060	1.201	1.094	1.393	1.079	-33.43
-29	0.946	0.930	0.982	1.060	1.044	1.053	1.196	1.088	1.398	1.071	-32.37
-28	0.951	0.934	0.984	1.060	1.037	1.046	1.192	1.081	1.394	1.065	-31.30
-27	0.952	0.934	0.982	1.056	1.034	1.044	1.184	1.079	1.391	1.062	-30.22
-26	0.963	0.945	0.996	1.064	1.038	1.047	1.189	1.083	1.383	1.068	-29.15
-25	0.975	0.954	1.010	1.074	1.045	1.056	1.191	1.091	1.370	1.074	-28.07
-24	0.983	0.960	1.023	1.083	1.054	1.067	1.190	1.100	1.350	1.078	-26.98
-23	0.989	0.965	1.034	1.092	1.063	1.076	1.184	1.106	1.327	1.087	-25.89
-22	0.992	0.967	1.036	1.097	1.066	1.081	1.177	1.108	1.305	1.082	-24.80
-21	0.986	0.963	1.030	1.094	1.062	1.077	1.169	1.107	1.295	1.071	-23.70
-20	0.961	0.941	1.004	1.076	1.045	1.064	1.144	1.094	1.277	1.048	-22.60
-19	0.939	0.921	0.983	1.065	1.027	1.051	1.128	1.078	1.268	1.034	-21.49
-18	0.903	0.890	0.952	1.044	1.015	1.039	1.115	1.067	1.261	1.031	-20.38
-17	0.870	0.860	0.922	1.021	1.007	1.030	1.106	1.062	1.260	1.041	-19.27
-16	0.841	0.835	0.903	1.002	1.000	1.023	1.106	1.055	1.260	1.051	-18.15
-15	0.823	0.818	0.895	0.993	0.999	1.025	1.113	1.058	1.268	1.049	-17.03
-14	0.815	0.813	0.896	0.991	0.999	1.025	1.120	1.064	1.286	1.035	-15.91
-13	0.809	0.810	0.891	0.985	0.989	1.014	1.106	1.056	1.286	1.014	-14.79
-12	0.806	0.809	0.886	0.979	0.971	0.997	1.084	1.041	1.288	1.002	-13.66
-11	0.810	0.812	0.888	0.979	0.960	0.987	1.057	1.034	1.288	1.001	-12.53
-10	0.814	0.816	0.892	0.981	0.958	0.989	1.034	1.036	1.288	1.005	-11.40
-9	0.837	0.836	0.912	0.999	0.962	0.992	1.026	1.042	1.295	1.014	-10.26
-8	0.855	0.854	0.930	1.011	0.967	0.998	1.044	1.046	1.300	1.018	-9.13
-7	0.883	0.879	0.954	1.027	0.978	1.010	1.082	1.051	1.313	1.029	-7.99
-6	0.915	0.909	0.981	1.045	0.994	1.024	1.116	1.066	1.320	1.043	-6.85
-5	0.941	0.935	1.000	1.058	1.007	1.033	1.134	1.078	1.322	1.055	-5.71
-4	0.955	0.949	1.009	1.064	1.011	1.036	1.138	1.081	1.330	1.060	-4.57
-3	0.958	0.953	1.012	1.067	1.011	1.038	1.141	1.082	1.334	1.060	-3.43
-2	0.956	0.953	1.013	1.069	1.011	1.038	1.141	1.083	1.331	1.060	-2.29
-1	0.952	0.950	1.013	1.070	1.009	1.037	1.138	1.082	1.327	1.057	-1.14
0	0.948	0.947	1.013	1.069	1.007	1.037	1.133	1.080	1.320	1.046	0.00

Lat PC (°)	K (UV)	K (Vio)	K (B)	K (V)	K (M1)	K (C1)	K (M2)	K (C2)	K (M3)	K (C3)	Lat PG (°)
0	0.948	0.947	1.013	1.069	1.007	1.037	1.133	1.080	1.320	1.046	0.00
1	0.942	0.941	1.011	1.065	1.002	1.034	1.123	1.074	1.305	1.035	1.14
2	0.936	0.933	1.007	1.060	0.998	1.029	1.112	1.071	1.293	1.032	2.29
3	0.925	0.923	0.999	1.056	0.994	1.026	1.107	1.071	1.284	1.030	3.43
4	0.908	0.905	0.985	1.046	0.984	1.018	1.097	1.066	1.281	1.029	4.57
5	0.887	0.883	0.964	1.032	0.970	1.005	1.087	1.057	1.280	1.025	5.71
6	0.859	0.856	0.937	1.013	0.953	0.990	1.080	1.047	1.285	1.014	6.85
7	0.829	0.825	0.907	0.993	0.938	0.976	1.076	1.034	1.297	1.008	7.99
8	0.802	0.797	0.883	0.978	0.930	0.966	1.079	1.026	1.309	1.002	9.13
9	0.783	0.777	0.872	0.972	0.923	0.959	1.083	1.021	1.312	0.987	10.26
10	0.774	0.767	0.868	0.970	0.918	0.953	1.084	1.017	1.314	0.981	11.40
11	0.777	0.767	0.869	0.972	0.921	0.954	1.091	1.018	1.315	0.985	12.53
12	0.788	0.777	0.873	0.978	0.929	0.962	1.103	1.025	1.314	0.999	13.66
13	0.809	0.796	0.884	0.988	0.938	0.971	1.113	1.031	1.312	1.008	14.79
14	0.836	0.821	0.904	1.004	0.949	0.980	1.122	1.037	1.314	1.013	15.91
15	0.868	0.849	0.931	1.022	0.963	0.995	1.130	1.043	1.312	1.026	17.03
16	0.903	0.881	0.958	1.043	0.980	1.011	1.141	1.057	1.318	1.045	18.15
17	0.930	0.904	0.978	1.054	0.991	1.020	1.144	1.064	1.314	1.057	19.27
18	0.948	0.918	0.993	1.060	0.998	1.025	1.146	1.068	1.310	1.061	20.38
19	0.957	0.926	1.001	1.060	0.999	1.025	1.146	1.067	1.308	1.058	21.49
20	0.954	0.927	0.999	1.054	0.995	1.016	1.144	1.063	1.309	1.048	22.60
21	0.953	0.928	0.997	1.054	0.995	1.013	1.159	1.061	1.324	1.050	23.70
22	0.936	0.916	0.984	1.040	0.992	1.010	1.157	1.057	1.328	1.044	24.80
23	0.930	0.914	0.980	1.034	0.987	1.005	1.151	1.051	1.328	1.031	25.89
24	0.927	0.915	0.979	1.029	0.981	1.000	1.140	1.044	1.313	1.022	26.98
25	0.929	0.922	0.982	1.028	0.978	0.999	1.132	1.037	1.304	1.019	28.07
26	0.937	0.933	0.989	1.033	0.978	0.999	1.134	1.036	1.296	1.023	29.15
27	0.940	0.942	0.993	1.037	0.980	0.996	1.134	1.037	1.294	1.022	30.22
28	0.946	0.949	0.997	1.040	0.982	1.000	1.133	1.037	1.293	1.018	31.30
29	0.952	0.954	0.997	1.040	0.985	1.006	1.131	1.036	1.292	1.023	32.37
30	0.957	0.956	0.999	1.040	0.985	1.004	1.132	1.032	1.285	1.022	33.43
31	0.949	0.949	0.990	1.027	0.985	1.005	1.121	1.025	1.262	1.024	34.49
32	0.952	0.949	0.995	1.022	0.987	1.004	1.119	1.025	1.252	1.030	35.54
33	0.968	0.960	1.008	1.025	0.999	1.013	1.125	1.032	1.239	1.046	36.60
34	0.985	0.972	1.019	1.027	1.005	1.018	1.129	1.034	1.225	1.052	37.64
35	0.998	0.985	1.028	1.030	1.005	1.017	1.127	1.034	1.210	1.048	38.68
36	1.016	1.000	1.038	1.038	1.000	1.012	1.124	1.028	1.199	1.042	39.72
37	1.019	1.005	1.037	1.036	1.000	1.012	1.115	1.026	1.170	1.040	40.75
38	1.027	1.013	1.039	1.038	0.997	1.011	1.112	1.023	1.137	1.034	41.78
39	1.033	1.020	1.037	1.037	0.994	1.005	1.105	1.019	1.099	1.031	42.80
40	1.039	1.026	1.038	1.037	0.994	1.007	1.100	1.016	1.063	1.036	43.81
41	1.052	1.036	1.043	1.041	0.989	1.005	1.095	1.011	1.029	1.038	44.83
42	1.046	1.033	1.034	1.029	0.981	0.998	1.073	1.004	0.983	1.034	45.83
43	1.053	1.033	1.034	1.027	0.978	0.995	1.060	0.997	0.938	1.032	46.84
44	1.063	1.041	1.038	1.031	0.972	0.991	1.053	0.989	0.904	1.022	47.83
45	1.054	1.036	1.030	1.021	0.967	0.986	1.034	0.983	0.859	1.009	48.83
46	1.057	1.036	1.029	1.017	0.962	0.983	1.021	0.976	0.825	0.998	49.82
47	1.058	1.040	1.031	1.021	0.956	0.977	1.013	0.972	0.796	0.982	50.80
48	1.052	1.033	1.022	1.013	0.950	0.973	0.995	0.965	0.762	0.971	51.78
49	1.051	1.034	1.022	1.011	0.947	0.970	0.983	0.963	0.727	0.968	52.76
50	1.059	1.038	1.026	1.015	0.943	0.969	0.973	0.956	0.695	0.960	53.73
51	1.053	1.032	1.020	1.008	0.942	0.968	0.957	0.957	0.655	0.962	54.69
52	1.060	1.041	1.025	1.013	0.942	0.969	0.951	0.957	0.632	0.970	55.66
53	1.053	1.034	1.020	1.006	0.940	0.969	0.936	0.956	0.603	0.969	56.61
54	1.059	1.042	1.025	1.011	0.939	0.971	0.934	0.954	0.583	0.975	57.57
55	1.054	1.036	1.018	1.002	0.935	0.966	0.915	0.948	0.561	0.968	58.52
56	1.058	1.044	1.019	1.002	0.934	0.967	0.902	0.947	0.555	0.961	59.46
57	1.068	1.051	1.026	1.004	0.933	0.966	0.900	0.943	0.552	0.948	60.41
58	1.068	1.051	1.022	0.998	0.930	0.965	0.891	0.942	0.545	0.939	61.34
59	1.071	1.056	1.024	0.997	0.929	0.964	0.885	0.939	0.545	0.933	62.28
60	1.077	1.063	1.027	0.999	0.928	0.961	0.882	0.938	0.546	0.926	63.21
61	1.089	1.071	1.038	1.003	0.925	0.960	0.881	0.934	0.550	0.927	64.14
62	1.097	1.078	1.043	1.004	0.924	0.959	0.876	0.931	0.551	0.946	65.06
63	1.105	1.083	1.047	1.005	0.922	0.957	0.875	0.932	0.555	0.954	65.98
64	1.106	1.083	1.049	1.004	0.927	0.961	0.873	0.933	0.563	0.957	66.90
65	1.110	1.084	1.053	1.002	0.921	0.955	0.878	0.931	0.578	0.953	67.81
66	1.126	1.093	1.062	1.010	0.917	0.952	0.885	0.934	0.602	0.940	68.72
67	1.139	1.094	1.068	1.014	0.916	0.963	0.898	0.940	0.621	0.941	69.63
68	1.136	1.091	1.071	1.011	0.917	0.960	0.902	0.942	0.652	0.932	70.54
69	1.138	1.083	1.071	1.011	0.923	0.957	0.921	0.942	0.687	0.967	71.44
70	1.133	1.079	1.078	1.016	0.933	0.972	0.929	0.947	0.717	0.962	72.34
71	1.156	1.078	1.088	1.024	0.952	0.982	0.944	0.955	0.759	1.043	73.24

Minnaert $(I/F)_0$ and K coefficients for Jupiter PlanetCam SWIR observations. March2015 (red), March2016 (cyan), May2016 (magenta), Jul2016 (black). Tables provide mean values.

Jupiter $(I/F)_0$ – SWIR

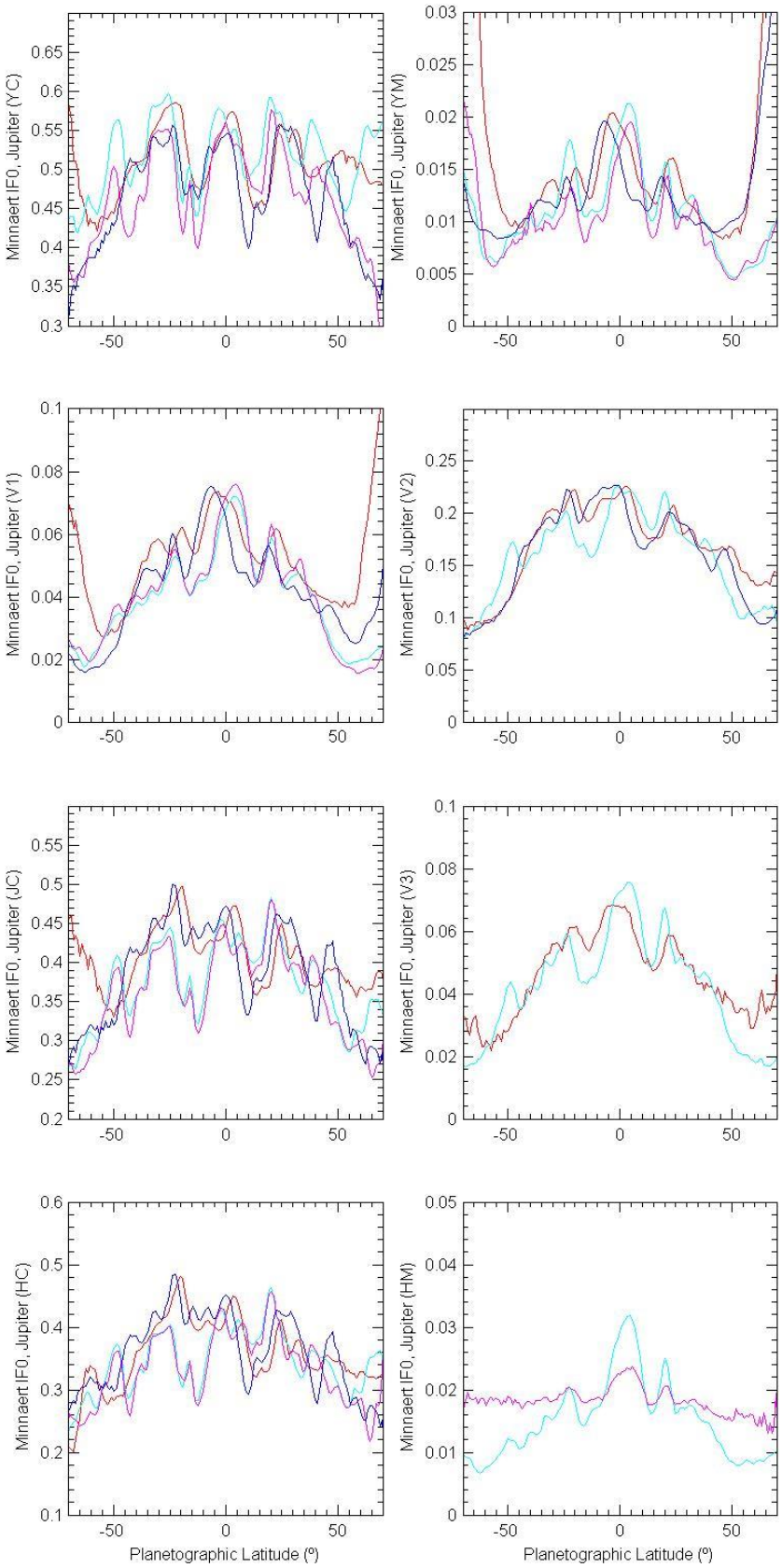

Jupiter *k* – SWIR

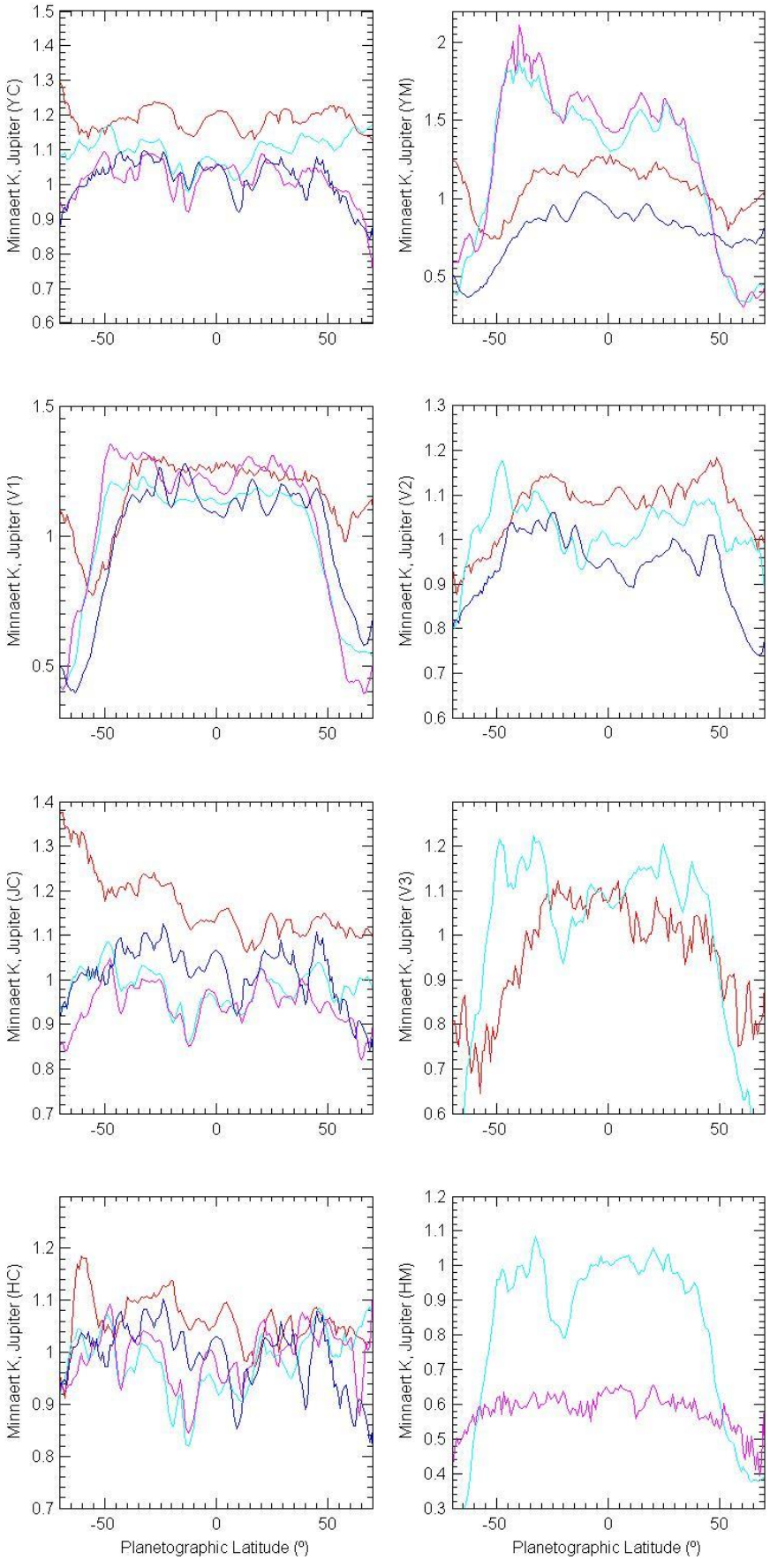

Jupiter $(I/F)_0$ – SWIR

Lat PC (°)	$(I/F)_o$ YC	$(I/F)_o$ YM	$(I/F)_o$ V1	$(I/F)_o$ V2	$(I/F)_o$ JC	$(I/F)_o$ V3	$(I/F)_o$ HC	$(I/F)_o$ HM	Lat PG (°)
-73	0.403	0.029	0.045	0.100	0.319	0.015	0.221	0.009	-75.03
-72	0.410	0.030	0.045	0.089	0.312	0.029	0.228	0.010	-74.14
-71	0.420	0.027	0.044	0.080	0.338	0.017	0.242	0.011	-73.24
-70	0.430	0.027	0.040	0.080	0.333	0.027	0.248	0.011	-72.34
-69	0.437	0.029	0.037	0.084	0.334	0.024	0.241	0.012	-71.44
-68	0.427	0.028	0.035	0.086	0.321	0.028	0.238	0.013	-70.54
-67	0.428	0.027	0.035	0.088	0.317	0.025	0.244	0.013	-69.63
-66	0.427	0.026	0.034	0.087	0.322	0.024	0.246	0.014	-68.72
-65	0.414	0.024	0.032	0.086	0.312	0.023	0.246	0.014	-67.81
-64	0.409	0.022	0.032	0.086	0.310	0.022	0.251	0.014	-66.90
-63	0.412	0.021	0.031	0.089	0.315	0.024	0.261	0.014	-65.98
-62	0.407	0.019	0.029	0.089	0.313	0.025	0.267	0.013	-65.06
-61	0.409	0.018	0.028	0.092	0.322	0.025	0.279	0.013	-64.14
-60	0.409	0.016	0.025	0.092	0.320	0.024	0.287	0.012	-63.21
-59	0.416	0.014	0.024	0.094	0.323	0.023	0.296	0.013	-62.28
-58	0.419	0.012	0.023	0.096	0.323	0.022	0.299	0.013	-61.34
-57	0.422	0.011	0.023	0.099	0.331	0.022	0.304	0.013	-60.41
-56	0.419	0.010	0.023	0.101	0.328	0.024	0.299	0.013	-59.46
-55	0.420	0.010	0.023	0.102	0.323	0.024	0.294	0.013	-58.52
-54	0.419	0.009	0.023	0.102	0.319	0.023	0.290	0.013	-57.57
-53	0.426	0.009	0.024	0.104	0.323	0.025	0.292	0.013	-56.61
-52	0.434	0.008	0.024	0.108	0.330	0.027	0.299	0.014	-55.66
-51	0.439	0.008	0.025	0.110	0.332	0.029	0.301	0.014	-54.69
-50	0.449	0.008	0.026	0.113	0.338	0.029	0.305	0.014	-53.73
-49	0.455	0.008	0.027	0.117	0.338	0.030	0.304	0.014	-52.76
-48	0.468	0.008	0.028	0.123	0.347	0.032	0.312	0.014	-51.78
-47	0.480	0.009	0.030	0.128	0.358	0.034	0.324	0.015	-50.80
-46	0.484	0.009	0.031	0.132	0.360	0.035	0.326	0.016	-49.82
-45	0.489	0.009	0.031	0.137	0.368	0.037	0.331	0.015	-48.83
-44	0.489	0.009	0.032	0.141	0.374	0.037	0.336	0.015	-47.83
-43	0.484	0.009	0.033	0.145	0.373	0.037	0.334	0.015	-46.84
-42	0.480	0.009	0.033	0.148	0.367	0.035	0.325	0.015	-45.83
-41	0.477	0.009	0.034	0.150	0.360	0.035	0.316	0.014	-44.83
-40	0.474	0.009	0.036	0.153	0.355	0.035	0.311	0.014	-43.81
-39	0.477	0.010	0.037	0.156	0.358	0.036	0.315	0.014	-42.80
-38	0.480	0.010	0.039	0.160	0.364	0.040	0.323	0.015	-41.78
-37	0.485	0.010	0.040	0.164	0.373	0.041	0.335	0.015	-40.75
-36	0.494	0.011	0.041	0.169	0.384	0.041	0.348	0.016	-39.72
-35	0.495	0.011	0.043	0.172	0.388	0.043	0.352	0.015	-38.68
-34	0.494	0.011	0.044	0.174	0.389	0.044	0.354	0.016	-37.64
-33	0.495	0.011	0.044	0.176	0.389	0.044	0.353	0.016	-36.60
-32	0.507	0.011	0.045	0.179	0.396	0.046	0.360	0.016	-35.54
-31	0.528	0.011	0.046	0.186	0.411	0.048	0.374	0.017	-34.49
-30	0.547	0.012	0.048	0.191	0.429	0.051	0.392	0.017	-33.43
-29	0.553	0.012	0.048	0.194	0.435	0.051	0.399	0.017	-32.37
-28	0.556	0.011	0.047	0.194	0.436	0.051	0.401	0.017	-31.30
-27	0.556	0.011	0.047	0.194	0.435	0.053	0.401	0.017	-30.22
-26	0.557	0.011	0.047	0.193	0.436	0.053	0.401	0.017	-29.15
-25	0.559	0.012	0.048	0.194	0.439	0.055	0.403	0.017	-28.07
-24	0.563	0.012	0.049	0.196	0.444	0.055	0.409	0.018	-26.98
-23	0.566	0.013	0.051	0.201	0.450	0.054	0.417	0.018	-25.89
-22	0.566	0.013	0.053	0.206	0.455	0.057	0.426	0.019	-24.80
-21	0.565	0.014	0.056	0.211	0.456	0.058	0.428	0.020	-23.70
-20	0.548	0.014	0.056	0.212	0.446	0.060	0.418	0.020	-22.60
-19	0.521	0.015	0.055	0.208	0.430	0.058	0.402	0.020	-21.49
-18	0.497	0.014	0.053	0.201	0.415	0.056	0.390	0.019	-20.38
-17	0.481	0.013	0.051	0.195	0.405	0.054	0.378	0.018	-19.27
-16	0.478	0.012	0.048	0.190	0.400	0.052	0.373	0.017	-18.15
-15	0.489	0.011	0.047	0.188	0.404	0.051	0.378	0.016	-17.03
-14	0.493	0.011	0.047	0.189	0.409	0.050	0.382	0.016	-15.91
-13	0.471	0.011	0.048	0.188	0.394	0.049	0.364	0.016	-14.79
-12	0.449	0.012	0.050	0.188	0.375	0.049	0.347	0.017	-13.66
-11	0.444	0.012	0.052	0.189	0.368	0.050	0.341	0.018	-12.53
-10	0.454	0.013	0.054	0.192	0.372	0.051	0.346	0.018	-11.40
-9	0.472	0.014	0.056	0.196	0.383	0.053	0.359	0.018	-10.26
-8	0.489	0.014	0.057	0.201	0.396	0.055	0.374	0.018	-9.13
-7	0.506	0.015	0.059	0.206	0.410	0.058	0.390	0.018	-7.99
-6	0.523	0.015	0.061	0.209	0.419	0.061	0.397	0.019	-6.85
-5	0.533	0.016	0.063	0.211	0.425	0.063	0.399	0.020	-5.71
-4	0.542	0.017	0.066	0.215	0.434	0.066	0.409	0.022	-4.57
-3	0.549	0.018	0.068	0.219	0.444	0.068	0.418	0.023	-3.43
-2	0.552	0.018	0.069	0.222	0.448	0.069	0.423	0.024	-2.29
-1	0.555	0.018	0.069	0.223	0.451	0.070	0.426	0.025	-1.14
0	0.557	0.018	0.069	0.223	0.450	0.070	0.424	0.026	0.00

Lat PC (°)	$(I/F)_o$ YC	$(I/F)_o$ YM	$(I/F)_o$ V1	$(I/F)_o$ V2	$(I/F)_o$ JC	$(I/F)_o$ V3	$(I/F)_o$ HC	$(I/F)_o$ HM	Lat PG (°)
0	0.557	0.018	0.069	0.223	0.450	0.070	0.424	0.026	0.00
1	0.554	0.018	0.069	0.221	0.446	0.070	0.418	0.027	1.14
2	0.550	0.018	0.068	0.219	0.440	0.071	0.413	0.027	2.29
3	0.546	0.018	0.067	0.216	0.437	0.071	0.411	0.028	3.43
4	0.540	0.018	0.066	0.211	0.434	0.071	0.410	0.028	4.57
5	0.526	0.017	0.065	0.206	0.430	0.068	0.406	0.027	5.71
6	0.508	0.017	0.063	0.199	0.419	0.065	0.393	0.026	6.85
7	0.489	0.016	0.060	0.192	0.405	0.063	0.377	0.025	7.99
8	0.473	0.014	0.057	0.187	0.393	0.059	0.364	0.023	9.13
9	0.464	0.013	0.054	0.183	0.382	0.055	0.348	0.021	10.26
10	0.461	0.012	0.050	0.179	0.376	0.052	0.343	0.019	11.40
11	0.469	0.011	0.048	0.178	0.381	0.050	0.350	0.017	12.53
12	0.472	0.011	0.046	0.177	0.384	0.049	0.357	0.017	13.66
13	0.471	0.011	0.047	0.178	0.385	0.048	0.357	0.017	14.79
14	0.473	0.011	0.048	0.181	0.388	0.049	0.360	0.018	15.91
15	0.483	0.012	0.051	0.185	0.399	0.052	0.373	0.019	17.03
16	0.504	0.013	0.055	0.191	0.416	0.056	0.390	0.020	18.15
17	0.522	0.014	0.058	0.197	0.431	0.060	0.403	0.022	19.27
18	0.539	0.015	0.059	0.202	0.443	0.062	0.414	0.023	20.38
19	0.550	0.015	0.058	0.203	0.451	0.061	0.420	0.022	21.49
20	0.554	0.014	0.055	0.202	0.447	0.057	0.414	0.020	22.60
21	0.558	0.012	0.051	0.200	0.445	0.056	0.414	0.018	23.70
22	0.557	0.012	0.048	0.195	0.440	0.053	0.405	0.017	24.80
23	0.548	0.011	0.047	0.191	0.429	0.052	0.391	0.017	25.89
24	0.538	0.011	0.047	0.186	0.420	0.052	0.380	0.017	26.98
25	0.529	0.011	0.047	0.183	0.412	0.052	0.374	0.018	28.07
26	0.526	0.011	0.047	0.182	0.414	0.050	0.376	0.018	29.15
27	0.518	0.011	0.047	0.182	0.411	0.049	0.373	0.018	30.22
28	0.517	0.011	0.047	0.181	0.407	0.049	0.369	0.018	31.30
29	0.512	0.011	0.047	0.177	0.401	0.048	0.363	0.018	32.37
30	0.503	0.011	0.046	0.173	0.393	0.046	0.354	0.018	33.43
31	0.495	0.011	0.045	0.169	0.385	0.044	0.345	0.017	34.49
32	0.490	0.010	0.043	0.167	0.379	0.044	0.341	0.017	35.54
33	0.494	0.010	0.042	0.167	0.382	0.045	0.348	0.016	36.60
34	0.497	0.009	0.041	0.167	0.385	0.044	0.349	0.016	37.64
35	0.499	0.009	0.040	0.165	0.383	0.045	0.344	0.016	38.68
36	0.490	0.009	0.039	0.161	0.375	0.044	0.334	0.016	39.72
37	0.488	0.009	0.038	0.158	0.372	0.043	0.331	0.015	40.75
38	0.490	0.008	0.037	0.157	0.374	0.041	0.333	0.015	41.78
39	0.490	0.008	0.035	0.156	0.375	0.039	0.337	0.014	42.80
40	0.495	0.008	0.034	0.157	0.379	0.040	0.343	0.014	43.81
41	0.500	0.008	0.033	0.158	0.383	0.038	0.348	0.013	44.83
42	0.495	0.007	0.032	0.157	0.377	0.035	0.344	0.013	45.83
43	0.493	0.007	0.031	0.154	0.373	0.036	0.343	0.013	46.84
44	0.494	0.007	0.030	0.153	0.372	0.033	0.342	0.012	47.83
45	0.485	0.007	0.029	0.150	0.364	0.032	0.335	0.012	48.83
46	0.481	0.007	0.028	0.146	0.359	0.031	0.331	0.012	49.82
47	0.469	0.007	0.027	0.139	0.347	0.030	0.320	0.012	50.80
48	0.465	0.007	0.026	0.134	0.339	0.028	0.312	0.012	51.78
49	0.454	0.007	0.026	0.129	0.327	0.028	0.301	0.012	52.76
50	0.450	0.007	0.025	0.124	0.322	0.028	0.296	0.012	53.73
51	0.449	0.008	0.025	0.121	0.319	0.028	0.292	0.012	54.69
52	0.443	0.008	0.025	0.119	0.312	0.028	0.288	0.012	55.66
53	0.449	0.009	0.025	0.120	0.318	0.028	0.294	0.012	56.61
54	0.453	0.009	0.024	0.118	0.320	0.027	0.297	0.012	57.57
55	0.452	0.010	0.025	0.114	0.318	0.024	0.296	0.012	58.52
56	0.454	0.011	0.027	0.113	0.317	0.024	0.295	0.012	59.46
57	0.453	0.012	0.029	0.111	0.315	0.024	0.293	0.011	60.41
58	0.451	0.013	0.031	0.111	0.313	0.026	0.290	0.011	61.34
59	0.447	0.015	0.032	0.110	0.311	0.029	0.287	0.012	62.28
60	0.448	0.016	0.034	0.111	0.317	0.030	0.291	0.011	63.21
61	0.445	0.018	0.035	0.113	0.317	0.027	0.291	0.012	64.14
62	0.441	0.019	0.037	0.113	0.316	0.025	0.293	0.012	65.06
63	0.435	0.021	0.039	0.112	0.318	0.026	0.298	0.011	65.98
64	0.431	0.023	0.041	0.112	0.324	0.026	0.305	0.012	66.90
65	0.421	0.024	0.043	0.117	0.323	0.027	0.302	0.011	67.81
66	0.414	0.026	0.046	0.117	0.318	0.029	0.302	0.012	68.72
67	0.417	0.029	0.049	0.116	0.324	0.031	0.315	0.015	69.63
68	0.396	0.029	0.049	0.116	0.318	0.038	0.315	0.011	70.54
69	0.402	0.028	0.049	0.115	0.339	0.033	0.347	0.015	71.44
70	0.415	0.035	0.055	0.110	0.351	0.023	0.390	0.015	72.34
71	0.426	0.037	0.056	0.107	0.422	0.024	0.475	0.014	73.24

Jupiter *k* – SWIR

Lat PC (°)	K (YC)	K (YM)	K (V1)	K (V2)	K (JC)	K (V3)	K (HC)	K (HM)	Lat PG (°)
-73	0.993	0.752	0.699	0.857	1.010	0.438	0.892	0.210	-75.03
-72	1.016	0.762	0.697	0.838	1.014	0.649	0.921	0.251	-74.14
-71	1.027	0.726	0.688	0.810	1.046	0.456	0.951	0.269	-73.24
-70	1.043	0.715	0.657	0.805	1.045	0.635	0.960	0.281	-72.34
-69	1.057	0.731	0.633	0.824	1.049	0.597	0.940	0.319	-71.44
-68	1.048	0.710	0.607	0.831	1.029	0.654	0.930	0.344	-70.54
-67	1.052	0.688	0.606	0.843	1.022	0.617	0.937	0.336	-69.63
-66	1.056	0.682	0.599	0.842	1.029	0.611	0.937	0.354	-68.72
-65	1.046	0.663	0.587	0.839	1.017	0.609	0.934	0.372	-67.81
-64	1.043	0.653	0.601	0.846	1.015	0.621	0.948	0.376	-66.90
-63	1.052	0.672	0.615	0.871	1.032	0.678	0.975	0.389	-65.98
-62	1.051	0.678	0.630	0.884	1.037	0.716	0.990	0.393	-65.06
-61	1.054	0.707	0.646	0.907	1.055	0.749	1.017	0.415	-64.14
-60	1.055	0.699	0.635	0.913	1.054	0.735	1.031	0.420	-63.21
-59	1.065	0.697	0.650	0.924	1.061	0.730	1.046	0.453	-62.28
-58	1.067	0.671	0.664	0.932	1.062	0.725	1.053	0.486	-61.34
-57	1.072	0.658	0.686	0.946	1.076	0.741	1.065	0.528	-60.41
-56	1.068	0.653	0.705	0.950	1.070	0.790	1.055	0.537	-59.46
-55	1.070	0.675	0.721	0.954	1.063	0.766	1.046	0.574	-58.52
-54	1.069	0.693	0.741	0.950	1.054	0.740	1.037	0.597	-57.57
-53	1.077	0.716	0.765	0.956	1.057	0.817	1.035	0.602	-56.61
-52	1.086	0.735	0.794	0.965	1.065	0.846	1.038	0.636	-55.66
-51	1.085	0.763	0.824	0.967	1.058	0.894	1.031	0.657	-54.69
-50	1.095	0.820	0.868	0.974	1.066	0.901	1.031	0.665	-53.73
-49	1.095	0.858	0.898	0.980	1.058	0.879	1.020	0.678	-52.76
-48	1.104	0.914	0.948	1.000	1.065	0.933	1.028	0.710	-51.78
-47	1.114	1.012	0.998	1.016	1.076	0.952	1.041	0.733	-50.80
-46	1.109	1.080	1.027	1.020	1.068	0.980	1.035	0.788	-49.82
-45	1.114	1.132	1.056	1.035	1.080	1.022	1.045	0.790	-48.83
-44	1.114	1.208	1.092	1.047	1.089	1.032	1.054	0.780	-47.83
-43	1.106	1.239	1.119	1.055	1.085	1.042	1.047	0.811	-46.84
-42	1.101	1.284	1.130	1.057	1.072	1.015	1.030	0.779	-45.83
-41	1.102	1.308	1.141	1.058	1.065	1.004	1.015	0.771	-44.83
-40	1.098	1.326	1.150	1.055	1.054	1.006	1.002	0.750	-43.81
-39	1.096	1.348	1.154	1.053	1.050	0.996	1.000	0.762	-42.80
-38	1.091	1.323	1.166	1.053	1.048	1.019	1.002	0.785	-41.78
-37	1.090	1.346	1.177	1.052	1.048	1.031	1.013	0.804	-40.75
-36	1.104	1.450	1.197	1.065	1.065	1.024	1.032	0.795	-39.72
-35	1.102	1.419	1.224	1.070	1.065	1.061	1.031	0.795	-38.68
-34	1.096	1.402	1.236	1.068	1.061	1.072	1.031	0.787	-37.64
-33	1.085	1.408	1.223	1.061	1.052	1.077	1.026	0.778	-36.60
-32	1.089	1.399	1.211	1.060	1.057	1.070	1.031	0.798	-35.54
-31	1.111	1.361	1.223	1.075	1.071	1.073	1.038	0.826	-34.49
-30	1.132	1.420	1.244	1.089	1.090	1.118	1.057	0.850	-33.43
-29	1.133	1.417	1.250	1.093	1.093	1.109	1.061	0.856	-32.37
-28	1.133	1.440	1.248	1.093	1.091	1.104	1.060	0.823	-31.30
-27	1.131	1.423	1.243	1.090	1.085	1.134	1.054	0.814	-30.22
-26	1.129	1.395	1.232	1.082	1.082	1.127	1.048	0.810	-29.15
-25	1.126	1.359	1.234	1.080	1.079	1.118	1.043	0.784	-28.07
-24	1.127	1.346	1.234	1.082	1.078	1.099	1.043	0.761	-26.98
-23	1.127	1.326	1.236	1.086	1.080	1.050	1.046	0.728	-25.89
-22	1.126	1.313	1.222	1.083	1.079	1.063	1.050	0.731	-24.80
-21	1.128	1.306	1.216	1.079	1.081	1.052	1.050	0.730	-23.70
-20	1.111	1.287	1.190	1.064	1.063	1.056	1.028	0.714	-22.60
-19	1.084	1.280	1.169	1.045	1.044	1.027	1.005	0.716	-21.49
-18	1.062	1.268	1.165	1.031	1.028	1.014	0.992	0.714	-20.38
-17	1.050	1.269	1.174	1.025	1.017	1.020	0.980	0.707	-19.27
-16	1.050	1.294	1.186	1.020	1.013	1.029	0.976	0.704	-18.15
-15	1.067	1.320	1.208	1.029	1.021	1.065	0.986	0.712	-17.03
-14	1.075	1.332	1.222	1.045	1.028	1.052	0.996	0.741	-15.91
-13	1.045	1.337	1.222	1.035	1.005	1.040	0.967	0.757	-14.79
-12	1.015	1.337	1.216	1.018	0.975	1.050	0.936	0.760	-13.66
-11	1.007	1.335	1.210	1.004	0.959	1.060	0.920	0.785	-12.53
-10	1.019	1.336	1.207	0.997	0.959	1.043	0.924	0.761	-11.40
-9	1.038	1.349	1.200	0.996	0.971	1.060	0.939	0.769	-10.26
-8	1.057	1.351	1.196	1.001	0.987	1.068	0.960	0.791	-9.13
-7	1.073	1.352	1.201	1.009	1.004	1.098	0.983	0.776	-7.99
-6	1.083	1.337	1.192	1.007	1.014	1.100	0.993	0.806	-6.85
-5	1.086	1.323	1.181	1.004	1.017	1.095	0.993	0.794	-5.71
-4	1.091	1.306	1.178	1.006	1.025	1.101	0.999	0.817	-4.57
-3	1.092	1.284	1.179	1.012	1.030	1.104	1.003	0.825	-3.43
-2	1.091	1.265	1.168	1.015	1.033	1.086	1.006	0.823	-2.29
-1	1.092	1.241	1.169	1.018	1.031	1.081	1.004	0.831	-1.14
0	1.095	1.240	1.172	1.016	1.029	1.072	0.999	0.825	0.00

Lat PC (°)	K (YC)	K (YM)	K (V1)	K (V2)	K (JC)	K (V3)	K (HC)	K (HM)	Lat PG (°)
0	1.095	1.240	1.172	1.016	1.029	1.072	0.999	0.825	0.00
1	1.095	1.234	1.159	1.014	1.024	1.072	0.992	0.816	1.14
2	1.092	1.213	1.159	1.013	1.020	1.083	0.992	0.818	2.29
3	1.088	1.215	1.155	1.013	1.018	1.084	0.995	0.830	3.43
4	1.083	1.216	1.164	1.012	1.015	1.098	0.995	0.830	4.57
5	1.072	1.222	1.172	1.009	1.011	1.068	0.989	0.839	5.71
6	1.060	1.228	1.180	1.001	0.999	1.088	0.975	0.834	6.85
7	1.049	1.245	1.195	0.996	0.987	1.100	0.960	0.832	7.99
8	1.035	1.264	1.195	0.993	0.980	1.090	0.950	0.834	9.13
9	1.029	1.276	1.204	0.992	0.973	1.068	0.937	0.824	10.26
10	1.026	1.283	1.199	0.991	0.963	1.061	0.928	0.808	11.40
11	1.045	1.295	1.205	0.995	0.979	1.096	0.948	0.774	12.53
12	1.050	1.306	1.216	1.004	0.984	1.091	0.960	0.778	13.66
13	1.050	1.325	1.229	1.015	0.989	1.066	0.962	0.784	14.79
14	1.052	1.323	1.232	1.025	0.996	1.073	0.966	0.788	15.91
15	1.057	1.306	1.224	1.022	1.004	1.065	0.974	0.811	17.03
16	1.081	1.301	1.220	1.029	1.022	1.076	0.996	0.821	18.15
17	1.094	1.271	1.213	1.032	1.036	1.079	1.013	0.842	19.27
18	1.105	1.266	1.202	1.037	1.047	1.085	1.029	0.853	20.38
19	1.113	1.261	1.193	1.041	1.053	1.106	1.038	0.837	21.49
20	1.112	1.245	1.184	1.041	1.047	1.093	1.030	0.818	22.60
21	1.115	1.267	1.194	1.050	1.048	1.118	1.033	0.802	23.70
22	1.112	1.315	1.198	1.050	1.046	1.122	1.031	0.791	24.80
23	1.107	1.317	1.210	1.046	1.037	1.113	1.018	0.811	25.89
24	1.101	1.298	1.208	1.043	1.028	1.077	1.007	0.820	26.98
25	1.094	1.269	1.203	1.038	1.018	1.100	0.998	0.796	28.07
26	1.103	1.258	1.214	1.050	1.034	1.071	1.017	0.803	29.15
27	1.091	1.234	1.206	1.053	1.029	1.055	1.014	0.778	30.22
28	1.091	1.224	1.209	1.053	1.028	1.056	1.014	0.793	31.30
29	1.087	1.212	1.200	1.045	1.023	1.047	1.012	0.781	32.37
30	1.082	1.218	1.196	1.040	1.022	1.024	1.011	0.788	33.43
31	1.078	1.220	1.191	1.034	1.020	1.004	1.007	0.754	34.49
32	1.075	1.186	1.181	1.041	1.011	1.023	1.001	0.755	35.54
33	1.082	1.147	1.174	1.049	1.017	1.072	1.011	0.766	36.60
34	1.084	1.121	1.171	1.055	1.020	1.063	1.014	0.758	37.64
35	1.091	1.110	1.167	1.055	1.024	1.092	1.017	0.784	38.68
36	1.077	1.091	1.162	1.041	1.010	1.085	1.004	0.760	39.72
37	1.081	1.062	1.143	1.045	1.016	1.079	1.010	0.733	40.75
38	1.095	1.024	1.137	1.054	1.031	1.060	1.028	0.716	41.78
39	1.096	0.989	1.131	1.062	1.035	1.041	1.038	0.703	42.80
40	1.105	0.964	1.123	1.074	1.043	1.070	1.050	0.695	43.81
41	1.114	0.938	1.109	1.090	1.056	1.041	1.065	0.685	44.83
42	1.106	0.889	1.078	1.091	1.047	0.997	1.058	0.678	45.83
43	1.105	0.854	1.044	1.084	1.045	1.009	1.060	0.640	46.84
44	1.111	0.811	1.018	1.085	1.052	0.968	1.065	0.606	47.83
45	1.098	0.752	0.986	1.076	1.038	0.955	1.049	0.598	48.83
46	1.096	0.725	0.952	1.062	1.034	0.920	1.046	0.568	49.82
47	1.082	0.689	0.905	1.033	1.014	0.878	1.026	0.561	50.80
48	1.083	0.667	0.874	1.015	1.005	0.840	1.018	0.573	51.78
49	1.071	0.643	0.851	0.993	0.988	0.838	1.002	0.543	52.76
50	1.071	0.619	0.818	0.979	0.988	0.842	0.999	0.536	53.73
51	1.074	0.621	0.790	0.976	0.988	0.835	0.997	0.520	54.69
52	1.064	0.606	0.764	0.970	0.975	0.827	0.989	0.506	55.66
53	1.072	0.598	0.740	0.979	0.987	0.823	1.002	0.510	56.61
54	1.073	0.589	0.711	0.975	0.989	0.789	1.008	0.485	57.57
55	1.067	0.578	0.692	0.960	0.984	0.713	1.001	0.487	58.52
56	1.063	0.580	0.696	0.955	0.979	0.706	0.996	0.469	59.46
57	1.055	0.573	0.703	0.946	0.973	0.709	0.988	0.441	60.41
58	1.047	0.583	0.697	0.942	0.965	0.719	0.978	0.425	61.34
59	1.037	0.590	0.689	0.933	0.957	0.771	0.967	0.456	62.28
60	1.035	0.599	0.678	0.930	0.964	0.767	0.969	0.415	63.21
61	1.030	0.611	0.671	0.928	0.959	0.696	0.966	0.441	64.14
62	1.024	0.617	0.666	0.918	0.954	0.658	0.973	0.422	65.06
63	1.017	0.617	0.656	0.907	0.955	0.673	0.985	0.397	65.98
64	1.012	0.633	0.662	0.898	0.964	0.655	0.997	0.419	66.90
65	0.998	0.643	0.670	0.908	0.961	0.671	0.989	0.386	67.81
66	0.987	0.654	0.688	0.901	0.951	0.682	0.985	0.411	68.72
67	0.989	0.674	0.707	0.888	0.959	0.703	1.004	0.480	69.63
68	0.957	0.681	0.710	0.884	0.949	0.768	0.999	0.378	70.54
69	0.964	0.676	0.720	0.875	0.978	0.724	1.033	0.478	71.44
70	0.982	0.739	0.756	0.853	0.989	0.599	1.063	0.475	72.34
71	1.000	0.762	0.771	0.846	1.036	0.612	1.119	0.467	73.24

Minnaert $(I/F)_0$ and K coefficients for Saturn PlanetCam VIS observations. April2013 (black), April2014 (blue), July2014 (green), May2015 (red), July2015 (cyan), March2016 (magenta). Tables provide mean values.

Saturn $(I/F)_0$ – VIS

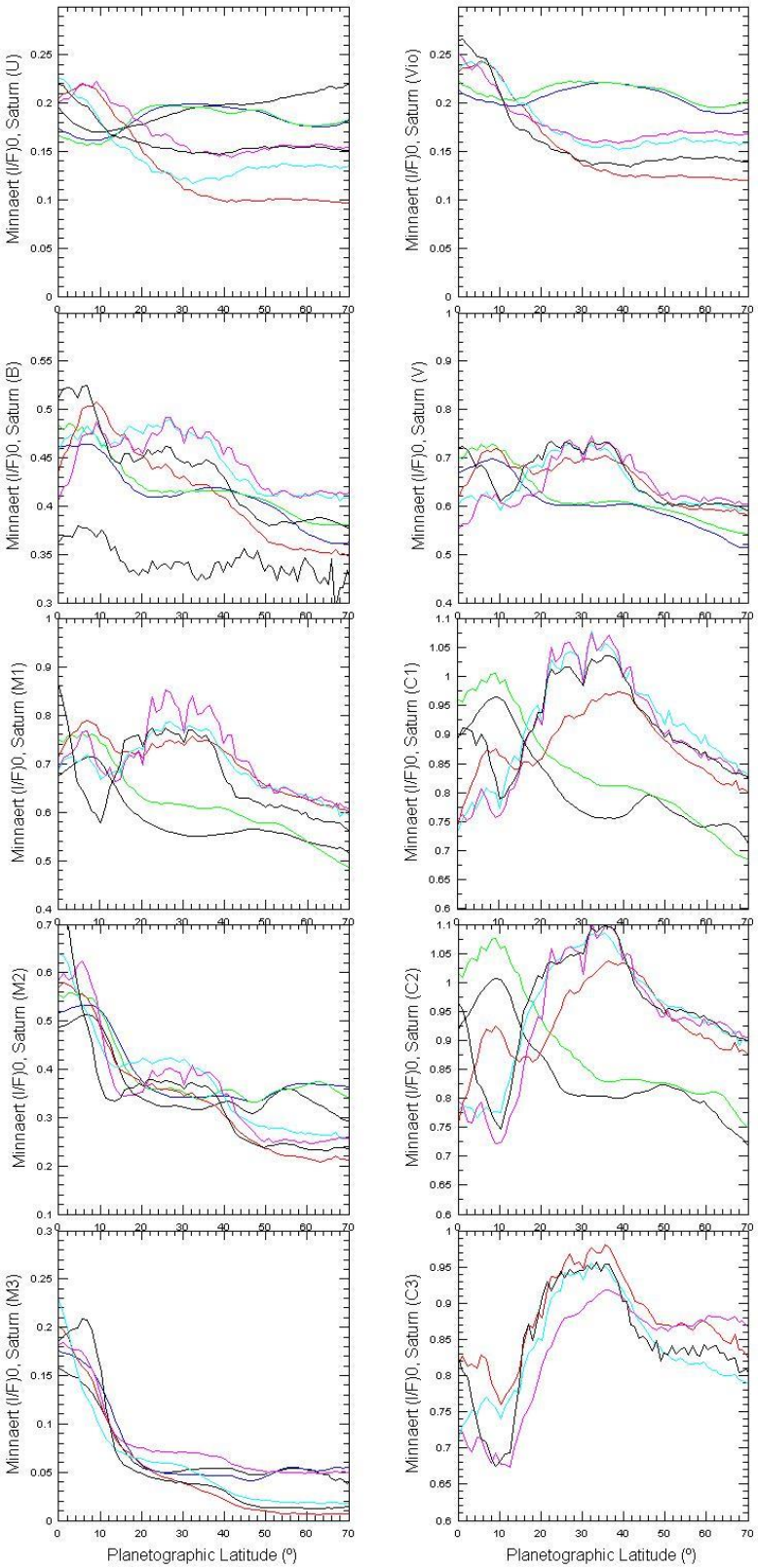

Saturn *k* – VIS

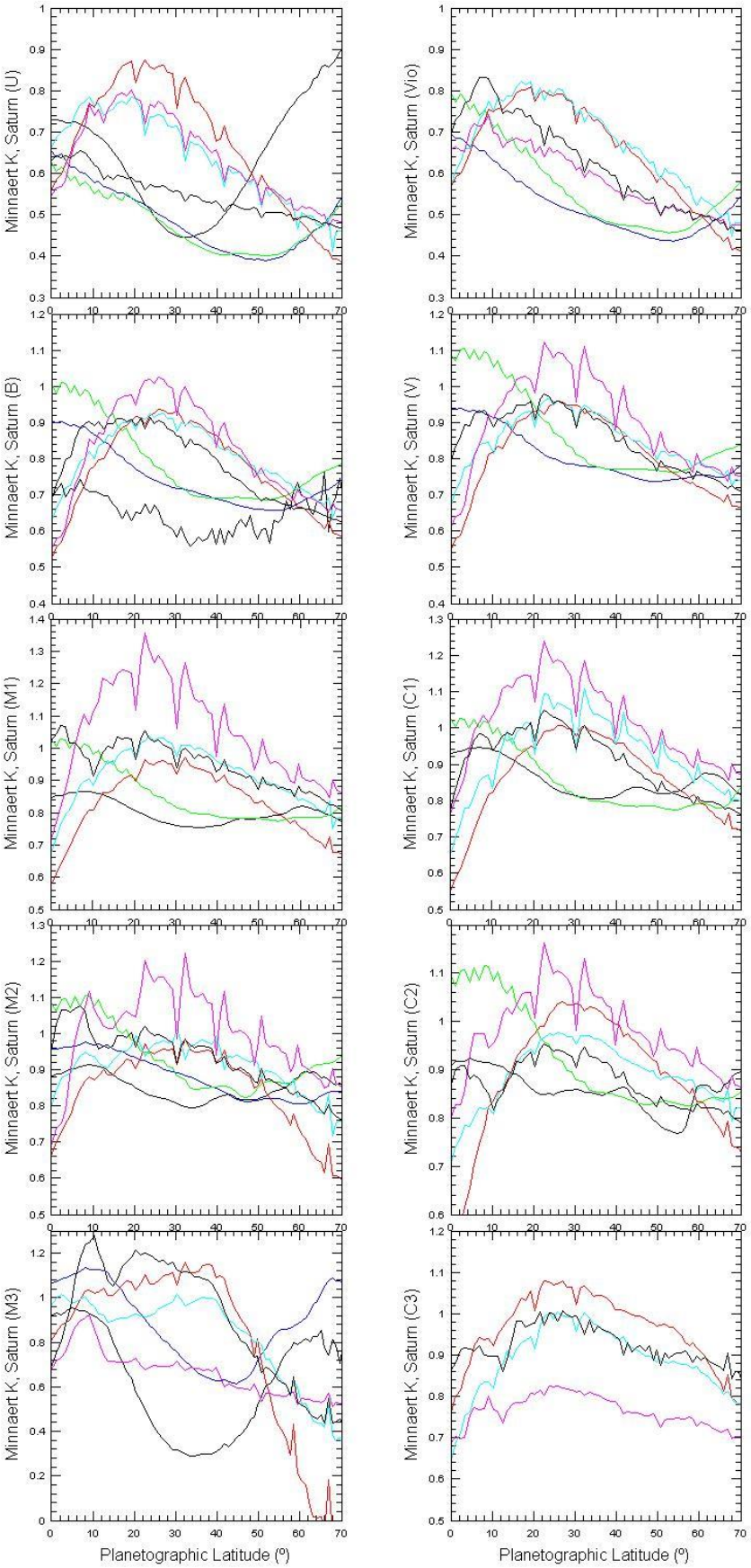
Minnaert K, Saturn (U)
Minnaert K, Saturn (Vio)
Minnaert K, Saturn (B)
Minnaert K, Saturn (V)
Minnaert K, Saturn (M1)
Minnaert K, Saturn (C1)
Minnaert K, Saturn (M2)
Minnaert K, Saturn (C2)
Minnaert K, Saturn (M3)
Minnaert K, Saturn (C3)
Planetographic Latitude (º)
Planetographic Latitude (º)

Saturn $(I/F)_0$ – VIS

Lat PC (°)	$(I/F)_0$ UV	$(I/F)_0$ Vio	$(I/F)_0$ B	$(I/F)_0$ V	$(I/F)_0$ M1	$(I/F)_0$ C1	$(I/F)_0$ M2	$(I/F)_0$ C2	$(I/F)_0$ M3	$(I/F)_0$ C3	Lat PG (°)
0	0.198	0.237	0.445	0.642	0.730	0.830	0.584	0.871	0.189	0.770	0.00
1	0.197	0.236	0.453	0.652	0.734	0.844	0.586	0.877	0.186	0.772	1.14
2	0.195	0.234	0.456	0.656	0.735	0.851	0.578	0.875	0.180	0.763	2.29
3	0.193	0.232	0.460	0.661	0.730	0.860	0.565	0.875	0.174	0.758	3.43
4	0.191	0.230	0.463	0.663	0.720	0.862	0.555	0.875	0.168	0.752	4.57
5	0.191	0.230	0.471	0.676	0.730	0.883	0.549	0.889	0.165	0.754	5.71
6	0.190	0.227	0.472	0.675	0.728	0.884	0.536	0.885	0.159	0.748	6.85
7	0.187	0.223	0.468	0.670	0.718	0.876	0.520	0.880	0.151	0.729	7.99
8	0.186	0.219	0.466	0.668	0.705	0.871	0.499	0.877	0.139	0.725	9.13
9	0.181	0.211	0.459	0.654	0.689	0.856	0.471	0.871	0.124	0.715	10.26
10	0.179	0.207	0.455	0.656	0.691	0.865	0.448	0.880	0.109	0.725	11.40
11	0.175	0.199	0.444	0.650	0.693	0.870	0.427	0.884	0.096	0.729	12.53
12	0.173	0.196	0.442	0.650	0.683	0.869	0.409	0.890	0.086	0.752	13.66
13	0.173	0.194	0.438	0.650	0.682	0.870	0.396	0.899	0.078	0.774	14.79
14	0.174	0.193	0.440	0.659	0.694	0.887	0.388	0.916	0.072	0.812	15.91
15	0.173	0.192	0.436	0.659	0.696	0.894	0.382	0.925	0.068	0.832	17.03
16	0.172	0.188	0.431	0.656	0.694	0.895	0.376	0.930	0.064	0.830	18.15
17	0.171	0.186	0.429	0.657	0.694	0.902	0.373	0.938	0.061	0.853	19.27
18	0.169	0.184	0.428	0.652	0.681	0.892	0.369	0.937	0.059	0.862	20.38
19	0.169	0.183	0.431	0.667	0.706	0.928	0.371	0.957	0.056	0.892	21.49
20	0.166	0.181	0.431	0.674	0.718	0.945	0.372	0.966	0.055	0.900	22.60
21	0.166	0.180	0.430	0.672	0.709	0.936	0.368	0.962	0.054	0.910	23.70
22	0.165	0.179	0.431	0.673	0.710	0.935	0.367	0.962	0.053	0.918	24.80
23	0.166	0.179	0.436	0.683	0.722	0.946	0.370	0.971	0.052	0.928	25.89
24	0.165	0.178	0.434	0.683	0.720	0.945	0.370	0.974	0.052	0.933	26.98
25	0.163	0.175	0.430	0.677	0.713	0.937	0.366	0.969	0.051	0.929	28.07
26	0.161	0.173	0.429	0.676	0.710	0.934	0.365	0.970	0.051	0.932	29.15
27	0.161	0.172	0.426	0.668	0.695	0.916	0.359	0.965	0.051	0.929	30.22
28	0.160	0.172	0.429	0.680	0.713	0.941	0.362	0.981	0.050	0.943	31.30
29	0.159	0.171	0.426	0.685	0.717	0.954	0.362	0.990	0.049	0.945	32.37
30	0.159	0.171	0.423	0.678	0.705	0.940	0.356	0.984	0.048	0.946	33.43
31	0.159	0.171	0.424	0.678	0.704	0.942	0.355	0.987	0.047	0.943	34.49
32	0.160	0.172	0.425	0.682	0.708	0.948	0.355	0.990	0.047	0.951	35.54
33	0.159	0.171	0.425	0.681	0.706	0.949	0.354	0.990	0.046	0.948	36.60
34	0.158	0.170	0.423	0.675	0.696	0.944	0.349	0.985	0.044	0.937	37.64
35	0.157	0.169	0.420	0.668	0.686	0.939	0.344	0.978	0.043	0.928	38.68
36	0.157	0.169	0.415	0.658	0.671	0.925	0.335	0.967	0.042	0.917	39.72
37	0.157	0.168	0.415	0.655	0.668	0.925	0.330	0.964	0.040	0.910	40.75
38	0.157	0.168	0.411	0.650	0.664	0.926	0.323	0.958	0.038	0.894	41.78
39	0.158	0.169	0.408	0.637	0.648	0.906	0.312	0.945	0.036	0.884	42.80
40	0.159	0.169	0.405	0.632	0.643	0.901	0.305	0.939	0.035	0.876	43.81
41	0.160	0.170	0.405	0.629	0.642	0.899	0.300	0.935	0.033	0.874	44.83
42	0.160	0.171	0.403	0.625	0.640	0.895	0.294	0.930	0.032	0.869	45.83
43	0.160	0.170	0.398	0.617	0.631	0.886	0.290	0.922	0.032	0.857	46.84
44	0.160	0.169	0.395	0.610	0.625	0.877	0.287	0.917	0.031	0.856	47.83
45	0.160	0.170	0.391	0.606	0.620	0.869	0.286	0.913	0.031	0.849	48.83
46	0.160	0.169	0.388	0.602	0.617	0.861	0.288	0.910	0.031	0.850	49.82
47	0.160	0.169	0.388	0.603	0.619	0.865	0.291	0.909	0.031	0.847	50.80
48	0.160	0.169	0.386	0.598	0.613	0.852	0.292	0.904	0.032	0.849	51.78
49	0.160	0.169	0.383	0.597	0.612	0.849	0.294	0.902	0.032	0.847	52.76
50	0.160	0.169	0.386	0.598	0.614	0.848	0.296	0.901	0.032	0.850	53.73
51	0.160	0.168	0.384	0.597	0.612	0.845	0.297	0.898	0.033	0.850	54.69
52	0.159	0.167	0.382	0.594	0.608	0.839	0.296	0.893	0.033	0.845	55.66
53	0.158	0.165	0.381	0.591	0.604	0.834	0.296	0.889	0.033	0.847	56.61
54	0.159	0.165	0.378	0.590	0.601	0.829	0.294	0.887	0.033	0.847	57.57
55	0.158	0.164	0.379	0.588	0.597	0.823	0.294	0.885	0.033	0.849	58.52
56	0.158	0.164	0.381	0.590	0.596	0.826	0.292	0.886	0.032	0.853	59.46
57	0.158	0.164	0.379	0.587	0.590	0.819	0.291	0.882	0.032	0.850	60.41
58	0.158	0.164	0.379	0.587	0.587	0.816	0.290	0.880	0.032	0.849	61.34
59	0.159	0.164	0.377	0.586	0.585	0.813	0.289	0.877	0.031	0.847	62.28
60	0.159	0.164	0.376	0.585	0.583	0.809	0.289	0.872	0.031	0.843	63.21
61	0.159	0.163	0.376	0.582	0.580	0.805	0.288	0.867	0.031	0.839	64.14
62	0.159	0.163	0.375	0.580	0.577	0.802	0.287	0.863	0.031	0.836	65.06
63	0.159	0.163	0.378	0.578	0.575	0.797	0.287	0.859	0.031	0.836	65.98
64	0.159	0.163	0.371	0.577	0.574	0.795	0.287	0.858	0.031	0.841	66.90
65	0.158	0.162	0.373	0.574	0.569	0.790	0.284	0.849	0.031	0.827	67.81
66	0.159	0.163	0.373	0.572	0.566	0.786	0.282	0.847	0.031	0.827	68.72
67	0.160	0.163	0.375	0.571	0.562	0.782	0.280	0.842	0.030	0.824	69.63
68	0.160	0.164	0.373	0.569	0.557	0.777	0.277	0.838	0.030	0.819	70.54
69	0.161	0.164	0.374	0.568	0.554	0.773	0.275	0.835	0.029	0.816	71.44
70	0.161	0.164	0.370	0.567	0.550	0.769	0.272	0.833	0.028	0.812	72.34
71	0.160	0.165	0.369	0.567	0.547	0.765	0.269	0.831	0.028	0.816	73.24
72	0.161	0.165	0.364	0.566	0.544	0.760	0.266	0.826	0.027	0.818	74.14
73	0.161	0.166	0.367	0.567	0.542	0.758	0.264	0.824	0.027	0.827	75.03
74	0.160	0.166	0.370	0.567	0.539	0.753	0.259	0.816	0.026	0.816	75.92
75	0.160	0.167	0.376	0.568	0.538	0.751	0.257	0.810	0.026	0.824	76.81
76	0.160	0.168	0.365	0.569	0.536	0.751	0.254	0.802	0.026	0.825	77.70
77	0.160	0.168	0.363	0.570	0.534	0.748	0.251	0.796	0.027	0.825	78.58
78	0.159	0.169	0.362	0.572	0.533	0.746	0.249	0.790	0.026	0.827	79.47
79	0.159	0.169	0.363	0.573	0.532	0.746	0.247	0.781	0.027	0.827	80.35
80	0.159	0.169	0.360	0.574	0.530	0.744	0.246	0.778	0.027	0.831	81.23

Saturn *k* – VIS

Lat PC (°)	K (UV)	K (Vio)	K (B)	K (V)	K (M1)	K (C1)	K (M2)	K (C2)	K (M3)	K (C3)	Lat PG (°)
0	0.629	0.663	0.713	0.773	0.811	0.782	0.860	0.816	0.853	0.738	0.00
1	0.636	0.675	0.732	0.795	0.834	0.809	0.887	0.836	0.885	0.767	1.14
2	0.642	0.683	0.750	0.813	0.861	0.832	0.910	0.849	0.907	0.785	2.29
3	0.645	0.693	0.762	0.834	0.881	0.861	0.921	0.865	0.925	0.806	3.43
4	0.651	0.702	0.777	0.849	0.883	0.875	0.937	0.876	0.953	0.828	4.57
5	0.668	0.723	0.803	0.880	0.914	0.910	0.964	0.900	0.988	0.850	5.71
6	0.673	0.729	0.820	0.892	0.929	0.925	0.978	0.904	1.020	0.864	6.85
7	0.681	0.738	0.832	0.907	0.941	0.937	0.992	0.911	1.043	0.860	7.99
8	0.689	0.747	0.845	0.917	0.937	0.938	0.990	0.911	1.040	0.868	9.13
9	0.673	0.723	0.834	0.900	0.927	0.925	0.973	0.902	1.027	0.852	10.26
10	0.679	0.727	0.848	0.920	0.952	0.952	0.968	0.921	0.999	0.868	11.40
11	0.661	0.706	0.838	0.916	0.970	0.965	0.961	0.927	0.979	0.860	12.53
12	0.667	0.711	0.850	0.931	0.973	0.976	0.953	0.938	0.946	0.886	13.66
13	0.670	0.712	0.851	0.932	0.969	0.971	0.955	0.943	0.925	0.900	14.79
14	0.675	0.715	0.856	0.940	0.982	0.982	0.957	0.953	0.924	0.924	15.91
15	0.676	0.715	0.855	0.942	0.985	0.985	0.962	0.957	0.927	0.933	17.03
16	0.673	0.710	0.858	0.942	0.988	0.988	0.964	0.962	0.919	0.931	18.15
17	0.673	0.709	0.853	0.938	0.983	0.986	0.961	0.962	0.916	0.945	19.27
18	0.656	0.685	0.843	0.914	0.942	0.948	0.952	0.945	0.906	0.926	20.38
19	0.653	0.690	0.852	0.941	0.990	0.997	0.964	0.969	0.889	0.962	21.49
20	0.630	0.671	0.849	0.950	1.010	1.017	0.976	0.980	0.884	0.961	22.60
21	0.639	0.683	0.854	0.947	0.997	1.008	0.966	0.977	0.865	0.977	23.70
22	0.631	0.671	0.848	0.934	0.981	0.990	0.959	0.967	0.857	0.970	24.80
23	0.631	0.673	0.851	0.939	0.987	0.994	0.962	0.972	0.852	0.971	25.89
24	0.626	0.668	0.842	0.933	0.980	0.988	0.962	0.971	0.848	0.976	26.98
25	0.612	0.653	0.830	0.921	0.968	0.977	0.953	0.964	0.842	0.967	28.07
26	0.607	0.649	0.824	0.916	0.962	0.970	0.949	0.960	0.840	0.965	29.15
27	0.591	0.627	0.802	0.878	0.911	0.918	0.916	0.936	0.831	0.945	30.22
28	0.591	0.631	0.815	0.908	0.954	0.965	0.941	0.958	0.826	0.960	31.30
29	0.571	0.615	0.804	0.918	0.969	0.987	0.953	0.967	0.822	0.955	32.37
30	0.579	0.621	0.800	0.900	0.948	0.962	0.934	0.952	0.811	0.959	33.43
31	0.571	0.613	0.793	0.890	0.935	0.950	0.928	0.947	0.807	0.944	34.49
32	0.570	0.610	0.793	0.888	0.935	0.948	0.929	0.944	0.806	0.948	35.54
33	0.562	0.603	0.786	0.883	0.933	0.944	0.932	0.941	0.809	0.941	36.60
34	0.553	0.592	0.779	0.874	0.924	0.937	0.928	0.935	0.807	0.935	37.64
35	0.545	0.584	0.776	0.866	0.918	0.932	0.926	0.931	0.800	0.929	38.68
36	0.543	0.575	0.755	0.838	0.884	0.899	0.899	0.912	0.788	0.920	39.72
37	0.536	0.568	0.762	0.848	0.902	0.916	0.912	0.920	0.776	0.915	40.75
38	0.526	0.557	0.749	0.854	0.918	0.938	0.919	0.922	0.753	0.902	41.78
39	0.536	0.565	0.751	0.836	0.896	0.911	0.899	0.908	0.731	0.905	42.80
40	0.533	0.557	0.739	0.826	0.889	0.903	0.891	0.900	0.715	0.896	43.81
41	0.533	0.556	0.740	0.822	0.888	0.898	0.889	0.894	0.704	0.896	44.83
42	0.532	0.551	0.738	0.818	0.887	0.895	0.886	0.889	0.694	0.896	45.83
43	0.525	0.540	0.725	0.808	0.878	0.886	0.879	0.881	0.691	0.887	46.84
44	0.524	0.534	0.722	0.800	0.872	0.878	0.875	0.876	0.686	0.888	47.83
45	0.527	0.533	0.707	0.787	0.855	0.863	0.860	0.867	0.671	0.879	48.83
46	0.520	0.520	0.699	0.782	0.854	0.856	0.869	0.865	0.697	0.878	49.82
47	0.510	0.512	0.700	0.795	0.872	0.882	0.886	0.869	0.667	0.867	50.80
48	0.524	0.521	0.701	0.785	0.857	0.861	0.870	0.862	0.663	0.876	51.78
49	0.521	0.516	0.689	0.779	0.850	0.853	0.868	0.858	0.660	0.872	52.76
50	0.524	0.517	0.697	0.779	0.851	0.852	0.866	0.857	0.642	0.874	53.73
51	0.523	0.511	0.694	0.776	0.846	0.848	0.861	0.853	0.632	0.873	54.69
52	0.520	0.507	0.690	0.772	0.842	0.845	0.855	0.850	0.633	0.869	55.66
53	0.519	0.501	0.693	0.768	0.837	0.842	0.850	0.848	0.626	0.866	56.61
54	0.524	0.504	0.688	0.764	0.831	0.836	0.838	0.849	0.604	0.861	57.57
55	0.516	0.492	0.691	0.759	0.829	0.831	0.848	0.853	0.659	0.857	58.52
56	0.514	0.491	0.698	0.772	0.839	0.851	0.848	0.860	0.588	0.854	59.46
57	0.524	0.499	0.693	0.766	0.830	0.838	0.839	0.855	0.577	0.848	60.41
58	0.523	0.497	0.690	0.763	0.824	0.835	0.837	0.853	0.577	0.844	61.34
59	0.525	0.497	0.684	0.762	0.821	0.830	0.829	0.848	0.550	0.835	62.28
60	0.527	0.494	0.681	0.760	0.815	0.827	0.826	0.844	0.543	0.826	63.21
61	0.524	0.492	0.683	0.755	0.809	0.820	0.819	0.838	0.542	0.817	64.14
62	0.525	0.488	0.682	0.752	0.804	0.816	0.815	0.834	0.556	0.809	65.06
63	0.528	0.491	0.690	0.748	0.796	0.808	0.806	0.830	0.531	0.799	65.98
64	0.528	0.489	0.671	0.751	0.803	0.812	0.830	0.840	0.606	0.822	66.90
65	0.520	0.481	0.674	0.748	0.790	0.807	0.804	0.825	0.524	0.783	67.81
66	0.530	0.488	0.679	0.747	0.789	0.802	0.803	0.827	0.519	0.785	68.72
67	0.536	0.491	0.685	0.747	0.786	0.800	0.801	0.826	0.506	0.781	69.63
68	0.540	0.493	0.676	0.747	0.783	0.797	0.797	0.823	0.501	0.771	70.54
69	0.543	0.495	0.679	0.747	0.782	0.795	0.796	0.822	0.481	0.772	71.44
70	0.545	0.495	0.669	0.748	0.780	0.793	0.795	0.822	0.477	0.768	72.34
71	0.546	0.497	0.667	0.748	0.778	0.790	0.795	0.821	0.480	0.771	73.24
72	0.553	0.503	0.658	0.747	0.774	0.785	0.790	0.818	0.456	0.770	74.14
73	0.556	0.510	0.672	0.752	0.780	0.792	0.808	0.824	0.529	0.792	75.03
74	0.549	0.501	0.674	0.751	0.773	0.789	0.789	0.816	0.438	0.762	75.92
75	0.556	0.512	0.690	0.752	0.774	0.788	0.792	0.815	0.450	0.772	76.81
76	0.560	0.516	0.669	0.754	0.775	0.791	0.792	0.813	0.488	0.779	77.70
77	0.566	0.522	0.666	0.756	0.775	0.791	0.793	0.813	0.500	0.785	78.58
78	0.566	0.526	0.665	0.759	0.778	0.792	0.793	0.814	0.488	0.788	79.47
79	0.571	0.531	0.671	0.762	0.780	0.796	0.796	0.811	0.525	0.793	80.35
80	0.574	0.535	0.667	0.764	0.781	0.797	0.797	0.813	0.545	0.798	81.23

Minnaert $(I/F)_0$ and K coefficients for Saturn PlanetCam SWIR observations. May2015 (red), July2015 (cyan), March2016 (magenta), May2016 (black), July2016 (blue). Tables provide mean values.

Saturn $(I/F)_0$ – SWIR

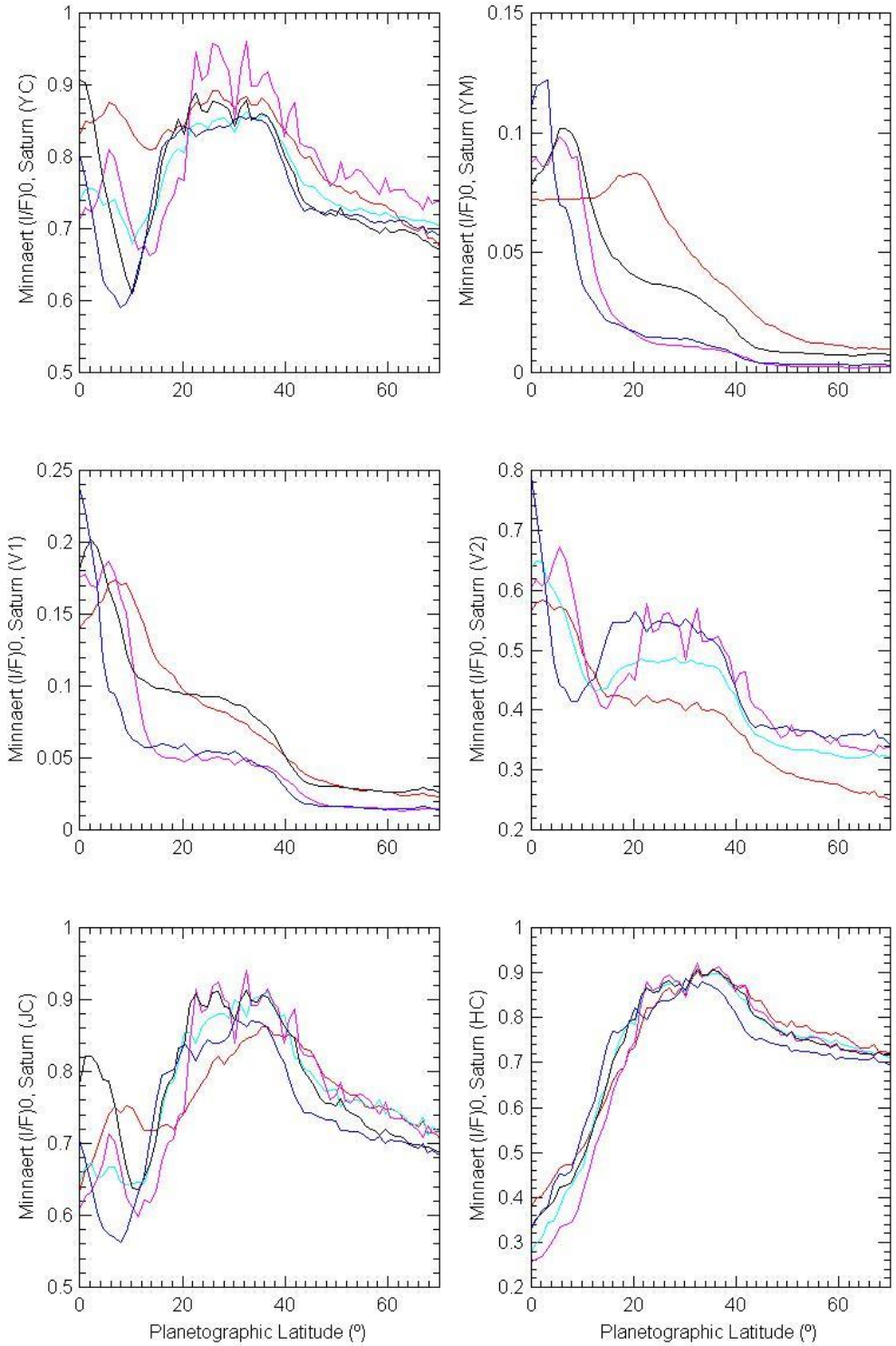

Saturn *k* – SWIR

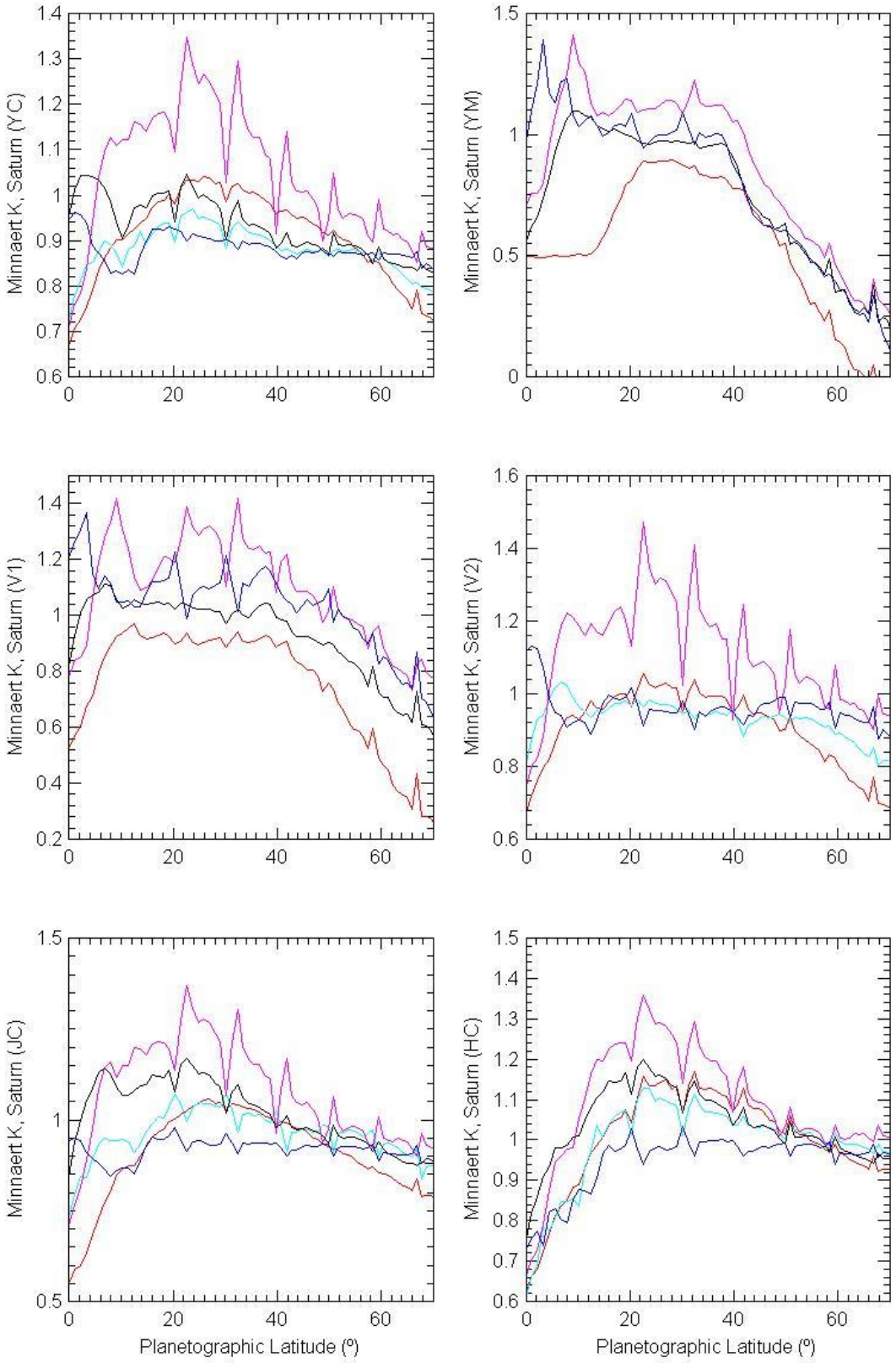

Saturn $(I/F)_0$ – SWIR

Lat PC (°)	$(I/F)_o$ YC	$(I/F)_o$ YM	$(I/F)_o$ V1	$(I/F)_o$ V2	$(I/F)_o$ JC	$(I/F)_o$ HC	Lat PG (°)
0	0.798	0.087	0.184	0.650	0.675	0.314	0.00
1	0.801	0.091	0.185	0.644	0.691	0.332	1.14
2	0.785	0.091	0.179	0.623	0.689	0.344	2.29
3	0.769	0.092	0.173	0.594	0.682	0.363	3.43
4	0.752	0.086	0.161	0.573	0.683	0.385	4.57
5	0.754	0.086	0.156	0.566	0.696	0.410	5.71
6	0.743	0.085	0.151	0.553	0.689	0.420	6.85
7	0.718	0.081	0.140	0.524	0.665	0.428	7.99
8	0.702	0.076	0.129	0.498	0.652	0.457	9.13
9	0.687	0.066	0.114	0.470	0.649	0.486	10.26
10	0.695	0.059	0.103	0.452	0.649	0.528	11.40
11	0.711	0.052	0.094	0.444	0.658	0.569	12.53
12	0.726	0.048	0.086	0.441	0.677	0.609	13.66
13	0.743	0.045	0.082	0.446	0.703	0.647	14.79
14	0.782	0.043	0.081	0.462	0.740	0.693	15.91
15	0.801	0.043	0.079	0.470	0.757	0.717	17.03
16	0.809	0.041	0.078	0.472	0.762	0.735	18.15
17	0.822	0.040	0.076	0.476	0.786	0.765	19.27
18	0.817	0.039	0.075	0.475	0.804	0.777	20.38
19	0.857	0.038	0.073	0.492	0.835	0.820	21.49
20	0.876	0.036	0.072	0.503	0.850	0.845	22.60
21	0.864	0.035	0.071	0.493	0.851	0.843	23.70
22	0.866	0.033	0.070	0.494	0.858	0.850	24.80
23	0.883	0.032	0.070	0.501	0.871	0.866	25.89
24	0.883	0.031	0.070	0.502	0.875	0.871	26.98
25	0.876	0.030	0.069	0.496	0.865	0.865	28.07
26	0.870	0.029	0.068	0.492	0.865	0.870	29.15
27	0.849	0.028	0.066	0.478	0.862	0.860	30.22
28	0.876	0.027	0.065	0.493	0.881	0.887	31.30
29	0.887	0.026	0.064	0.497	0.887	0.901	32.37
30	0.867	0.024	0.061	0.481	0.882	0.890	33.43
31	0.866	0.023	0.058	0.476	0.883	0.891	34.49
32	0.872	0.022	0.057	0.477	0.888	0.897	35.54
33	0.870	0.021	0.055	0.474	0.891	0.895	36.60
34	0.853	0.020	0.052	0.458	0.875	0.882	37.64
35	0.838	0.018	0.048	0.443	0.864	0.871	38.68
36	0.815	0.016	0.043	0.420	0.848	0.854	39.72
37	0.809	0.015	0.039	0.410	0.845	0.847	40.75
38	0.802	0.013	0.035	0.398	0.832	0.840	41.78
39	0.776	0.012	0.031	0.376	0.811	0.813	42.80
40	0.767	0.011	0.029	0.367	0.800	0.803	43.81
41	0.766	0.010	0.027	0.363	0.797	0.800	44.83
42	0.762	0.009	0.026	0.358	0.790	0.792	45.83
43	0.752	0.009	0.025	0.350	0.776	0.779	46.84
44	0.744	0.009	0.024	0.345	0.767	0.771	47.83
45	0.742	0.008	0.024	0.341	0.763	0.766	48.83
46	0.740	0.008	0.024	0.341	0.761	0.760	49.82
47	0.747	0.007	0.023	0.342	0.759	0.764	50.80
48	0.737	0.007	0.023	0.337	0.751	0.754	51.78
49	0.736	0.007	0.022	0.336	0.748	0.752	52.76
50	0.738	0.007	0.022	0.337	0.750	0.754	53.73
51	0.736	0.006	0.022	0.336	0.747	0.752	54.69
52	0.731	0.006	0.021	0.333	0.741	0.748	55.66
53	0.726	0.006	0.021	0.330	0.736	0.745	56.61
54	0.724	0.006	0.021	0.328	0.735	0.743	57.57
55	0.721	0.006	0.021	0.327	0.735	0.739	58.52
56	0.727	0.006	0.020	0.326	0.733	0.741	59.46
57	0.720	0.006	0.020	0.323	0.730	0.734	60.41
58	0.720	0.006	0.020	0.322	0.728	0.731	61.34
59	0.718	0.006	0.020	0.320	0.726	0.729	62.28
60	0.717	0.006	0.020	0.320	0.723	0.727	63.21
61	0.712	0.006	0.020	0.319	0.717	0.723	64.14
62	0.709	0.006	0.020	0.319	0.714	0.721	65.06
63	0.707	0.006	0.020	0.319	0.712	0.720	65.98
64	0.706	0.006	0.021	0.322	0.714	0.720	66.90
65	0.704	0.006	0.020	0.319	0.706	0.719	67.81
66	0.700	0.006	0.020	0.317	0.707	0.716	68.72
67	0.697	0.006	0.019	0.314	0.704	0.712	69.63
68	0.694	0.005	0.018	0.310	0.700	0.708	70.54
69	0.692	0.005	0.018	0.307	0.697	0.707	71.44
70	0.690	0.005	0.017	0.304	0.694	0.703	72.34
71	0.689	0.005	0.017	0.302	0.692	0.702	73.24
72	0.688	0.005	0.017	0.301	0.691	0.703	74.14
73	0.689	0.005	0.018	0.304	0.695	0.705	75.03
74	0.694	0.005	0.017	0.306	0.695	0.709	75.92
75	0.698	0.005	0.018	0.311	0.702	0.712	76.81
76	0.701	0.005	0.018	0.315	0.706	0.714	77.70
77	0.705	0.005	0.018	0.319	0.708	0.715	78.58
78	0.707	0.005	0.018	0.322	0.709	0.715	79.47
79	0.708	0.005	0.019	0.324	0.710	0.714	80.35
80	0.708	0.005	0.020	0.327	0.709	0.712	81.23

Saturn *k* – SWIR

Lat PC (°)	K (YC)	K (YM)	K (V1)	K (V2)	K (JC)	K (HC)	Lat PG (°)
0	0.802	0.679	0.833	0.833	0.755	0.674	0.00
1	0.844	0.743	0.902	0.880	0.808	0.719	1.14
2	0.864	0.780	0.944	0.910	0.840	0.746	2.29
3	0.885	0.854	0.998	0.923	0.866	0.790	3.43
4	0.903	0.860	1.001	0.950	0.906	0.834	4.57
5	0.930	0.910	1.040	0.987	0.951	0.875	5.71
6	0.947	0.972	1.096	1.018	0.974	0.886	6.85
7	0.943	1.010	1.112	1.022	0.974	0.892	7.99
8	0.932	1.024	1.113	1.015	0.971	0.916	9.13
9	0.919	0.983	1.080	1.002	0.978	0.933	10.26
10	0.937	0.975	1.070	0.996	0.978	0.977	11.40
11	0.954	0.946	1.049	0.999	0.983	1.010	12.53
12	0.972	0.921	1.024	1.003	1.001	1.047	13.66
13	0.971	0.921	1.034	1.009	1.020	1.059	14.79
14	0.996	0.932	1.052	1.033	1.045	1.087	15.91
15	1.004	0.961	1.068	1.045	1.051	1.092	17.03
16	1.007	0.976	1.079	1.049	1.050	1.098	18.15
17	1.009	0.992	1.076	1.043	1.063	1.109	19.27
18	0.968	1.008	1.085	1.020	1.052	1.079	20.38
19	1.030	0.984	1.081	1.068	1.086	1.134	21.49
20	1.058	0.975	1.087	1.100	1.094	1.157	22.60
21	1.044	0.980	1.080	1.079	1.093	1.147	23.70
22	1.026	0.988	1.075	1.062	1.086	1.132	24.80
23	1.033	0.994	1.084	1.067	1.089	1.137	25.89
24	1.026	1.001	1.087	1.065	1.084	1.130	26.98
25	1.015	1.004	1.085	1.053	1.069	1.118	28.07
26	1.006	1.002	1.080	1.044	1.064	1.114	29.15
27	0.940	1.005	1.044	0.974	1.030	1.064	30.22
28	1.000	0.998	1.080	1.040	1.059	1.113	31.30
29	1.026	1.005	1.100	1.071	1.063	1.136	32.37
30	0.994	0.981	1.074	1.034	1.049	1.111	33.43
31	0.977	0.971	1.060	1.017	1.038	1.099	34.49
32	0.976	0.972	1.073	1.018	1.034	1.098	35.54
33	0.973	0.976	1.089	1.025	1.033	1.095	36.60
34	0.959	0.977	1.094	1.013	1.017	1.086	37.64
35	0.952	0.953	1.087	1.009	1.011	1.079	38.68
36	0.904	0.904	1.019	0.946	0.978	1.042	39.72
37	0.929	0.884	1.038	0.985	0.995	1.060	40.75
38	0.953	0.840	1.040	1.011	0.997	1.082	41.78
39	0.923	0.782	0.989	0.977	0.982	1.050	42.80
40	0.915	0.738	0.964	0.969	0.975	1.042	43.81
41	0.919	0.708	0.967	0.981	0.978	1.043	44.83
42	0.922	0.677	0.968	0.986	0.978	1.043	45.83
43	0.914	0.666	0.956	0.979	0.968	1.032	46.84
44	0.908	0.639	0.945	0.974	0.962	1.027	47.83
45	0.891	0.620	0.913	0.944	0.949	1.010	48.83
46	0.893	0.619	0.945	0.963	0.951	1.006	49.82
47	0.926	0.565	0.928	0.992	0.955	1.038	50.80
48	0.905	0.546	0.899	0.966	0.949	1.015	51.78
49	0.898	0.529	0.878	0.955	0.944	1.010	52.76
50	0.900	0.488	0.856	0.957	0.947	1.011	53.73
51	0.898	0.457	0.840	0.952	0.944	1.009	54.69
52	0.892	0.449	0.829	0.944	0.938	1.003	55.66
53	0.887	0.424	0.808	0.934	0.932	0.999	56.61
54	0.873	0.390	0.763	0.912	0.924	0.988	57.57
55	0.866	0.435	0.822	0.919	0.921	0.980	58.52
56	0.892	0.340	0.751	0.924	0.918	0.999	59.46
57	0.871	0.321	0.728	0.905	0.912	0.982	60.41
58	0.863	0.306	0.711	0.897	0.908	0.978	61.34
59	0.856	0.256	0.670	0.886	0.903	0.976	62.28
60	0.852	0.223	0.652	0.880	0.900	0.975	63.21
61	0.844	0.215	0.637	0.868	0.892	0.972	64.14
62	0.838	0.213	0.636	0.861	0.888	0.970	65.06
63	0.827	0.182	0.599	0.844	0.881	0.965	65.98
64	0.831	0.292	0.715	0.872	0.893	0.971	66.90
65	0.828	0.180	0.610	0.844	0.870	0.974	67.81
66	0.820	0.162	0.594	0.839	0.873	0.967	68.72
67	0.815	0.141	0.574	0.834	0.871	0.965	69.63
68	0.810	0.099	0.544	0.829	0.867	0.963	70.54
69	0.807	0.071	0.532	0.831	0.865	0.965	71.44
70	0.806	0.063	0.527	0.834	0.865	0.966	72.34
71	0.807	0.050	0.527	0.837	0.866	0.968	73.24
72	0.806	0.016	0.506	0.834	0.867	0.967	74.14
73	0.813	0.091	0.604	0.859	0.881	0.975	75.03
74	0.821	0.029	0.537	0.852	0.872	0.981	75.92
75	0.823	0.024	0.552	0.858	0.880	0.977	76.81
76	0.828	0.046	0.574	0.863	0.884	0.978	77.70
77	0.831	0.040	0.572	0.865	0.886	0.978	78.58
78	0.834	0.043	0.576	0.867	0.887	0.978	79.47
79	0.837	0.069	0.598	0.870	0.889	0.979	80.35
80	0.839	0.094	0.619	0.873	0.888	0.979	81.23

A3. Absolute reflectivity of Jupiter from December 2012 to July 2016 in both VIS and SWIR channels

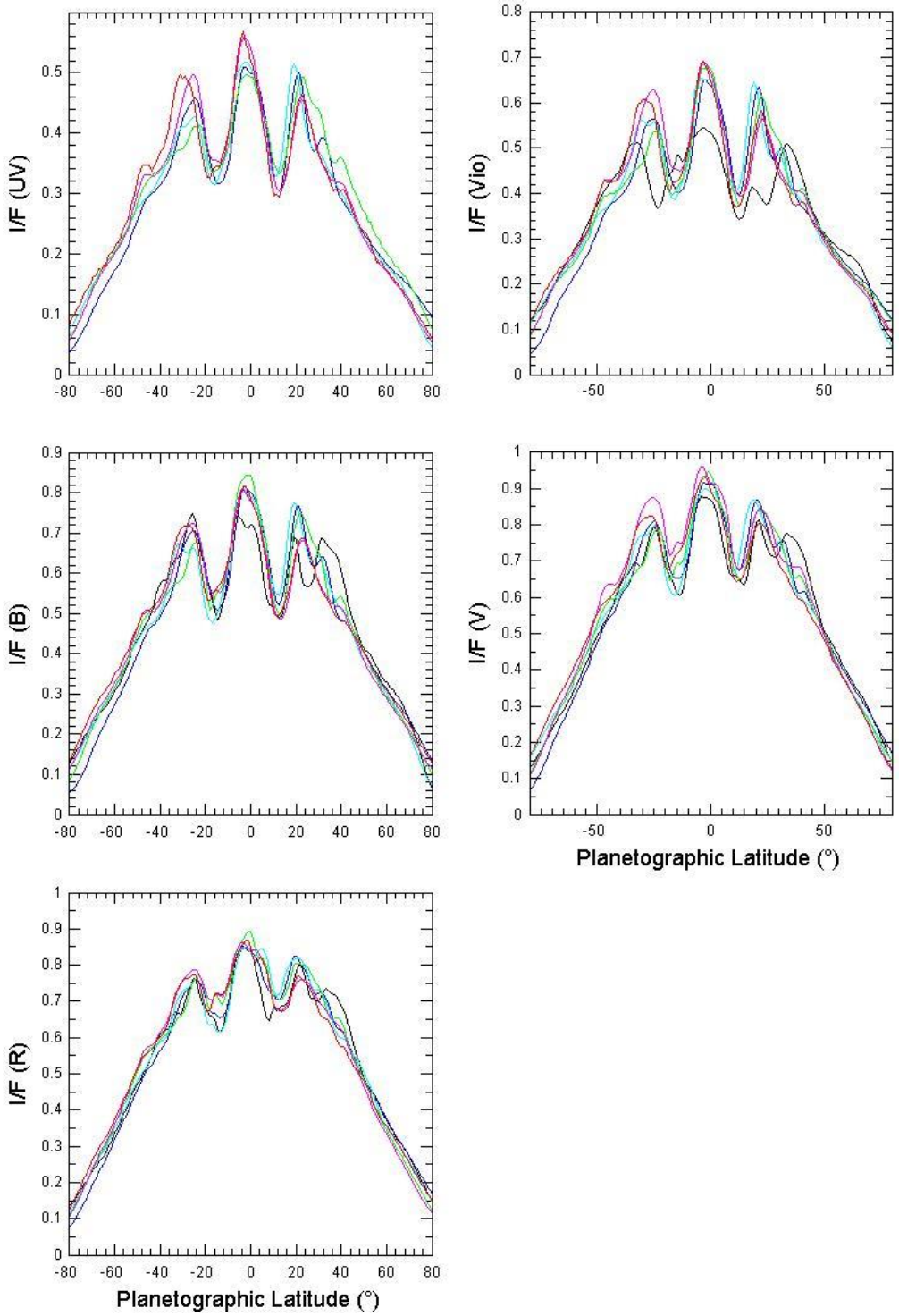

Absolute reflectivity of Jupiter from December 2012 to July 2016 in VIS channel U, Vio, B, V and R filters (black corresponds to December 2012, blue to December 2013, cyan to April 2014, green to March 2015, magenta to March 2016, red to May2016).

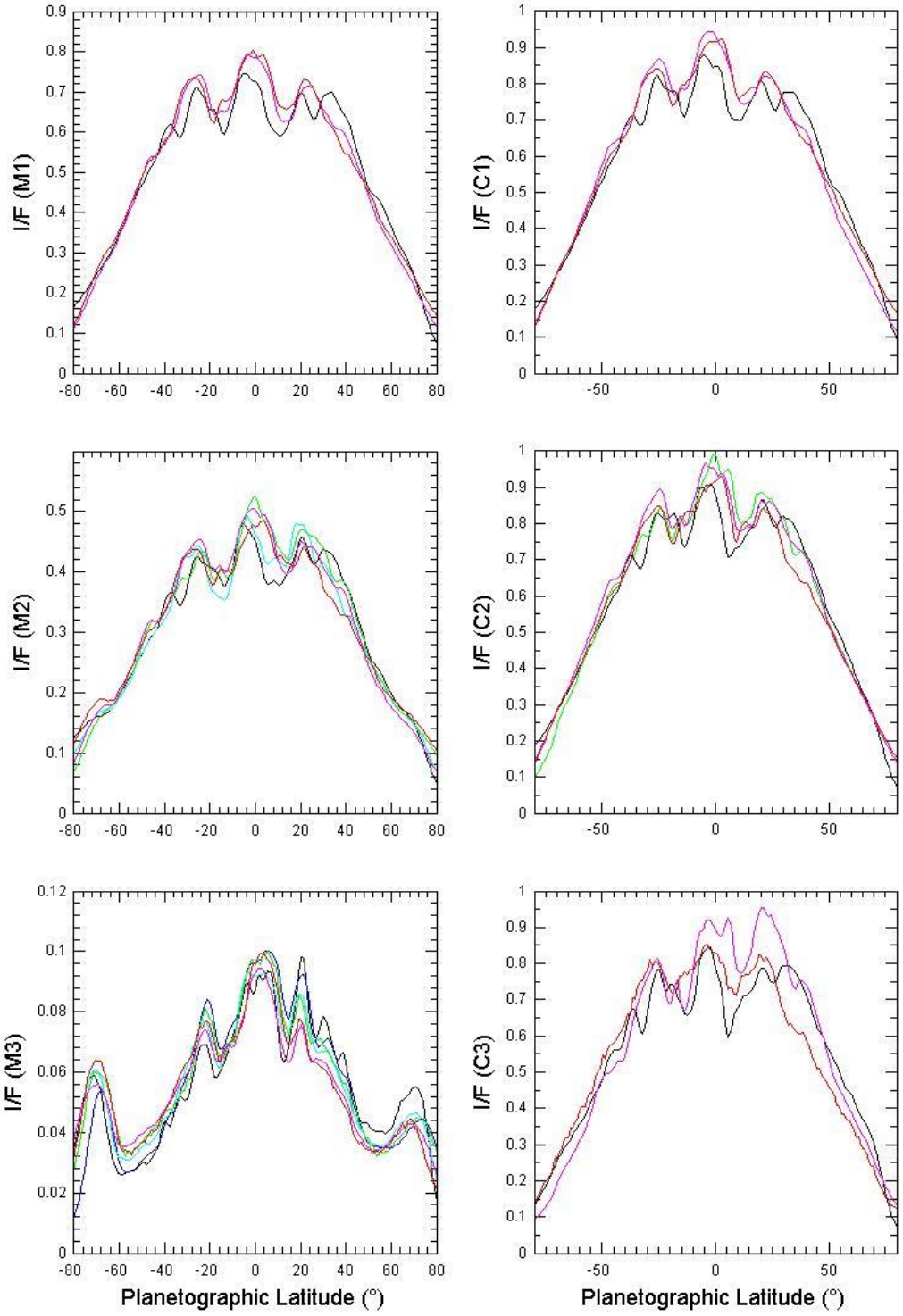

Absolute reflectivity of Jupiter from December 2012 to July 2016 in VIS channel methane and continuum filters (black corresponds to December 2012, blue to December 2013, cyan to April 2014, green to March 2015, magenta to March 2016, red to May2016).

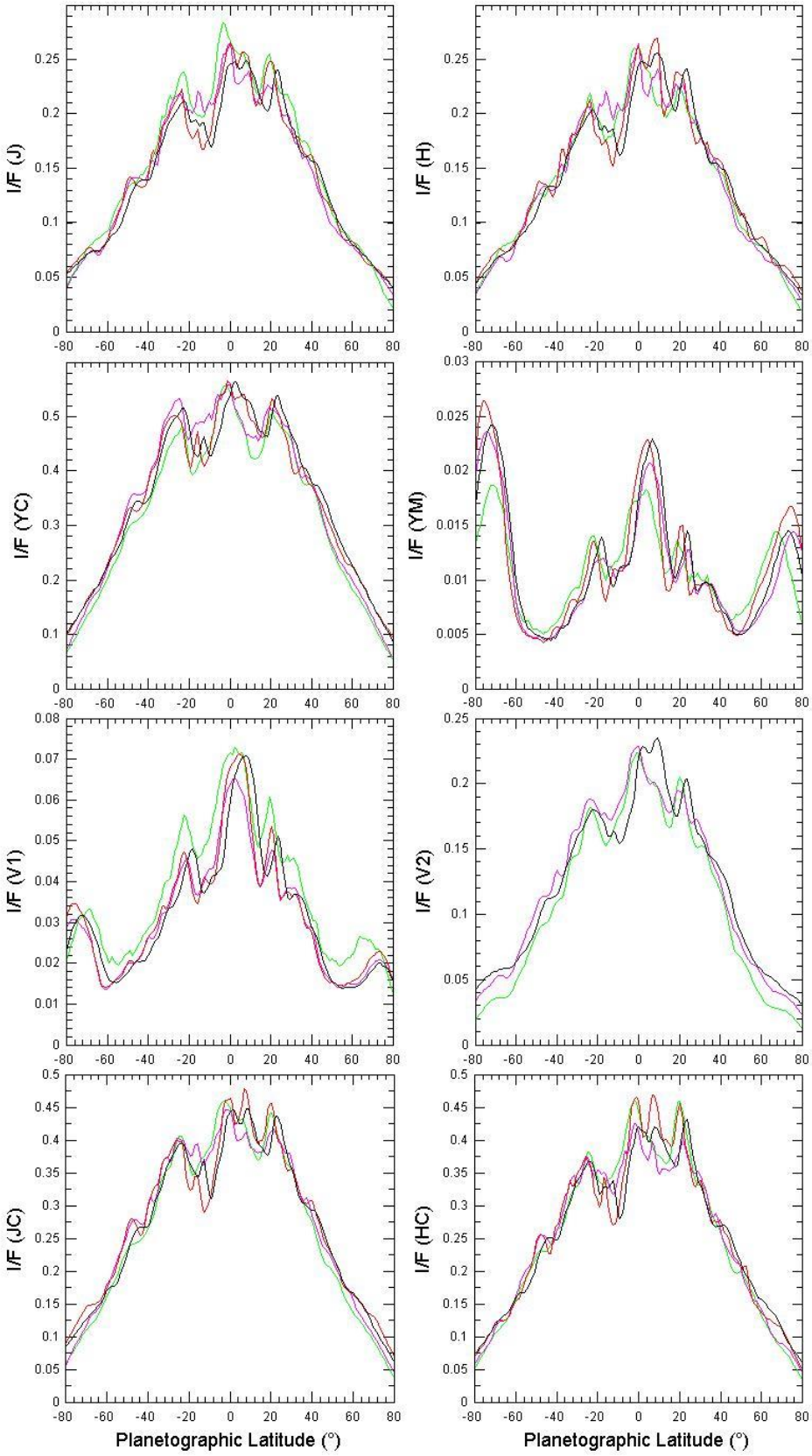

Absolute reflectivity of Jupiter from December 2012 to July 2016 in SWIR filters (black corresponds to December 2012, blue to December 2013, cyan to April 2014, green to March 2015, magenta to March 2016, red to May2016).

A4. Observation campaigns with PlanetCam

Observatory	Telescope	Instrument	Date
Pic du Midi	1m	PlanetCam 1	June 2012 (15-16)
CAHA	1.23m	PlanetCam 1	July 2012 (28-30)
CAHA	1.23m/2.2m	PlanetCam 1	Dec 2012 (2-3)
IAC	TCS	PlanetCam 1	Jan 2013 (17-21)
CAHA	1.23m	PlanetCam 1	April 2013 (17-20)
CAHA	1.23m	PlanetCam 1	May 2013 (24-28)
CAHA	1.23m	PlanetCam 1	Nov 2013 (21-24)
CAHA	1.23m/2.2m	PlanetCam 1	Dec 2013 (13-20)
CAHA	2.2m/1.23m	PlanetCam 1	April 2014 (5-10)
CAHA	1.23m	PlanetCam 1	May 2014 (12-15)
CAHA	2.2m	PlanetCam 1	July 2014 (21-25)
CAHA	2.2m	PlanetCam 2	Dec 2014 (11-13)
CAHA	1.23m	PlanetCam 2	March 2015 (2-4)
CAHA	2.2m	PlanetCam 2	May 2015 (21-25)
CAHA	2.2m	PlanetCam 2	July 2015 (10-13)
CAHA	2.2m	PlanetCam 2	Oct 2015 (27-28)
CAHA	2.2m	PlanetCam 2	Dec 2015 (28-30)
CAHA	2.2m	PlanetCam 2	March 2016 (3-7)
CAHA	2.2m	PlanetCam 2	May 2016 (16-20)
CAHA	2.2m	PlanetCam 2	July 2016 (1-5)
CAHA	2.2m	PlanetCam 2	Sept 2016 (15-19)
CAHA	2.2m	PlanetCam 2	Jan 2017 (11-18)
CAHA	2.2m	PlanetCam 2	March 2017 (27-30)

Pic du Midi: Observatoire du Pic du Midi
CAHA: Observatorio Astronómico Hispano-Alemán de Calar Alto
IAC: Instituto de Astrofísica de Canarias

A5. List of Publications

List of Publications related to PlanetCam instrument

Mendikoa I., Sánchez-Lavega A., Pérez-Hoyos S., Hueso R., Rojas J.F., and López-Santiago J. *Temporal and spatial variations of Jupiter's and Saturn's absolute reflectivity from 0.38 to 1.7 μm using PlanetCam-UPV/EHU* (2017). Astronomy & Astrophysics (submitted May 2017)

Mendikoa I., Sánchez-Lavega A., Pérez-Hoyos S., Hueso R., Rojas J.F., Aceituno J., Aceituno F., Murga G., De Bilbao L., García-Melendo E. *PlanetCam UPV/EHU: A two channel lucky imaging camera for Solar System studies in the spectral range 0.38-1.7 microns* (2016). Publications of the Astronomical Society of the Pacific, 128, doi: 10.1088/1538-3873/128/961/035002

Sanchez-Lavega A., Rojas J.F., Hueso R., Pérez-Hoyos S., De Bilbao L., Murga G., Ariño J. *PlanetCam UPV/EHU: a simultaneous visible and near infrared lucky-imaging camera to study solar system objects* (2012). Ground-based and Airborne Instrumentation for Astronomy IV, edited by Ian S. McLean, Suzanne K. Ramsay, Hideki Takami, Proc. of SPIE Vol. 8446, 84467X1-X9, doi: 10.1117/12.926149

Scientific Publications including contributions from PlanetCam

Hueso R. et al. *Jupiter cloud morphology and zonal winds from ground based observations before and during Juno's first perijove* (2017). Geophysical Research Letters, Special Section (Early Results: Juno at Jupiter), doi: 10.1002/2017GL073444

Sánchez-Lavega A. et al. *A planetary-scale disturbance in the most intense Jovian atmospheric jet from JunoCam and ground-based observations* (2017). Geophysical Research Letters, Special Section (Early Results: Juno at Jupiter), doi: 10.1002/2017GL073421

Sánchez-Lavega A. et al. *The long-term steady motion of Saturn's Hexagon and the stability of its enclosed jet-stream under seasonal changes* (2014). Geophysical Research Letter, 41, 1425-1431, doi:10.1002/2013GL059078

Sánchez-Lavega A. et al. *An enduring rapidly moving storm as a guide to Saturn's Equatorial jet's complex structure* (2016). Nature Communications 13262, doi:10.1038/ncomms13262

Sánchez-Lavega A. et al. *Venus cloud morphology and motions from ground-based images at the time of the Akatsuki orbit insertion* (2016). Astrophysical Journal Letters, 833, L7, doi:10.3847/2041-8205/833/1/L7

Hueso R. et al. *Neptune long-lived atmospheric features in 2013-2015 from small (28 cm) and large (10 m) telescopes* (2017). ICARUS (in press)

List of Conferences where PlanetCam has been presented

Sánchez-Lavega A. et al. *PlanetCam: A visible and near infrared lucky imaging camera to study planetary atmospheres and solar system objects*. (Poster)
SPIE 2012 Astronomical Telescopes + Instrumentation
Amsterdam (The Netherlands), 1-6 July 2012
SPIE Abstracts Conference 8446, p. 87

Sánchez Lavega A. et al. *PlanetCam: Una cámara para la observación planetaria usando la técnica lucky imaging*. (Oral)
X Reunión Científica de la Sociedad Española de Astronomía
Valencia (Spain), 9-13 Julio 2012

Sanchez-Lavega A. et al. *PlanetCam UPV/EHU: A lucky-imaging camera to study Solar System objects in the visible and near infrared* (Oral)
EPSC2012-216. European Planetary Science Congress 2012
Madrid (Spain), 23-28 Sept. 2012

Sanchez-Lavega, A. et al. *Planetcam: A Visible And Near Infrared Lucky-imaging Camera To Study Planetary Atmospheres And Solar System Objects* (Oral)
44th Meeting Division Planetary Sciences DPS-AAS
Bull. AAS, Vol 44 (No.5), 12, 196, 198, 214
Reno (USA), 14-19 October 2012

Sánchez-Lavega A. et al. *PlanetCam UPV/EHU visual arm characterization for solar system observations* (Oral)
EPSC2014-489. European Planetary Science Congress 2014.
Estoril (Portugal), 9-12 September 2014

Mendikoa I. et al. *Caracterización del canal visible de la cámara PlanetCam UPV/EHU para observaciones del Sistema Solar*. (Oral)
X Reunión Científica de la Sociedad Española de Astronomía
Teruel (Spain), 9-12 September 2014

Hueso R. et al., *PlanetCam UPV/EHU: Una cámara "lucky-imaging" para el estudio del sistema solar en el rango de longitudes de onda 0.38-1.7 micras* (Oral)
IV Reunión de Ciencias Planetarias y exploración del Sistema Solar (CPESS4)
Alicante (Spain), 8-10 June, 2015

Hueso R. et al. *Planetcam UPV/EHU – A lucky imaging camera for multi-spectral observations of the Giant Planets in 0.38-1.7 microns* (Oral)
EPSC Abstracts, Vol., 10. European Planetary Science Congress 2015
Nantes (France), 27 Sept – 3 Oct. 2015

Sanchez-Lavega A. et al. *Calar Alto PlanetCam and 14" CCD Monitoring in support to Juno Mission. Workshop on Earth-Based Observations to Support Juno Mission* (Oral)
47th Meeting Division Planetary Sciences DPS-AAS
Bull. AAS, Vol 47 (No.5).2015
National Harbor (USA), 8-13 November 2015.

Hueso R. et al. *Observaciones de Urano y Neptuno en telescopios españoles: Calar Alto/PlanetCam, WHT/Ingrid y GTC/Osiris* (Poster)
XII Reunión Científica Sociedad Española de Astronomía
Bilbao (Spain), 18-22 July 2016